

Editorial corner – a personal view

Challenges and opportunities of polymer recycling in the changing landscape of European legislation

Andrea Toldy* 

Department of Polymer Engineering, Faculty of Mechanical Engineering, Budapest University of Technology and Economics, Műegyetem rkp. 3., Budapest H-1111, Hungary
MTA-BME Lendület Sustainable Polymers Research Group, Műegyetem rkp. 3, H-1111 Budapest, Hungary

The European Union is committed to achieving sustainable growth and climate neutrality by 2050 through the [European Green Deal](#), with the [new circular economy action plan](#) adopted in 2020 as a key component. The transition to a circular economy is proposed by closing the loop of product life cycles through increased recycling and reuse, providing both environmental and economic benefits. The role of polymeric materials is essential in achieving these goals as ecodesign and recirculation of plastic products can substantially decrease waste generation and demand for raw materials and energy. Adopting the circular economy approach to polymers does not only mean reducing the negative impact on the environment but also fundamentally and comprehensively changing the way we design polymers. The circularity of the polymers is rooted in their tailored chemical structure and the design of polymeric systems enabling recycling. The material recycling of thermoplastic polymers is already an industrially viable method by simple mechanical recycling by melting and reprocessing. Therefore, the main challenges of this field involve developing inherently recyclable thermoset polymers (<https://doi.org/10.3144/expresspolymlett.2021.89>) and the design of easily recyclable thermoplastic polymer systems that allow the use of long-fibre reinforcement for structural applications (<https://doi.org/10.1016/j.polymdegradstab.2021.109797>). As most current applications of thermoplastics assume a very short









lifetime, in their case, the focus should be on recycling rather than increasing the lifetime. Therefore, enhancing the lifespan can be a relevant strategy, primarily in the case of thermosetting composites (<https://doi.org/10.3144/expresspolymlett.2022.81>) and can be achieved by a variety of approaches, e.g. structural health monitoring (<https://doi.org/10.1016/j.compscitech.2020.108317>, <https://doi.org/10.3390/polym11030523>) (including non-destructive testing) and repair during operation.

Although it is estimated that product design determines up to 80% of the environmental footprint of a product during its lifecycle, sustainable strategies are often not exploited to their full potential at the design stage. This is particularly true for polymer waste, where downcycling is the most common way of recycling, leading to quality degradation and a shorter lifetime. The additional functionalities introduced by upcycling can be key to increasing the industrial acceptance and uptake of recyclates. The high thermal stability and good fire resistance (<https://doi.org/10.3144/expresspolymlett.2018.17>) of polymers are crucial when replacing metals in structural applications to reduce weight. As the ‘[Proposal for a Regulation on circularity requirements for vehicle design and on management of end-of-life vehicles](#)’ of the European Union aims to set a mandatory recycled content target for plastics in newly type-approved vehicles of 25% by 2030, upcycling of secondary polymers will be a fundamental aspect in the future.

*Corresponding author, e-mail: atoldy@edu.bme.hu
© BME-PT

Research article

Four-dimensional printing of acrylonitrile butadiene styrene – thermoplastic polyurethane shape memory polymers with excellent material and interfacial adhesion performance

Kianoosh Soltanmohammadi¹, Mohammad Aberoumand¹, Davood Rahmatabadi¹,
Elyas Soleyman¹, Sogol Ghasemi², Ismaeil Ghasemi^{3*}, Majid Baniassadi¹,
Karen Abrinia¹, Mahdi Bodaghi⁴, Mostafa Baghani¹

¹School of Mechanical Engineering, College of Engineering, University of Tehran, Tehran, Iran

²Department of Polymer Engineering and Color Technology, Amirkabir University of Technology, Tehran, Iran

³Faculty of Processing, Iran Polymer and Petrochemical Institute, Tehran, Iran

⁴Department of Engineering, School of Science and Technology, Nottingham Trent University, Nottingham NG11 8NS, UK

Received 11 February 2023; accepted in revised form 11 July 2023

Abstract. There are a limited number of thermoplastics with intrinsic shape memory effect (SME) that are four-dimensional (4D) printable. Development of other shape memory polymers (SMPs) entails synthesis with a complicated chemical experimental lab effort. In this paper, for the first time, a novel layered multi-material structure is developed based on a deep comprehension of SMEs' macromolecular requisites. The fused deposition modeling (FDM) method is used for the four-dimensional printing of layered structures whose base materials show no SME. Commercial acrylonitrile butadiene styrene (ABS), toughened ABS-thermoplastic polyurethane (TPU) blend, and TPU, all with no SME, are used to fabricate bi-layers of ABS-TPU blends and TPU with different volumetric proportions. Different thermo-mechanical tests, including dynamic mechanical thermal analysis (DMTA), and constrained and free shape recovery, are conducted. Also, the interfacial properties of the layered 4D printed structure are assessed by the mean of shear testing and scanning electron microscopy (SEM). Experimental results reveal that the 4D printed bi-layer composites possess a high level of programmability, SME (90–96%), and perfect interfaces without any porosity and detachment between layers. The results of this research can potentially eliminate the desperate need for SMPs for 4D printing and broaden the opportunity to have smart parts using commercial thermoplastics.

Keywords: smart polymers, 4D printing, bi-layer structure, material testing, adhesion

1. Introduction

Additive manufacturing (AM) or three-dimensional (3D) printing is an emerging approach for fabricating prototypes or final parts with sophisticated geometries which cannot be produced by traditional manufacturing methods [1, 2]. This manufacturing technology has diverse usages in academics and distinctive fields of industry such as automotive, aerospace, soft robotics, fashion, and health care. The basic idea of 3D printing is the creation of a two-dimensional layer with a simple geometry on another layer to produce

a complex solid object [3, 4]. Fused deposition modeling (FDM) is the easiest, most controllable, and most efficient technique of AM to manufacture thermoplastic parts. Furthermore, because of the low cost of base materials in this technique, it is surprisingly economical [5]. The fundamental concept of its procedure is the extrusion of semi-liquid thermoplastic. In the last decade, there have been many prominent experimental and numerical investigations on the FDM technique related to improving the material properties of 3D printed parts [6] and multi-material

*Corresponding author, e-mail: i.ghasemi@ippi.ac.ir

© BME-PT

and gradient printing [7–9]. Multi-material FDM printing is related to printing different filaments by dual extruder printers [7, 9–11] or using continuous fibers embedded in filaments and printing them with an especially designed extruder [12, 13]. Of course, the manufacturing of composite shape memory polymers (SMPs) has also been developed to achieve non-thermal stimulation, such as electrical [14]. Shape memory materials (SMMs) are a kind of smart materials that have captivated industries and academic researchers for the last couple of decades. These materials' shapes can be converted in response to a specific stimulus [15]. The most important characteristic of the SMMs is the shape memory effect (SME), in which the original shape is 'memorized' and recovered freely without any additional mechanical force [16, 17]. SMPs are the most well-known types of SMMs due to their unique properties. Some of their features and advantages are: fixing and recovering large strains, high recovery rate, tailorable properties (e.g., transition temperature), programmability and controllability of recovery, low cost, lightweight, acquiring potential of biodegradability and biocompatibility, and vast types of stimuli including joule heating, electrical current, magnetic field, light exposure, UV exposure, moisture, pH and mechanical loading, etc. [18–20]. For manifestation SME, polymers must have net points or hard phase and soft phase. The hard phase is needed to form an integrated polymeric network that stores the strain energy and releases it in the recovery step for memorization of the permanent shape. These net points can be chemical crosslinks for thermosets and crystalline or molecular entanglements as physical crosslinks for thermoplastic polymers. The responsibility of fixing the temporary shape after the programming steps and recovering the applied deformation is due to the soft phase [21, 22]. Four-dimensional (4D) printing is a scientific horizon that is the integration of two concepts of AM and the capability to change the shape like an SME [23]. The dynamic properties of 4D-printed SMMs are related to the fourth dimension of printing. FDM is the most used technique in 4D printing [24, 25]. Nevertheless, only a few thermoplastic SMPs like polylactic acid (PLA) and polyurethane (PU) are 4D printable, and to make novel SMPs, additional operations such as blending polymers are needed [17, 26]. In this regard, based on the multi-material printing and the microscopic concept of SMPs, a shape memory bi-layer structure is developed here.

Acrylonitrile butadiene styrene (ABS) and thermoplastic polyurethane (TPU) are commercial filaments in 3D printing that are employed in this research. In multi-material printing, the adhesion of the polymers in joint surfaces is one of the most prominent points and is generally limited to three theories, including mechanical interlocking, diffusion, and thermodynamic theory of adhesion [27–30]. There are only a few experimental and numerical investigations on the adhesion of these two materials, specifically in the AM field. Harris *et al.* [31] printed a three-layered ABS/TPU/ABS structure. The shear test results suggested that TPU adheres to ABS, which was comparable to the commercial adhesive. Another achievement of their work was that the TPU layer adheres to lower ABS better than the upper ABS layer. The reason was that at the printing temperature of TPU (218 °C), the complex viscosity of this material is much lower than ABS at its printing temperature (240 °C). This phenomenon led to excellent interlocking and filling of voids in bottom-layered ABS with TPU. In contrast, the top layer of ABS could not establish the same interlocking as TPU. Yin *et al.* [32] conducted an experimental and numerical investigation on the interfacial bonding of ABS and TPU based on the diffusion aspect of adhesion. They evaluated the effects of building stage temperature, print speed, and nozzle temperature on the quality of the interfacial bonding of the ABS and TPU printed alongside each other. They have found that by increasing the building stage temperature from 30 to 68 °C, the bonding significantly improved from 0.86 to 1.66 MPa. By decreasing the printing speed and increasing the nozzle temperature, also the bonding was enhanced, but these parameters had minor effects. They also insisted that for diffusion, both materials must be above their glass transition temperature (T_g) during the printing of each layer. de León *et al.* [27] blended the ABS and TPU with different weight percentages (the blends contained 10, 20, and 30 wt% of TPU) to study the compatibility of these materials. Fourier transform infrared (FTIR) spectroscopy analysis in attenuated total reflectance mode (ATR), atomic force microscopy (AFM) and Raman spectroscopy were carried out in the study. The results showed a homogeneous distribution of ABS and TPU in the blends, probably due to hydrogen bonding supramolecular interactions between TPU polar groups and ABS acrylonitrile and aromatic moieties. AFM phase images presented that in the

blends with 10 wt% TPU, it was homogeneously distributed within the ABS matrix, while for blends containing 30 wt% TPU, it tended to form a continuous phase along the ABS matrix. They also printed tensile test specimens with the blend to obtain mechanical properties. Due to the observations, the presence of TPU improved interlayer adhesion without deterioration of yield strength for composition up to 20 wt%.

As it is aforementioned, ABS is the common filament for FDM, and it also has perfect mechanical properties. Due to the importance of producing functional objects, for example, actuators or shock absorbers, scientists have utilized distinctive approaches [33]. One of these approaches is the printing of flexible materials [34]. Therefore, ABS, as the common material, has been toughened with different elastomers and plasticizers in different examinations [27, 34, 35]. Also, the toughening of ABS through blending with another compatible material has another functional advantage which is the reduction of its T_g [34, 36]. de León *et al.* [27] blended ABS with 30 wt% of TPU. They could triple the elongation at the breaking point without any remarkable drop in yield strength in comparison to the neat ABS. Siqueiros *et al.* [34] developed a new filament with ABS and thermoplastic elastomer styrene ethylene butylene grafted with maleic anhydride (SEBS-*g*-MA). They melted and blended these two materials with distinctive concentrations and could increase the elongation at the break values from 8.5% for neat ABS to 50% for ABS/SEBS-*g*-MA 50/50 composition.

In this article, for the first time, 4D printed shape memory bi-layer structures were developed from a non-shape memory thermoplastic (ABS) and an elastomer (TPU). The generalization of SMPs' microstructural concept to a macrostructural structure is employed to achieve the SME in these 4D printed specimens. Also, in comparison to the previous investigations of multilayer SMPs produced by co-extrusion, these 4D printed structures benefited from the 3D printing's positive points, especially for producing complex geometries for applications like pipe fasteners. To achieve high deformability, reduce the T_g and improve the adhesion between the materials, ABS was blended with TPU at two different weight percentages (80 and 60 wt%). Bi-layer ABS-TPU structures were printed with different layer thicknesses of components, and SME (shape fixity, shape

recovery, and stress recovery) was investigated through constrained and free stress recovery. Additionally, a dynamic mechanical thermal analysis (DMTA), a shear test, and scanning electron microscopy (SEM) were conducted to scrutinize the thermal behavior and adhesion between TPU and the neat ABS and blends.

2. Experimental procedures

2.1. Materials and filament preparation

Commercial ABS granules were purchased from Baspar Chemi Sepidan Co, Ltd (Iran). Also, polyester-based TPU granules with the grade of 365A were prepared from Xiamen Keyuan Plastic Co., Ltd (China) to be used for ABS/TPU blends. A black-colored filament of TPU was obtained from Shenzhen Esun Industrial Co., Ltd. (China) that is printed as the elastomeric layer. Before starting any process, all of the materials were dried for 3 h at 80 °C. Different ABS-TPU blends were mixed by varying weight percentages of 365A TPU: 20, and 40% (in terms of ABS80, ABS60). The materials were blended using a Coperion twin screw extruder (Model ZSK-25, Coperion GmbH, Stuttgart, Germany) with an L/D of 40 and a screw diameter of 25 mm to produce a filament. The processing temperature window was between 200 to 220 °C with a screw speed of 70 rpm. The filament was cut into palettes. Then, neat ABS, ABS80, and ABS60 blend palettes were used to prepare FDM filaments with 1.75 mm diameter by a lab-made single screw extruder with an L/D of 15 and screw diameter of 15 mm with a speed and temperature of 30 rpm and 230 °C, respectively.

2.2. Printing procedure

A desktop two-nozzle FDM printer with a 0.8 mm nozzle diameter was employed to print all samples. The infill density of parts was 100% with a raster angle of 0° and layer thickness of 200 μm. For all bi-layer samples, the black-colored TPU was printed above the neat ABS and toughened ABS blend according to Harris *et al.* [31] investigations. Regarding Yin *et al.* [32] and de León *et al.* [27] experiments, the bed temperature was chosen to be 65 °C and the printing temperatures for neat ABS, toughened ABS blends, and the black TPU were set to be 240, 240, and 230 °C, respectively. Also, the printing speed for neat ABS and toughened ABS blends was 50 mm/s, and for the black TPU was 15 mm/s.

2.3. Dynamic mechanical thermal analysis (DMTA)

A thermal analysis was performed on the neat ABS and the ABS-TPU blends and the black-colored TPU to observe the storage modulus and the glass-rubbery transitional behavior at different temperatures. In this respect, a cantilever beam with a geometry of 40×10×1 mm was printed based on the ASTM D4065-01 standard. The test was carried out from –100 to 140 °C with a heating rate of 5 °C/min and a constant 1 Hz frequency by a dynamic mechanical thermal analyzer (Mettler Toledo GmbH, Switzerland).

2.4. Shape memory performance

For assessment of the shape memory performance of the bi-layer structures, the free and constrained shape recovery tests were executed in bending mode using a universal testing machine with a 1 kN load cell. A programmable logic controller (PLC) was employed to manipulate the temperature, heating, and cooling rates of the tests. All the bi-layer structures were printed in the geometry of 50×10×4 mm with three different ratios of TPU layer thickness to the ABS or ABS-TPU blend layer thickness (thermoplastic layer) listed in Table 1. The samples are bi-layer structures in which the thermoplastic was printed beneath the black TPU. For the free and constrained shape recovery tests, all of the samples were printed and tested three times to ensure the accuracy and repeatability of the findings.

2.4.1. Free shape recovery test

For programming, all of the twelve specimens (nine and three for shape recovery and stress recovery)

Table 1. Sample codes considering the used thermoplastic type, the thickness ratio of layers, and the structure layout.

Sample code	TPU/thermoplastic layer thickness ratio	Thermoplastic layer type
I	1:3	ABS
II	1:1	
III	3:1	
IV	1:3	ABS80
V	1:1	
VI	3:1	
VII	1:3	ABS60
VIII	1:1	
IX	3:1	

were constrained and heated to 85 °C at an 8 °C/min rate and remain in this condition for 120 s (heating step). Then a 7 mm deflection was applied to the samples at a rate of 3 mm/min (deformation step). Without any delay, the structures were quenched to ambient temperature at a rate of 30 °C/min and fixed in this circumstance for the next 240 s (cooling step). Afterward, the specimens were unloaded, and the fixity ratio was evaluated by Equation (1) (unloading step). For the shape recovery, samples were reheated to 100 °C with a high rate of 30 °C/min (recovery step). The recovery ratios were gauged after one minute of remaining at a high temperature using Equation (2). The explained cycle is a well-known SME programming cycle:

$$\text{Shape fixity ratio [\%]} = \frac{\text{Remained deflection}}{\text{Applied deflection}} \cdot 100 \quad (1)$$

$$\text{Shape recovery ratio [\%]} = \frac{\text{Recovered deflection}}{\text{Remained deflection}} \cdot 100 \quad (2)$$

2.4.2. Constrained shape recovery test

The constrained shape recovery test was executed for two-layer structures and only in the same ratio of TPU thickness to ABS thickness (Samples II, V, VIII). The three first steps of the test were exactly the same as the free shape recovery test. Then the samples were unloaded, and after holding the condition for a few seconds, the samples were confined again without any further deformation and reheated to 90 °C at the rate of 15 °C/min to examine the recovered force.

2.5. Shear test

The shear test was performed by a universal testing machine equipped with a 1 kN load cell and a sliding shear fixture. As depicted in Figure 1, the design of the fixture consists of two different pieces. A 5 mm depth groove and hole were craved on the first and second pieces. By sliding the two pieces on each other, pure shear is applied to the samples. The shear samples were designed considering the fixture geometry. The samples consist of two cubes with the geometry of 10×10×5 mm and 8×8×5 mm (Figure 1). The three reference samples of neat ABS, ABS80, and ABS60 and the three bi-layer structures consisting of them and the TPU layer were printed.

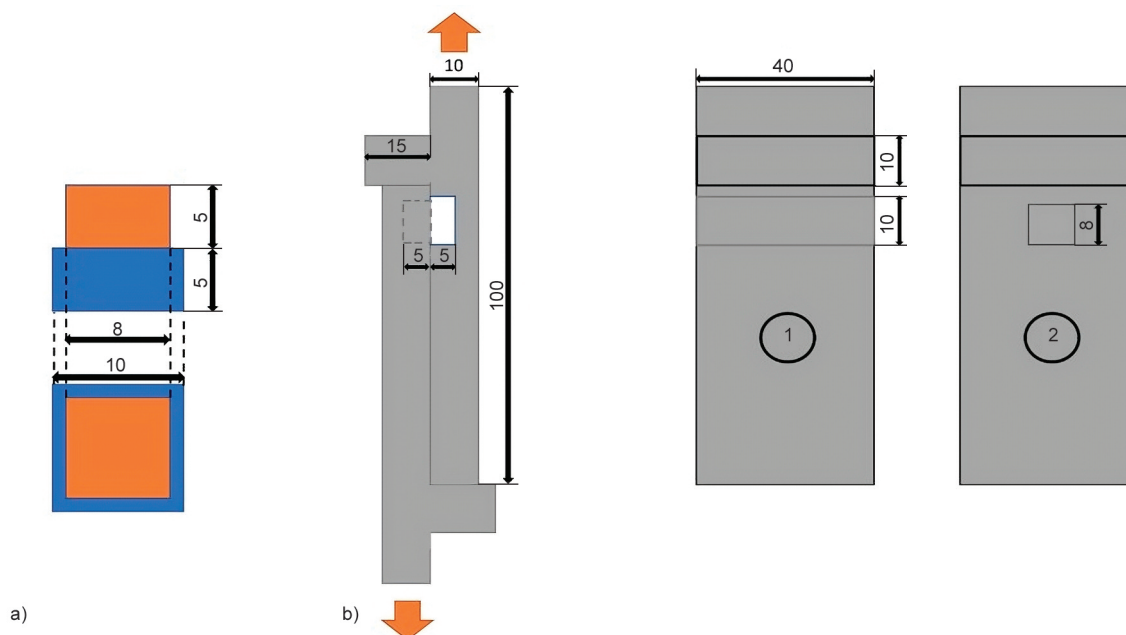


Figure 1. a) The dimensions of the shear test specimens, b) the dimensions of the sliding shear fixture, and the sliding direction (all in mm).

2.6. Scanning electron microscopy (SEM)

For the evaluation of the bond quality between the materials, imaging was also performed using SEM. Before imaging, the samples were frozen and broken down in liquid nitrogen and then coated with gold. Imaging was performed using Philips XL30 Scanning Electron Microscope (Koninklijke Philips N.V., The Netherlands) in secondary electron imaging mode.

3. Results and discussion

3.1. DMTA

The DMTA results of TPU are shown in Table 2. According to the storage modulus change, -40°C is the starting point of the glass-to-rubbery transition, and it continues until 25°C , demonstrating a wide transition range of 65°C . The $\tan \delta$ peak representing the T_g of TPU is about -1°C and its value is 0.32. Also, the storage modulus drops from 80 MPa at room temperature to 25 MPa at 85°C . This decreasing trend continues until 100°C , and the storage modulus reaches the least value of 19 MPa, which is consistent

Table 2. Storage moduli of TPU.

Quality	Temperature [°C]	Storage modulus [MPa]
Glass transition starting point	-40	2234
Glass transition ending point	25	80
Deformation point	85	25
Recovery point	100	19

with observations in [37]. The slight rise in the storage modulus of TPU during the cooling process in the shape memory cycle may slightly help the imposed strain to be stored. On the other hand, the slight increase in storage modulus upon cooling makes the TPU stiffer while it is in a rubbery state, causing the entropic force to be intensified with the same imposed strain. However, this intensified retracting force would not deteriorate the shape fixity because even the increased storage modulus of TPU at room temperature is far smaller than that of materials that possess high storage moduli in their glassy state at room temperature like ABS.

The storage modulus changes for ABS, ABS80 and ABS60 according to temperature are presented in Figure 2 and Table 3. As it is depicted in Figures 2a and 2b the glass-to-rubber transition of ABS starts from 90 to 135°C and $\tan \delta$ picks at 118°C (T_g). Also, α transition of this material occurs at 103°C , which is the middle point of the storage modulus's drop from 760 to 55 MPa. In addition, between 0 and 85°C , the storage modulus decreases from 995 to 780 MPa gradually. Also, there is a β transition for ABS between -85 and -62°C , which is consistent with observations in [37]. As aforementioned, de León *et al.* [27] reported superior compatibility between ABS and TPU, which can be distinguished in the DMTA results of ABS80 and ABS60 composites, as shown in Figures 2a and 2b. Initially, the glass transition of ABS80 and ABS60 read from 87 to

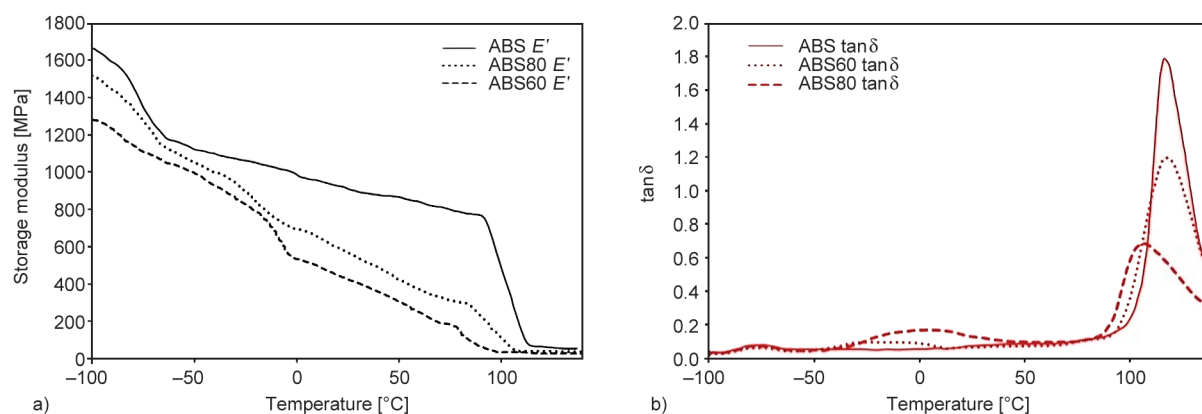


Figure 2. The results of the DMTA: a) the storage modulus, and b) $\tan \delta$ of ABS, ABS80, and ABS 60.

Table 3. The storage modulus changes according to temperature for ABS, ABS80, and ABS 60.

T [°C]	Storage modulus [MPa]		
	ABS	ABS60	ABS80
-85	1540	1400	1180
-62	1170	1110	10463
0	995	695	540
100	465	88	33
110	112	40	33
120	54	39	31

130 °C and 81 to 125 °C, respectively. Furthermore, with the increase of TPU content in the ABS matrix, the storage modulus of composite blends gets lower in the whole temperature range. Also, the reduction rate of the storage modulus in the β transition of ABS is slightly decreased for both composites. Moreover, there are additional drops from around -40 to 0 °C for both blends, especially in ABS60, which are associated with the contribution of the TPU's glass-to-rubber transition. Besides, significant continuous declining slopes in the storage modulus curves of composites are detected between 0 and 85 °C due to the corporation of TPU, which are from 695 to 270 MPa and 540 to 97 MPa for ABS80 and ABS60, respectively. Also, the glass and α transition temperatures of ABS80 are fallen to 114 and 95 °C, respectively. After surpassing the α transition temperature, the storage modulus dropped from 220 to 32 MPa. In the case of ABS60, the T_α is 87 °C, and the storage modulus decreases from 153 to 27 MPa during this transition. The T_g of this composite is 106 °C. The basic concept of the SMEs in this work, which will be discussed in the next section, is based on the storage modulus of hard material above the switching temperature, which is the α transition temperature of ABS, and both composites. Therefore, the

recovery occurs at 100 °C where the α transition is completed, and the storage moduli of ABS80 and ABS60 reach 88 and 33 MPa, respectively. This notable softening of the ABS blends at this temperature can lead to the effective release of the stress stored in the TPU layer during the recovery procedure.

3.2. Shape fixity and recovery

A comprehensive schematic representing the essential microstructural requisites for exhibiting SME is illustrated in Figure 3, separately for each programming step. The elastomeric (storing phase) and switching phase (hard material) layers in Figure 3 refer to TPU and different types of ABS, respectively. In this article, the hard phase as a network and the soft phase are generalized to a novel bi-layer macroscopic-designed SMP structure using multi-material printing and the basic microscopic concept of SMPs. These SMP structures are the assembly of a stiff non-shape memory thermoplastic with a high T_g and an elastomer with a lower T_g (below room temperature) on top of the former layer. To make a clear association between the microstructural requisites for exhibiting SME and the characteristics that belong to the proposed bi-layer, the physical state of each layer in each programming stage is shown in Figure 3. An SMP has two microstructural features that have powered it to emerge SME. First, there should be net points, forming an integrated network to restrict relative movements of the polymer chains and permanent deformations. In the designed bi-layer structure, these net points are formed from the interconnected hard phases in TPU as a thermoplastic elastomer. This feature of TPU has brought hyperelastic properties along with negligible permanent deformation. Second, there should be a phase transition for storing and relieving the applied deformation. In the bi-layer

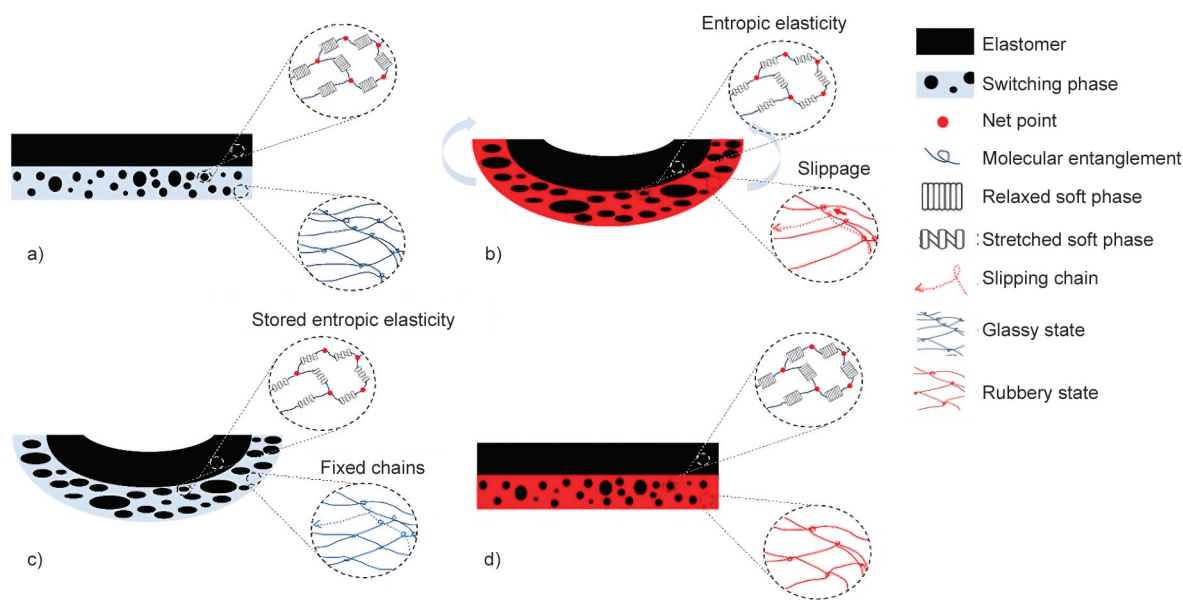


Figure 3. Schematic of samples during the shape memory cycle: a) as-printed condition, b) after heating and deformation, c) after cooling, d) recovery step.

structure, the glass transition of the polymer chains in the hard ABS layer acts similarly to an SMP. The collection of net points and phase switchable chains are found within the microstructure of an SMP. In the designed layered composite, the combination of two layers acts as a parallel spring system with the same amount of strain in each layer. The combination of the microstructural features of each layer and the parallel structural behavior can well be associated with the exact microstructural requisites that are found within an SMP. The thermoplastic is responsible for fixing the temporary shape in temperatures below T_g by the rubber-to-glass hardening transition accompanied by a substantial increase in modulus. During the programming steps, by deforming the structure, elastic stress emerges in the elastomer, and with the aid of the cooling of the deformed structure below the thermoplastic T_g , the elastic stress can be stored in the elastomer by the resists of the stiffed glassy thermoplastic. When the structure is heated above the thermoplastic T_g , the mentioned layer starts to soften, and the steep decrease in the storage modulus leads to the stored stress in the elastomer layer being released. During programming, the stress is applied to the structures, and the elastomeric layer has the duty of stabilizing most of the imposed stress thanks to the presence of an integrated network in its molecular architecture, restricting stress relaxation. Also, the thermoplastic is responsible for fixing the deflection due to its hardening behavior caused by reaching the glassy state of the material during the

cooling step (Figure 3c). The resistance of the thermoplastic layer to preserve the stored stress in the elastomeric layer (TPU) without a substantial spring back is reduced when its portion decreases. This alternation causes the structural stiffness to be lessened, which is well accompanied by a decrease in the shape fixity. In contrast, higher stress can be stored in the structure by raising the portion of the TPU layer. This phenomenon leads to a more complete shape recovery during the stimulation process (recovery step).

The shape memory performance ratios for different 4D printed bi-layer structures are named in Table 4 regarding the differences in hard material and the TPU thickness to hard material thickness ratio. All the fixed and recovered shapes of the samples are summarised in Figure 4. By comparing the samples in each set, decreasing and increasing trends are observed in shape fixity and shape recovery, respectively,

Table 4. Shape recovery and shape fixity of the samples.

Sample code	Shape fixity ratio [%]	Shape recovery ratio [%]
I	84.0	66.3
II	78.9	76.5
III	67.6	83.9
IV	94.1	87.4
V	88.6	90.5
VI	81.7	94.1
VII	89.7	93.0
VIII	86.1	94.7
IX	78.3	96.2

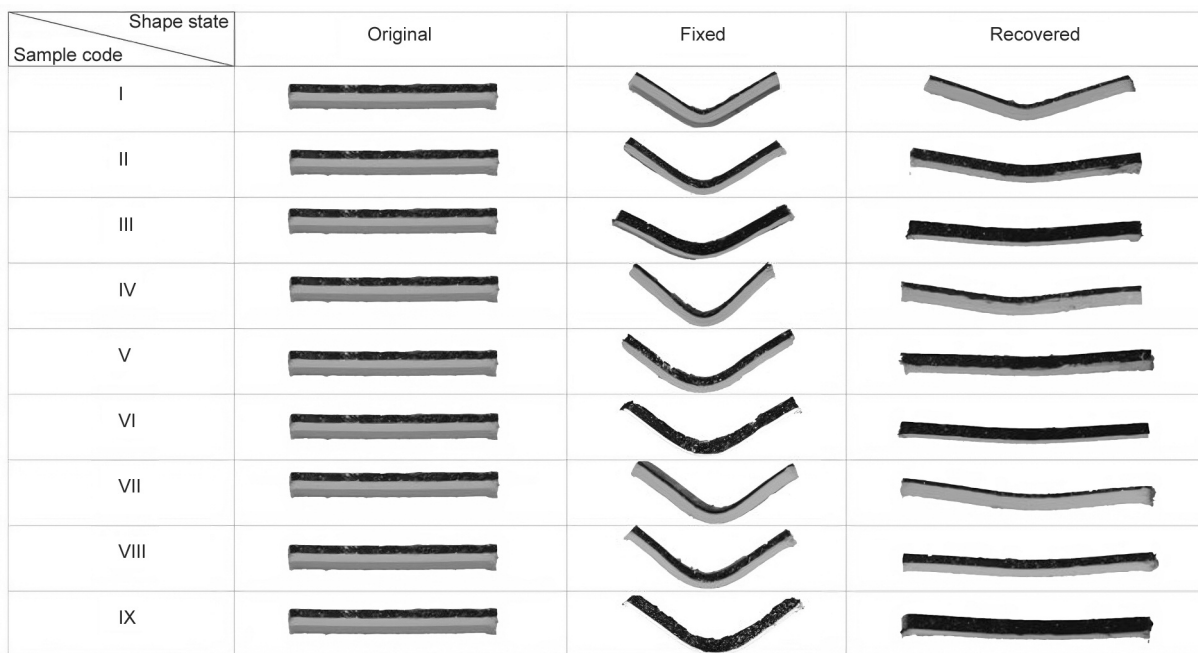


Figure 4. Fixed and recovered conditions of the coded samples.

regarding the increasing portion of the TPU layer thickness in these structures. The shape fixity ratios for the two-layer ABS-TPU structures in terms of TPU layer thickness are in the range of 67.6 to 84%, and the highest and lowest values are obtained for the highest and lowest TPU ratios, respectively. This trend is repeated for two ABS80 and ABS60 structures because increasing the layer thickness ratio of the ABS, due to its higher modulus, provides more resistance to relax the TPU layer. On the other hand, the highest amount of recovery ratio is also obtained for the lowest thickness ratio of the ABS layer because in the recovery step, the lower resistance means more recovery of the TPU elastic layer and the original shape. Shape recovery ratios are observed in the range of 66.3 and 83.9% for the two-layer structure. Shape fixity is improved in the second set compared to the first set, which is specifically related to different glass-rubber transitions of the neat ABS and ABS80. At the programming temperature (85 °C), the neat ABS structures are just at the start of their α transition, and most regions of these layers are glassy. The glassy regions can cause a more pronounced elastic and visco-elastic spring back of the structures after the unloading step at ambient temperature, which has been observed in previous sources [38]. Vice versa, the mentioned spring backs are much less in the structures with thermoplastic layers of ABS80 due to the lower temperature range of glass-to-rubber and α transitions as well as the less

portion of glassy regions in the thermoplastic layer, which contributed to the better shape fixity [39]. In the third set's samples, a drop in shape fixity compared to the second set can be observed. Less structural stiffness is achieved with the aid of the highest content of the TPU toughened into these thermoplastic layers of ABS60, which is linked to a lower shape fixity and excellent shape recovery, regardless of the thickness ratio of TPU to hard material [40].

Overall, the improving trend for shape recovery is correlated with the different glass-to-rubber regions of the neat ABS, ABS80, and ABS60 composites. As mentioned earlier, the glass-to-rubber transition is shifted to a lower range of temperatures by blending neat ABS with TPU elastomer. At 100 °C (recovery temperature), ABS60 shows the least storage moduli (33 MPa) among all three thermoplastics concerning DMTA results. This storage modulus is related to more softening of the thermoplastic composite layer at the recovery temperature, indicating weakened resistance for the release of the stored stress in the elastic layer and a resultant higher recovery ratio [40]. Also, the neat ABS and the ABS80 composites have storage moduli of 450 and 88 MPa at 100 °C, respectively, which results in a lower shape recovery ratio. From another point of view, the existence of more TPU content in the thermoplastics increases the portion of elastic material in the whole structure, which may aid in a better recovery ratio. Also, in videos 1 and 2, the programming,

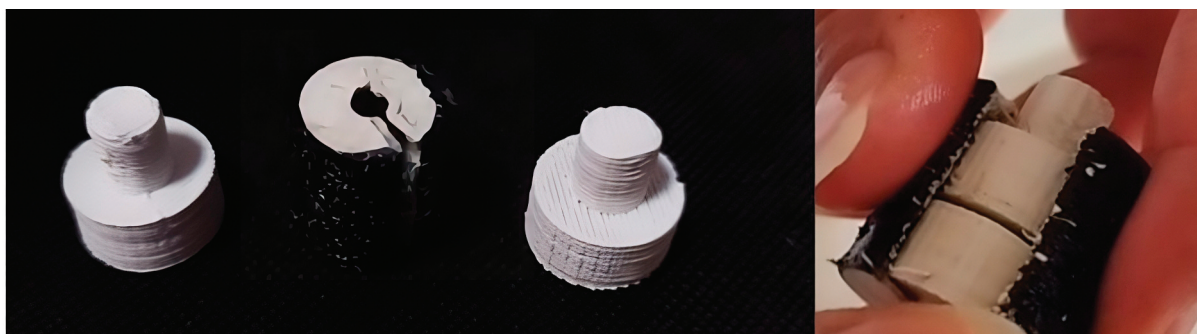


Figure 5. The customized tubular self-active bi-layer mechanical fastening.

fixity, and recovery steps of these two-layer structures can be seen.

Furthermore, a customized complex tubular self-active bi-layer structure as one of the most prominent applications of SMPs has been manufactured and presented in Figure 5. The structure is a mechanical fastening that can be used to fasten pipes [41].

3.3. Stress recovery

The stress recovery results of Samples II, V, and VIII are illustrated in Figure 6, respectively. The deformation stress of Sample II, which contains the neat ABS as the thermoplastic layer, is 10.8 MPa. Also, the maximum recovered stress for this specimen is 3.7 MPa, and it occurs at 87°C. For Sample V (ABS80 composite as a thermoplastic layer), a significant drop is observed in deformation stress which

is 5.5 MPa, and this can be related to the more softening of the ABS80 composite at the deformation temperature. This sample demonstrates a 2.45 MPa recovery stress which represents the recovery of a higher proportion of the deformation stress in comparison with the previous sample. This result is along with the earlier discussed results of the DMTA and shape memory performance that was attributed to the more softening of the thermoplastic composite layer, enabling the 4D printed bi-layer structure to recover the shape and force more intactly. The superior shape fixity of Sample V causes the TPU layer to store more of the deformation stress, and the excellent shape recovery helps this sample to recover a higher portion of the deformation stress.

Regarding DMTA results, the glass-to-rubber transition of the ABS80 composite starts at a lower

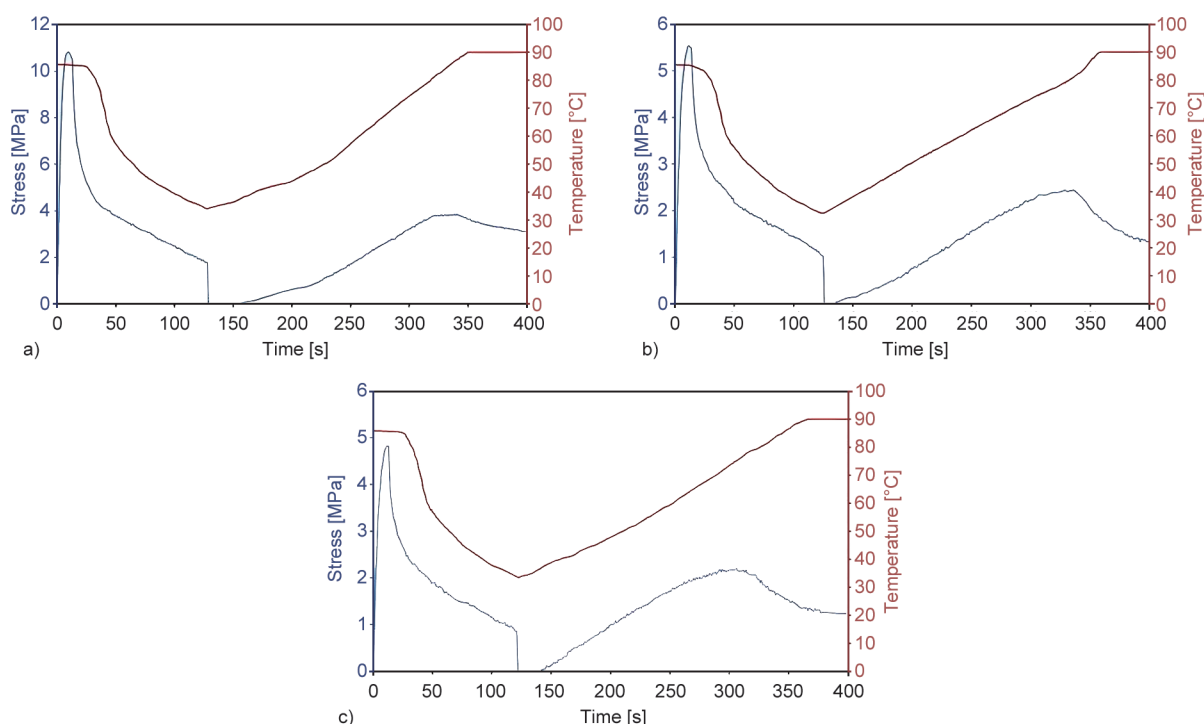


Figure 6. Stress recovery plots of the sample: a) Sample II, b) Sample V, and c) Sample VIII.

temperature. Therefore, the maximum recovery stress happens at lower temperatures of 81 °C. The last specimen's deformation stress is 4.82 MPa. This low deformation stress contributed to the smallest storage modulus of the ABS60 composite among all used thermoplastics. Furthermore, the maximum recovery stress is 2.21 MPa and occurs at 74 °C. Sample VIII is also shown a substantial stress recovery of the deformation stress, almost the same as Sample V because both samples have exhibited superior shape fixity and recovery ratios in close range to one another. By considering all of the plots, the stress in Samples V and VIII rises more sharply than the Sample II at lower temperatures. It is associated with the progressive decline of storage modulus observed in DMTA curves of the ABS80 and ABS60 composites all over the temperature range, and their lower storage modulus in each temperature leads to the release of stress progressively at lower temperatures which does not exist in the neat ABS. Moreover, by increasing the temperature, there are drops in stress after the stress recovery peaks for all samples. However, the drop for Sample II is obviously slighter than the two other specimens. This distinction is correlated to the storage modulus of the samples at 9 °C and the higher α transition temperature of the neat ABS. The prominent decrease in the storage modulus after the recovery peak results in more softening of the material and represents lower stress. For the neat ABS, the α transition starts at a high temperature of 86 °C (based on the DMTA curve). This phenomenon can cause a neglectable drop in the storage modulus and also a slight drop in the stress recovery plot for this structure. But for the other structures, due to the significant change in the storage modulus between the stress peak's temperature and 90 °C, the drops of stress in them are more obvious, causing a peak in stress recovery to be made, which is consistent with previous sources [38, 42]. These differences in actuation temperatures and stresses can provide us with a wide range of actuators for distinctive applications like grippers in soft robotics or pipe fasteners and splints in biomedical applications.

3.4. Adhesion

Figure 7 demonstrates the shear test results for each set of materials. As can be seen, the specimen that was made of the neat ABS shows the best shear strength, and its maximum shear stress is 21.70 MPa. Furthermore, there is a significant declining trend for

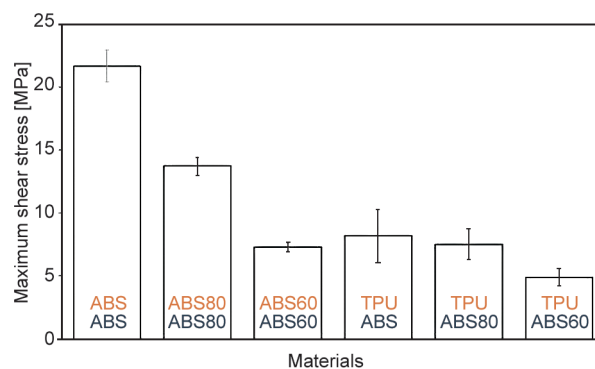


Figure 7. Maximum shear stress of each set of materials.

the maximum shear stress of the ABS80 and ABS60 specimens, which is associated with the softening of materials due to the incorporation of TPU in these composites. The maximum shear stresses are 13.70 and 7.30 MPa for ABS80 and ABS60 specimens, respectively. Also, there is a marginal descending trend for the maximum shear stress of bi-material structures. As it is depicted in Figure 7, the sample with the neat ABS and TPU has an 8.8 MPa maximum shear stress which is approximately 40% of the value associated with the ABS-ABS sample. These results have an excellent resemblance to Harris *et al.*'s [31] investigations of the maximum shear stress of ABS/ABS/ABS (15 MPa) and ABS/TPU/ABS (5 MPa). Based on the report of the comparison of the bi-material ABS-TPU structure with an industrial adhesive by Harris *et al.* [31], it can be deduced that the adhesion between the TPU and ABS is perfectly acceptable in this study. It is proof of the multi-material printability of these two materials for variant applications. Besides, the ABS80/TPU and ABS60/TPU structures manifest 7.2 and 4.5 MPa maximum shear stresses, which are about 50 and 60% of the values associated with relevant mono-material specimens, respectively. This ascending trend of these percentages could be related to the better adhesion of these composites to the TPU, which may be attributed to the presence of the dispersed TPU microdomains in the ABS matrix and the high affinity of the TPU layer to adhere to itself.

3.5. SEM

The interface of the TPU with the neat ABS and the composites printed layers is shown in Figure 8a–8c. As can be observed, there are excellent interfaces without any porosity and detachment between two materials in each image. Therefore, mechanical interlocking and filling all the voids and roughness of the

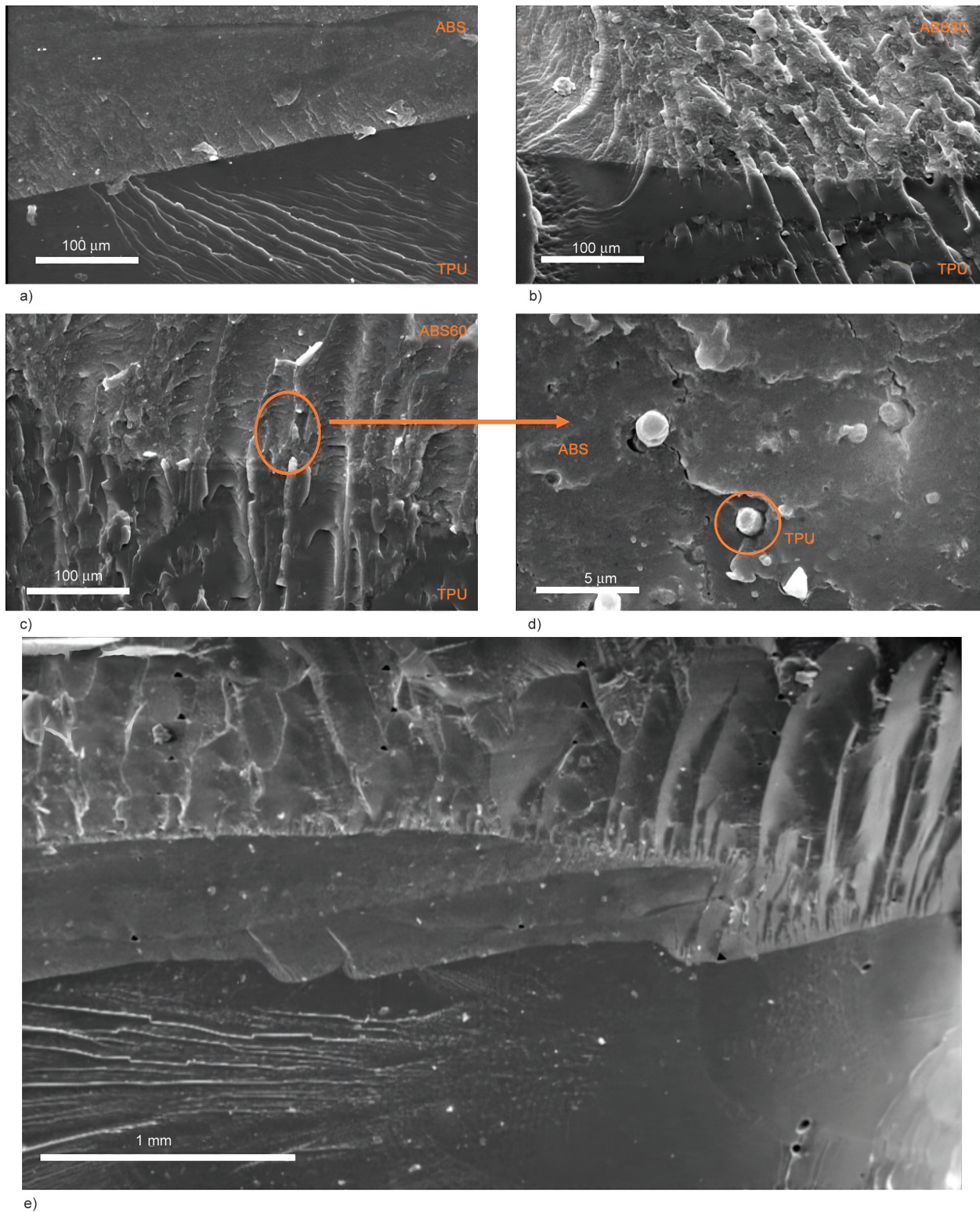


Figure 8. Scanning electron microscope of interface of a) ABS and TPU, b) ABS80 and TPU, c) ABS60 and TPU, d) morphology of the ABS60 composite; and e) bi-layer structure of the neat ABS and TPU.

thermoplastic layer's surface with the elastomeric material (TPU) is a promising approach for the good adhesion of the neat ABS and the blends with TPU. The reason for these phenomena is the low viscosity of the TPU at its printing temperature (220 °C). Also, as it was aforementioned, the TPU was printed on

the thermoplastics. Thus, during the printing procedure, high nozzle temperature (220 °C) and the hot extruded TPU may warm the surface of the thermoplastic up to even more than its glass transition temperature. Based on examinations of Yin *et al.* [32], the diffusion phenomenon can happen at the surface

of two polymers when the polymers reach above their glass transition temperatures. Concerning this matter, the TPU may have diffused into the neat ABS and the composites. In addition, Figure 8d shows the microscopic droplets of TPU in the ABS matrix. The average diameter of these droplets is 1 μm , which indicates the compatibility of the polyester-based TPU with the ABS [27]. Also, in Figure 8e, it can be seen that the bilayer specimens were printed in their best quality. Due to the low viscosity of TPU, the material was printed without any porosity. Furthermore, the thermoplastic layer has some neglectable voids between raster, but these voids don't deteriorate the shear stress results due to what was discussed above.

4. Conclusions

In this paper, a novel bi-layer macroscopic designed SMP structure was introduced using multi-material 4D printing and the basic microscopic concept of SMPs, hard and soft segments as network, and switching phases. The SME comes from the lamination assembly of stiff non-shape-memory thermoplastics like neat ABS, ABS80, and ABS60 composites and TPU elastomer TPU. Bi-layer ABS-TPU structures were 4D printed considering the thermoplastic and the thickness ratio of the constituent layers, and shape memory properties, thermal analysis, and microstructure were investigated. The below results were concluded.

- In the bi-layer structure, the thermoplastic is responsible for fixing the temporary shape in temperatures below its T_g by the rubber-to-glass hardening transition. During the programming steps, by cooling the deformed structure below the thermoplastic T_g , the elastic stress can be stored in the elastomer by the resistance of the stiffed glassy thermoplastic. When the structure is heated above the thermoplastic's T_g , the mentioned layer starts to soften, and the steep decrease in storage modulus leads to stored stress in the elastomer layer to be released.
- The highest shape fixity values (87.4 to 94.1%) were achieved for the ABS80. The reason for its superiority compared to pure ABS and ABS60 is the lower glass transition temperature and higher elastic modulus, respectively. On the other hand, ABS60 showed shape recovery ranges of 93% to 96.2% in the different thickness ratios of components, which is due to the more TPU phase.

The softening of the ABS80 and ABS60 composites at the deformation temperature caused the reduction of programming stress. The highest values of recovery ratio were obtained for ABS composites, which were 2.45 and 2.14 MPa for ABS80 and ABS60, respectively.

- Increasing the thickness ratio of the ABS layer caused more resistance against the release of the TPU layer in the programming step, and this trend was observed in all three bi-layer structures that, with the increase of ABS, fixity and recovery ratios increased and decreased, respectively.
- Neat ABS showed the best shear strength, and its maximum shear stress was 21.70 MPa. A significant declining trend for the maximum shear stress of the ABS composites was associated with the softening due to the incorporation of TPU in these composites. Besides, the ABS80/TPU and ABS60/TPU structures manifested 7.2 and 4.5 MPa maximum shear stresses, which were about 50 and 60% of the values associated with relevant mono-material specimens, respectively.
- The SEM results proved the excellent interfaces without any porosity and detachment between two ABS-TPU layers and mechanical interlocking, filling of all the voids and roughness of the thermoplastic layer's surface with the TPU was a promising approach for the good adhesion of the neat and ABS composites with TPU.

References



- [1] Soleyman E., Aberoumand M., Rahmatabadi D., Soltanmohammadi K., Ghasemi I., Baniassadi M., Abrinia K., Baghani M.: Assessment of controllable shape transformation, potential applications, and tensile shape memory properties of 3D printed PETG. *Journal of Materials Research and Technology*, **18**, 4201–4215 (2022).
<https://doi.org/10.1016/j.jmrt.2022.04.076>
- [2] Latif M., Jiang Y., Song J., Kim J.: Additively-manufactured high-concentration nanocellulose composites: Structure and mechanical properties. *Polymers*, **15**, 669 (2023).
<https://doi.org/10.3390/polym15030669>
- [3] Moradi M., Aminzadeh A., Rahmatabadi D., Rasouli S. A.: Statistical and experimental analysis of process parameters of 3D nylon printed parts by fused deposition modeling: Response surface modeling and optimization. *Journal of Materials Engineering and Performance*, **30**, 5441–5454 (2021).
<https://doi.org/10.1007/S11665-021-05848-4>

- [4] Rahmatabadi D., Soltanmohammadi K., Pahlavani M., Aberoumand M., Soleyman E., Ghasemi I., Baniassadi M., Abrinia K., Bodaghi M., Baghani M.: Shape memory performance assessment of FDM 3D printed PLA-TPU composites by Box-Behnken response surface methodology. *International Journal of Advanced Manufacturing Technology*, **127**, 935–950 (2023).
<https://doi.org/10.1007/s00170-023-11571-2>
- [5] Hassanien M., Alkhalder M., Abu-Nabah B. A., Abuzaid W.: A low-cost process for fabricating reinforced 3D printing thermoplastic filaments. *Polymers*, **15**, 315 (2023).
<https://doi.org/10.3390/polym15020315>
- [6] Rahmatabadi D., Soltanmohammadi K., Aberoumand M., Soleyman E., Ghasemi I., Baniassadi M., Abrinia K., Bodaghi M., Baghani M.: Development of pure poly (vinyl-chloride) (PVC) with excellent 3D printability and macro- and micro-structural properties. *Macromolecular Materials and Engineering*, **308**, 2200568 (2022).
<https://doi.org/10.1002/mame.202200568>
- [7] Leist S. K., Gao D., Chiou R., Zhou J.: Investigating the shape memory properties of 4D printed polylactic acid (PLA) and the concept of 4D printing onto nylon fabrics for the creation of smart textiles. *Virtual and Physical Prototyping*, **12**, 290–300 (2017).
<https://doi.org/10.1080/17452759.2017.1341815>
- [8] Vaezi M., Chianrabutra S., Mellor B., Yang S.: Multiple material additive manufacturing – Part 1: A review. *Virtual and Physical Prototyping*, **8**, 19–50 (2013).
<https://doi.org/10.1080/17452759.2013.778175>
- [9] Lumpe T. S., Mueller J., Shea K.: Tensile properties of multi-material interfaces in 3D printed parts. *Materials and Design*, **162**, 1–9 (2019).
<https://doi.org/10.1016/j.matdes.2018.11.024>
- [10] Tamburrino F., Graziosi S., Bordegoni M.: The influence of slicing parameters on the multi-material adhesion mechanisms of FDM printed parts: An exploratory study. *Virtual and Physical Prototyping*, **14**, 316–332 (2019).
<https://doi.org/10.1080/17452759.2019.1607758>
- [11] Li L., Liu W., Wang Y., Zhao Z.: Mechanical performance and damage monitoring of CFRP thermoplastic laminates with an open hole repaired by 3D printed patches. *Composite Structures*, **303**, 116308 (2023).
<https://doi.org/10.1016/j.compstruct.2022.116308>
- [12] Yang C., Wang B., Li D., Tian X.: Modelling and characterisation for the responsive performance of CF/PLA and CF/PEEK smart materials fabricated by 4D printing. *Virtual and Physical Prototyping*, **12**, 69–76 (2017).
<https://doi.org/10.1080/17452759.2016.1265992>
- [13] Gardan J.: Smart materials in additive manufacturing: State of the art and trends. *Virtual and Physical Prototyping*, **14**, 1–18 (2018).
<https://doi.org/10.1080/17452759.2018.1518016>
- [14] Yarali E., Baniassadi M., Zolfagharian A., Chavoshi M., Arefi F., Hossain M., Bastola A., Ansari M., Foyouzat A., Dabbagh A., Ebrahimi M., Mirzaali M. J., Bodaghi M.: Magneto-/ electro-responsive polymers toward manufacturing, characterization, and biomedical/ soft robotic applications. *Applied Materials Today*, **26**, 101306 (2022).
<https://doi.org/10.1016/j.apmt.2021.101306>
- [15] Leng J., Lan X., Liu Y., Du S.: Shape-memory polymers and their composites: Stimulus methods and applications. *Progress in Materials Science*, **56**, 1077–1135 (2011).
<https://doi.org/10.1016/j.pmatsci.2011.03.001>
- [16] Hager M. D., Bode S., Weber C., Schubert U. S.: Shape memory polymers: Past, present and future developments. *Progress in Polymer Science*, **49–50**, 3–33 (2015).
<https://doi.org/10.1016/j.progpolymsci.2015.04.002>
- [17] Soleyman E., Aberoumand M., Soltanmohammadi K., Rahmatabadi D., Ghasemi I., Baniassadi M., Abrinia K., Baghani M.: 4D printing of PET-G via FDM including tailor-made excess third shape. *Manufacturing Letters*, **33**, 1–4 (2022).
<https://doi.org/10.1016/j.mfglet.2022.05.002>
- [18] Xia L., Zhang M., Gao H., Qiu G., Xin Z., Fu W.: Thermal- and water-induced shape memory *Eucommia ulmoides* rubber and microcrystalline cellulose composites. *Polymer Testing*, **77**, 105910 (2019).
<https://doi.org/10.1016/j.polymertesting.2019.105910>
- [19] Melly S. K., Liu L., Liu Y., Leng J.: Active composites based on shape memory polymers: Overview, fabrication methods, applications, and future prospects. *Journal of Materials Science*, **55**, 10975–11051 (2020).
<https://doi.org/10.1007/s10853-020-04761-w>
- [20] Chen Y., Li J., Lu J., Ding M., Chen Y.: Synthesis and properties of poly(vinyl alcohol) hydrogels with high strength and toughness. *Polymer Testing*, **108**, 107516 (2022).
<https://doi.org/10.1016/j.polymertesting.2022.107516>
- [21] Xin X., Liu L., Liu Y., Leng J.: Mechanical models, structures, and applications of shape-memory polymers and their composites. *Acta Mechanica Solida Sinica*, **32**, 535–565 (2019).
<https://doi.org/10.1007/s10338-019-00103-9>
- [22] Meng H., Li G.: A review of stimuli-responsive shape memory polymer composites. *Polymer*, **54**, 2199–2221 (2013).
<https://doi.org/10.1016/j.polymer.2013.02.023>
- [23] Aberoumand M., Soltanmohammadi K., Rahmatabadi D., Soleyman E., Ghasemi I., Baniassadi M., Abrinia K., Bodaghi M., Baghani M.: 4D printing of poly(vinyl-chloride) (PVC): A detailed analysis of microstructure, programming, and shape memory performance. *Macromolecular Materials and Engineering*, **2023**, 2200677 (2023).
<https://doi.org/10.1002/MAME.202200677>

- [24] Wankhede V., Jagetiya D., Joshi A., Chaudhari R.: Experimental investigation of FDM process parameters using Taguchi analysis. *Materials Today: Proceedings*, **27**, 2117–2120 (2019).
<https://doi.org/10.1016/j.matpr.2019.09.078>
- [25] Rahmatabadi D., Ghasemi I., Baniassadi M., Abrinia K., Baghani M.: 4D printing of PLA-TPU blends: Effect of PLA concentration, loading mode, and programming temperature on the shape memory effect. *Journal of Materials Science*, **58**, 7227–7243 (2023).
<https://doi.org/10.1007/S10853-023-08460-0>
- [26] Huang X., Panahi-Sarmad M., Dong K., Cui Z., Zhang K., Gelis Gonzalez O., Xiao X.: 4D printed TPU/PLA/CNT wave structural composite with intelligent thermal-induced shape memory effect and synergistically enhanced mechanical properties. *Composites Part A: Applied Science and Manufacturing*, **158**, 106946 (2022).
<https://doi.org/10.1016/j.compositesa.2022.106946>
- [27] de León A. S., Domínguez-Calvo A., Molina S. I.: Materials with enhanced adhesive properties based on acrylonitrile-butadiene-styrene (ABS)/thermoplastic polyurethane (TPU) blends for fused filament fabrication (FFF). *Materials and Design*, **182**, 108044 (2019).
<https://doi.org/10.1016/j.matdes.2019.108044>
- [28] Packham D. E.: Surface energy, surface topography and adhesion. *International Journal of Adhesion and Adhesives*, **23**, 437–448 (2003).
[https://doi.org/10.1016/S0143-7496\(03\)00068-X](https://doi.org/10.1016/S0143-7496(03)00068-X)
- [29] Schultz J., Nardin M.: Theories and mechanisms of adhesion. in ‘Handbook of adhesive technology: Revised and expanded’ (eds.: Pizzi A., Mittal K. L.) CRC Press, Boca Raton, 3–18 (2017).
- [30] da Silva L. F. M., Öchsner A., Adams R. D.: *Handbook of adhesion technology*. Springer, Cham (2018).
<https://doi.org/10.1007/978-3-319-55411-2>
- [31] Harris C. G., Jursik N. J. S., Rochefort W. E., Walker T. W.: Additive manufacturing with soft TPU – Adhesion strength in multimaterial flexible joints. *Frontiers in Mechanical Engineering*, **5**, 37 (2019).
<https://doi.org/10.3389/fmech.2019.00037>
- [32] Yin J., Lu C., Fu J., Huang Y., Zheng Y.: Interfacial bonding during multi-material fused deposition modeling (FDM) process due to inter-molecular diffusion. *Materials and Design*, **150**, 104–112 (2018).
<https://doi.org/10.1016/j.matdes.2018.04.029>
- [33] Rahmatabadi D., Aberoumand M., Soltanmohammadi K., Soleyman E., Ghasemi I., Baniassadi M., Abrinia K., Bodaghi M., Baghani M.: Toughening PVC with biocompatible PCL softeners for supreme mechanical properties, morphology, shape memory effects, and FFF printability. *Macromolecular Materials and Engineering*, in press, 2300114 (2023).
<https://doi.org/10.1002/mame.202300114>
- [34] Siqueiros J. G., Schnittker K., Roberson D. A.: ABS-maleated SEBS blend as a 3D printable material. *Virtual and Physical Prototyping*, **11**, 123–131 (2016).
<https://doi.org/10.1080/17452759.2016.1175045>
- [35] Rocha C. R., Torrado Perez A. R., Roberson D. A., Shemelya C. M., Macdonald E., Wicker R. B.: Novel ABS-based binary and ternary polymer blends for material extrusion 3D printing. *Journal of Materials Research*, **29**, 1859–1866 (2014).
<https://doi.org/10.1557/JMR.2014.158>
- [36] Chávez A. F., Siqueiros J. G., Carrete I. A., Delgado I. L., Ritter G. W., Roberson D. A.: Characterisation of phases and deformation temperature for additively manufactured shape memory polymer components fabricated from rubberised acrylonitrile butadiene styrene. *Virtual and Physical Prototyping*, **14**, 188–202 (2018).
<https://doi.org/10.1080/17452759.2018.1550694>
- [37] Gnatowski A., Gołębski R., Sikora P.: Analysis of thermomechanical properties of polymeric materials produced by a 3D printing method. *Tehnički Glasnik*, **13**, 343–348 (2019).
<https://doi.org/10.31803/TG-20191102120738>
- [38] Soleyman E., Rahmatabadi D., Soltanmohammadi K., Aberoumand M., Ghasemi I., Abrinia K., Baniassadi M., Wang K., Baghani M.: Shape memory performance of PETG 4D printed parts under compression in cold, warm, and hot programming. *Smart Materials and Structures*, **31**, 085002 (2022).
<https://doi.org/10.1088/1361-665x/ac77cb>
- [39] Li G., Wang A.: Cold, warm, and hot programming of shape memory polymers. *Journal of Polymer Science Part B: Polymer Physics*, **54**, 1319–1339 (2016).
<https://doi.org/10.1002/polb.24041>
- [40] Du J., Armstrong S. R., Baer E.: Co-extruded multilayer shape memory materials: Comparing layered and blend architectures. *Polymer*, **54**, 5399–5407 (2013).
<https://doi.org/10.1016/j.polymer.2013.07.012>
- [41] Kim J-S., Lee D-Y., Koh J-S., Jung G-P., Cho K-J.: Component assembly with shape memory polymer fastener for microrobots. *Smart Materials and Structures*, **23**, 015011 (2013).
<https://doi.org/10.1088/0964-1726/23/1/015011>
- [42] Lim J. Y., Kim S. Y.: Thermal shrinkage stress in high-speed-spun, high molecular weight poly(ethylene terephthalate) filaments. *Journal of Polymer Science Part B: Polymer Physics*, **39**, 964–972 (2001).
<https://doi.org/10.1002/polb.1072>

Research article

Bio-based composites of sago starch and natural rubber reinforced with nanoclays

Jareerat Ruamcharoen^{1*}, Ruzana Munlee¹, Lapporn Vayachuta², Polphat Ruamcharoen³

¹Faculty of Science and Technology, Prince of Songkla University, Muang, 94000 Pattani, Thailand

²National Nanotechnology Center (NANOTEC), National Science and Technology Development Agency (NSTDA), Khlong Luang, 12120 Pathum Thani, Thailand

³Rubber and Polymer Technology Program, Faculty of Science and Technology, Songkhla Rajabhat University, Muang, 90000 Songkhla, Thailand

Received 6 May 2023; accepted in revised form 12 July 2023

Abstract. Sago starch (SS) was blended with natural rubber (NR) using nanoclays, namely montmorillonite (MMT), kaolinite (KAO), and kaolinite modified by dimethyl sulfoxide (KAO-D) to enhance its physical and mechanical properties. Each nanoclay was incorporated at 2, 4, 6, and 8 wt%, respectively. The SS80NR20 (80 wt% of sago starch and 20 wt% of natural rubber) biocomposites were characterized by solubility of water, water vapor transmission, mechanical and thermal properties. The constituent interaction and morphology of the SS80NR20 biocomposites were also presented by using X-ray diffraction (XRD) technique and scanning electron microscope (SEM). The findings demonstrated that the inclusion of clays significantly improved both the water resistance and tensile properties when compared to the SS80NR20 blend. In the SS80NR20 biocomposites, MMT at 6 wt% exhibited the lowest moisture content, solubility in water, and water vapor transmission. As the amount of nanoclay in the biocomposites increased, their tensile strength dramatically increased whilst their strain at break had a tendency to diminish. Strong interaction by establishing the intercalated structure of MMT, and KAO within SS80NR20 biocomposites were attributed to both physical and mechanical properties, while the weak interaction at the interface of SS and NR was attributed to KAO-D.

Keywords: sago starch, clay, natural rubber, biocomposites

1. Introduction

Utilizing natural resources effectively and creating innovative eco-friendly technology are the cornerstones of the sustainable development concept. As the environmental crisis and petroleum depletion grow more seriously and in response to the Sustainable Development Goals (SDGs) policy, chemicals and materials made from natural and recycled resources have attracted a lot of attention [1]. One of several strategies for minimizing the negative impact of petroleum-based plastic materials on the environment is the use of biodegradable materials for replacement of synthetic materials [2–7]. Due to its

naturally renewable nature, low cost, and wide availability, starch is one of the most prominent raw materials used to produce biodegradable materials. There have been many research studies on the development of starch-based films made from different starches *i.e.*, potato, and cassava starch including high-amylose starch [8–14], but there has been relatively few research on sago starch film formation and its application [15–17].

Sago starch is extracted from sago palm (*Metroxylon* spp.) which is distributed throughout Southeast Asia. It has distinctive features, nevertheless, some of its physicochemical characteristics are extremely

*Corresponding author, e-mail: jareerat.su@psu.ac.th

© BME-PT

comparable to those of typical starches like potato and cassava [17, 18]. The features of the hot paste and the temperatures are also extremely like potato starch, whereas the amylose amount and the temperatures of gelatinization are very similar to maize starches [18]. The intriguing thing about sago starch is that it contains more fiber, phenolic compounds, waxes, and lipids than other starches, which helps the starch film swell in water relatively slowly [17]. Therefore, it is possible that sago starch (SS) can be developed as a biopolymer film for packaging. Unfortunately, numerous limitations make sago starch-based polymers show poor inherent properties, such as relatively low mechanical properties, poor water resistance, and barrier properties [13–17].

To enhance their mechanical properties and minimize the dependence of their behavior on the presence of water, thermoplastic starches have, on the other hand, been successfully blended with other appropriate polymers to generate the interesting renewable polymer, associated with starch [19–23]. For instance, the blend of cassava starch (CS) with natural rubber (NR) is based on the different characteristics between CS and NR, resulting blend with distinctive properties different from the initial polymers are expected. NR is an emulsion (latex state) composed primarily of long linear chains of cis-1,4 polyisoprene and trace amounts of mineral salts, phospholipids, and glycoproteins. Chemical compatibility between starch and NR blend, which is currently very poor due to the hydrophobic-hydrophilic antagonistic relationship, is another factor that affects blend performance [19–23].

The mechanical properties of blends of starch and NR produced using conventional methods are considered extremely poor owing to incompatibility and poor water resistance. The apparent immiscibility of hydrophilic starch and hydrophobic NR, however, results in phase-separated blends with poor interfacial characteristics that can be solved by compatibilization [20–23].

Furthermore, gelatinizing starch is an effective method for improving the interfacial interaction between different phases. The addition of the compatibilizer is also generally preferred due to its ability to improve the system's properties. The addition of fillers into a binary polymer which is incompatible has been shown to influence phase morphology caused by the interaction of the blend's individual components with the solid surface. Organoclay has

been used as a reinforcing and compatibilizing filler in polymer blends [22–30]. The extent of the silicate nanolayer dispersion, as well as the clay type and elastomer compatibility, have all been found to have a strong influence on the properties of the compounds. Furthermore, the smaller size of the dispersed phase droplets was obtained. This suggested that the clay could act as a compatibilizer, decreasing the interfacial tension between the two polymer phases [24–28]. However, there are not many studies on NR disperse phase added to the starch in gelatinized form. Hydrophilic starch and hydrophobic NR are inherently incompatible, resulting in phase-separated blends with interfacial properties that can be improved by nanoclay compatibilization [22, 23].

In this research, preliminary experiments have already been performed by varying the ratios between sago starch and natural rubber as follows: 100:0, 95:05, 90:10, 80:20, 70:30 60:40, and 50:50 by weight, respectively. The addition of rubber into the blend was limited by phase separation. The appearance of which also depended on the glycerol content. It was found that the ratio of SS and NR with 80:20 is the ratio in which the minimum content of sago starch begins phase separation of both phases, resulting in a decrease in mechanical properties and water vapor permeability. This also agrees with other reports [19, 21]. Numerous factors, such as the distinctive formulation ratio of SS and NR (80:20), and the incorporation of nanoclays namely montmorillonite, kaolinite, and kaolinite modified with dimethyl sulfoxide as reinforcing agents, could contribute to the originality of the blend. These factors may contribute to improved physical and mechanical properties, such as increased tensile strength, enhanced flexibility, improved tear resistance, or better thermal stability. Regarding the applications, it would be valuable to highlight the potential industries or fields where the SS-NR blend could find utility. For example, it could be relevant in the development of biodegradable packaging materials, eco-friendly adhesives, or biomedical products with enhanced mechanical properties and biocompatibility [15, 17].

Additionally, gelatinizing starch is an effective way to increase the affinity at the interfaces between the different phases. Besides that, it is always desirable to enhance the properties of the blends through the addition of the compatibilizer. This research studied the effects of different types and amounts of nanoclays on sago starch blended with NR prepared

via a solution blending and casting process. The nanoclays were used in various amounts, and their effects on the structure and properties of the bio-based composites were characterized. The goals of this study were to identify the optimal nanoclay contents that provided the greatest properties and to elucidate the relationship between the structures and properties of various biocomposite film formulations.

2. Experimental

2.1. Materials

Sago starch was extracted from the starch granules found in the sago palm (*Metroxylon* spp.) in the southern part of Thailand. It comprises 23.9 wt% of amylose, 0.19 wt% of protein, 0.04 wt% of lipid, 0.13 wt% of lignin, and 0.54 wt% of acid detergent fiber. High ammonia natural rubber latex with 60% dry rubber content was purchased from Chana Latex company. Glycerol used as a plasticizer in starch was supplied from Ajax Finechem Pty Ltd. (Australia). Montmorillonite (MMT) and kaolinite (KAO) clays were purchased by Amarin Ceramics Co., Ltd. (Nonthaburi, Thailand). 100 g of clays (MMT and KAO) was dispersed in distilled water with a homogenizer at 15000 rpm for 1 h. The MMT and KAO clays were cleaned by soaking in a concentrated HCl solution overnight to remove the iron oxide. After that, white clay was collected by filtration and dried in an oven at 60 °C. Then it was kept in a container that was sealed. The kaolinite clay was modified by dimethyl sulfoxide to enhance the d-spacing of silicate layers of kaolinite [16].

2.2. Bio-based composite preparation

100 ml of de-ionized water and sago starch (80 wt% of starch) were dispersed in a beaker, and the mixture was continuously agitated at 80 °C to produce a homogenous solution and ensure even dispersion of all ingredients. After that, glycerol (30 wt% of starch) as a plasticizer was added to the gelatinized starch solution, and NR latex (20 wt% of dry rubber) was also mixed. Three types of nanoclay *i.e.* montmorillonite, kaolinite, and KAO modified with dimethyl sulfoxide (KAO-D) with various amounts of 2, 4, 6, and 8 wt% of starch were added and stirred for 1 h. The SS80NR20 blended solution was then poured onto the polyethylene plates and allowed to dry for 48 h at 50 °C. The thickness of the biocomposite film was then measured in five replications with a micrometer. All abbreviations of the formula used are

shown as follows: SS80NR20 represents the 80 wt% of sago starch and 20 wt% of natural rubber while SS80NR20MMT, SS80NR20KAO, and SS80NR20KAO-D represent 80 wt% of sago starch, 20 wt% of natural rubber containing MMT, KAO and KAO-D, respectively.

2.3. Bio-based composites characterization

2.3.1. Moisture test

The moisture content of SS80NR20 biocomposite films was determined according to ASTM D789 with some modifications. Five samples with 2.0×2.0 cm were weighed to gain the initial weight (W_0). Then, bio-based composite samples were dried in an oven at 110 °C and weighed every hour until constant weight (W_f). The percentage moisture content was given by Equation (1):

$$\text{Moisture content [\%]} = \frac{W_0 - W_f}{W_0} \cdot 100 \quad (1)$$

2.3.2. Water solubility test

The solubility of SS80NR20 biocomposite specimens was measured to gain the weight lost in the water. Five specimens with 2.0×2.0 cm were weighed as the initial weight (W_1). Then, specimens were immersed in distilled water at room temperature. After 24 h, the specimens were dried in an oven at 50 °C for 24 h and weighed to obtain the final weight (W_2). The percentage of solubility was calculated in the Equation (2):

$$\text{Water solubility [\%]} = \frac{W_1 - W_2}{W_1} \cdot 100 \quad (2)$$

2.3.3. Water vapor transmission test

Testing for water vapor transmission (WVT) was done in line with ASTM E96-80 (ASTM 1998). The top of the container was then tightly sealed with a piece of SS80NR20 biocomposite film. The biocomposite film was measured for thickness and diameter and placed in a 75% humidity chamber. The weight change of specimens was measured every 12 h until the sample weight remained constant. The water vapor transmission rate of the sample was calculated from the weight, diameter, and thickness of the film sample as Equation (3):

$$\text{WVT rate} = \frac{W}{A \cdot t} \quad (3)$$

where W is the weight loss of the cup [g], A is the water vapor transmission area [cm²], and t is the time of water vapor transmission [h].

2.3.4. Tensile measurement

Tensile testing was performed in accordance with ASTM 638. The modulus, tensile strength, and elongation at break of SS80NR20 biocomposite films were measured using a universal tensile testing machine (H10KS Hounsfield Test, Tinius Olsen Ltd., United Kingdom) with a 500 N load cell in tensile mode. For each formulation, at least 7 samples with rectangular samples (100×12×~0.25 mm) were clamped between the grips (30 mm initial distance), and tested with a speed of 50 mm/min. The stress and strain were recorded during the test.

2.3.5. X-ray diffraction measurement

Biocomposite specimens were analyzed by X-ray diffractometer (Philips X'Pert MPD, Netherlands) with Cu K_α radiation ($\lambda = 0.154$ nm), operating at 35 kV and 15 mA. The diffraction patterns were recorded from 2.5 to 50° at a scanning rate of 1.5°/min. The d -spacing (d) was calculated according to Bragg's law as shown in Equation (4):

$$2d \sin \theta = n\lambda \quad (4)$$

where n is the order of diffraction, θ is the diffraction angle and λ is the wavelength.

2.3.6. Morphological study

A morphology study was done at the tensile fracture surface of the SS80NR20 biocomposites by using a scanning electron microscope (Quanta 400 model) to observe the NR and nanoclays phase distribution and aggregation. The test specimens were attached to an aluminum mount with double-sided adhesive tape and sputtered with gold (10 nm thickness), on a Polaron SC 515 sputter coater to eliminate electron-charging effects. The samples were examined at an accelerating voltage of 20 kV in the vertical direction. Scanning electron microscope (SEM) micrographs of the biocomposite films were taken at 5000× magnification.

2.3.7. Thermal stability analysis

The thermal decomposition temperature of the SS80NR20 biocomposites was carried out by using

a Perkin Elmer TGA 8000 apparatus. The thermogravimetric analyzer (TGA) was operated at a heating rate of 10 °C/min from 50 to 600 °C under a nitrogen atmosphere.

2.3.8. Dynamic mechanical analysis

Rectangular specimens of the SS80NR20 biocomposites were conditioned for two weeks at 25 °C and 60±5% RH, before being tested using a dual cantilever clamp on a model DMA 1 (Mettler Toledo, Switzerland) dynamic thermo-mechanical analyzer. The measurement was performed at a frequency of 1 Hz and at an amplitude of 2 μm over a temperature range from –100 to 200 °C, at a scanning rate of 5 °C/min. The temperature dependence of storage modulus (E') and $\tan \delta$ was measured in the temperature range from –100 to 200 °C.

3. Results and discussion

3.1. Moisture content and solubility

When natural rubber was blended with sago starch, and clays a lower moisture content compared to pristine sago starch film was obtained as illustrated in Figure 1. It is due to the hydrophobicity of rubber. However, the result of incorporating clays as filler showed a slightly decreased in moisture content. The decrease in the number of water molecules in the internal of SS80NR20 biocomposites due to the insertion of polysaccharide chains of sago starch and rubber molecular chains in the silicate layer, leading to lower water molecule adsorption while kaolinite-added biocomposites absorbed more water molecules. It was due to the less distribution of clay in the biocomposite films. While adding KAO-D presented more decreased moisture content compared

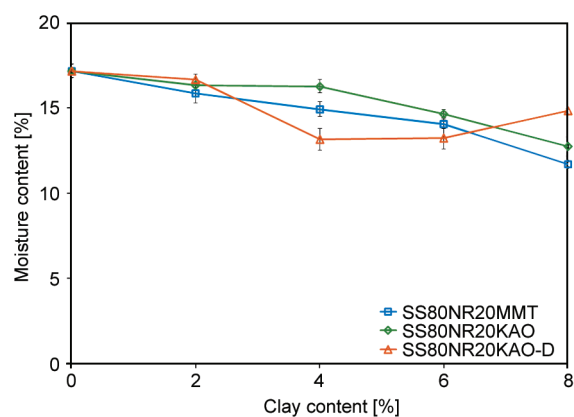


Figure 1. The moisture content of biocomposite films with MMT, KAO, and KAO-D.

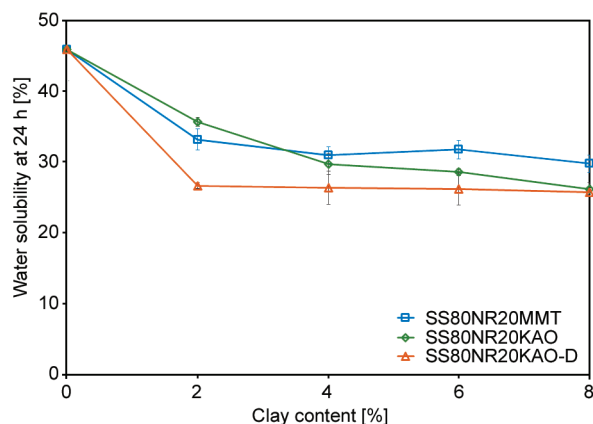


Figure 2. The water solubility of biocomposite films with MMT, KAO, and KAO-D.

with the SS80NR20 blend. This is expected that the silicate layer dispersion of KAO-D in the starch matrix led to diminishing the interaction of water molecules and the polysaccharide chain.

From [Figure 2](#), the escalation of NR to SS increased the water solubility of composites compared to the SS80NR20 blend because of poor compatibility between polar starch and non-polar rubber. However, the addition of clays tended to present that the water solubility of biocomposite films was reduced with the least water-soluble modified kaolinite added biocomposites. It was assumed that the internal structure of KAO-D displayed the separated silicate layers which are facilitated by a better dispersion of the clay in the polymer matrix (exfoliated structure), [16, 24] expecting in good distribution in SS80NR20 biocomposites. This was due to interactions at the interface of nanoclay and polymer whereas SS80NR20 biocomposites blended with MMT exhibited higher water-soluble than those of KAO and KAO-D added on account of the hydroxyl group of the glucose unit of sago starch absorbing the MMT. While MMT clay and rubber are less active, water molecules are easier to insert [8, 23]. Some studies reported a rise in the intermolecular forces between the film's respective components and speculated that hydrogen bonds generated between MMT, and starch chains were stronger than those formed between MMT and starch as well as water [25].

3.2. Water vapor transmission

In assessing SS80NR20 biocomposites for usage in protective coating for food packaging and other applications requiring efficient polymer barriers, the observed dramatic reduction in *WVT* is significant. The water vapor transmission of SS80NR20

biocomposites is exhibited in [Figure 3](#). It was demonstrated that the *WVT* of SS80NR20 biocomposites with the addition of MMT, KAO, and KAO-D was reduced as compared with SS80NR20 blend. In turn, this indicated that nanoclays could improve the *WVT* of SS80NR20 biocomposite films. Surprisingly, when MMT clay was incorporated into SS80NR20 biocomposites, the *WVT* at 24 h was significantly decreased as shown in [Figure 3a](#). *WVT* of the biocomposites with 2 wt% clay decreased by 55% compared to SS80NR20 biocomposites as well as the water vapor transmission slightly decreased with increasing time. A possible explanation for its effect could be that the glucose unit in sago starch was able to form hydrogen bonds with the hydroxyl group of MMT and its stronger structure improve water vapor transmission. This behavior agreed with previous reports [23, 31]. The *WVT* of SS80NR20 biocomposites containing MMT presented the lowest values, indicating that MMT might reduce the number of active sites where water molecules can interact with starch chains, and owing to the presence of dispersed large aspect ratio silicate layers in the polymer matrix as seen in other polymer-layered silicate composites [8, 26]. When kaolinite clay was added to the SS80NR20 biocomposites, it was obviously seen that the water vapor transmission decreased with the addition of 4 and 6 wt% of KAO and KAO-D clay compared to the SS80NR20 biocomposite film as illustrated in [Figures 3b, 3c](#).

It was noteworthy that the water vapor transmission increased with the incorporation of 8 wt% of KAO and KAO-D. This can be explained by the addition of 4 and 6 wt% clay, as well as the good distribution of KAO in the SS80NR20 composites. However, the increment in the amount of kaolinite clay generated the agglomeration of the silicate layer leading to a decrease in water vapor transmission. KAO-D decreased the *WVT* and gave the minimum *WVT* at 6 wt%. This is consistent with the biocomposite film morphology ([Figure 6i–6k](#)) as discussed in Section 3.5. It was found that the clay plates separated to form a silicate layer, the larger the volume resulting in better water vapor transmission. According to the materials' water vapor barrier capacity evaluation, the nanostructure of the SS80NR20 films reinforced with the nanoclay created a more tortuous path for the permeant gas to pass through. The molecules of water vapor diffused through the biocomposite film, following the path of low resistance. Due

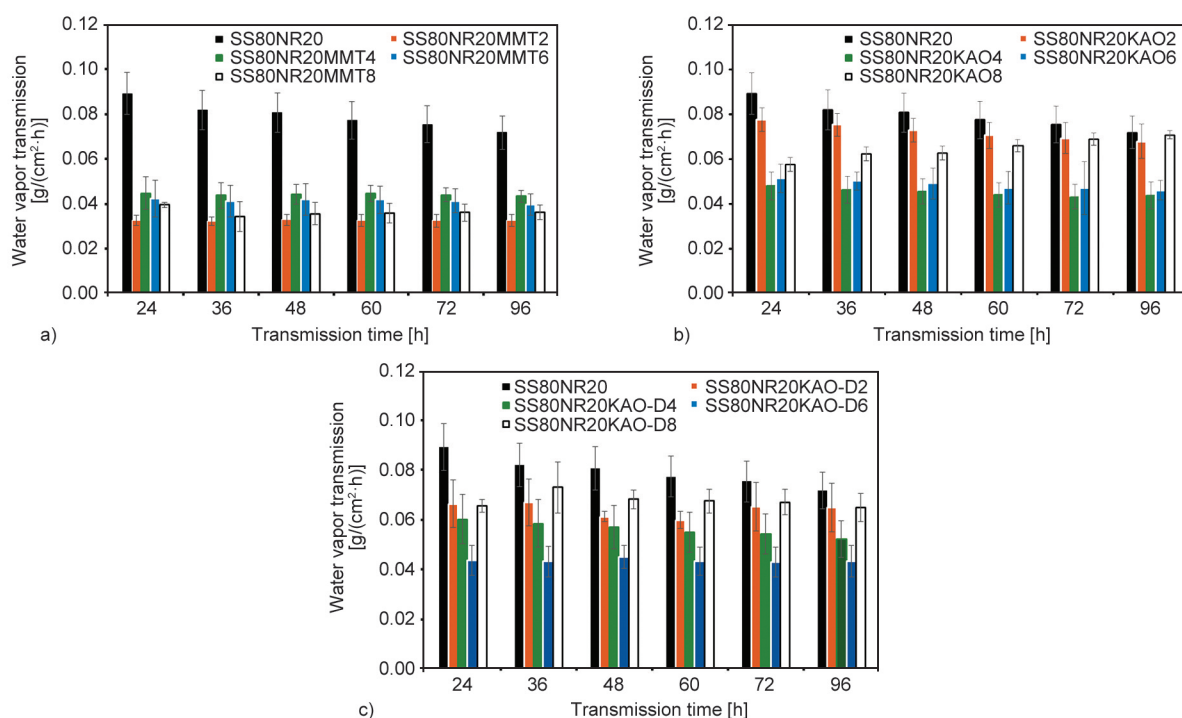


Figure 3. Water vapor transmission of biocomposite films with a) MMT, b) KAO and c) KAO-D.

to the lower specific surface area and the strong polymer/filler interaction of MMT, the *WVT* reduction was slightly greater than that of KAO and KAO-D [16, 23].

3.3. Tensile properties

Regarding the tensile properties of the SS80NR20 biocomposites, the average values of tensile strength, Young's modulus, and elongation at break are shown in Figure 4. Tensile strength and Young's modulus values exhibited a significant increment for the SS80NR20 biocomposites with the addition of MMT clay. With the variation of MMT content from 2 to 8 wt% in the SS80NR20 biocomposites, the change in the tensile characteristics can be explained more clearly as shown in Figure 4b. The maximum Young's modulus and tensile strength found for SS80NR20 biocomposites containing 6 wt% of MMT, were about 3 times higher than that of SS80NR20 blend. As observed in Figure 4b, Young's modulus for the SS80NR20 film was 23 MPa which was enhanced to 53.2 and 90.5 MPa for 2 and 6 wt% of MMT, respectively. The enhancement of the tensile strength of SS80NR20MMT composites might be caused by the strong surface interaction between MMT and the polymer matrix because of the intercalation of SS and NR in the clay silicate layer. This improvement of the tensile strength is likely to be due to the strong interfacial interaction between MMT and polymer

matrix caused by the intercalation of SS and NR into the clay silicate layers. It is indicated that the distribution of MMT in the self-assembled film is homogeneous [23, 26]. Interestingly, the elongation at break of MMT-filled SS80NR20 biocomposites was also significantly increased. It was possible through the insertion of polysaccharide and rubber chains into the silicate layer of MMT resulting in an intercalated structure as well as a mechanical interlocking between the polymer chain and silicate layer was formed [24, 26]. The tensile properties of KAO-filled SS80NR20 composites slightly increased. An increase in these properties may be due to the reinforcement of kaolinite clay, which was a structurally strong inorganic filler. The tensile strength of SS80NR20 biocomposites containing 4 wt% of kaolinite presented the maximum value when increasing kaolinite content markedly tended to decrease. However, for modulus at 1% strain, the SS80NR20 biocomposites gave the maximum value with 4 wt% of kaolinite. It can be explained that the more kaolinite content up to 6 wt% more coagulation of kaolinite clay was found. This corresponds to the results of X-ray diffraction analysis as shown in Figure 5b. It can be assumed that some polysaccharide and rubber chains can be inserted into the silicate layer of kaolinite acting as intercalated phenomena, while some silicate layers do not alter. This is owing to the very weak interaction between polymer

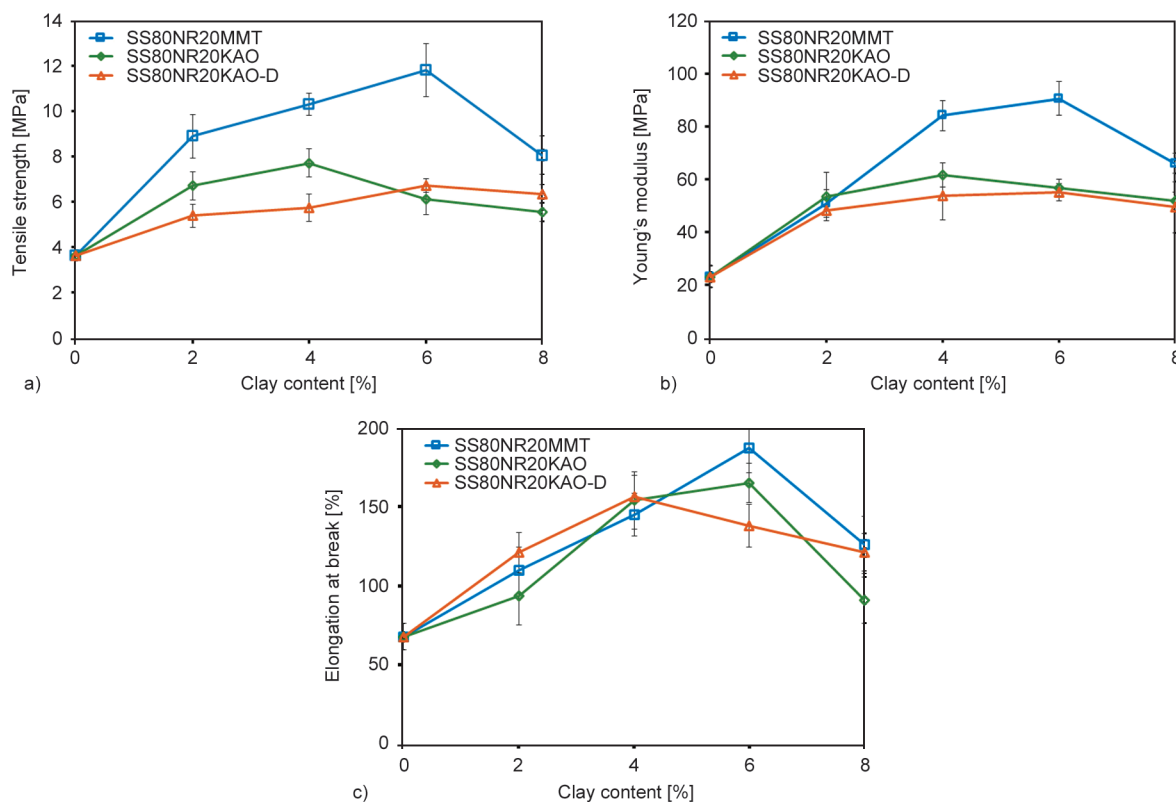


Figure 4. Tensile properties of biocomposite films; a) tensile strength, b) Young's modulus, and c) elongation at break.

and kaolinite clay as the interlayer space of kaolinite is an asymmetrical structure. The asymmetrical structure of $\text{AlO}_2(\text{OH})_4$ octahedral and SiO_4 tetrahedral sheets led to induce strong superposed polarity, in conjunction with hydrogen bonds between the silicon oxide and the alumina surface. As a result, the strong cohesive energy of the kaolinite mineral was reported [13, 16]. By comparing clay effects on the tensile strength and modulus of the SS80NR20 blend with the inclusion of an equal amount of clay (2, 4, 6, and 8 wt%), it was also revealed that the MMT had more reinforcing and compatibilizing effects on SS80NR20 blend. These can be attributed to the stronger interactions of the nanoclay with SS chains in comparison to rubber chains, as evidenced by the SEM results (Figure 6). The results shown in Figure 4c also indicated that the incorporation of the nanoclay into the SS80NR20 blend increased its elongation at break. It is attributed to the compatibilizing role of clay, which promotes interfacial interactions between the SS and NR components. For the SS-rich phase, the reinforcement of the interfacial interactions between the phases due to the presence of the nanoclay in the interface could positively influence their elongation at break. On the other hand,

the localization of the nanoclay in the individual phases, especially the matrix phase, and its interaction with the components decreased the mobility of chains and therefore could negatively affect the elongation at break. Surprisingly, when nanoclay was added to the SS80NR20 system, the elongation at break (*EB*) was markedly increased by the maximum *EB* when 6 wt% nanoclay was added in which the SS80NR20 biocomposites with the addition of MMT having the highest elongation at break of 3 times compared to the SS80NR20 film. The *EB* of 8 wt% of nanoclays in the SS80NR20 blend was significantly reduced. It can be explained that, at higher clay content, the clay particles have a greater tendency to interact and form aggregates. These aggregates can act as stress concentration points, minimizing the overall strength and mechanical properties of the blend. The presence of larger clay aggregates can create voids or weak points within the biocomposites (as seen in Figures 6e, 6h, 6k), leading to a decrease in mechanical performance. Additionally, at higher clay content in the blend, poor dispersion results in weak interfacial bonding between the clay and the polymer matrix, leading to reduce load transfer and lower mechanical properties. It is well known that

the physical and mechanical properties of native SS and NR components are very weak in the absence of compatible or reinforcing agents. Therefore, the physical and mechanical properties of the mixture are also inferior, and this is mainly due to the incompatibility of the two components with each other. The mechanical properties are in accordance with the morphology in Section 3.5.

3.4. Nanoclays dispersion in biocomposites

The X-ray diffraction patterns of SS80NR20 biocomposites are shown in Figure 5. After solution blending, the diffraction character of SS80NR20 biocomposites indicated amorphous sago starch with broad, featureless peaks throughout the whole 2θ scanning range. The X-ray diffraction (XRD) pattern of biocomposites; however, exhibited the MMT-specific peaks with the addition of layered silicates. The MMT presented a diffraction peak crystal plane 001 at $2\theta = 6.92^\circ$ corresponding to the d_{001} of 1.28 nm, whereas the 001 diffraction peaks of MMT in the biocomposites shift toward lower angles, *i.e.*, 6.92° to 5.37° , 5.12° , and 4.87° , which indicated that the interlayer distances increased as shown in Figure 5a. The basal spacings of the MMT were calculated from the XRD peak position using Bragg's equation,

where the d_{001} of MMT in the biocomposites was found to be in the broader range of 1.64 to 1.81 nm. The lateral dimensions of this structural amylose unit were approximately 1.5 nm for each elementary chain, while the *cis*-1,4 polyisoprene structure was approximately 1.5 nm for each chain. The result implied that intercalation of the polysaccharide of SS and rubber chains into the silicate interlayers occurred and expanded the basal spacing. All polymer-clay nanocomposites have XRD patterns that were suggestive of an intercalated structure in which the polysaccharide chains or rubber incorporated between the silicate layers, expanding their gallery height but preserving their layered stacking with interchanging biopolymer/silicate layers as described in a previous report [23, 25].

Characteristic diffraction peaks of the purified KAO can be observed at $2\theta = 8.92^\circ$, 12.37° , and 24.9° . The X-ray diffraction patterns of SS80NR20 biocomposites loading kaolinite clay are shown in Figure 5b. The increase in the kaolinite content in the SS80NR20 biocomposites led the peaks at 8.92° and 12.37° to be more intense, suggesting that the pseudo-crystals were still present. Especially, the intensity of peaks at 8.92° presenting in the SS80NR20 biocomposites revealed the intercalated structure of

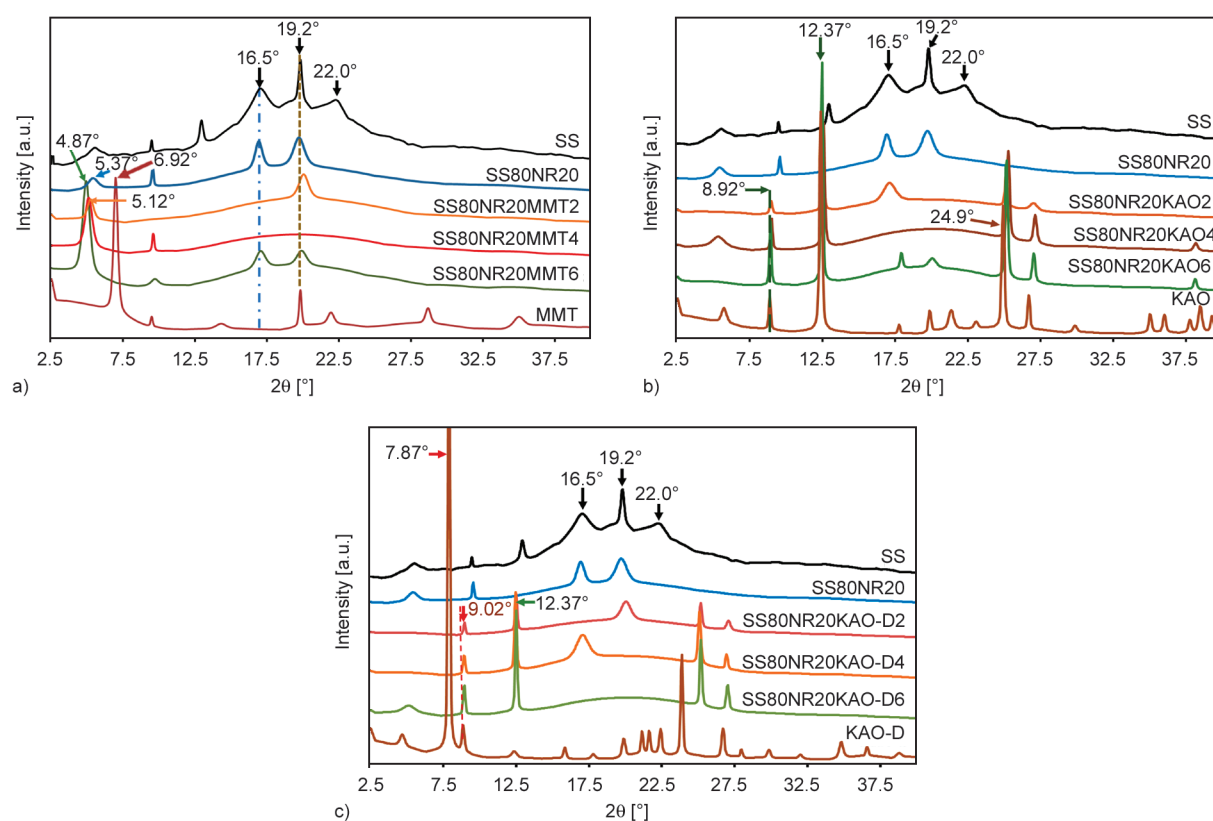


Figure 5. XRD pattern of biocomposite films with a) MMT, b) KAO, and c) KAO-D.

silicate layers by the insertion of some polysaccharide and rubber chains in the silicate layer of kaolinite [13, 16, 23]. Nonetheless, the disappearance of the 7.87° in the dimethyl sulfoxide (DMSO) intercalated kaolinite (KAO-D) in the SS80NR20 biocomposites implied that this component was almost disorganized (Figure 5c). It was found that when added KAO-D, a peak at position 12.37° presented, and more intensity of this peak was observed, while peak 7.87° disappeared. It can be explained that the KAO-D gave more reorganized its silicate layer to form the compact silicate layers in the SS80NR20 biocomposites. This is due to the kaolinite intercalation process explained as a diffusion process, the driving force of which is strong hydrogen bonds formed between the intercalation agent and the hydroxyl group ($-OH$) of the octahedral sheet. The release of the original crystal interlayer bonds could be a primary or a secondary effect of the intercalation agent. A large dipole moment of organic compound combined with a significant number of intercalated molecules per unit cell favors the formation of an intercalation complex. Therefore, the conventional intercalation agents consisting of both dipole moment and polarizability of glycerol and DMSO with lower values than that of kaolinite are not suitable to intercalate the finer structure of kaolinite. Therefore, in the system there is glycerol, which is more polar than DMSO, thereby reducing the activity rate within the silicate layer, leading to the restoration of the original structure again. As a result, the mechanical properties and water vapor transmission of the SS80NR20 biocomposites adding KAO-D clay were therefore reduced.

3.5. Morphological study

Starch and natural rubber have different properties, and when blended, their stability can be influenced by composition and processing techniques since starch is hygroscopic which can absorb moisture from the surrounding environment. To improve stability, glycerol as a plasticizer [19] and clays were added to the blend to reduce moisture sensitivity [16, 23, 25]. SEM micrographs of the SS80NR20 biocomposites are shown in Figure 6.

The separated phase boundaries of the SS80NR20 blend and clays are seen. The fracture surface of SS and SS80NR20 in Figures 6a, 6b were fairly smooth. The SEM micrographs show rubber particles on the surface of the biocomposite that has undergone tensile fractures, indicating that the compatibility of NR

and SS is less. The surface roughness of the SS80NR20 composite films increased with the nanoclay content. Figure 6c–6k confirmed that the addition of nanoclays with 2, 4, and 6 wt% in the SS80NR20 blend had a significant effect on fracture morphology and behavior. The distinctive phase boundaries of the SS and NR blend can be clearly seen, and they gradually diminished with the addition of 2 and 4 wt% of clays. This suggested that nanoclays may act as interfacial interfaces. It reduced the inter-surface tension by simultaneous dissociation of the NR phase and resulted in a reduction in particle size [23, 27]. It may be inferred that the MMT and KAO clays can help SS and NR become compatible with each other. However, some agglomeration of modified-kaolinite clay particles can also be seen in Figure 6i–6k. The agglomerating domains of KAO-D clay which are highlighted in yellow circle particles may cause the reduction of tensile strength and elongation at the break of biocomposites. The high surface area and strong interfacial interactions of nanoclays with both starch and natural rubber can promote better interfacial adhesion, leading to improved blend stability.

3.6. Thermal stabilities

Due to their inherent configuration characteristics, inorganic materials exhibited greater thermal stability and thermal resistance qualities than organic ones. Hence, incorporating inorganic particles into polymers could significantly increase the thermal stability of composites consisting of natural polymers. Figure 7 depicts the thermogravimetry (TG) and derivative thermogravimetry (DTG) curves of biocomposites containing 4 wt% of MMT, KAO, and KAO-D. A preliminary weight loss was observed between 30 and 115°C . The evaporation of the water accounted for the weight loss. Three steps of decomposition were observed for biocomposites. The onset and peak temperatures were determined as shown in Table 1. Water loss occurred in the first step at temperatures below 100°C , whereas starch degradation occurred in the second step at temperatures about $270\text{--}340^\circ\text{C}$, and degradation of NR was presented in the temperature range of $360\text{--}430^\circ\text{C}$ as shown in Figure 7a. When nanoclays were mixed with SS80NR20, their decomposition temperatures increased indicating an improvement in the stability. Similar trends have been seen, with the stability improvement being ascribed to the strong interactions

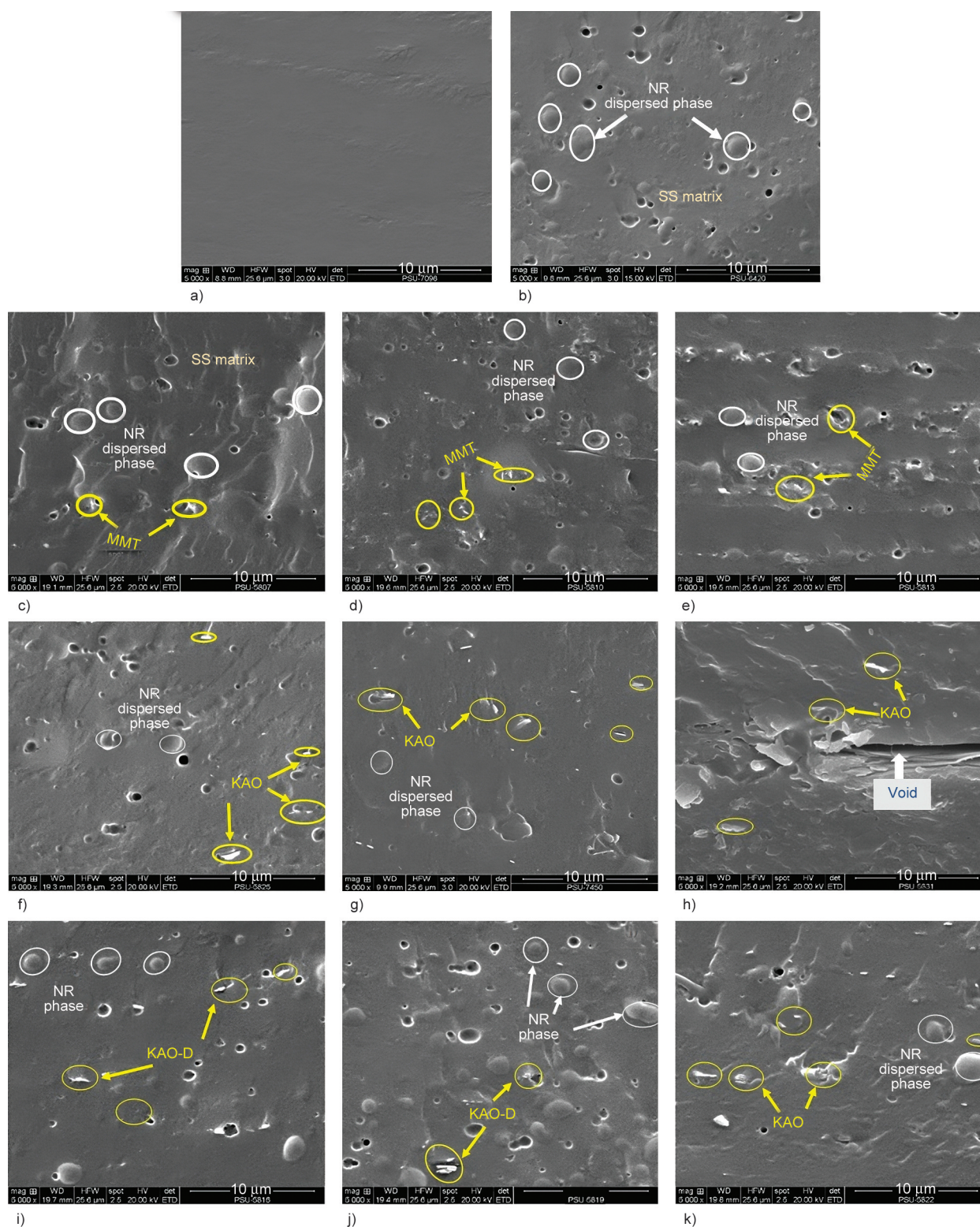


Figure 6. SEM micrographs of a) SS and b) SS80NR20 films, and biocomposites with the addition of 2, 4, and 6 wt% of c), d) e) MMT, f), g), h) KAO, and i), j), k) KAO-D.

between starch and MMT [8, 10, 32]. However, even around the temperature of 600 °C, there are some residues for all SS80NR20 blends with 9–15 wt%. These phenomena can be described that sago starch and natural rubber are polymers composed primarily of glucose and polyisoprene units, respectively. When

subjected to elevated temperatures, both starch and NR undergo thermal degradation. This degradation process involves chain scission, the release of volatile compounds, and the residual carbonaceous material. The SS80NR20 blend contains clays as inorganic materials that are not easily decomposed at the given

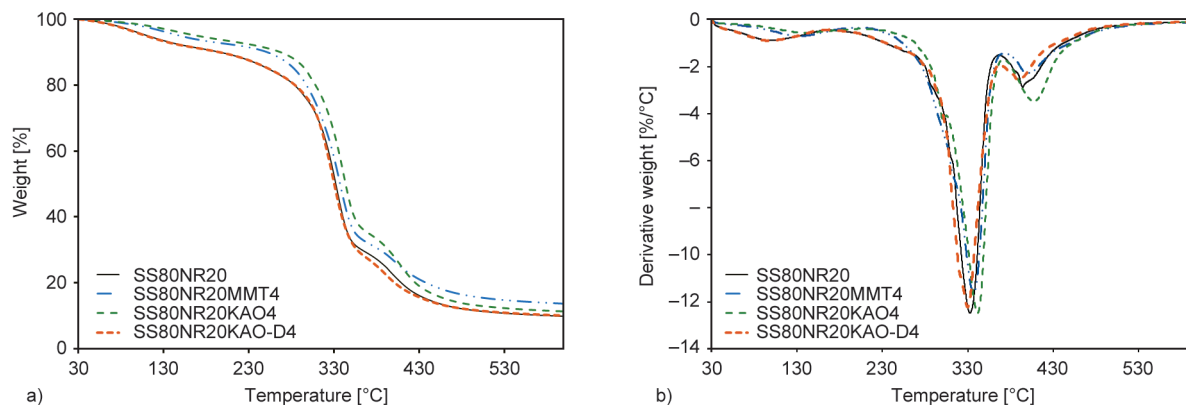


Figure 7. a) TGA and b) derivative gravimetric weight loss of biocomposites with 4 wt% of MMT, KAO, and KAO-D.

temperature range contributing to the observed residue. This improvement in the thermal stability was evident in the DTA peaks as shown in [Figure 7b](#). It is worthy of note that the thermal stability of the SS80NR20 biocomposites increased with an increase in the addition of nanoclays. The interfacial combination between NR and starch is strong when the addition of nanoclays, leads to the enhancement of thermal stability. This implies that improving the dispersion state of the nanoclay in the SS80NR20 for the intercalated nanocomposites is necessary for heat stability. The formation of a tortuous path structure in the SS80NR20 in intercalated structures could prevent or restrict the diffusion of the gases and volatile compounds produced during the decomposition. Therefore, it can be concluded that the introduction of inorganic particles would greatly improve the thermal stability of organic polymer materials [8, 32].

3.7. Dynamic mechanical investigation

DMA measures the changes in stiffness and damping by applying an oscillatory force at an established

frequency on the sample. Elastic, storage Moduli and $\tan \delta$ information were obtained using DMA data. Temperature-dependent modulus values and SS80NR20 biocomposite transitions can be observed in [Figure 8](#) which are E' and $\tan \delta$ curves. If the blends are immiscible, the $\tan \delta$ curves will indicate the presence of two damping peaks corresponding to the T_g of the different polymers [20]. If the two polymer phases are completely miscible, only one peak will be observed, which is found between the T_g of the component polymers. In SS80NR20 biocomposites with 4 wt% of kaolinite, the value of the storage modulus (E') was found to be highest at the glassy and rubbery areas, indicating that these samples were more brittle than other samples. A significant increase is noticed in T_g for all the samples compared to SS80NR20 as seen in [Table 1](#). This increases in the value of T_g is an indication of improvement in the intermolecular bonding within the SS80NR20 biocomposites. For an efficient reinforcement of S80NR20 with clays, it is crucial to a favorable interaction and a homogeneous dispersion of the

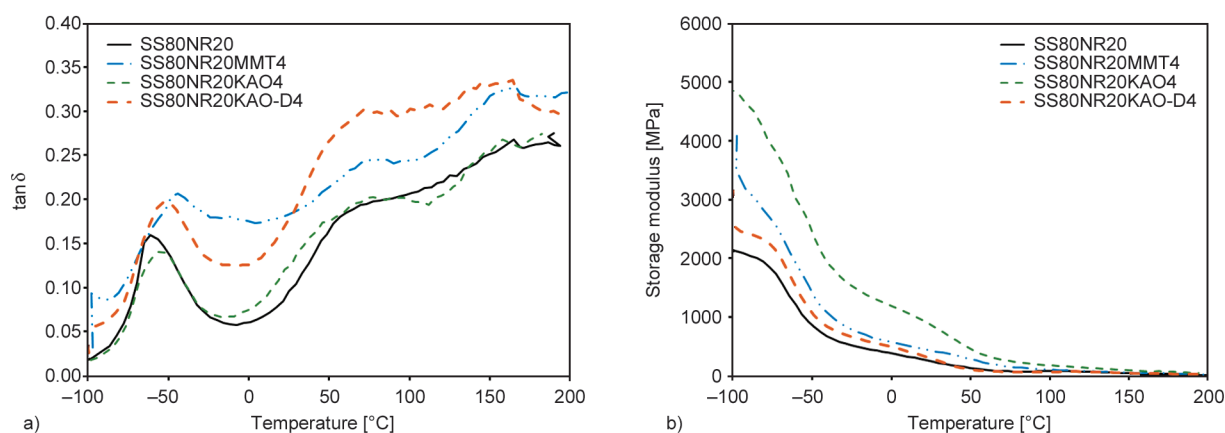


Figure 8. DMA characteristics of a) mechanical loss factor ($\tan \delta$) and b) storage modulus (E') of biocomposites with 4 wt% of clays.

Table 1. Thermal characteristics of SS80NR20 biocomposites with 4 wt% of clays.

Samples	2 nd step		3 rd step		T_g (DMA) [°C]
	T_{onset} [°C]	T_{peak} [°C]	T_{onset} [°C]	T_{peak} [°C]	
SS80NR20	222.6	333.3	362.2	394.3	-56.7
SS80NR20MMT4	253.0	337.2	371.9	404.2	-44.6
SS80NR20KAO4	266.3	341.8	371.6	408.1	-49.0
SS80NR20KAO-D4	223.0	330.8	367.9	396.4	-52.2

MMT and KAO in the SS80NR20, which will facilitate the stress transfer from the SS80NR20 to the nanoclay, increasing the rigidity of the material. $\tan \delta$ curves as a function of temperature of SS80NR20 biocomposites are shown in Figure 8b. All the samples showed three relaxation peaks in $\tan \delta$ curves. The relaxation located at lower temperatures, next to -50°C is associated with the glass transition of the NR phase, in glycerol plasticizer, while the broad relaxation that occurs at higher temperatures corresponds to the glass transition of the starch-rich phase. This contributes that when clay was present, starch and natural rubber chain mobility were more constrained [24, 32]. The SS80NR20 blends with the addition of nanoclay showed the broadening and shifting of damping peaks glass transition temperature (T_g) of NR was shifted to higher than that SS80NR20 blend which revealed some interaction between the sago starch and NR. This is related to a partially miscible blend. It was also found that, at room temperature, the stiffness of SS80NR20 is improved by the incorporation of nanoclays. These findings indicate that favorable contact and uniform dispersion of the nanoclays in the SS80NR20 blend are important for an efficient reinforcement of SS80NR20 with nanoclays. It will enable the stress transfer from the matrix to the nanoclays and increase the stiffness of the material. Comparing the types of clays, MMT helps the most improvement of the compatibility.

4. Conclusions

The following conclusions may be taken from the findings and discussion. In the blending solution process, the SS80NR20 biocomposites can be accomplished with nanoclays as reinforcing and compatibilizing fillers. The XRD characterization revealed evidence that the layered silicate is intercalated by polysaccharide and rubber chains. According to the results of XRD and SEM micrographs, it

was indicated that MMT and kaolinite clays help improve interfacial adhesion. The mechanical and physical characteristics of SS80NR20 biocomposites were attributed to the strong interaction that resulted in the intercalated structure of MMT and KAO, whereas KAO-D was accountable for the weak interaction at the SS80NR20 interface. The glass transition temperature (T_g) of the NR or SS-glycerol phase is higher than that of the SS80NR20 blend, which is another indication of the compatibilizing action of nanoclay in SS80NR20 biocomposites.

Acknowledgements

The first author gratefully acknowledges the grant support provided by the M.Sc. scholarship of Prince of Songkla University and the Scholarship Awards for graduate student.

References

- [1] Elsheekh K. M., Kamel R. R., Elsherif D. M., Shalaby A. M.: Achieving sustainable development goals from the perspective of solid waste management plans. *Journal of Engineering and Applied Science*, **68**, 9 (2021). <https://doi.org/10.1186/s44147-021-00009-9>
- [2] Moshood T. D., Nawanir G., Mahmud F., Mohamad F., Ahmad M. H., Abdulghani A.: Biodegradable plastic applications towards sustainability: A recent innovations in the green product. *Cleaner Engineering and Technology*, **6**, 100404 (2022). <https://doi.org/10.1016/j.clet.2022.100404>
- [3] Gupta V., Biswas D., Roy S.: A comprehensive review of biodegradable polymer-based films and coatings and their food packaging applications. *Materials*, **15**, 5899 (2022). <https://doi.org/10.3390/ma15175899>
- [4] Onyeaka H., Obileke K., Makaka G., Nwokolo N.: Current research and applications of starch-based biodegradable films for food packaging. *Polymers*, **14**, 1126 (2022). <https://doi.org/10.3390/polym14061126>
- [5] Mangaraj S., Yadav A., Bal L. M., Dash S. K., Mahanti N. K.: Application of biodegradable polymers in food packaging industry: A comprehensive review. *Journal of Packaging Technology and Research*, **3**, 77–96 (2019). <https://doi.org/10.1007/s41783-018-0049-y>
- [6] Chavan P., Sinhmar A., Sharma S., Dufresne A., Thory R., Kaur M., Sandhu K. S., Nehra M., Vikash N.: Nanocomposite starch films: A new approach for biodegradable packaging materials. *Starch*, **74**, 2100302 (2022). <https://doi.org/10.1002/star.202100302>
- [7] Ordoñez R., Atarés L., Chiralt V.: Biodegradable active materials containing phenolic acids for food packaging applications. *Comprehensive Review Food Science and Food Safety*, **21**, 3910–3930 (2022). <https://doi.org/10.1111/1541-4337.13011>

- [8] Romero-Bastida C. A., Tapia-Blácido D. R., Méndez-Montealvo G., Bello-Pérez L. A., Velázquez G., Alvarez-Ramirez J.: Effect of amylose content and nano-clay incorporation order in physicochemical properties of starch/montmorillonite composites. *Carbohydrate Polymers*, **152**, 351–360 (2016).
<https://doi.org/10.1016/j.carbpol.2016.07.009>
- [9] Csiszár E., Nagy A., Fekete E.: Contribution of flax-cellulose nanocrystals on the structural properties and performance of starch-based biocomposite films. *Express Polymer Letters*, **17**, 458–470 (2023).
<https://doi.org/10.3144/expresspolymlett.2023.34>
- [10] Luchese C. L., Benelli P., Spada J. C., Tessaro I. C.: Impact of the starch source on the physicochemical properties and biodegradability of different starch-based films. *Journal of Applied Polymer Science*, **135**, 46564 (2018).
<https://doi.org/10.1002/app.46564>
- [11] Behera A. K., Mohanty C., Pradhan S. K., Das N.: Assessment of soil and fungal degradability of thermoplastic starch reinforced natural fiber composite. *Journal of Polymers and the Environment*, **29**, 1031–1039 (2021).
<https://doi.org/10.1007/s10924-020-01944-z>
- [12] Müller C. M. O., Laurindo J. B., Yamashita F.: Effect of nanoclay incorporation method on mechanical and water vapor barrier properties of starch-based films. *Industrial Crops and Products*, **33**, 605–610 (2011).
<https://doi.org/10.1016/j.indcrop.2010.12.021>
- [13] Mbey J. A., Thomas F.: Components interactions controlling starch-kaolinite composite films properties. *Carbohydrate Polymers*, **117**, 739–745 (2015).
<https://doi.org/10.1016/j.carbpol.2014.10.053>
- [14] Yang J., Ching Y. C., Ching K. Y., Ran X., Al-Hada N. M., Sui X., Wei Y., Xu S., Yu J., Wang J., Zhou J.: Preparation and characterization of starch-based bioplastic films modified by citric acid-epoxidized soybean oil oligomers. *Journal of Polymers and the Environment*, **31**, 954–964 (2023).
<https://doi.org/10.1007/s10924-022-02661-5>
- [15] Ismail H., Zaaba N. F.: Tensile properties, degradation behavior, and water absorption of sago starch plastic films. *Journal of Vinyl Additive Technology*, **18**, 235–240 (2012).
<https://doi.org/10.1002/vnl.20300>
- [16] Ruamcharoen J., Munlee R., Ruamcharoen P.: Improvement of water vapor barrier and mechanical properties of sago starch-kaolinite nanocomposites. *Polymer Composites*, **41**, 201–209 (2020).
<https://doi.org/10.1002/pc.25360>
- [17] Wannaphatchaiyong S., Suksaeree J., Waiprib R., Kaewpuang A., Saelee W., Pichayakorn W.: Gelatin/gelatinized sago starch biomembranes as a drug delivery system using rubber latex as plasticizer. *Journal of Polymers and the Environment*, **27**, 2380–2394 (2019).
<https://doi.org/10.1007/s10924-019-01510-2>
- [18] Ahmad F. B., Williams P. A., Doublier J-L., Durand S., Buleon A.: Physico-chemical characterisation of sago starch. *Carbohydrate Polymers*, **38**, 361–370 (1999).
[https://doi.org/10.1016/S0144-8617\(98\)00123-4](https://doi.org/10.1016/S0144-8617(98)00123-4)
- [19] Carvalho A. J. F., Job A. E., Alves N., Curvelo A. A. S., Gandini A.: Thermoplastic starch/natural rubber blends. *Carbohydrate Polymers*, **53**, 95–99 (2003).
[https://doi.org/10.1016/S0144-8617\(03\)00005-5](https://doi.org/10.1016/S0144-8617(03)00005-5)
- [20] Rouilly A., Rigal L., Gilbert R. G.: Synthesis and properties of composites of starch and chemically modified natural rubber. *Polymer*, **45**, 7813–7820 (2004).
<https://doi.org/10.1016/j.polymer.2004.09.043>
- [21] Trovatti E., Carvalho A., Gandini A.: A new approach to blending starch with natural rubber. *Polymer International*, **64**, 605–610 (2015).
<https://doi.org/10.1002/pi.4808>
- [22] Mondragón M., Hernández E. M., Rivera-Armenta J. L., Rodríguez-González F. J.: Injection molded thermoplastic starch/natural rubber/clay nanocomposites: Morphology and mechanical properties. *Carbohydrate Polymers*, **77**, 80–86 (2009).
<https://doi.org/10.1016/j.carbpol.2008.12.008>
- [23] Ruamcharoen J., Munlee R., Ruamcharoen P.: Eco-friendly bio-based composites of cassava starch and natural rubber compatibilized with nanoclays. *Polymer Composites*, **44**, 1071–1082 (2023).
<https://doi.org/10.1002/pc.27154>
- [24] Ruamcharoen J., Ratana T., Ruamcharoen P.: Bentonite as a reinforcing and compatibilizing filler for natural rubber and polystyrene blends in latex stage. *Polymer Engineering and Science*, **54**, 1436–1443 (2014).
<https://doi.org/10.1002/pen.23665>
- [25] Katerinopoulou K., Giannakas A., Grigoriadi K., Barkoula N. M., Ladavos A.: Preparation and characterization of acetylated corn starch-(PVOH)/clay nanocomposite films. *Carbohydrate Polymer*, **102**, 216–222 (2014).
<https://doi.org/10.1016/j.carbpol.2013.11.030>
- [26] Dean K., Do M., Petinakis E., Yu L.: Key interactions in biodegradable thermoplastic starch/poly(vinyl alcohol)/montmorillonite micro- and nanocomposites. *Composites Science and Technology*, **68**, 1453–1462 (2008).
<https://doi.org/10.1016/j.compscitech.2007.10.037>
- [27] Chuayjuljit S., Worawas C.: Nanocomposites of EVA/polystyrene nanoparticles/montmorillonite. *Journal of Composite Materials*, **45**, 631–638 (2010).
<https://doi.org/10.1177/0021998310376116>
- [28] Ock H. G., Ahn K. H., Lee S. J., Hyun K.: Characterization of compatibilizing effect of organoclay in poly(lactic acid) and natural rubber blends by FT-rheology. *Macromolecules*, **49**, 2832–2842 (2016).
<https://doi.org/10.1021/acs.macromol.5b02157>
- [29] Olivato J. B., Marini J., Yamashita F., Pollet E., Grossmann M. V. E., Avérous L.: Sepiolite as a promising nanoclay for nano-biocomposites based on starch and biodegradable polyester. *Materials Science and Engineering C*, **70**, 296–302 (2017).
<https://doi.org/10.1016/j.msec.2016.08.077>

- [30] Chuayjuljit S., Wiriya-soonthorn S., Jiratumnukul N., Limpanart S.: Preparation of natural rubber/cassava starch/organomontmorillonite biodegradable nanocomposite elastomers. *Polymers and Polymer Composites*, **17**, 173–179 (2009).
<https://doi.org/10.1177/096739110901700306>
- [31] Almasi H., Ghanbarzadeh B., Entezmi A. A.: Physico-chemical properties of starch-CMC-nanoclay biodegradable films. *International Journal of Biological Macromolecules*, **46**, 1–5 (2010).
<https://doi.org/10.1016/j.ijbiomac.2009.10.001>
- [32] Derungs I., Rico M., López J., Barral L., Montero B., Bouza R.: Influence of the hydrophilicity of montmorillonite on structure and properties of thermoplastic wheat starch/montmorillonite bionanocomposites. *Polymer for Advance Technologies*, **32**, 4479–4489 (2021).
<https://doi.org/10.1002/pat.5450>

Research article

The competition between self-seeding and specific nucleation in crystallization of long-chain branched polypropylene

Sona Zenzingerova^{ID}, Michal Kudlacek^{ID}, Jana Navratilova*^{ID}, Lenka Gajzlerova^{ID},
David Jaska^{ID}, Lubomir Benicek^{ID}, Roman Cermak^{ID}

Department of Polymer Engineering, Faculty of Technology, Tomas Bata University in Zlin, Vavreckova 5669,
760 01 Zlin, Czech Republic

Received 12 May 2023; accepted in revised form 7 July 2023

Abstract. The main purpose of this work is to present the effect of long-chain branching and specific α -nucleation on the optical properties, crystallization and supermolecular structure of polypropylene (PP). Commercially available α -nucleating/clarifying agent 1,3;2,4-bis(3,4-dimethylbenzylidene)sorbitol (Millad 3988) was mixed into linear PP and long-chain branched PP (LCB-PP) in the concentration of 0.2 wt%. For the study of polymorphic composition, crystallinity, and crystallization process under isothermal conditions in the temperature range of 130–150 °C, differential scanning calorimetry and wide-angle X-ray scattering were used. Although the used nucleating/clarifying agent appears to have a slight effect on the optical properties of long-chain branched polypropylene, it does not appear to affect the crystallization kinetics significantly. LCB-PP exhibited self-nucleation, favored over nucleation by a specific nucleating agent.

Keywords: polyolefins, crystallization, crystal structure, morphology, differential scanning calorimetry, X-ray, nucleating agent

1. Introduction

Isotactic polypropylene (PP) is one of the most essential semi-crystalline polymers of modern times due to its wide range of applications, suitable mechanical properties and low price. Polypropylene is characterized by low density, relatively high melting point and good chemical resistance. Commercial PP is commonly prepared using iso-specific Ziegler-Natta or metallocene catalysts. This type of preparation produces highly linear chains and narrow molecular weight distribution, resulting in low melt strength and no strain hardening, which limits its processing by thermoforming, coating, foaming, or film-blowing [1, 2]. An effective method for improving these limiting properties is the introduction of long chains on the polypropylene backbone [3–6].

Two main methods are used to prepare the long-chain branched polypropylene (LCB-PP). The post-reactor method is based on the disruption of the main chain of PP and subsequent grafting of long branches onto the main chain of the polymer by chemical grafting reaction in the molten state, for example, in the presence of peroxides [7–9] or by high-energy irradiation in solid state [10, 11]. Long-chain branching can also be achieved in situ during polypropylene polymerization by adding a suitable comonomer [12, 13]. Polypropylene exhibits a polymorphic structure with well-defined distinct α -, β -, γ - and smectic phases, the last formed during high undercooling [14]. Monoclinic α -phase, developed during ordinary processing conditions, forms two variants; α_1 with random down-up directions of methyl groups and more stable α_2

*Corresponding author, e-mail: j1navratilova@utb.cz
© BME-PT

with ordered methyl groups [15]. β -phase can be obtained by creating favorable crystallization conditions, such as a high-temperature gradient, the presence of shear forces, or by using heterogeneous β -nucleating agents, resulting in a trigonal lattice. Compared to the α -phase, it exhibits much better toughness and ductility but is thermodynamically less stable. β -phase can recrystallize into the α -phase upon stretching at high temperatures [16–19]. The third crystalline phase of polypropylene is the orthorhombic γ -phase which rarely occurs under particular thermodynamic conditions, either by the action of very high pressure or by using samples with a low molecular weight [20].

The change of the PP molecular architecture, by introducing long-chain branching, strongly influences the process of crystallization and resulting morphology. LCB-PP contains structural defects, which affect both the nucleation and growth of crystallites. In the case of LCB-PP produced by a radical-driven synthesis process using peroxides in the melt state, not only are long branches created, but the process is also accompanied by chain scission and gel formation, which can strongly affect the nucleation rate. The self-seeding effect of LCB-PP has already been observed [21–23]. The presence of defects in the form of branching points, on the other hand, reduces the rate of crystallite growth. However, the overall crystallization is faster in the case of LCB-PP. [4, 22] As for polymorphic composition, the presence of long branches and thus a higher amount of irregularities on the polymer backbone causes a higher ability of PP to crystallize into the orthorhombic γ -phase side by side to α -phase [24], even at elevated pressures [3]. At the same time, the crystallization temperature itself has a non-negligible effect, which affects the helical conformation regularity. It, therefore, strongly influences the resulting crystalline phase structure of LCB-PP [1].

Nucleating agents are often used in PP to shorten processing cycles and to modify final properties, mainly mechanical and optical properties. For the improvement of the optical properties, so-called clarifying agents are used, which nucleate into the α -phase and significantly reduce the size of the crystallites, resulting in less light scattering [25–27]. Due to the polymorphism of PP, several nucleating agents are also used to cause crystallization into the β -phase. The effectiveness of a commercial β -nucleating agent in LCB-PP and mixtures of LCB-PP with

linear PP was investigated in the work of Gajzlerova et al. [22]. It was found that the self-nucleation effect of LCB-PP is dominant, and the formation of β -phase is suppressed [22, 28–31].

The process of nucleation of PP by the sorbitol-based clarifying α -nucleating agent is well documented and widely studied [32–36]; however, LCB-PP has not been appropriately investigated in this context yet. Thus, this work analyzes the effect of a sorbitol-based clarifying agent on the optical properties and crystallization of LCB-PP under isothermal conditions. The main aims are to provide an overview of the influence of long branches and the nucleating agent on polypropylene during the crystallization process at high crystallization temperatures (T_c).

2. Experimental

2.1. Materials

Two types of commercially available polypropylene grades used for the experiment were obtained from Borealis AG company, Vienna, Austria. Long-chain branched PP was Daploy WB140HMS with melt flow rate (MFR) 2.1 g/10 min, weight-averaged molecular weight of 600 000, and polydispersity index of 5.2. Linear PP was homopolymer Borclean HC300BF with MFR 3.3 g/10 min (both measured at 230 °C, 2.16 kg, ISO 1133), weight-averaged molecular weight of 300 000, and polydispersity index of 8.0. In LCB-PP, long branches were incorporated into the main chain by grafting a monomer by radical means with the help of peroxides. Specific α -nucleating/clarifying agent Millad 3988 (1,3;2,4-bis(3,4-dimethylbenzylidene)sorbitol) [37] supplied by Milliken Chemical Co., (USA) was applied in the concentration of 0.2 wt%.

2.2. Samples preparation

The nucleating agent was mixed into the polypropylenes in two steps, first manually, then using a twin-screw extrusion machine [38]. During the first step, 0.3 wt% of paraffin oil was added to the granulate to improve subsequent dispersion of the nucleating agent Millad 3988 at the concentration of 0.2 wt%. This was followed by mixing using a co-rotating twin screw extruder (Brabender GmbH & Co, Germany) with cooling and pelletizing. The processing conditions during extrusion were set as follows: screw speed 50 min⁻¹, temperatures of barrel zones 180, 200, and 210 °C. To ensure the same processing and thermal history for all samples, neat PP and neat

LCB-PP underwent the same procedure: mixing with paraffin oil and extrusion under the same conditions as those containing nucleating agent.

From the prepared pellets, the plates of a thickness of approx. 0.5 mm were compression-molded: pressing temperature 210 °C for 5 min and cooling temperature 60 °C for 10 min, and polyethylene terephthalate films were used as a separator. Afterward, the specimens were examined by wide-angle X-ray scattering (WAXS) and differential scanning calorimetry (DSC), and optical properties were observed via spectrophotometer. In the following part, nucleated and neat materials are marked as follows: neat linear PP as L-PP, neat long-chain branched PP as LCB-PP, nucleated linear PP as α -L-PP, and nucleated long-chain branched PP as α -LCB-PP.

2.3. Methods

The effect of the α -nucleating/clarifying agent on optical properties was analyzed by haze measurement on as-processed plates using UltraScan Pro D65 instrument, HunterLab, Reston, Virginia, USA, according to ASTM D1003. The measurements were taken five times, and the arithmetic mean was determined. The effect of long branches and the addition of an α -nucleating agent on the crystallization process was studied under isothermal conditions using a differential scanning calorimeter DSC1 (Mettler Toledo, USA). Samples of approx. 5 mg weights were placed in aluminum pans and measured with an empty pan as a reference. Measurements were taken under an inert nitrogen atmosphere with a gas flow of 20 ml/s. The thermal regime was following: heating from 50 to 220 °C by the heating rate of 10 °C/min, annealing at 220 °C for 5 min to remove thermal history, cooling to crystallization temperature (130, 135, 140, 142, 144, 146, 148 and 150 °C) by cooling rate 50 °C/min. Then samples were maintained at crystallization temperature until the crystallization peak was completed, but no longer than 180 min, followed by heating to 190 °C by 10 °C/min to observe the melting profile. The crystalline structure was examined by wide-angle X-ray diffractometer PANalytical X'Pert PRO (Malvern PANalytical, United Kingdom). Diffractometer was equipped with Bragg-Brentano geometry in reflection mode with $\text{CuK}\alpha$ radiation with Ni filter ($\lambda = 0.154$ nm, $I = 30$ mA, $U = 40$ kV) and employed in the diffraction angle interval of $2\theta = 5$ – 30° . Diffractometer was additionally equipped with temperature cell TCU 110 (Anton Paar GmbH, Austria).

Samples were cut to the dimensions $10.0 \times 14.0 \times 0.5$ mm to fit in the temperature cell, and the conductive paste was used to ensure good and even thermal conductivity throughout the whole sample. Samples were then heated to 220 °C by 10 °C/min and held at this temperature for 5 min, followed by amorphous halo measurement. After, the samples were cooled to the desired crystallization temperature 140 or 150 °C based on the limit temperatures from DSC measurements by the cooling rate 20 °C/min. At this point, the samples were held at the crystallization temperature for 171 min, and X-ray diffractograms were obtained during the isothermal crystallization process at the given intervals (0, 4, 8, 12, 99, 171 min). The crystallinity of the samples was calculated from the share of the fitted areas of the crystalline part (A_C) and amorphous part (A_A) using Equation (1) [39]:

$$X = \frac{A_C}{A_C + A_A} \cdot 100 [\%] \quad (1)$$

X-ray patterns were analyzed by Scherrer equation (Equation (2)), which gives the length L_{hkl} of the crystallite domain in the direction perpendicular to (hkl):

$$L_{hkl} = \frac{K \cdot \lambda}{FWHM \cdot \cos 2\theta} \quad (2)$$

where λ is the wavelength of the used X-ray, $FWHM$ is the full width at half maximum of the relevant peak, and 2θ is the peak position; both values are in radians. The constant K is omitted by setting it to 1, as in a previous study [39].

3. Results and discussion

3.1. Optical properties

The effectiveness of the nucleating/clarifying agent was examined by measuring the optical properties, namely the haze, of the prepared samples (see Table 1). As can be seen, for L-PP, the addition of the clarifying agent reduced the haze significantly, from 55.0 to 39.7%. Thus, the agent clearly serves its purpose by reducing light scattering, which is a well-known and described effect [25–27]. The haze value of branched polypropylene is very low, even slightly lower than that of α -L-PP (36.5%). This is due to the

Table 1. The haze of the samples.

Sample	L-PP	α -L-PP	LCB-PP	α -LCB-PP
Haze [%]	55.0±0.4	39.7±0.3	36.5±0.3	32.1±0.4

self-nucleation effect of LCB-PP, where the crystallites cannot grow to larger sizes leading to a reduced haze [2–4, 22]. This self-nucleation appears to be more efficient in terms of optical properties than the used clarifying agent Millad 3988. The addition of this agent to the LCB-PP leads to a further slight haze reduction to a value of 32.1%. Although the change is not dramatic, the clarifying agent performs its function even in branched polypropylene.

3.2. Thermal behavior

Using DSC, the effect of long branches and nucleating agent on crystallization was observed under isothermal crystallization conditions. Crystallization temperature varied from 130 to 150 °C, and crystallization time was not longer than 180 min. In the case of linear polypropylene, the crystallization was completed only at 130 and 135 °C in the given time frame. On the other hand, at these temperatures, the crystallization exotherms of LCB-PP and both nucleated polypropylenes were not possible to examine due to continuous crystallization even during cooling to crystallization temperature; thus, the exotherms were not complete. Figure 1 shows the sigmoidal crystallization curves of samples isothermally crystallized at temperatures 140, 142, 144, 146, 148 and 150 °C. Only the samples where whole crystallization exotherms were obtained are shown. Figure 2 depicts the correlation between the crystallization half-time and the crystallization temperature across all samples, obtained from the sigmoidal curves from Figure 1. It is evident that the addition of an α -nucleating agent significantly accelerates the crystallization of linear PP. On the contrary, neat LCB-PP behaves as if it already contains heterogeneous nucleation seeds. These heterogeneous nucleation seeds could be local cross-linking formed during the production of branched polypropylene. LCB-PP used in this study was produced by a radical mechanism with the help of peroxides, and during this process, in addition to branching, a gel may also be formed, or even chain splitting can occur [40]. This heterogeneous self-nucleation significantly influences crystallization, and the addition of nucleating agents does not significantly affect the kinetics of crystallization. Indeed, crystallization curves of branched polypropylenes with/without a nucleating agent are very similar, especially at higher crystallization temperatures. The slight acceleration of crystallization after the addition of the nucleating agent is clearly

visible only at a crystallization temperature of 140 °C. This observation may be related to the minor improvement in the optical properties of LCB-PP after the addition of the agent used. The crystallization curve of nucleated linear PP is always shifted to higher times compared to those of branched PP, and the difference is more significant the higher the crystallization temperature. Moreover, at higher temperatures, the curve is deformed (144 and 146 °C), and at temperatures of 148 and 150 °C, the crystallization was not complete in the given time of 180 min. The curves are, therefore, not shown. Evidently, the nucleating agent loses its nucleating capability at such high temperatures. The above-mentioned deformation of the α -L-PP crystallization curves is due to the formation of asymmetric crystallization exotherms that exhibited shoulder or doubling (Figure 3). This phenomenon is probably caused by two crystallization mechanisms occurring simultaneously. At such high temperatures, the nucleating agent that dissolves in the PP melt apparently crystallizes only to a limited extent, and its function fails [37].

The crystallization half-time of LCB-PP with and without a nucleating agent follows a similar pattern, with differences only apparent at high crystallization temperatures of 148 and 150 °C, where the presence of the nucleating agent decelerates the crystallization process (Figure 2). This is likely due to the nucleating agent not being able to fully crystallize at these high temperatures and potentially diluting the PP melt [37]. The nucleating agent only slightly accelerates the crystallization of LCB-PP at a crystallization temperature of 140 °C. Evidently, the effect of the nucleating agent used depends on the thermal regime applied. Notably, neat LCB-PP was found to crystallize faster than α -L-PP. Thus, the effect of self-nucleation in LCB-PP is more pronounced than the addition of the α -nucleating agent to L-PP.

The isothermally crystallized samples were then heated to determine the melting temperature (melting temperature is the peak of the endotherm). The results are shown in Figure 4. A correlation between the increase in crystallization temperature and the increase in melting temperature is observed. In the case of neat L-PP, the full crystallization was achieved only at temperatures of 130 and 135 °C, and thus only these samples were melted. The melting behavior of such material shows the presence of both α - and β -phases with melting temperatures approx. 155 and 167 °C, respectively, in the case of lower crystallization

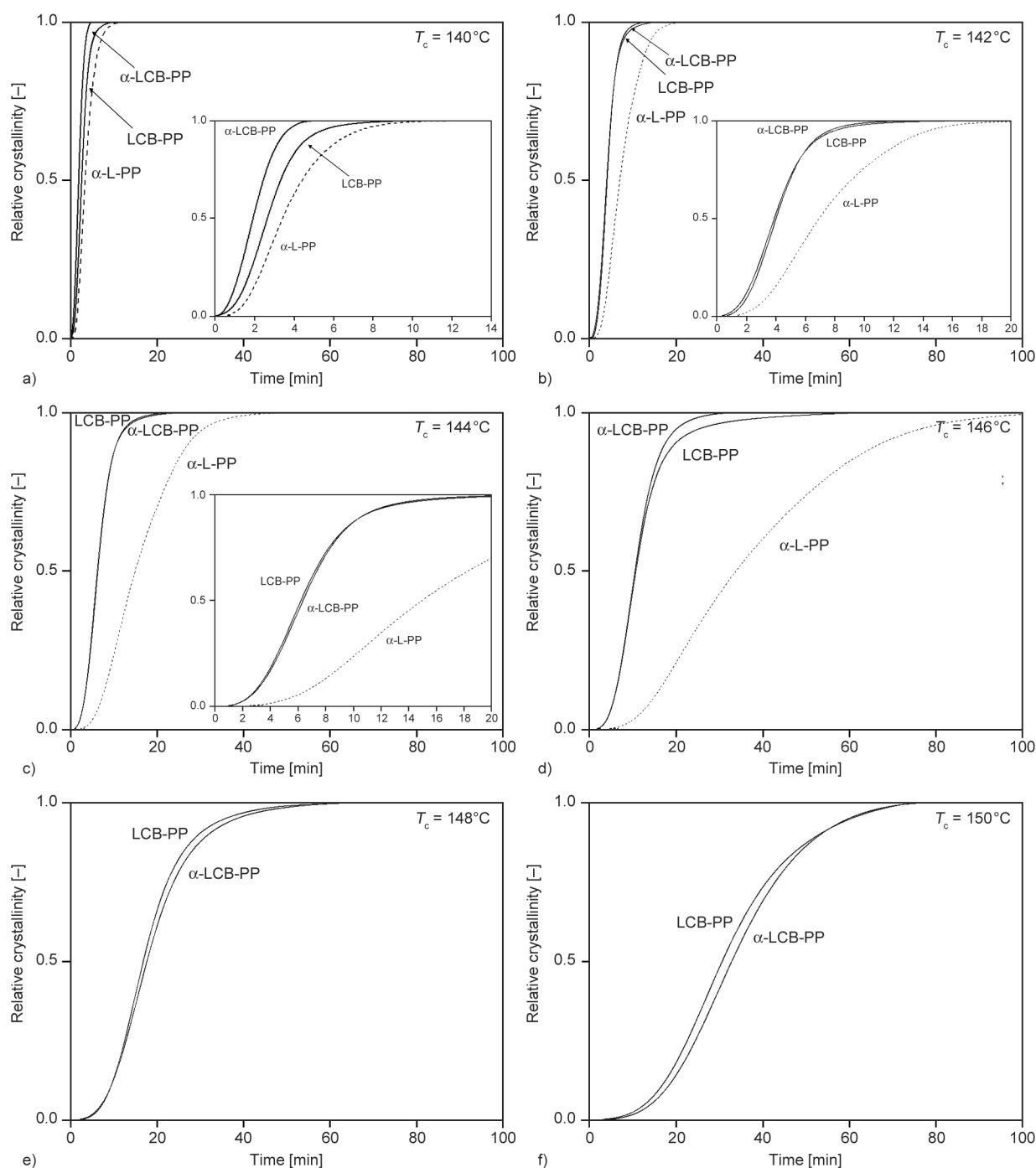


Figure 1. Crystallization curves of isothermally crystallized samples at various crystallization temperatures (the inset shows an x-axis cutout), a) $T_c = 140^\circ\text{C}$, b) $T_c = 142^\circ\text{C}$, c) $T_c = 144^\circ\text{C}$, d) $T_c = 146^\circ\text{C}$, e) $T_c = 148^\circ\text{C}$, f) $T_c = 150^\circ\text{C}$.

temperature. It should be noted that the melting peak of the β -phase was significantly smaller compared to that of the α -phase, corresponding to the very low content of β -phase in the sample (this will be proved thereafter by X-ray analysis). On the contrary, when adding an α -nucleating agent, no melting endotherm of β -phase was observed. Two values of melting point in the case of samples crystallized at high temperatures 144 and 146°C refer to the presence of α_1 (at approx. 170°C) and α_2 (at approx.

174°C) phases [41, 42]. All LCB-PP samples show only one endotherm corresponding to the melting of α -phase, and, moreover, the values are very similar independently of the presence of the nucleating agent. Compared to linear polypropylene, the melting temperatures of LCB-PP samples are significantly lower, approx. 162 vs. 167°C for a crystallization temperature of 140°C . This suggests that the formation of thinner lamellae is associated with the presence of branching in polypropylene.

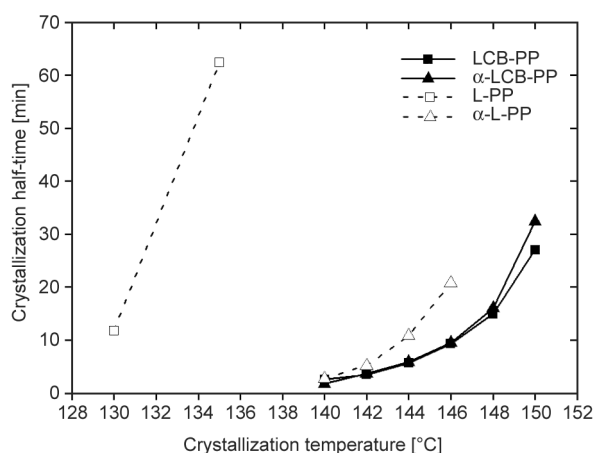


Figure 2. Crystallization half-time of samples crystallized at various crystallization temperatures.

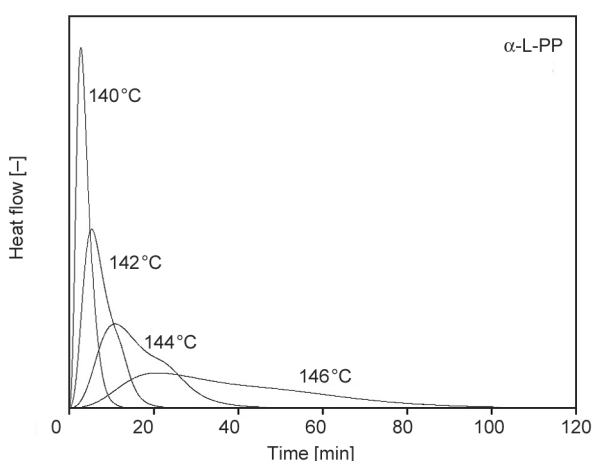


Figure 3. Crystallization exotherms of α -L-PP at various crystallization temperatures.

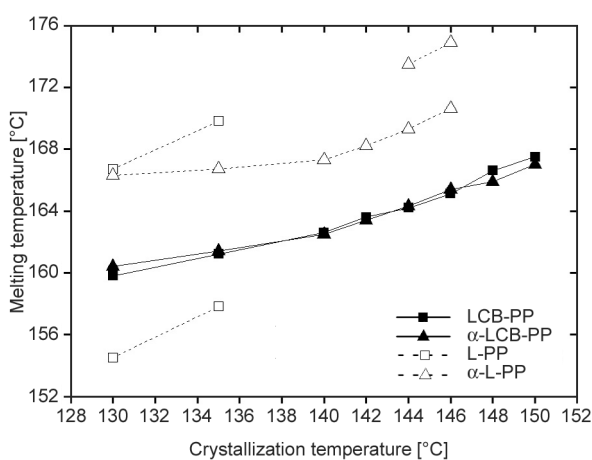


Figure 4. Melting temperatures of samples crystallized at various crystallization temperatures.

3.3. Supermolecular structure

Wide-angle X-ray scattering (WAXS) equipped with a temperature cell was used to study the morphology of isothermally crystallized samples. The crystallization temperatures 140 and 150 °C were chosen as

representatives based on the results from thermal analysis. The measurement took place after melting the sample, then after reaching the crystallization temperature, and during crystallization at specified intervals. It is worth mentioning that the thermal conditions in the sample were different for WAXS than for DSC due to the different sizes of the sample, the atmosphere during the measurement, and mainly the cooling rate. Therefore, the results are not entirely comparable to the results from the DSC.

The presence of peaks corresponding to the main planes of the α -phase $\alpha(110)$, $\alpha(040)$, and $\alpha(130)$, β -phase (300) and γ -phase (117) can be observed in the typical diffraction spectra of three-phase crystalline systems [22]. X-ray diffractograms of all polypropylene samples, see Figure 5, show the evolution of phases during isothermal crystallization at selected times. The initiation of the crystallization process in neat L-PP isothermally crystallized at 140 °C occurred at crystallization time (t_c) 8 min of time-dependent crystallization. The final pattern (after t_c 171 min at 140 °C) contains, in addition to the α -diffraction peaks at angles $2\theta = 14.20$, 17.00 and 18.80° , a small diffraction peak associated with the presence of the β -phase (16.20°) and also a small broad γ -phase diffraction peak (20.05°). Thus, a three-phase system with a dominant amount of α -phase was formed. Adding of a nucleating agent to the linear polypropylene significantly accelerated the crystallization process, which proceeded even upon cooling to a crystallization temperature of 140 °C. Moreover, the formation of the β -phase was suppressed entirely, while the diffraction peak corresponding to the γ -phase was observed. Thus, a two-phase α/γ system with α -phase dominance was formed. Increasing the crystallization temperature to 150 °C leads to a retardation of crystallization in both cases, with/without the nucleating agent, and also to the exclusive formation of the α -phase: no β - and γ -diffraction peaks were observed. Indeed, these phases cannot be formed at such a high temperature [43].

Diffraction patterns of LCB-PP crystallized at 140 and 150 °C are also shown in Figure 5. Since the patterns of nucleated LCB-PP were the same as those of neat LCB-PP, they are not shown in the figure. LCB-PP crystallized into both the α - and γ -phases at 140 °C. At 150 °C, the crystallization was slightly slower, and the γ -phase diffraction peak disappeared.

From the crystallization patterns, crystallinity was calculated and plotted as a function of time in Figure 6.

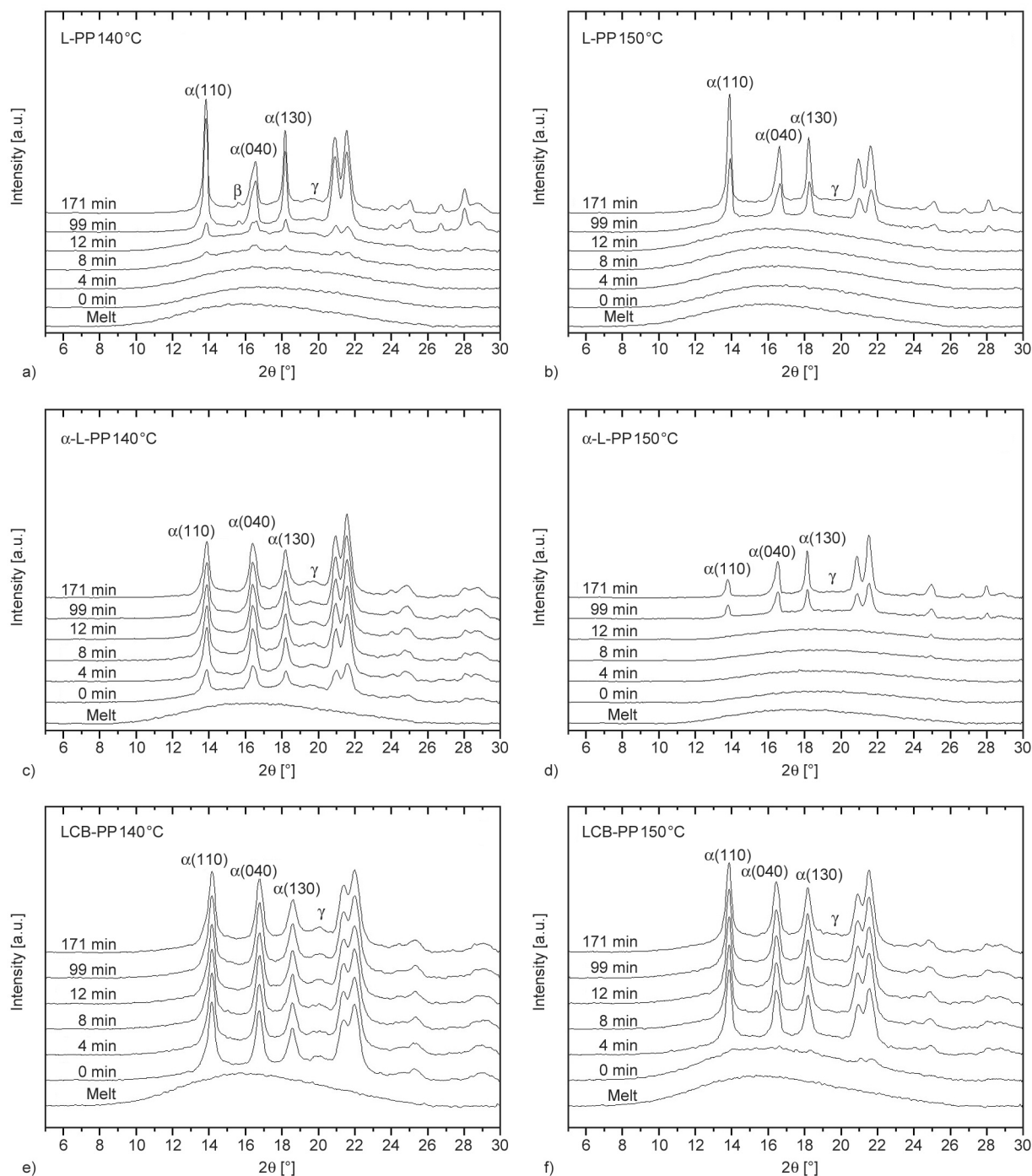


Figure 5. WAXS patterns of neat and nucleated linear polypropylene and neat long-chain branched polypropylene crystallized at 140 and 150 °C, a) L-PP at 140 °C, b) L-PP at 150 °C, c) α -L-PP at 140 °C, d) α -L-PP at 150 °C, e) LCB-PP at 140 °C, f) LCB-PP at 150 °C.

In the case of crystallization at 140 °C, except for L-PP, all samples crystallized upon cooling to the crystallization temperature. Both LCB-PP samples crystallize faster than α -L-PP due to their ability to self-nucleate, which is consistent with the DSC measurement results. The achieved crystallinity is higher for linear PP than for LCB-PP. Adding a nucleating agent leads to a slight decrease in crystallinity

in the case of L-PP. However, no effect is observed in the case of LCB-PP. At a higher crystallization temperature of 150 °C, the addition of a nucleating agent to LCB-PP leads to a very slight acceleration of crystallization and also to a slightly higher crystallinity. Linear polypropylene crystallizes reluctantly at this high temperature, and adding the nucleating agent leads to acceleration, but not significantly. In

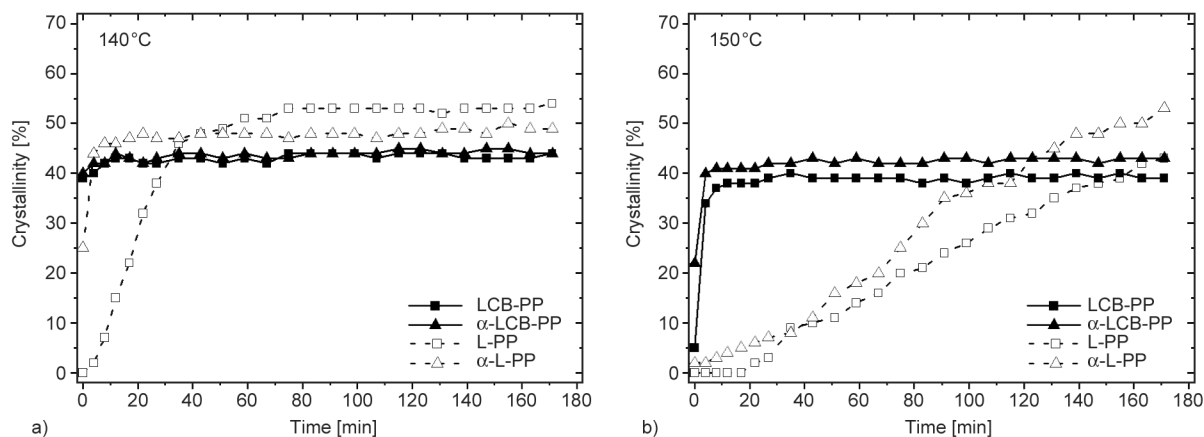


Figure 6. Evolution of overall crystallinity during time-dependent isothermal crystallization at a) 140 °C and b) 150 °C.

the time taken for isothermal crystallization, the plateau was not reached, so the final crystallinity values could not be evaluated, but they are certainly higher than in the case of LCB-PP. Although it is impossible to fully compare these results with those from the DSC due to the different analysis conditions, the trends are the same, and the results confirm and complement each other.

From the diffractograms obtained at the longest crystallization time, *i.e.*, 171 min, the values of the lamellae length in the (110), (040), and (130) directions of the α -crystallites were calculated (Table 2). In the case of linear PP crystallized at 140 °C, the addition of the nucleating agent leads to a significant reduction in lamellae length. However, for a crystallization temperature of 150 °C, this is not the case; the length of the lamellae remains the same independently of the addition of the nucleating agent; thus, at this high temperature, it does not fulfill its function. The length of the lamellae of branched polypropylene crystallized at 140 °C is even shorter than in the case of linear with the nucleating agent, and the addition of the agent leads to a further slight decrease, indicating its efficiency. This is in good agreement with haze measurement. However, the same trend is observed at the higher crystallization temperature of 150 °C: the addition of the nucleating agent also

leads to a reduction in lamellae length. Thus, the molecular structure of polypropylene seems to influence the efficiency of the nucleating agent.

4. Conclusions

This study shows the combined effect of long-chain branches and the addition of commercial sorbitol-based α -nucleating/clarifying agent Millad 3988 on the optical properties, crystallization, and supermolecular structure of polypropylene. As expected, adding this nucleating agent significantly reduces the haze of common linear polypropylene. In the case of LCB-PP, which itself shows lower haze than L-PP with the nucleating agent, a slight reduction is also observed.

Used nucleating agent selectively affects polymorphic phases, suppresses β -phase growth, and slightly decreases crystallinity in L-PP. Moreover, it significantly speeds up the crystallization at lower crystallization temperatures up to 146 °C while affecting the mechanism of crystallization, forming double exotherms, especially at higher crystallization temperatures. For LCB-PP, it was found that polymorphic composition does not depend on the addition of the nucleating agent; however, the crystallinity slightly increases. Also, the crystallization rate is not considerably affected by the addition of nucleating agent into LCB-PP, which is nevertheless higher than that of nucleated linear polypropylene. Only a slight positive effect is observed at the lowest crystallization temperature and a negative effect at higher crystallization temperatures. LCB-PP favors self-nucleation due to long branches acting as defects in structure and, thus, as heterogeneous nucleation seeds.

To conclude, although the used nucleating/clarifying agent appears to have a slight effect on the optical

Table 2. Lamellae length calculated from WAXS data.

Material	140 °C			150 °C		
	L_{110} [nm]	L_{040} [nm]	L_{130} [nm]	L_{110} [nm]	L_{040} [nm]	L_{130} [nm]
L-PP	42.8	19.0	42.6	42.8	42.7	42.6
α -L-PP	34.3	21.4	34.1	42.8	42.7	42.6
LCB-PP	28.5	24.4	21.3	34.3	28.5	28.4
α -LCB-PP	24.5	19.0	18.9	28.5	24.4	24.3

properties of long-chain branched polypropylene, it does not affect the crystallization kinetics significantly.

Acknowledgements

The article was supported within the project OP VVV Junior Grants TBU in Zlin, no. CZ.02.2.69/0.0/0.0/19_073/0016941.

References

- [1] Su Z., Wang H., Dong J., Zhang X., Dong X., Zhao Y., Yu J., Han C. C., Xu D., Wang D.: Conformation transition and crystalline phase variation of long chain branched isotactic polypropylenes (LCB-iPP). *Polymer*, **48**, 870–876 (2007).
<https://doi.org/10.1016/j.polymer.2006.12.013>
- [2] Nam G. J., Yoo J. H., Lee J. W.: Effect of long-chain branches of polypropylene on rheological properties and foam-extrusion performances. *Journal of Applied Polymer Science*, **96**, 1793–1800 (2005).
<https://doi.org/10.1002/app.21619>
- [3] Navratilova J., Gajzlerova L., Kovar L., Cermak R.: Long-chain branched polypropylene: Crystallization under high pressure and polymorphic composition. *Journal of Thermal Analysis and Calorimetry*, **143**, 3377–3383 (2021).
<https://doi.org/10.1007/s10973-020-09931-1>
- [4] Tian J., Yu W., Zhou C.: Crystallization kinetics of linear and long-chain branched polypropylene. *Journal of Macromolecular Science Part B: Physics*, **45**, 969–985 (2006).
<https://doi.org/10.1080/00222340600870507>
- [5] Parent J. S., Bodsworth A., Sengupta S. S., Kontopoulou M., Chaudhary B. I., Poche D., Cousteaux S.: Structure–rheology relationships of long-chain branched polypropylene: Comparative analysis of acrylic and allylic coagent chemistry. *Polymer*, **50**, 85–94 (2009).
<https://doi.org/10.1016/j.polymer.2008.11.014>
- [6] Liu P., Liu W., Wang W.-J., Li B.-G., Zhu S.: A comprehensive review on controlled synthesis of long-chain branched polyolefins: Part 3, characterization of long-chain branched polymers. *Macromolecular Reaction Engineering*, **11**, 1600012 (2017).
<https://doi.org/10.1002/mren.201600012>
- [7] Maubane L., Lekalakala R., Orasugh J. T., Letwaba J.: Effect of short-chain architecture on the resulting thermal properties of polypropylene. *Polymer*, **264**, 125533 (2023).
<https://doi.org/10.1016/j.polymer.2022.125533>
- [8] Tian J., Yu W., Zhou C.: The preparation and rheology characterization of long chain branching polypropylene. *Polymer*, **47**, 7962–7969 (2006).
<https://doi.org/10.1016/j.polymer.2006.09.042>
- [9] Lagendijk R. P., Hogt A. H., Buijtenhuijs A., Gotsis A. D.: Peroxydicarbonate modification of polypropylene and extensional flow properties. *Polymer*, **42**, 10035–10043 (2001).
[https://doi.org/10.1016/S0032-3861\(01\)00553-5](https://doi.org/10.1016/S0032-3861(01)00553-5)
- [10] Auhl D., Stange J., Münstedt H., Krause B., Voigt D., Lederer A., Lappan U., Lunkwitz K.: Long-chain branched polypropylenes by electron beam irradiation and their rheological properties. *Macromolecules*, **37**, 9465–9472 (2004).
<https://doi.org/10.1021/ma030579w>
- [11] Krause B., Stephan M., Volkland S., Voigt D., Häußler L., Dorschner H.: Long-chain branching of polypropylene by electron-beam irradiation in the molten state. *Journal of Applied Polymer Science*, **99**, 260–265 (2006).
<https://doi.org/10.1002/app.22471>
- [12] Wang L., Wan D., Zhang Z., Liu F., Xing H., Wang Y., Tang T.: Synthesis and structure–property relationships of polypropylene-*g*-poly(ethylene-*co*-1-butene) graft copolymers with well-defined long chain branched molecular structures. *Macromolecules*, **44**, 4167–4179 (2011).
<https://doi.org/10.1021/ma200604y>
- [13] Langston J. A., Colby R. H., Chung T. C. M., Shimizu F., Suzuki T., Aoki M.: Synthesis and characterization of long chain branched isotactic polypropylene via metallocene catalyst and T-reagent. *Macromolecules*, **40**, 2712–2720 (2007).
<https://doi.org/10.1021/ma062111>
- [14] Qian C., Zhao Y., Wang Z., Liu L., Wang D.: Probing the difference of crystalline modifications and structural disorder of isotactic polypropylene *via* high-resolution FTIR spectroscopy. *Polymer*, **224**, 123722 (2021).
<https://doi.org/10.1016/j.polymer.2021.123722>
- [15] Hirose M., Yamamoto T., Naiki M.: Crystal structures of the α and β forms of isotactic polypropylene: A Monte Carlo simulation. *Computational and Theoretical Polymer Science*, **10**, 345–353 (2000).
[https://doi.org/10.1016/S1089-3156\(99\)00039-2](https://doi.org/10.1016/S1089-3156(99)00039-2)
- [16] Zhang C., Liu G., Song Y., Zhao Y., Wang D.: Structural evolution of β – iPP during uniaxial stretching studied by *in-situ* WAXS and SAXS. *Polymer*, **55**, 6915–6923 (2014).
<https://doi.org/10.1016/j.polymer.2014.10.049>
- [17] Mollova A., Androsch R., Mileva D., Gahleitner M., Funari S. S.: Crystallization of isotactic polypropylene containing beta-phase nucleating agent at rapid cooling. *European Polymer Journal*, **49**, 1057–1065 (2013).
<https://doi.org/10.1016/j.eurpolymj.2013.01.015>
- [18] Rhoades A. M., Wonderling N., Gohn A., Williams J., Mileva D., Gahleitner M., Androsch R.: Effect of cooling rate on crystal polymorphism in beta-nucleated isotactic polypropylene as revealed by a combined WAXS/FSC analysis. *Polymer*, **90**, 67–75 (2016).
<https://doi.org/10.1016/j.polymer.2016.02.047>

- [19] Bednarek W. H., Paukszta D., Szostak M., Szymańska J.: Fundamental studies on shear-induced nucleation and beta-phase formation in the isotactic polypropylene–effect of the temperature. *Journal of Polymer Research*, **28**, 439 (2021).
<https://doi.org/10.1007/s10965-021-02652-5>
- [20] Alamo R. G., Kim M.-H., Galante M. J., Isasi J. R., Mandelkern L.: Structural and kinetic factors governing the formation of the γ polymorph of isotactic polypropylene. *Macromolecules*, **32**, 4050–4064 (1999).
<https://doi.org/10.1021/ma981849r>
- [21] Auriemma F., Alfonso G. C., de Rosa C.: *Polymer crystallization I. From chain microstructure to processing*. Springer, Cham (2016).
<https://doi.org/10.1007/978-3-319-49203-2>
- [22] Gajzlerova L., Navratilova J., Ryzi A., Slabenakova T., Cermak R.: Joint effects of long-chain branching and specific nucleation on morphology and thermal properties of polypropylene blends. *Express Polymer Letters*, **14**, 952–961 (2020).
<https://doi.org/10.3144/expresspolymlett.2020.77>
- [23] Xu J., Reiter G., Alamo R. G.: Concepts of nucleation in polymer crystallization. *Crystals*, **11**, 304 (2021).
<https://doi.org/10.3390/cryst11030304>
- [24] di Sacco F., de Jong L., Pelras T., Portale G.: Confined crystallization and polymorphism in iPP thin films. *Polymer*, **255**, 125126 (2022).
<https://doi.org/10.1016/j.polymer.2022.125126>
- [25] Kristiansen P. M., Gress A., Smith P., Hanft D., Schmidt H.-W.: Phase behavior, nucleation and optical properties of the binary system isotactic polypropylene/*N,N,N'*-tris-isopentyl-1,3,5-benzene-tricarboxamide. *Polymer*, **47**, 249–253 (2006).
<https://doi.org/10.1016/j.polymer.2005.08.053>
- [26] Blomenhofer M., Ganzleben S., Hanft D., Schmidt H.-W., Kristiansen M., Smith P., Stoll K., Mäder D., Hoffmann K.: ‘Designer’ nucleating agents for polypropylene. *Macromolecules*, **38**, 3688–3695 (2005).
<https://doi.org/10.1021/ma0473317>
- [27] Bernland K., Tervoort T., Smith P.: Phase behavior and optical- and mechanical properties of the binary system isotactic polypropylene and the nucleating/clarifying agent 1,2,3-trideoxy-4,6:5,7-bis-O-[(4-propylphenyl)methylene]-nonitol. *Polymer*, **50**, 2460–2464 (2009).
<https://doi.org/10.1016/j.polymer.2009.03.010>
- [28] Alcazar D., Ruan J., Thierry A., Lotz B.: Structural matching between the polymeric nucleating agent isotactic poly(vinylcyclohexane) and isotactic polypropylene. *Macromolecules*, **39**, 2832–2840 (2006).
<https://doi.org/10.1021/ma052651r>
- [29] Carmeli E., Kandioller G., Gahleitner M., Müller A. J., Tranchida D., Cavallo D.: Continuous cooling curve diagrams of isotactic-polypropylene/polyethylene blends: Mutual nucleating effects under fast cooling conditions. *Macromolecules*, **54**, 4834–4846 (2021).
<https://doi.org/10.1021/acs.macromol.1c00699>
- [30] Zhang X., Qin W., Wu T., Zhao S.: A new insight into the formation of β -crystals of isotactic polypropylene induced by zinc dicarboxylic acids. *Polymer*, **262**, 125500 (2022).
<https://doi.org/10.1016/j.polymer.2022.125500>
- [31] Wittmann J. C., Lotz B.: Epitaxial crystallization of polymers on organic and polymeric substrates. *Progress in Polymer Science*, **15**, 909–948 (1990).
[https://doi.org/10.1016/0079-6700\(90\)90025-V](https://doi.org/10.1016/0079-6700(90)90025-V)
- [32] Luo F., Xu C., Wang K., Deng H., Chen F., Fu Q.: Exploring temperature dependence of the toughening behavior of β -nucleated impact polypropylene copolymer. *Polymer*, **53**, 1783–1790 (2012).
<https://doi.org/10.1016/j.polymer.2012.02.024>
- [33] Masirek R., Piorkowska E.: Nucleation of crystallization in isotactic polypropylene and polyoxymethylene with poly(tetrafluoroethylene) particles. *European Polymer Journal*, **46**, 1436–1445 (2010).
<https://doi.org/10.1016/j.eurpolymj.2010.04.021>
- [34] Barczewski M., Mysiukiewicz O., Andrzejewski J., Piasecki A., Strzemięcka B., Adamek G.: The inhibiting effect of basalt powder on crystallization behavior and the structure-property relationship of α -nucleated polypropylene composites. *Polymer Testing*, **103**, 107372 (2021).
<https://doi.org/10.1016/j.polymertesting.2021.107372>
- [35] Menyhárd A., Gahleitner M., Varga J., Bernreitner K., Jääskeläinen P., Øysæd H., Pukánszky B.: The influence of nucleus density on optical properties in nucleated isotactic polypropylene. *European Polymer Journal*, **45**, 3138–3148 (2009).
<https://doi.org/10.1016/j.eurpolymj.2009.08.006>
- [36] Dobrzyńska-Mizera M., Dutkiewicz M., Sterzyński T., di Lorenzo M. L.: Isotactic polypropylene modified with sorbitol-based derivative and siloxane-silsesquioxane resin. *European Polymer Journal*, **85**, 62–71 (2016).
<https://doi.org/10.1016/j.eurpolymj.2016.09.049>
- [37] Horváth Z., Gyarmati B., Menyhárd A., Doshev P., Gahleitner M., Varga J., Pukánszky B.: The role of solubility and critical temperatures for the efficiency of sorbitol clarifiers in polypropylene. *RSC Advances*, **4**, 19737 (2014).
<https://doi.org/10.1039/c4ra01917b>
- [38] Chvátalová L., Navrátilová J., Čermák R., Raab M., Obadal M.: Joint effects of molecular structure and processing history on specific nucleation of isotactic polypropylene. *Macromolecules*, **42**, 7413–7417 (2009).
<https://doi.org/10.1021/ma9005878>
- [39] Gajzlerova L., Navratilova J., Zenzingerova S., Jaska D., Benicek L., Kudlacek M., Cermak R., Obadal M.: On isotactic polypropylene annealing: Difference in final properties of neat and β -nucleated polypropylene. *Express Polymer Letters*, **16**, 453–464 (2022).
<https://doi.org/10.3144/expresspolymlett.2022.34>

- [40] Coiai S., Augier S., Pinzino C., Passaglia E.: Control of degradation of polypropylene during its radical functionalisation with furan and thiophene derivatives. *Polymer Degradation and Stability*, **95**, 298–305 (2010).
<https://doi.org/10.1016/j.polymdegradstab.2009.11.014>
- [41] Naiki M., Kikkawa T., Endo Y., Nozaki K., Yamamoto T., Hara T.: Crystal ordering of α phase isotactic polypropylene. *Polymer*, **42**, 5471–5477 (2001).
[https://doi.org/10.1016/S0032-3861\(00\)00848-X](https://doi.org/10.1016/S0032-3861(00)00848-X)
- [42] Hikosaka M., Seto T.: The order of the molecular chains in isotactic polypropylene crystals. *Polymer Journal*, **5**, 111–127 (1973).
<https://doi.org/10.1295/polymj.5.111>
- [43] Varga J.: Supermolecular structure of isotactic polypropylene. *Journal of Material Science*, **27**, 2557–2579 (1992).
<https://doi.org/10.1007/bf00540671>

Research article

Synthesis and characteristics of α -carboxyl, ω -hydroxyl natural rubber toughened poly(lactic acid)

Abdulahkim Masa¹, Varaporn Tanrattanakul², Ruedee Jaratrotkamjorn^{1*}

¹Rubber Engineering and Technology Program, International College, Prince of Songkla University, 90110 Hat Yai, Songkhla, Thailand

²Division of Physical Science, Prince of Songkla University, 90110 Hat Yai, Songkhla, Thailand

Received 10 June 2023; accepted in revised form 24 July 2023

Abstract. This work presented the synthesis of α -carboxyl, ω -hydroxyl natural rubber (CHNR) for use as an alternative toughening agent for poly(lactic acid) (PLA). The proton nuclear magnetic resonance spectroscopy (¹H-NMR) and Fourier transform infrared spectroscopy (FTIR) analyses verified the chemical structure of CHNR consisting of the hydroxyl and carboxyl end groups. The molecular weights of CHNR were set from 5000 to 15 000 g·mol⁻¹ which were determined by gel permeation chromatography (GPC) and ¹H-NMR. The PLA and CHNR were prepared by reactive blending using a twin-screw extruder. It was found that the reaction between PLA and CHNR proceeded through transesterification without a catalyst. The formation of copolymer (PLA-co-CHNR) at the interface of PLA and CHNR increased the interfacial adhesion between the two phases. Differential scanning calorimetry (DSC) analysis revealed that CHNR was more compatible with PLA than natural rubber (NR). The compatibilization affected the blend morphology by reducing the interfacial tension. It resulted in a reduction of rubber particle size. The CHNR with a molecular weight of 5000 g·mol⁻¹ showed the greatest improvement in the toughness and ductility of PLA.

Keywords: biopolymers, rubber, poly(lactic acid), polymer blends, copolymer, mechanical properties

1. Introduction

Poly(lactic acid) (PLA) is an aliphatic polyester produced from renewable resources, such as sugarcane and starch. It is also known as a biodegradable and compostable polymer. It is widely used in food packaging and consumer products [1, 2]. The mechanical properties of PLA are comparable to conventional polymers, such as polystyrene (PS) and polyethylene terephthalate (PET) [3]. Therefore, it has great potential to replace conventional petroleum-based polymers because of environmental concerns and energy savings. Although PLA is environmentally friendly, biocompatible, and processable, its brittleness is a major problem that restricts its applications [2]. Several works have been studied to solve this problem. Binary blends of PLA and other polymers have

successfully enhanced the toughness of PLA. It acted as a toughening agent for PLA, such as poly (polyethylene glycol-co-citric acid) [4], poly(β -hydroxybutyrate-co- β -hydroxyvalerate) [5], epoxidized polybutadiene [6], poly(styrene-*b*-butadiene-*b*-styrene) [7], poly(ethylene oxide)-poly(propylene oxide)-poly(ethylene oxide) triblock copolymers [8], poly (butylene adipate-co-terephthalate) [9], poly (ethylene-butylacrylate-glycidyl methacrylate) [10], poly (butylene 2,5-furandicarboxylate)-*b*-poly(ethylene glycol) [11], and poly(1,4-cyclohexanedimethylene isosorbide terephthalate) [12]. Natural rubber (NR; *cis*-1,4-polyisoprene) is an aliphatic hydrocarbon polymer that is harvested from the *Hevea brasiliensis* tree. It has several interesting properties including good mechanical properties, abrasion

*Corresponding author, e-mail: ruedee.j@psu.ac.th
© BME-PT

resistance, and electrical insulation. It served as a good toughening agent for PLA. The toughness [13, 14] and ductility [15, 16] of PLA have been improved by blending with 10 wt% of NR. The high content of NR (>10 wt%) caused the coalescence phenomena and deteriorated the mechanical properties of the blends [13, 15]. The NR particles dispersed in the PLA matrix. It plays an important role in the mechanical properties of the blend. The craze initiates and terminates by NR particles. The compatibility of the blend is strongly associated with its mechanical properties. The difference in polarity of PLA and NR caused phase separation in the blend. It was due to the poor interfacial adhesion between the two phases. Compatibilization was a useful method to improve the compatibility of PLA and NR by adding the third component. Block and graft copolymers have been used as the compatibilizers for PLA and NR blends, such as NR-based diblock copolymer [17], NR-based triblock copolymer [18], NR grafted with poly(methyl methacrylate) [13], NR grafted with poly(vinyl acetate) [19], NR grafted with PLA [20], NR grafted with poly(butyl acrylate) [21], and NR grafted with poly(vinyl propionate) [22]. These studies were successful in improving the interfacial adhesion between the two phases and enhancing the toughness of the PLA/NR blends. These copolymers placed themselves at the interface between PLA and NR. One part was miscible with PLA and the other one was miscible with NR. Thus, the interfacial adhesion was enhanced. It allowed the stress to transform from one phase to the other one, which was efficient for craze initiation and propagation [23].

The addition of a second component with a reactive group is another approach for the compatibilization of PLA through reactive blending. If the chains of the second component are terminated by hydroxyl or carboxyl groups, three interchange reactions are possible during mixing: alcoholysis, acidolysis, and ester-ester interchange [24]. It is also known as transesterification. The block copolymer was initially formed and finally converted to the random copolymer. The blends of PLA with a second polymer through transesterification have been reported. For example, the melt blending of PLA and poly(ethylene-*co*-vinyl alcohol) through transesterification revealed a reduction of the interfacial tension and improved the interfacial adhesion between the two

phases [25]. The interchange reaction between PLA and polycarbonate (PC) enhanced the compatibility of the blend and increased the interfacial adhesion between the two phases [26]. The ductility of PLA improved with the addition of maleic acid anhydride end-capped poly(propylene carbonate) [27].

The purpose of this work was to synthesize the α -carboxyl, ω -hydroxyl natural rubber (CHNR) for use as an alternative toughening agent for PLA. The blends were performed by melt mixing. We assumed that the reactive blend could proceed and generate a new copolymer. The effects of compatibilization on morphology, thermal and mechanical properties of the blends were investigated.

2. Experimental

2.1. Materials

Poly(lactic acid) (PLA Ingeo[®] 4043D) was produced by NatureWorks LLC, USA. The content of *d*-lactide content is approximately 6%, and a Melt Flow Index (MFI) of 6 g (10 min⁻¹) at 210 °C with a load of 2.16 kg. The melting temperature (T_m) and glass transition temperature (T_g) are approximately 145–160 and 55–60 °C, respectively. Natural rubber (NR; STR5L) with a Mooney viscosity (ML1+4 at 100 °C) of 80 was produced by Chalong Latex Industry Co., Ltd., Thailand. Periodic acid (H₅IO₆, 99%), *N,N*-dimethyl-4-aminopyridine (DMAP, ≥99%), and succinic anhydride (SA, ≥99%) were purchased from Sigma-Aldrich. Sodium borohydride (NaBH₄, 97%) was purchased from Loba Chemie Pvt. Ltd. Sodium bicarbonate (NaHCO₃), sodium thiosulfate pentahydrate (Na₂S₂O₃·5H₂O), dichloromethane (DCM) and tetrahydrofuran (THF) were all purchased from RCI Labscan Ltd.

2.2. Synthesis of carbonyl telechelic natural rubber (CTNR)

CTNR was synthesized according to previous work [28]. NR (60 g) was dissolved in 1500 ml of THF overnight. An amount of 8.84 g of H₅IO₆ was dissolved in 97 ml of THF and added to the reactor. The reaction was carried out at room temperature for 6 h. The organic solution was filtered and washed with aqueous solutions (70/30% vol/vol of NaHCO₃/NaCl and 50/50% vol/vol of Na₂S₂O₃/NaCl). Then it dried over MgSO₄ and filtered through a filter paper. Finally, the organic solution was evaporated in a rotary evaporator and dried in a vacuum oven.

2.3. Synthesis of hydroxyl telechelic natural rubber (HTNR)

HTNR was synthesized according to previous work [28]. CTNR (46 g) was dissolved in 1270 ml of THF. The NaBH₄ (13.98 g) was added to the reactor. The reaction was carried out at 60 °C for 6 h under a nitrogen atmosphere. The organic solution was hydrolyzed with ice and washed with a saturated NaCl solution. The organic phase was dried over MgSO₄ and filtered. Finally, it was evaporated in a rotary evaporator and dried in a vacuum oven.

2.4. Synthesis of α -carboxyl, ω -hydroxyl natural rubber (CHNR)

HTNR (38 g) was dissolved in 1200 ml of DCM. Then the DMAP (3.19 g) and SA (7.47 g) were added to the reactor. The reaction was carried out at 30 °C for 24 h under a nitrogen atmosphere. The organic solution was washed twice with saturated NaHCO₃ and saturated NaCl solutions. Then it was dried over MgSO₄ and evaporated to remove the DCM. The obtained CHNR was dried in a vacuum oven to remove the residual DCM.

The chemical structures of all oligo-isoprenes (CTNR, HTNR, and CHNR) were verified by proton nuclear magnetic resonance spectroscopy (¹H-NMR) and Fourier transform infrared spectroscopy (FTIR) techniques. The molecular weights of oligo-isoprenes were determined by gel permeation chromatography (GPC) and ¹H-NMR.

2.5. Preparation of polymer blends

The neat PLA was dried overnight in an oven at 105 °C to remove moisture. Then it was kept in a desiccator before blending. The proportion of PLA to rubber (NR and CHNR) was fixed at 90/10 wt%. The binary blends of PLA/NR and PLA/CHNR were prepared by melt blending using a twin-screw extruder (LTE16-44, LAB TECH Engineering Co., Ltd., Thailand) at a rotor speed of 100 rpm. The temperatures of the eleven zones were set at 140 °C (feed zone), 140 °C (zone 2), 150 °C (zone 3), and 160 °C (zones 4–11). The PLA and obtained blends were shaped at 160 °C for 9 min with a pressure of 140 kg·cm⁻² using a compression molding machine (SLLP50, Siamlab Engineering Co., Ltd., Thailand). The obtained sheet was cooled in the air at room temperature for 10 min. The thickness of the obtained sheets was approximately 2 mm.

2.6. Chemical structure analysis

The chemical structures of NR and oligo-isoprenes were verified by FTIR and ¹H-NMR. The FTIR spectra were recorded on the Fourier transform infrared spectrometer (Perkin-Elmer, Spotlight 200i). The absorption bands were reported in the range of 400–4000 cm⁻¹ based on 16 scans at a resolution of 4 cm⁻¹. The ¹H-NMR data were recorded on the Varian Unity Inova NMR spectrometer (500 MHz). Deuterated chloroform (CDCl₃) was used as a solvent. The number-average molecular weight (\bar{M}_n) of all oligo-isoprenes (CTNR, HTNR, and CHNR) was determined by ¹H-NMR using the integrated peak areas, repeating unit of NR (68), and total mass of the rest molecule. The \bar{M}_n of CTNR was calculated according to Equation (1):

$$\bar{M}_{n,CTNR} = \left[\frac{I_b}{\frac{I_{f,i}}{4}} \cdot 68 \right] + 100 \quad (1)$$

where I_b and $I_{f,i}$ are the integrated peak areas at 5.10 and 2.43–2.52 ppm, respectively. 100 is the total molar mass of the rest molecule. The \bar{M}_n of HTNR was calculated according to Equation (2):

$$\bar{M}_{n,HTNR} = \left[\frac{I_b}{\frac{I_c}{2}} \cdot 68 \right] + 104 \quad (2)$$

where I_b and I_c are the integrated peak areas at 5.10 and 3.65 ppm, respectively. 104 is the total molar mass of the rest molecule. The \bar{M}_n of CHNR was calculated according to Equation (3):

$$\bar{M}_{n,CHNR} = \left[\frac{I_b}{\frac{I_c}{2}} \cdot 68 \right] + 204 \quad (3)$$

where I_b and I_c are the integrated peak areas at 5.10 and 4.08 ppm, respectively. 204 is the total molar mass of the rest molecule.

2.7. Measurement of molecular weight

The molecular weights and molecular weight distributions of PLA, NR, oligo-isoprenes, and the blends were measured by gel permeation chromatography (GPC; Agilent, 1260 Infinity II) performed with two columns (PLgel MIXED-C, 5 μ m, 7.5×300 mm) and a refractive index detector. The tests were performed at 40 °C. The flow rate of eluent (THF) was 1 ml·min⁻¹. The data were calibrated with polystyrene

standards and corrected with the Benoit factor (0.67) [29].

2.8. Blend characterization

2.8.1. Mechanical properties

Izod and Charpy impact tests of PLA and the blends were carried out according to ASTM D256. Six V-notched and unnotched specimens were prepared for each test. The depth of the V-notch was 2.5 mm. The tensile properties were tested according to ASTM D412C. Six dumbbell-shaped specimens were tested using a universal testing machine (Instron 5569) at a crosshead speed of $5 \text{ mm} \cdot \text{min}^{-1}$.

2.8.2. Blend morphology

The morphologies of PLA and the blends were investigated using a scanning electron microscope (FEI Quanta 400). All specimens were prepared by freeze fracturing. It was frozen in liquid nitrogen. Then the frozen specimen was rapidly fractured. The fractured surfaces were coated with gold before analysis.

2.8.3. Thermal properties

The thermal properties of PLA and the blends were investigated using differential scanning calorimetry (Perkin-Elmer, DSC7). The first heating scan was heated from -70 to 180°C , followed by cooling from 180 to -70°C , then heating again as in the first heating scan. The tests were performed at the heating rate of $10^\circ\text{C} \cdot \text{min}^{-1}$ under a nitrogen atmosphere. The glass transition temperature (T_g), melting temperature (T_m), and cold crystallization temperature (T_{cc}) were determined from the second heating thermograms. The degree of crystallinity (X_c) was calculated according to Equation (4):

$$X_c [\%] = \frac{\Delta H_m + \Delta H_{cc}}{93} \cdot 100 \quad (4)$$

where ΔH_m and ΔH_{cc} are the enthalpies of fusion and cold crystallization in $\text{J} \cdot \text{g}^{-1}$, respectively. $93 \text{ J} \cdot \text{g}^{-1}$ is the enthalpy of fusion of 100% PLA crystal [30].

The dynamic mechanical thermal analysis (DMA) was performed with a dynamic mechanical analyzer (DMA8000, PerkinElmer, USA). The specimens were

tested in dual cantilever mode with a temperature scan from -70 to 180°C at a heating rate of $3^\circ\text{C} \cdot \text{min}^{-1}$. The frequency was 1 Hz and the strain control was 0.01%.

3. Results and discussion

3.1. Characterization of oligo-isoprenes

Three types of oligo-isoprenes were synthesized from NR (Figure 1). The new oligo-isoprene (CHNR) was prepared in three steps. The first step was the synthesis of CTNR containing an aldehyde and a ketone chain ends through the controlled oxidative degradation of NR. The initial molecular weight (\bar{M}_n) of CTNR was set around 5000, 10000 and 15000 $\text{g} \cdot \text{mol}^{-1}$. The CTNR was used as a starting oligo-isoprene to produce further HTNR and CHNR. A second step was the reduction of CTNR with NaBH_4 to generate the HTNR containing hydroxyl chain ends. The last step was the synthesis of CHNR from the HTNR by using SA in the presence of DMAP as a catalyst.

All chemical structures of the oligo-isoprenes were characterized by $^1\text{H-NMR}$ and FTIR. The $^1\text{H-NMR}$ spectra of NR and oligo-isoprenes with a targeted molecular weight of $5000 \text{ g} \cdot \text{mol}^{-1}$ are shown in Figure 2. NR presented the characteristic peak of CH protons at 5.10 ppm. The characteristic peaks of CTNR were observed at 9.77 and 2.13 ppm belonging to the aldehyde and ketonic protons, respectively. For the HTNR spectrum, the disappearance of the peak at 9.77 ppm was clearly observed. The presence of the new peaks at 3.80 (CH proton) and 3.65 (CH_2 protons) ppm confirmed the change of carbonyl to hydroxyl groups. The characteristic peaks of CHNR were observed at 4.08 and 2.65 ppm corresponding to the CH_2 protons adjacent to ester groups, while the peak at 3.80 ppm still appeared at the same position that was close to the hydroxyl group. These verify that the CHNR was terminated by hydroxyl and carboxyl groups.

The FTIR spectrum of NR presented the characteristic peak at 1665 cm^{-1} for the stretching vibrations of $\text{C}=\text{C}$ (Figure 3). The CTNR presented the new absorption band at 1721 cm^{-1} corresponding to the stretching vibrations of $\text{C}=\text{O}$, whereas this peak

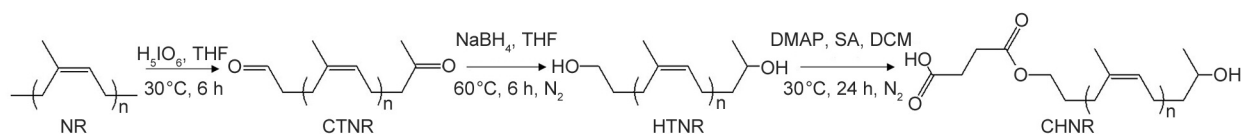


Figure 1. Synthesis of CHNR.

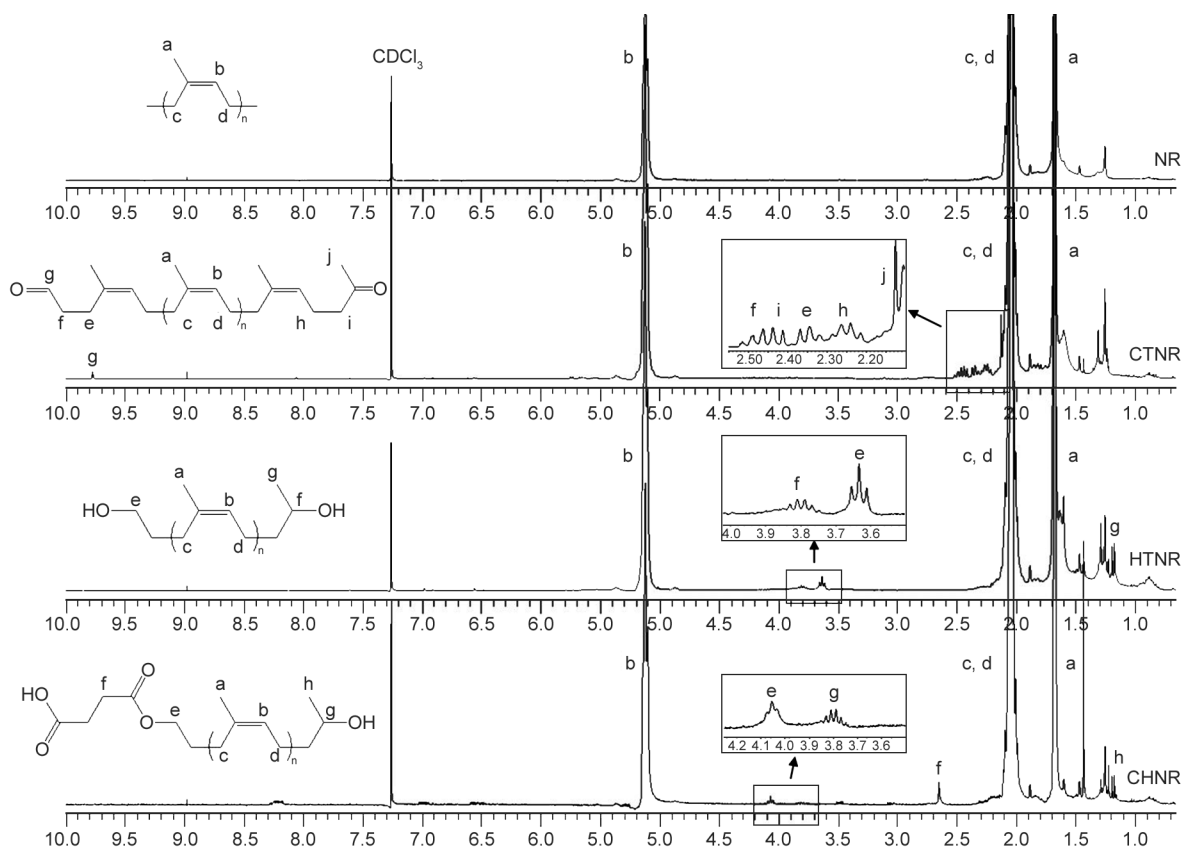


Figure 2. $^1\text{H-NMR}$ spectra of NR and obtained oligo-isoprenes with the targeted molecular weight of $5000\text{ g}\cdot\text{mol}^{-1}$.

disappeared after conversion to HTNR. The new absorption band of OH stretching appeared at 3378 cm^{-1} . This was due to all carbonyl groups of CTNR changing to hydroxyl groups. In the CHNR spectrum, new absorption bands were observed at 1734 and 1722 cm^{-1} . Both were assigned to the stretching vibrations of $\text{C}=\text{O}$ in different functional groups (ester and carboxylic groups), whereas the absorption band of OH stretching at 3378 cm^{-1} still appeared. Both $^1\text{H-NMR}$ and FTIR data confirmed

the synthesis of CHNR containing hydroxyl and carboxyl groups at the chain ends.

The molecular weights of obtained oligo-isoprenes were determined by $^1\text{H-NMR}$ and GPC (Table 1). It was found that the \bar{M}_n of all CTNR (4466 , 9018 and $14049\text{ g}\cdot\text{mol}^{-1}$) was close to the targeted molecular weights (5000 , 10000 , and $15000\text{ g}\cdot\text{mol}^{-1}$). From GPC analysis, the \bar{M}_n of all CTNR were 5100 , 10100 , and $14100\text{ g}\cdot\text{mol}^{-1}$. The CTNR with initial \bar{M}_n of 5000 , 10000 , and $15000\text{ g}\cdot\text{mol}^{-1}$ were labeled

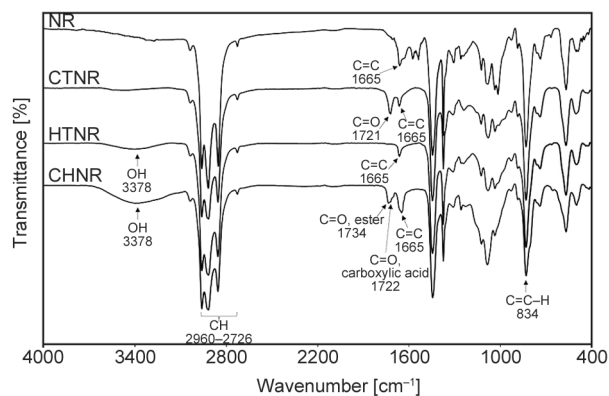


Figure 3. FTIR spectra of NR and oligo-isoprenes with the targeted molecular weight of $5000\text{ g}\cdot\text{mol}^{-1}$.

Table 1. Molecular weights of oligo-isoprenes.

Sample	\bar{M}_n [$\text{g}\cdot\text{mol}^{-1}$] ^a	\bar{M}_n [$\text{g}\cdot\text{mol}^{-1}$] ^b	\bar{M}_w [$\text{g}\cdot\text{mol}^{-1}$] ^b	PDI ^b
CTNR5	4466	5100	11300	2.22
HTNR5	4746	5700	12800	2.25
CHNR5	5096	6200	12900	2.08
CTNR10	9018	10100	19700	1.95
HTNR10	9614	10600	20900	1.97
CHNR10	10747	12400	23600	1.90
CTNR15	14049	14100	36000	2.55
HTNR15	14887	15300	43900	2.87
CHNR15	15315	16600	38000	2.29

^aDetermined by $^1\text{H-NMR}$.

^bDetermined by GPC.

with CTNR5, CTNR10, and CTNR15, respectively. Then they were used for the preparation of HTNR and CHNR. Both $^1\text{H-NMR}$ and GPC techniques gave a slight increase in \bar{M}_n values of HTNR (HTNR5, HTNR10, and HTNR15) and CHNR (CHNR5, CHNR10, and CHNR15) from those of the CTNR because the chemical structures of their oligo-isoprenes were changed to the new ones. The polydispersity index (PDI) of all oligo-isoprenes was approximately 2.

3.2. Blend characterization

The binary blends of (PLA/NR and PLA/CHNR) were prepared by melt blending. It is known that functional groups play an important role in controlling chemical reactions. Both PLA and CHNR contained two different reactive end groups (hydroxyl and carboxyl groups). Thus, it was possible to generate new random copolymers through transesterification. The

proposed mechanisms are illustrated in Figure 4. It involved three reactions: acidolysis, alcoholysis, and direct ester exchange. The block copolymer (PLA-co-CHNR) was initially formed in the acidolysis reaction. The PLA homopolymer and succinic acid could occur in this reaction. Succinic acid might react with PLA-co-CHNR, PLA, and CHNR. In this case, it acted as a chain extender that expanded the polymer chain. In the alcoholysis reaction, the formation of PLA-co-CHNR, PLA homopolymer, HTNR, and PLA-succinic acid might occur. HTNR could react with PLA to form the PLA-HTNR block copolymer and/or it was likely a chain extender for the polymer. The PLA-succinic acid had a chance to react with PLA, CHNR, and HTNR generating the copolymers. For direct ester exchange, the PLA-co-CHNR and PLA-succinic acid were formed. The block copolymers (PLA-co-CHNR) were initially formed and they subsequently reacted with themselves and starting

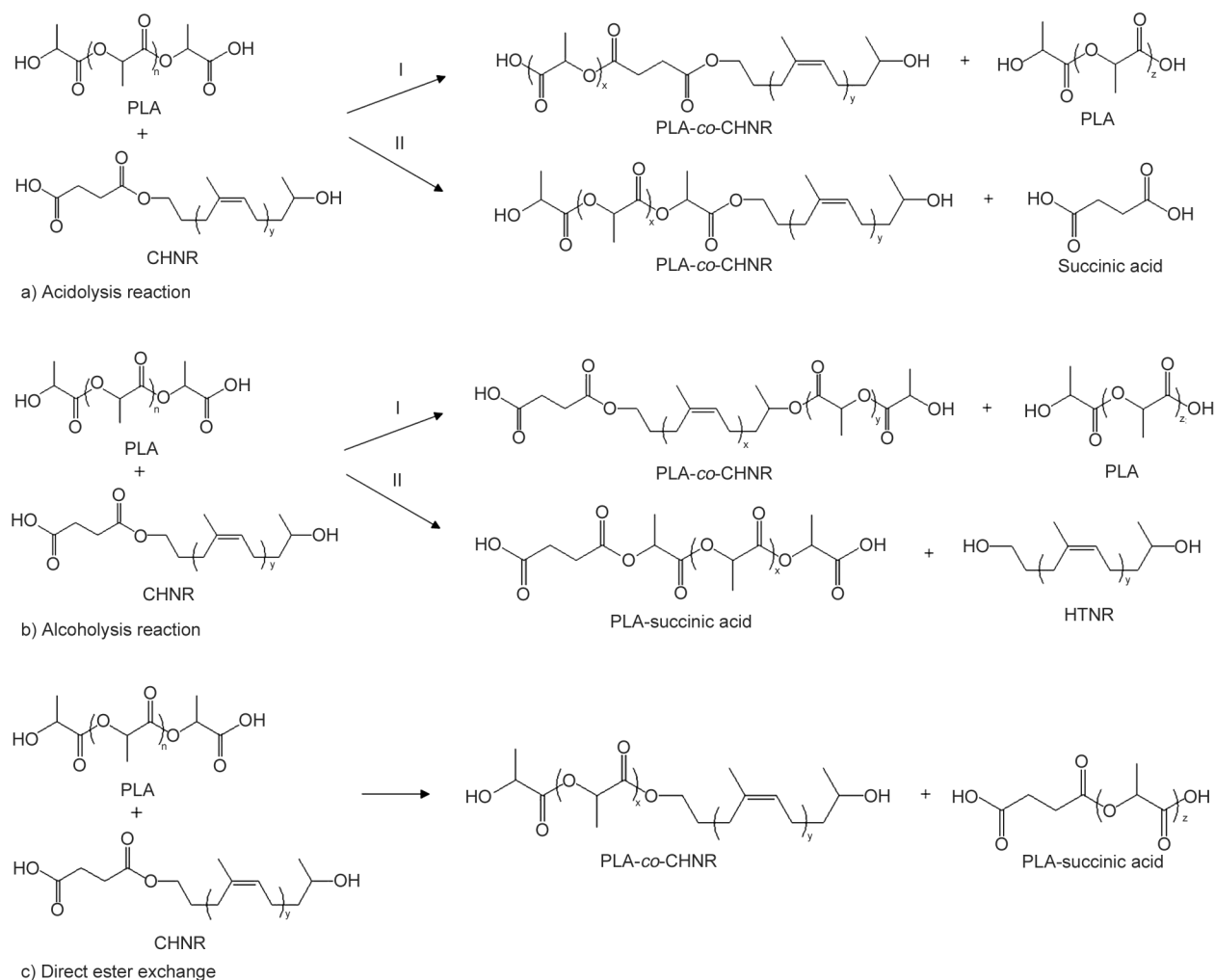


Figure 4. Transesterification reactions between PLA and CHNR. a) Acidolysis reaction, b) alcoholysis reaction, and c) direct ester exchange.

polymers (PLA and CHNR) converting to random copolymers. Based on the proposed mechanisms, it was concluded that there are different chain lengths of copolymers, homopolymers, diols, and diacids in the reaction mixture.

In fact, transesterification causes the breakage of polymer chains which leads to a decrease in the molecular weight of the polymer. In order to confirm these reactions, the measurement of molecular weight by GPC was utilized. The molecular weights and molecular weight distributions of the PLA and the blends are listed in Table 2. The \bar{M}_n of PLA and NR were 81 500 and 289 000 $\text{g}\cdot\text{mol}^{-1}$, respectively. The \bar{M}_n of the PLA/NR was 88000 $\text{g}\cdot\text{mol}^{-1}$ and it increased from the \bar{M}_n of PLA. This indicated that there was no chemical reaction during the melt blending. In the case of all PLA/CHNR blends, \bar{M}_n had dramatically decreased from the PLA. This was due to the formation of shorter chains (new copolymers) through transesterification, as proposed in Figure 4. This is similar to a prior study on the blend between polycaprolactone and PLA through transesterification [31].

The molecular weight distribution curves of PLA, NR, and the blends are shown in Figure 5. A broad

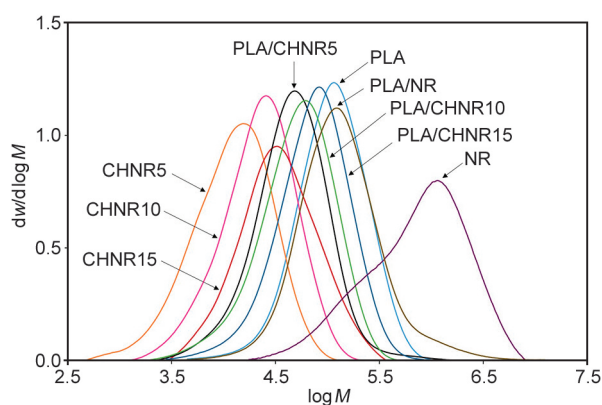


Figure 5. Molecular weight distributions of PLA and the blends.

peak indicated that the molecular weight distribution of the sample was wide. In fact, polymer distributions can be wide because there are many high molecular-weight and low molecular-weight components. The PDI of the PLA/NR was approximately 2.61. Meanwhile, the PDI of PLA/CHNR was approximately 2.00. This was known as a broad distribution of polymer indicating that polymers have the distribution of chain lengths. A broad distribution of PLA/NR was due to the nature of NR. Generally, natural polymers such as NR have a wide distribution. In the case of PLA/CHNR, the formation of new copolymers with different chain lengths caused the wide distribution. Thus, the GPC analysis confirmed the transesterification during the melt blending of PLA/CHNR.

3.3. Morphological analysis

The morphology of the blends was investigated by SEM. The SEM images of PLA and the blends at the same 500 \times magnification are shown in Figure 6. PLA showed fine phase morphology (Figure 6a), while phase separation was observed in the PLA/NR and PLA/CHNR blends (Figure 6b–6e). Especially, a coarse and heterogeneous morphology was clearly observed for the PLA/NR (Figure 6b). NR was dispersed in a PLA matrix. The polar PLA and non-polar NR made an immiscible blend with poor interfacial adhesion between the two phases. All PLA/CHNR blends showed a finer phase morphology than PLA/NR. Rubber particle size could indicate the compatibility in the blend. The particle size of rubber was around 10.8 μm in the PLA/NR, while the PLA/CHNR5, PLA/CHNR10, and PLA/CHNR15 were 4.2, 5.5, and 7.2 μm , respectively. The smaller particle size of the rubber indicated a reduction of the interfacial tension between the two phases [23]. It was also observed in other works [13, 19, 20, 32]. This implied that CHNR was more compatible with PLA than NR.

Table 2. Molecular weights and thermal properties of PLA and the blends.

Sample	\bar{M}_n [$\text{g}\cdot\text{mol}^{-1}$]	\bar{M}_w [$\text{g}\cdot\text{mol}^{-1}$]	PDI	T_g [$^{\circ}\text{C}$]	T_m [$^{\circ}\text{C}$]	T_{CC} [$^{\circ}\text{C}$]	ΔH_m [$\text{J}\cdot\text{g}^{-1}$]	ΔH_{CC} [$\text{J}\cdot\text{g}^{-1}$]	X_c [%]
PLA	81 500	149 000	1.82	60	150	119	24.5	24.0	52.2
NR	289 000	1 197 000	4.14	-63	-	-	-	-	-
PLA/NR	88 000	230 000	2.61	-63, 60	150	-	6.6	6.7	14.3
PLA/CHNR5	31 000	64 300	2.07	-60, 50	141, 148	110	25.6	30.1	60.1
PLA/CHNR10	35 000	71 000	2.02	-61, 51	140, 149	101	30.9	34.8	70.6
PLA/CHNR15	49 000	98 000	2.00	-62, 52	144, 150	111	28.4	33.0	66.1

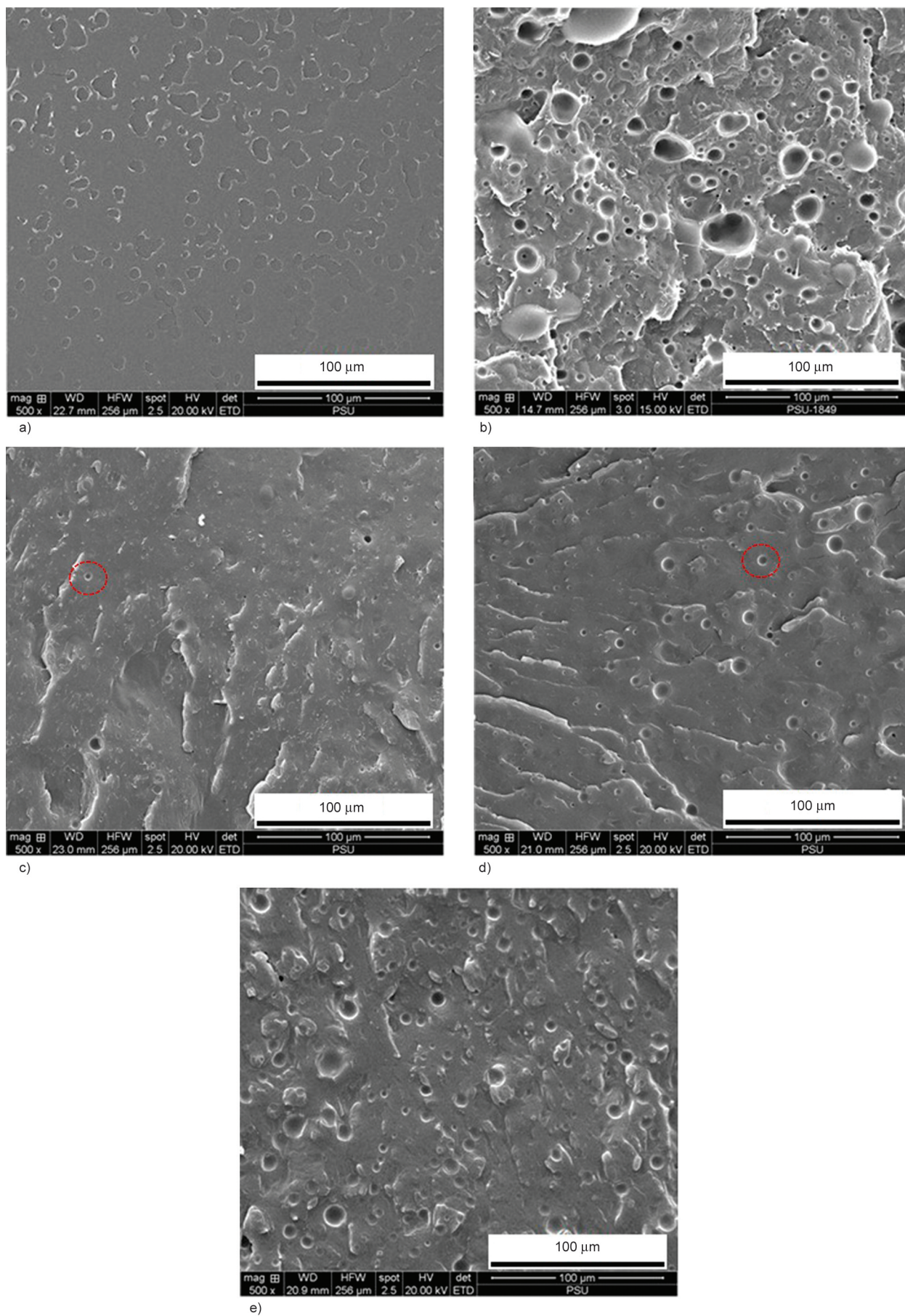


Figure 6. SEM images of PLA and the blends: a) PLA, b) PLA/NR, c) PLA/CHNR5, d) PLA/CHNR10, and e) PLA/CHNR15.

3.4. Thermal analysis

Besides the morphological analysis, the miscibility of the blend could be investigated from T_g . All thermograms were recorded during the second heating scan (Figure 7). The neat PLA and NR presented a single T_g at 60 and -63°C , respectively. The PLA/NR exhibited two T_g s at -63 and 60°C . The lower T_g belonged to NR, while the higher T_g belonged to PLA. The blend showed two T_g s of pure components and it was no shift from the values of their T_g s. This was a type of immiscible blend. Two T_g s and the shift of them were observed in all PLA/CHNR blends. The T_g of CHNR shifted to a higher temperature (-62 – -60°C), while the T_g of PLA shifted to a lower temperature (50 – 52°C). It is known that a shift of T_g from one blend component towards the T_g of the other blend component is referred to as a partially miscible blend. Interestingly, the maximum shift for PLA/CHNR5 was 2°C (T_g of CHNR) and 10°C (T_g of PLA). It implied that CHNR5 was more compatible with PLA. Two melting peaks were notably observed for all blends, except for PLA/NR. When the sample was heated at a low rate during the temperature scan, small crystals melted and then recrystallized, resulting in the appearance of a second melting peak at a higher temperature [33]. This is a common phenomenon found in several rubbers toughened PLA [13, 16, 22, 25, 34]. The degree of crystallinity (X_c) of PLA was approximately 52.2% (Table 2). It seems that blending with NR caused a reduction in X_c of PLA to 14.3%. This was probably because the high molecular weight of NR caused more chain entanglement and hindered the nucleation of PLA. It was similarly observed in a previous study [35]. It was found that the

X_c of PLA slightly increased up to 60.1–70.6% after blending with CHNR. It implied that CHNR acted as a good nucleating agent for PLA.

The mechanical and thermal properties of the material could be determined by DMA. Figure 8 shows the DMA curves of PLA and the blends. Generally, the storage modulus (E') measures the elastic response of the material. The E' (at 30°C) of PLA decreased with the addition of NR (Figure 8a). This was due to the elastomeric nature of NR. It is known that E' is associated with the stiffness of a material. It indicated that the NR decreased the stiffness of PLA. This observation was similar to the previous report [36]. The enhancement of E' was found in the PLA/CHNR10. This can be caused by the highest crystallinity which affected the stiffness of the blend. From the DSC analysis, the X_c of the PLA/CHNR blends could be ranked in the following order: PLA/CHNR10 > PLA/CHNR15 > PLA/CHNR5. It could be concluded that the crystallinity promoted the stiffness of the blend. This behavior was similarly found in PLA blended with spent coffee grounds [37]. The E' was suddenly dropped in the temperature range of 70 to 75°C . This is known as a glass transition region and the onset temperature is identified as a T_g . The T_g of PLA was observed at 73°C (Figure 8b). Two T_g s were found in PLA/NR at -60 and 73°C corresponding to the T_g of NR and PLA, respectively. The T_g of PLA in all PLA/CHNR blends was slightly shifted to the lower temperature (70 – 72°C), while the T_g of CHNR was seen from -54 to -59°C . It indicated that CHNR was more compatible with PLA than NR. All the blends showed a broad $\tan\delta$ peak because the mixture had more heterogeneous polymers. The differences in the polymer

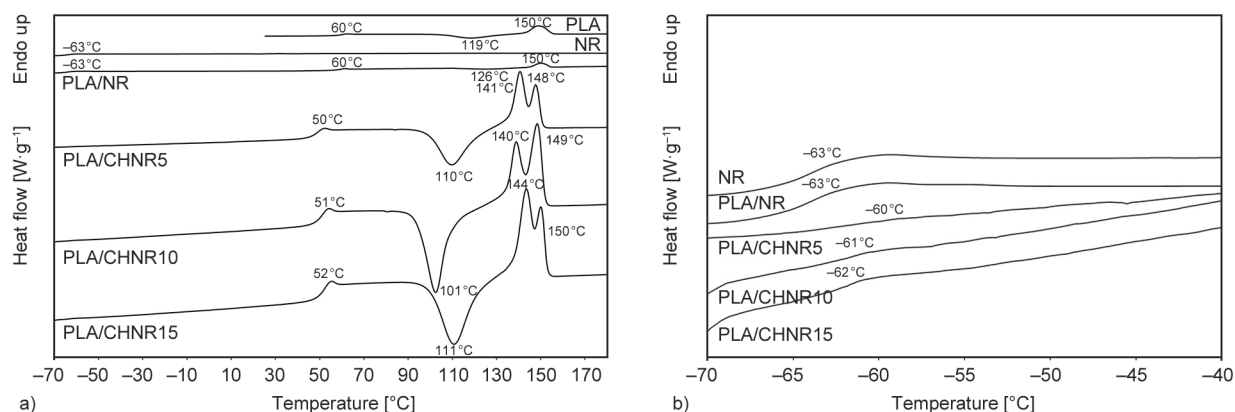


Figure 7. DSC thermograms of PLA, NR, and the blends: a) overall view, and b) expanded view for the temperature range from -70 to -40°C .

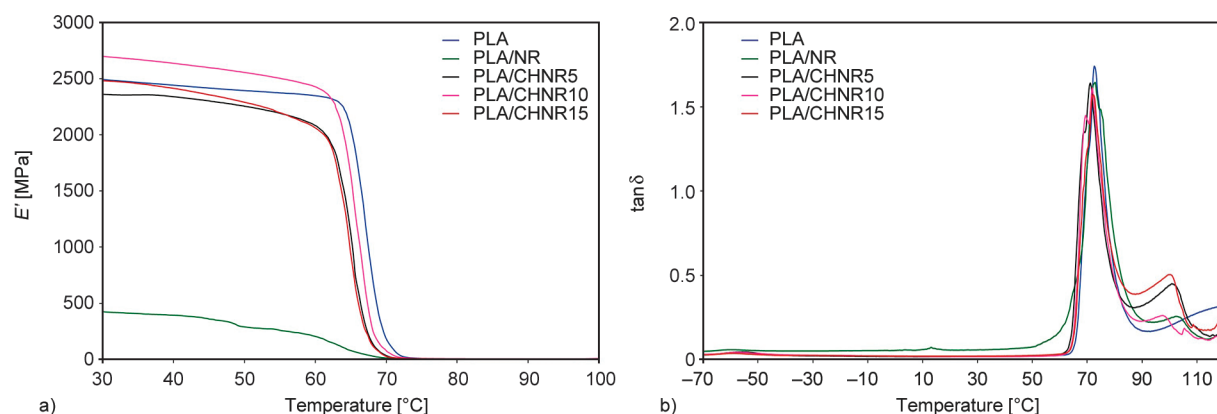


Figure 8. DMA curves of PLA and the blends: a) storage modulus and b) $\tan \delta$.

chain lengths lead to a wide distribution of relaxation times [38].

3.5. Mechanical properties

The mechanical properties of PLA and the blends are summarized in Table 3. The rubber content was 10 wt% in all blends. The impact resistance was investigated by both Izod and Charpy impact tests. Generally, the impact strength determines the toughness of a material. It measures the energy absorption during its fracture. The brittle material has lower energy absorption than ductile material. The Izod impact test differs from the Charpy impact test by the direction of the specimens in the machine. In the Izod impact test, the impact strengths of notched and unnotched PLA (2.2 and $8.2 \text{ kJ}\cdot\text{m}^{-2}$) were insignificantly changed after blending with NR (3.3 and $8.7 \text{ kJ}\cdot\text{m}^{-2}$). It is known that the compatibility of the blend relates to its mechanical properties. The PLA/NR was an immiscible blend that caused poor interfacial adhesion between PLA and NR phases. Therefore, it was insufficient for stress transfer between the two phases. In rubber-toughened plastic, the deformation mechanism involves shear and cavitation processes [39]. The shear processes consist of shear yielding and shear band. The cavitation

processes involve crazing, voids, and fractures. The crazing and shear yielding occur simultaneously. However, crazing is currently accepted as a principal mechanism for toughening. When stress is applied to the polymer, it initiates a craze and leads to the formation of an interpenetrating network of voids. The craze initiates at a stress concentration produced by rubber particles. The craze growth propagates and terminates at rubber particles. The impact strengths of un-notched and notched specimens of PLA increased with the addition of CHNR. Interestingly, the unbroken specimens without notch of PLA/CHNR5 and PLA/CHNR10 indicated the high toughness of these blends. According to the proposed mechanism in Figure 4, the transesterification occurred at the interface of PLA and CHNR. The formation of the PLA-*co*-CHNR behaved as a bridge connecting the two phases. The stress could transfer between two phases resulting in the enhancement of impact strength. In the Charpy impact test, blending with NR slightly decreased the impact strength of un-notched PLA and insignificant changed the impact strength of notched PLA. CHNR5 and CHNR10 showed a significant enhancement in both notched and unnotched specimens. In the case of CHNR5, the impact strength increased up to 60.0 and $17.0 \text{ kJ}\cdot\text{m}^{-2}$

Table 3. Impact strength and tensile properties of PLA and the blends.

Sample	Izod impact strength [$\text{kJ}\cdot\text{m}^{-2}$]		Charpy impact strength [$\text{kJ}\cdot\text{m}^{-2}$]		E [MPa]	σ_b [MPa]	ϵ_b [%]
	Unnotched	Notched	Unnotched	Notched			
PLA	8.2 ± 0.1	2.2 ± 0.2	18.7 ± 0.4	2.6 ± 0.2	1827 ± 48	69.57 ± 1.19	5.80 ± 0.12
PLA/NR	8.7 ± 0.1	3.3 ± 0.2	15.4 ± 0.3	3.2 ± 0.2	1232 ± 52	31.87 ± 1.09	6.08 ± 0.06
PLA/CHNR5	Unbroken	7.4 ± 0.2	60.0 ± 0.6	17.0 ± 0.7	1450 ± 64	36.88 ± 0.35	14.52 ± 0.11
PLA/CHNR10	Unbroken	5.1 ± 0.1	30.1 ± 0.3	8.7 ± 0.6	1385 ± 41	30.76 ± 0.92	11.26 ± 0.09
PLA/CHNR15	17.7 ± 0.3	4.2 ± 0.1	18.4 ± 0.6	4.2 ± 0.5	1406 ± 53	24.81 ± 0.96	3.04 ± 0.04

from those of PLA at 18.7 and 2.6 kJ·m⁻². It seems that CHNR5 was a good toughening agent for PLA. Due to the good interfacial adhesion between the two phases, the initiation of the craze at the interface of the matrix and the dispersed phase was prevented and retarded the fracture growth. It resulted in an increase in impact strength. The chain lengths of copolymers affected their mechanical properties. The impact strength tended to decrease with molecular weight. Rubber particle size plays an important role in the mechanical properties of the blend. Larger rubber particle size promotes craze propagation, while smaller rubber particle size is insufficient to stop craze propagation and fracture. Therefore, the optimal rubber particle size could stabilize the craze growth and stop the crack. In this work, the optimal rubber particle size in PLA/CHNR blends was approximately 4–5 μm. It has been reported that the optimal rubber particle size provided the optimum mechanical properties [13, 15, 20, 22].

The tensile properties are listed in Table 3. The Young's modulus (E) and tensile strength (σ_b) of PLA dramatically decreased with the addition of NR and CHNR. Generally, the addition of soft polymers like rubber to the plastic matrix causes deterioration of E and σ_b [13, 15, 16, 20–22]. No improvement in elongation at break (ϵ_b) was observed for PLA/NR in comparison with the PLA. This suggests that the compatibility of the blend is strongly related to its mechanical properties. The ϵ_b of PLA increased significantly with the addition of CHNR5 and CHNR10, except for CHNR15. This implied that CHNR5 and CHNR10 increased the ductility of PLA. The stress-strain behaviors of PLA and the blends are shown in Figure 9. Generally, the area under the stress-strain curve correlates to the toughness of a material. The stress-strain curve of PLA showed a straight line

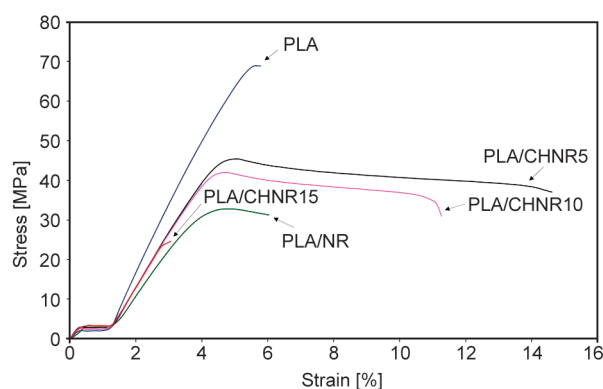


Figure 9. Stress-strain curves of PLA and the blends.

that dropped suddenly after reaching the maximum stress point. This is a characteristic of a brittle material that has a limit absorbing the energy before failure. The stress-strain curves of PLA/CHNR5 and PLA/CHNR10 showed a larger plastic region after the yield point than PLA/NR. The large area under the curve indicates that it absorbs a large amount of energy during the plastic deformation before failure. It implied that PLA/CHNR5 and PLA/CHNR10 were more ductile materials than PLA/NR. Figure 10 presents the different types of tensile fracture surfaces. The smooth and fine fracture surface of PLA indicates a brittle fracture (Figure 10a). The immiscibility of PLA and NR caused weak interfacial adhesion between the two phases. The rubber particles were pulled away from the PLA matrix during the fracture and left the holes (Figure 10b). As a result of the absence of rubber particles, there was no prevention of craze growth. Finally, it led to the fracture of a material. The coarse surface and stress whitening were observed in all PLA/CHNR blends, which indicated the ductile fracture (Figure 10c–10e). Moreover, the presence of an optimal rubber particle size in the PLA/CHNR could retard the craze propagation and fracture. These observations supposed that the enhancement in the compatibility of the blends could improve their mechanical properties.

4. Conclusions

Binary blends (PLA/NR and PLA/CHNR) were prepared by melt mixing. The blend between PLA and NR was a physical blend, while the blend of PLA and CHNR was a reactive blend. The GPC analysis confirmed the formation of PLA-co-CHNR during blending. The compatibility of the blend is related to its mechanical properties. The CHNR was more compatible with PLA than NR. The addition of CHNR5 and CHNR10 increased the interfacial adhesion between the two phases and enhanced the impact strength and elongation at break of the PLA. The mechanical properties of the PLA/CHNR blends decreased with the molecular weight. The shorter chain length of the copolymer was more effective than the longer one. The DSC thermograms and SEM images also confirmed the compatibility of PLA and CHNR. The significant shift of T_g values in all PLA/CHNR blends implied an improvement in compatibility. The addition of CHNR did not hinder the crystallization in PLA. The optimal rubber

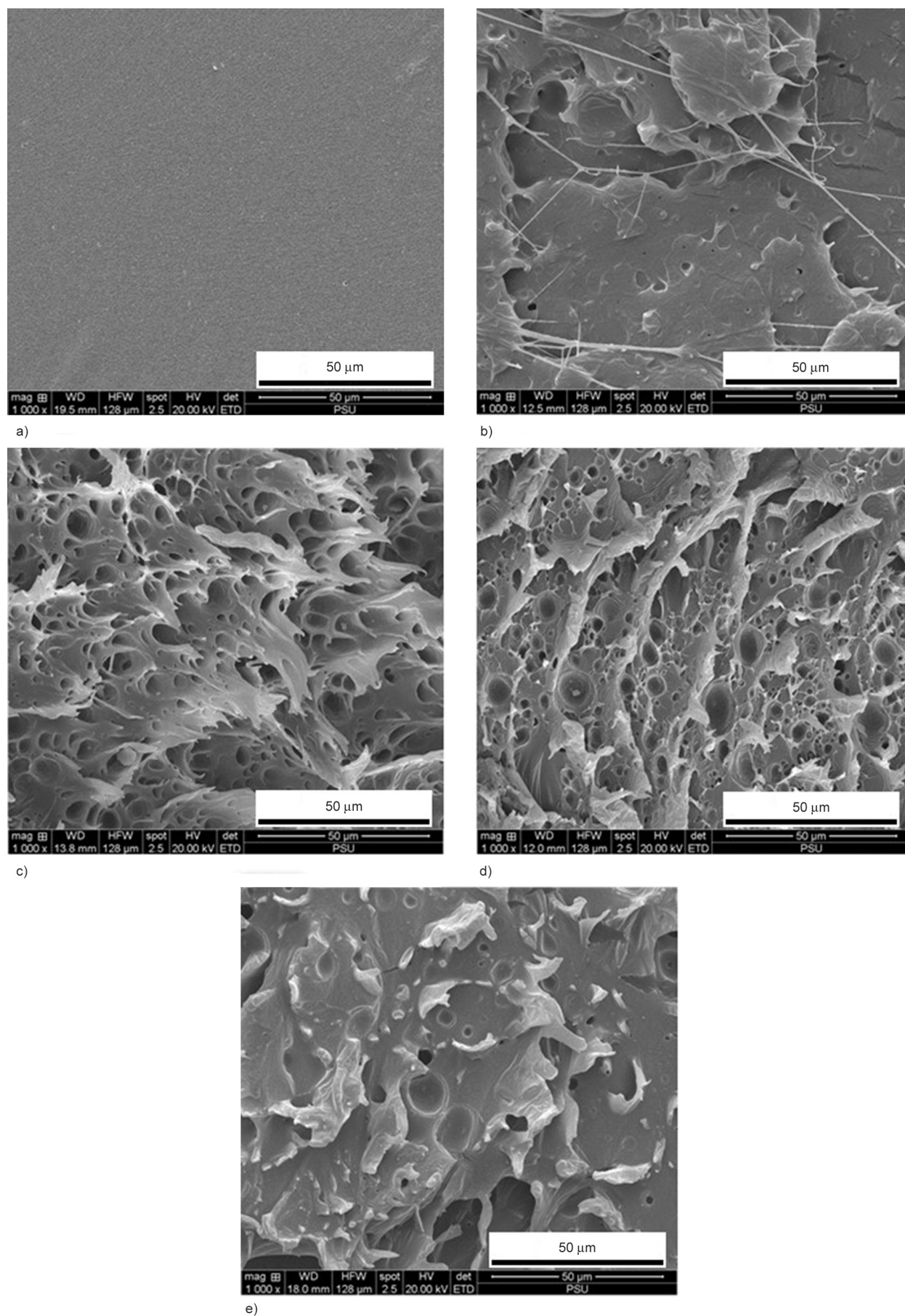


Figure 10. Tensile fracture surfaces: a) PLA, b) PLA/NR, c) PLA/CHNR5, d) PLA/CHNR10, and e) PLA/CHNR15.

particle size in the PLA/CHNR was 4.2 and 5.5 μm . It could retard the craze propagation and fracture.

Acknowledgements

This research was supported by the Prince of Songkla University (Grant No. UIC6402031S).

References

- [1] Lim L-T., Auras R., Rubino M.: Processing technologies for poly(lactic acid). *Progress in Polymer Science*, **33**, 820–852 (2008).
<https://doi.org/10.1016/j.progpolymsci.2008.05.004>
- [2] Rasal R. M., Janorkar A. V., Hirt D. E.: Poly(lactic acid) modifications. *Progress in Polymer Science*, **35**, 338–356 (2010).
<https://doi.org/10.1016/j.progpolymsci.2009.12.003>
- [3] Carrasco F., Pagès P., Gámez-Pérez J., Santana O. O., MasPOCH M. L.: Processing of poly(lactic acid): Characterization of chemical structure, thermal stability and mechanical properties. *Polymer Degradation and Stability*, **95**, 116–125 (2010).
<https://doi.org/10.1016/j.polymdegradstab.2009.11.045>
- [4] Gui Z., Xu Y., Gao Y., Lu C., Cheng S.: Novel polyethylene glycol-based polyester-toughened polylactide. *Materials Letters*, **71**, 63–65 (2012).
<https://doi.org/10.1016/j.matlet.2011.12.045>
- [5] Ma P., Spoelstra A. B., Schmit P., Lemstra P. J.: Toughening of poly(lactic acid) by poly(β -hydroxybutyrate-co- β -hydroxyvalerate) with high β -hydroxyvalerate content. *European Polymer Journal*, **49**, 1523–1531 (2013).
<https://doi.org/10.1016/j.eurpolymj.2013.01.016>
- [6] Wang Y., Wei Z., Leng X., Shen K., Li Y.: Highly toughened polylactide with epoxidized polybutadiene by *in-situ* reactive compatibilization. *Polymer*, **92**, 74–83 (2016).
<https://doi.org/10.1016/j.polymer.2016.03.081>
- [7] Wang Y., Wei Z., Li Y.: Highly toughened polylactide/epoxidized poly(styrene-*b*-butadiene-*b*-styrene) blends with excellent tensile performance. *European Polymer Journal*, **85**, 92–104 (2016).
<https://doi.org/10.1016/j.eurpolymj.2016.10.019>
- [8] Gu L., Nessim E. E., Li T., Macosko C. W.: Toughening poly(lactic acid) with poly(ethylene oxide)-poly(propylene oxide)-poly(ethylene oxide) triblock copolymers. *Polymer*, **156**, 261–269 (2018).
<https://doi.org/10.1016/j.polymer.2018.09.027>
- [9] Gigante V., Canesi I., Cinelli P., Coltelli M. B., Lazzeri A.: Rubber toughening of polylactic acid (PLA) with poly(butylene adipate-co-terephthalate) (PBAT): Mechanical properties, fracture mechanics and analysis of ductile-to-brittle behavior while varying temperature and test speed. *European Polymer Journal*, **115**, 125–137 (2019).
<https://doi.org/10.1016/j.eurpolymj.2019.03.015>
- [10] Zhao J., Pan H., Yang H., Bian J., Zhang H., Gao G., Dong L.: Study on miscibility, thermal properties, degradation behaviors, and toughening mechanism of poly(lactic acid)/poly(ethylene-butylacrylate-glycidyl methacrylate) blends. *International Journal of Biological Macromolecules*, **143**, 443–452 (2020).
<https://doi.org/10.1016/j.ijbiomac.2019.11.226>
- [11] Chen C., Tian Y., Li F., Hu H., Wang K., Kong Z., Ying W. B., Zhang R., Zhu J.: Toughening polylactic acid by a biobased poly(butylene 2,5-furandicarboxylate)-*b*-poly(ethylene glycol) copolymer: Balanced mechanical properties and potential biodegradability. *Biomacromolecules*, **22**, 374–385 (2021).
<https://doi.org/10.1021/acs.biomac.0c01236>
- [12] Park C. K., Jang D. J., Lee J. H., Kim S. H.: Toughening of polylactide by *in-situ* reactive compatibilization with an isosorbide-containing copolyester. *Polymer Testing*, **95**, 107136 (2021).
<https://doi.org/10.1016/j.polymertesting.2021.107136>
- [13] Jaratrotkamjorn R., Khaokong C., Tanrattanakul V.: Toughness enhancement of poly(lactic acid) by melt blending with natural rubber. *Journal of Applied Polymer Science*, **124**, 5027–5036 (2012).
<https://doi.org/10.1002/app.35617>
- [14] Juntuek P., Ruksakulpiwat C., Chumsamrong P., Ruksakulpiwat Y.: Effect of glycidyl methacrylate-grafted natural rubber on physical properties of polylactic acid and natural rubber blends. *Journal of Applied Polymer Science*, **125**, 745–754 (2012).
<https://doi.org/10.1002/app.36263>
- [15] Bitinis N., Verdejo R., Cassagnau P., Lopez-Manchado M. A.: Structure and properties of polylactide/natural rubber blends. *Materials Chemistry and Physics*, **129**, 823–831 (2011).
<https://doi.org/10.1016/j.matchemphys.2011.05.016>
- [16] Pongtanayut K., Thongpin C., Santawitee O.: The effect of rubber on morphology, thermal properties and mechanical properties of PLA/NR and PLA/ENR blends. *Energy Procedia*, **34**, 888–897 (2013).
<https://doi.org/10.1016/j.egypro.2013.06.826>
- [17] Chumeka W., Pasetto P., Pilard J-F., Tanrattanakul V.: Bio-based diblock copolymers prepared from poly(lactic acid) and natural rubber. *Journal of Applied Polymer Science*, **132**, 41426 (2015).
<https://doi.org/10.1002/app.41426>
- [18] Chumeka W., Pasetto P., Pilard J-F., Tanrattanakul V.: Bio-based triblock copolymers from natural rubber and poly(lactic acid): Synthesis and application in polymer blending. *Polymer*, **55**, 4478–4487 (2014).
<https://doi.org/10.1016/j.polymer.2014.06.091>
- [19] Chumeka W., Tanrattanakul V., Pilard J-F., Pasetto P.: Effect of poly(vinyl acetate) on mechanical properties and characteristics of poly(lactic acid)/natural rubber blends. *Journal of Polymer and the Environment*, **21**, 450–460 (2013).
<https://doi.org/10.1007/s10924-012-0531-5>

- [20] Sookprasert P., Hinchiranan N.: Morphology, mechanical and thermal properties of poly(lactic acid) (PLA)/natural rubber (NR) blends compatibilized by NR-graft-PLA. *Journal of Materials Research*, **32**, 788–800 (2017). <https://doi.org/10.1557/jmr.2017.9>
- [21] Zhang C., Man C., Pan Y., Wang W., Jiang L., Dan Y.: Toughening of poly(lactide) with natural rubber grafted with poly(butyl acrylate). *Polymer International*, **60**, 1548–1555 (2011). <https://doi.org/10.1002/pi.3118>
- [22] Jaratrotkamjorn R., Tanrattanakul V.: Toughness improvement of poly(lactic acid) with poly(vinyl propionate)-grafted natural rubber. *Journal of Applied Polymer Science*, **138**, 50980 (2021). <https://doi.org/10.1002/app.50980>
- [23] Koning C., van Duin M., Pagnouille C., Jerome R.: Strategies for compatibilization of polymer blends. *Progress in Polymer Science*, **23**, 707–757 (1998). [https://doi.org/10.1016/S0079-6700\(97\)00054-3](https://doi.org/10.1016/S0079-6700(97)00054-3)
- [24] Kotliar A. M.: Interchange reactions involving condensation polymers. *Journal of Polymer Science: Macromolecular Reviews*, **16**, 367–395 (1981). <https://doi.org/10.1002/pol.1981.230160106>
- [25] Sadik T., Becquart F., Majesté J-C., Taha M.: In-melt transesterification of poly(lactic acid) and poly(ethylene-co-vinylalcohol). *Materials Chemistry and Physics*, **140**, 559–569 (2013). <https://doi.org/10.1016/j.matchemphys.2013.04.004>
- [26] Chelghoum N., Guessoum M., Fois M., Haddaoui N.: Contribution of catalytic transesterification reactions to the compatibilization of poly(lactic acid)/polycarbonate blends: Thermal, morphological and viscoelastic characterization. *Journal of Polymers and the Environment*, **26**, 342–354 (2018). <https://doi.org/10.1007/s10924-017-0950-4>
- [27] Zhou L., Zhao G., Jiang W.: Effects of catalytic transesterification and composition on the toughness of poly(lactic acid)/poly(propylene carbonate) blends. *Industrial and Engineering Chemistry Research*, **55**, 5565–5573 (2016). <https://doi.org/10.1021/acs.iecr.6b00315>
- [28] Jaratrotkamjorn R., Nourry A., Pasetto P., Choppé E., Panwiryarat W., Tanrattanakul V., Pilard J-F.: Synthesis and characterization of elastomeric, biobased, nonisocyanate polyurethane from natural rubber. *Journal of Applied Polymer Science*, **134**, 45427 (2017). <https://doi.org/10.1002/app.45427>
- [29] Busnel J. P.: Data handling in g.p.c. for routine operations. *Polymer*, **23**, 137–141 (1982). [https://doi.org/10.1016/0032-3861\(82\)90027-1](https://doi.org/10.1016/0032-3861(82)90027-1)
- [30] Tsuji H., Ikada Y.: Properties and morphologies of poly(L-lactide): 1. Annealing condition effects on properties and morphologies of poly(L-lactide). *Polymer*, **36**, 2709–2716 (1995). [https://doi.org/10.1016/0032-3861\(95\)93647-5](https://doi.org/10.1016/0032-3861(95)93647-5)
- [31] Lipik V. T., Widjaja L. K., Liow S. S., Abadie M. J. M., Venkatraman S. S.: Effects of transesterification and degradation on properties and structure of polycaprolactone-poly(lactide) copolymers. *Polymer Degradation and Stability*, **95**, 2596–2602 (2010). <https://doi.org/10.1016%2Fj.polyimdegradstab.2010.07.027>
- [32] Klinkajorn J., Tanrattanakul V.: Compatibilization of poly(lactic acid)/epoxidized natural rubber blend with maleic anhydride. *Journal of Applied Polymer Science*, **15**, 48297 (2020). <https://doi.org/10.1002/app.48297>
- [33] Sarasua J-R., Prud'homme R. E., Wisniewski M., le Borgne A., Spassky N.: Crystallization and melting behavior of polylactides. *Macromolecules*, **31**, 3895–3905 (1998). <https://doi.org/10.1021/ma971545p>
- [34] Zhang C., Wang W., Huang Y., Pan Y., Jiang L., Dan Y., Luo Y., Peng Z.: Thermal, mechanical and rheological properties of poly(lactide) toughened by epoxidized natural rubber. *Materials and Design*, **45**, 198–205 (2013). <https://doi.org/10.1016/j.matdes.2012.09.024>
- [35] Suksut B., Deeprasertkul C.: Effect of nucleating agents on physical properties of poly(lactic acid) and its blend with natural rubber. *Journal of Polymers and the Environment*, **19**, 288–296 (2011). <https://doi.org/10.1007/s10924-010-0278-9>
- [36] Tissanan W., Chanthateyanonth R., Yamaguchi M., Phinyocheep P.: Improvement of mechanical and impact performance of poly(lactic acid) by renewable modified natural rubber. *Journal of Cleaner Production*, **276**, 123800 (2020). <https://doi.org/10.1016/j.jclepro.2020.123800>
- [37] de Bomfim A. S. C., de Oliveira D. M., de Cavalho Benini K. C. C., Cioffi M. O. H., Voorwald H. J. C., Rodrigue D.: Effect of spent coffee grounds on the crystallinity and viscoelastic behavior of polylactic acid composites. *Polymers*, **15**, 2719 (2023). <https://doi.org/10.3390/polym15122719>
- [38] Kannurpatti A. R., Anseth J. W., Bowman C. N.: A study of the evolution of mechanical properties and structural heterogeneity of polymer networks formed by photopolymerizations of multifunctional (meth)acrylates. *Polymer*, **39**, 2507–2513 (1998). [https://doi.org/10.1016/S0032-3861\(97\)00585-5](https://doi.org/10.1016/S0032-3861(97)00585-5)
- [39] Bucknall C. B.: *Toughened plastics*. Applied Science Publishers, London (1977).

Research article

A comparison of the mechanical behaviour of natural rubber-based blends using waste rubber particles obtained by cryogrinding and high-shear mixing

Nicolas Candau*^{ID}, Rachel LeBlanc, Maria Lluïsa Maspoch^{ID}

Departament de Ciència i Enginyeria de Materials (CEM), Escola d'Enginyeria Barcelona-Est (EEBE),
Universitat Politècnica de Catalunya BARCELONATECH (UPC)- Av. Eduard Maristany 16, 08019 Barcelona, Spain

Received 24 June 2023; accepted in revised form 25 July 2023

Abstract. The influence of the type of mechanical recycling of waste rubber particles on the tensile properties of waste/natural rubber blends has been investigated. The wastes originating from ground tyre rubber (GTR) had been treated by two distinct processes: cryo-grinding and high shear mixing (HSM). For both processes, the resulting composites show enhanced stiffness and strength for all strain rates and temperatures tested. This is attributed to both the reinforcing effect of the waste as well as the nucleation ability of the wastes on strain induced crystallization (SIC) in the natural rubber (NR) matrix. Cryo-grinding was shown to provide the finest particle size with an average diameter of 34 μm , while the HSM process was found to show an elastic modulus of aggregated GTR powder of 7 MPa at 1 Hz at room temperature. Within these characteristics, the NR/GTR blends using the HSM process show the best tensile performance under single loading, with the highest strength and highest ability to crystallize under strain. Under cyclic loading, NR/GTR blends using cryo-ground GTR particles show the best performance, which we ascribed to their ability to better distribute and accommodate the stress from one cycle to another owing to their finest size. Both explored recycling techniques provide the natural/waste rubber blends interesting properties such as mechanical reinforcement and strain-induced crystallization ability under various testing conditions.

Keywords: natural rubber, recycling of rubbers, revulcanization, waste testing, tensile testing, strain induced crystallization

1. Introduction

With a growing concern about the environmental impact of waste and the need to conserve resources, there is an increasing interest in recycling and reusing polymeric materials, such as plastics and rubbers [1]. In recent years, there has been significant progress in developing technologies and processes for recycling rubber in line with the 2030 Sustainable Development Goals (SDGs) and the 2050 European Green Deal. These processes can potentially recover valuable materials from waste rubber and reduce the amount of waste accumulated in landfills and oceans [2]. The demand for recycled rubber products is also increasing as companies and consumers seek more

sustainable alternatives to virgin rubber [3], including the construction, automotive, sports, and footwear industries. However, there are still challenges to overcome in rubber recycling, such as technical limitations or cost-effectiveness.

The main recycling methods for rubbers include (i) mechanical recycling, which involves shredding or grinding of rubber waste into small pieces [4], (ii) chemical recycling which involves breaking down the rubber waste into its constituent chemicals using chemical processes, such as depolymerization [5], (iii) devulcanization that is the process of breaking the chemical cross-links that provides to rubber its elasticity, making it possible to reuse the material

*Corresponding author, e-mail: nicolas.candau@upc.edu
© BME-PT

[6], (iv) pyrolysis that is a thermal decomposition process that breaks down waste rubber into smaller molecules in the absence of oxygen, producing gases, oils, and carbon black [7]. While there may be some energy and resource inputs associated with the grinding or shredding process, mechanical processes are generally considered to be one of the more environmentally friendly options for rubber recycling, as it does not involve the use of chemicals and usually do not generate toxins. Among these mechanical methods, cryo-grinding and high shear mixing are promising processes to obtain residues with high added values.

Cryogrinding involves using liquid nitrogen or other cryogenic gases to cool the material being ground to very low temperatures. The material is then ground using types of equipment such as cryo-mills, which operate at very high speeds to reduce the size of the waste particles. Cryogrinding can produce particles with a narrow size distribution and a fine particle size [8], especially compared to ambient grinding [9]. High shear mixing involves the application of mechanical forces onto materials to achieve mixing, dispersion, or emulsification. This can be carried out using equipment such as rotor-stator mixers, high-pressure homogenizers, or colloid mills. The resulting products can have a homogeneous texture and fine particle size distribution. High shear mixing is a more complex and expensive process compared to traditional grinding, but it can offer greater control over the final product properties [10].

The waste rubber originated from the treatment of pneumatic tyres (so-called ground tyre rubber), and can be re-compounded without any addition of other raw material, showing high mechanical resistance but low strain at break (around 200%) [11]. To get materials with high deformability and/or toughness, providing them sufficient properties for novel application with high added value, the waste rubber can be blended with polymeric matrices, such as fresh plastic, thermoset rubber matrices [12] or concrete [13]. Among these materials, natural rubber (NR) is an interesting candidate to be used as the rubber matrix owing its excellent large strain properties such as fatigue behaviour, strain-induced crystallization ability as well as its compatibility with the waste rubber from the pneumatic tires as the latter contains vulcanized (and/or partially devulcanized) natural rubber.

The incorporation of waste rubber as reinforcing filler has been used as a strategy to improve the tensile

properties of NR. The tensile strength and modulus of the waste/natural rubber blends usually increase while the elongation at break decreases [14]. Moreover, it has been shown that the reinforcement efficiency of traditional fillers, such as carbon black and silica, can sometimes be improved by substituting them with waste fillers [15]. The thermal and dynamic mechanical properties of waste rubber/natural rubber blends demonstrate that the resulting composites containing a natural rubber matrix and waste rubber as fillers show excellent damping behaviour [16]. Finally, the use of waste rubber in natural rubber matrices has been shown to reduce the environmental impact and carbon footprint compared to traditional rubber materials [15].

As mentioned above, strain-induced crystallization (SIC) in NR is one crucial factor that has been considered in recent studies dedicated to the design of waste/natural rubber blends. SIC is a phenomenon in which the application of deformation to natural rubber leads to the alignment of polymer chains and the formation of crystalline domains, resulting in improved mechanical properties (large strain reinforcement and increased fatigue life). Incorporating waste rubber into the natural rubber matrix can positively affect SIC, as has been shown recently by *in-situ* X-rays [17] and *in-situ* IR thermography [18, 19]. Nonetheless, none of these studies focused on the possible effect of the type of treatment applied to the wastes (devulcanization, grinding, *etc.*), while they are expected to result in a drastic modification of the ultimate properties of the waste/rubber blend.

In this paper, we prepared waste/natural rubber blends using two distinct mechanical waste treatments: the cryo-grinding process and the high-shear mixing process. The properties of the wastes, as well as the tensile properties of the resulting waste/natural rubber composites, are discussed, and a focus is done on the impact of the type of waste treatment on the large strain reinforcement of the blends.

2. Materials and experiments

2.1. Materials processing

Natural rubber (NR) is a Standard Malaysian Rubber (SMR, Akrochem company, Akron, USA). It has a CV60 of about 55–60 (Mooney viscosity ML 1 + 4, 100 °C:). It contains 0.15% of hydroxylamine that had been added to the latex stage to prevent the raw rubber from stiffening while storing. Ground tire rubber (GTR, J. Allcock & Sons Ltd Company, Manchester,

United Kingdom). Tire buffing was used to transform the rubber from the pneumatic tire into millimeter size crumbs. Two types of particles were obtained using a cryogrinding process or a high-shear mixing process (HSM, REP-International company, Corbas, France), as indicated in Table 1.

The crumbs, size-reduced via a controlled cryogrinding, are free of contaminants such as textile, metal, and road dirt. Nonetheless, they look grey as talc had to be added to make the material flow and sieve correctly during the cryogrinding process. The cryoground GTR ($GTR_{(d)}$) was subsequently sieved using a vibratory sieve shaker (Analysette 3, Fritsch GmbH, Idar-Oberstein, Germany) with a mesh 230's (size $<63 \mu\text{m}$).

The high shear mixing process consists of two metallic cones (a stator and a rotor) with a series of grooves on their surfaces were used. The distance between the surfaces of both cones (gap) was optimized to provide the finest waste particle sizes. The rotation speed and the direction of rotation make the rubber move into the grooves of the cones, stressing and relaxing in a continuous and rapid way. Based on the geometry of the cones, the material is highly sheared when the material is located between the zenith flat parts. Three sequences of 5 min were applied to the waste rubber to avoid continuous processing and hence limit the self-heating that may cause thermal degradation and/or re-vulcanization *in situ*. The crumbs obtained from HSM ($GTR_{(h)}$) were subsequently sieved using a vibratory sieve shaker (Analysette 3, FRITSCHE Bakery Technologies GmbH &

Co. KG, Germany) with a mesh 120's (size $<125 \mu\text{m}$).

To prepare the NR/GTR blends, the NR was first masticated inside the chamber of an internal mixer (Brabender Plastic-Corder W50EHT, Brabender GmbH & Co., Duisburg, Germany) at a temperature of 80°C , for 5 min and a rotation speed of 40 rpm. 5 more minutes the vulcanizing agent dicumyl peroxide (DCP, Thermo Fisher Scientific, Waltham, Massachusetts, USA) was added (see Table 1) and mixed for 5 min. The masterbatch containing NR, GTR and DCP was vulcanized according to the estimated optimal time at 170°C under 4 MPa. The curing curves were recorded by using a Moving Die Rheometer (Monsanto moving die rheometer MDR 2000E, MonTech, Columbia City, USA) oscillating at a constant frequency of 1.677 Hz and an amplitude of deformation of 1.38% (5°) at the vulcanization temperature ($166\text{--}171^\circ\text{C}$). To perform the tensile tests, dogbone-shaped specimens with a 1 mm thickness, 4 mm width and 15 mm length were extracted from hot moulded sheets by die-cutting with a specimen preparation punching machine (Manual Hollow Die Punch, CEAST company, Torino, Italy).

2.2. Dynamic mechanical analysis

Dynamic mechanical analysis (DMA) was performed on rectangular samples using DMA equipment (Q800, TA Instruments, New Castle, USA). Specimens were tested in tension mode using pre-stress of 1 N, an amplitude of cyclic deformation of 0.5%, and a frequency varying from 1 to 100 Hz (frequency sweep method). The temperature was maintained at 25°C .

2.3. Fourier-transform infrared spectroscopy

Fourier-transform infrared spectroscopy (FTIR) was performed at room temperature (25°C). Absorbance spectra were recorded on an FTIR spectrometer (Nicolet 6700 FTIR, Thermo Scientific, Waltham, Massachusetts, USA) equipped with Cesium Iodide (CsI) beamsplitter to measure in attenuated total reflection modes. Spectra were obtained in the wavenumber interval ranging from 600 to 4000 cm^{-1} .

2.4. Swelling

The rubber was immersed in cyclohexane (Cyclohexane, ACS, 99+%, Thermo Scientific Chemicals, Waltham, Massachusetts, USA) for 72 h. After 72 h the swollen mass was measured. The rubber was then placed under a hood at room temperature for 72 h to

Table 1. Materials codes. The mesh size indicates the size of the sieving used to extract the GTR that is further used to prepare the NR/GTR blends.

Material code	GTR [wt%]	Mesh size*	Curing T [$^\circ\text{C}$]	DCP** [wt%]	DCP/NR*** [wt%]
$GTR_{(g)}$	100	230's	×	×	×
$GTR_{(h)}$	100	120's	×	×	×
NR	0	×	170	1.50	1.50
NR/GTR $_{(g-)}$	20	230's	170	1.30	1.50
NR/GTR $_{(g+)}$	20	230's	170	1.63	1.88
NR/GTR $_{(h-)}$	20	120's	170	1.30	1.50
NR/GTR $_{(h+)}$	20	120's	170	1.63	1.88

*Values are based on the American National Standard for Industrial Wire Cloth (American Standard ASTM-E 11).

**The DCP was introduced as a weight percent of the overall rubber phase quantity *i.e.*, the NR phase in the case of vulcanized NR and the NR phase + rubber phase in the GTR in the case of the vulcanized NR/GTR blends.

***The DCP calculated as a function of the NR content only.

remove the solvent. The mass of the dry samples was then measured. The average network chain density has been calculated from swelling experiments and the Flory-Rehner equation (Equation 1) [20]:

$$v = \frac{\ln(1 - v_2) + v_2 + \chi_1 v_2^2}{V_1 \left(-v_2^{\frac{1}{3}} + \frac{2}{f} v_2 \right)} \quad (1)$$

where $V_1 = 108 \text{ cm}^3/\text{mol}$ is the molar volume of the solvent (cyclohexane), χ_1 is the Flory-Huggins polymer solvent dimensionless interaction term (χ_1 is the Flory-Huggins polymer solvent dimensionless interaction term and is equal to 0.363 in the case of NR-cyclohexane [21]). $v_2 = 1/Q_r$, with Q_r the swelling ratio of the rubber matrix. $Q_r = V/V_0$ where V and V_0 are the volumes of the rubber network, at swelling equilibrium and after swelling and drying respectively. The ratio $2/f$ is associated with the phantom model that assumes spatial fluctuation of crosslinks (non-affine) used for high deformation ratios. f , the crosslink functionality, is chosen equal to 4. For filled compounds the Kraus correction [22] is used to account for the contribution of filler in the swelling ratio (Equation (2)):

$$Q_r = \frac{Q_c - \phi}{1 - \phi} \quad (2)$$

with ϕ is the volume fraction of fillers, and Q_c the swelling ratio of the composite. Equation (2) assumes non-adhesion of the fillers to the rubbery matrix, hence creating vacuoles in the swollen state.

2.5. Thermogravimetry analysis

Thermogravimetric analysis (TGA) is performed on GTR particles and on NR/GTR blends (DSC 1 Star System, Mettler Toledo, Columbus, OH, USA). The materials are put into an alumina crucible with a quantity of around 5–10 mg. The standard IEC 60811-100 is used for the determination of the carbon black content. To do so, the GTR is heated from 30 to 1000 °C with a heating ramp of 10 °C/min working under a nitrogen environment from 30 to 850 °C, and under an air environment from 850 to 1000 °C.

2.6. Micro-computed tomography (μ CT)

3D morphological information of rubber blends was obtained by micro-computed X-ray tomography (μ CT) carried out on a microtomograph Skyscan 1272 by Bruker (Billerica, Massachusetts, USA) equipped with an X-ray generator of 10 W, 20–100 kV, an

X-ray detector of 11 MP (4032×2688 pixels), with a maximum resolution of 0.45 μm . The volume-of-interest (VOI) was chosen around 7–13 mm^3 . An acceleration voltage of 50 kV at a current of 200 μA was employed. A full rotation (360°) was used with projections taken every 0.25°. The source-to-object-distance (SOD) and source-to-detector-distance (SDD) were set to obtain a voxel size of 3 μm . The 3D volume reconstruction of the projections was generated by Bruker software. Image treatment and analysis were performed with the commercial software Avizo (Thermo Fisher Scientific Inc., USA). The inherent noise of the acquired images was reduced by means of a median filter. Finally, images were binarized by thresholding the grayscale histogram.

2.7. Uniaxial tensile tests and uniaxial cyclic tests

Uniaxial tests were performed on a universal testing machine equipped with a 5 kN force sensor (Z008 Zwick/Roell, Ars Laquenexy, France). The first test type consists of a uniaxial stretching up to failure at a constant crosshead speed and temperature. Several conditions have been tested, with a crosshead speed varying from 100 to 2000 mm/min, corresponding to a nominal strain rate of 1.1 and 222 %/s, respectively, according to the specimen dimensions (15 mm length), and a temperature varying from –25 to 80 °C. The second type of test is an incremental test performed at a constant crosshead speed and at room temperature that consists of the application of a series of cycles, with an increment of the maximum deformation reached during cycles (from 50% for the first cycles to 500% for the last cycles). The test generally stops due to specimen breakage. At each applied cycle, the specimen is unloaded until reaching the relaxed state (zero force). The third type of test is a cyclic test performed at a constant frequency of 0.3 Hz. The strain amplitude of the cycles is chosen to equal 200%, which means a nominal strain rate of 120 %/s. Before the cyclic deformation, the rubber specimen is pre-deformed up to 400%. The cyclic tests start with an unloading and then a loading, meaning that the cyclic tests are performed between the deformation of 200 and 400%. For each type of test, the specimen deformation was estimated by measuring the local displacement between two white lines drawn in the central part of the specimen, separated by an initial distance of 10 mm and orthogonal to the specimen tensile axis. The local

Table 2. Testing conditions for the three types of tests: tensile test, incremental test, and cyclic test.

Type of test	Nominal strain rate [%/s]	Temperature [°C]	Cyclic deformation [%]	Pre-deformation [%]
Tensile test	1.1	21	×	×
	11	21	×	×
	56	21	×	×
	222	21	×	×
	11	−25	×	×
	11	80	×	×
Incremental test	11	21	Incremental*	×
Cyclic test	120	21	200	400**

*During the incremental tests, the maximum loading is increased from 50 to 500%, with an increment of around 30–35%. Each cycle is performed with an unloading down to zero force.

**During the cyclic test, after the pre-deformation at 400% the cycles start with an unloading followed by a loading, *i.e.*, the cycle occurs between 200 and 400%.

strain rate accounting for this correction has been estimated and found to decrease slightly with applied strain. A summary of the testing conditions for the three types of tests is shown in Table 2.

3. Results and discussion

3.1. Characterization of the waste rubber and waste rubber-based blends

Prior to the preparation of the natural rubber/ground tyre rubber blends, the GTR waste from the same batch was passed through two distinct processes: cryo-grinding or high shear mixing (HSM). The wastes obtained after these processes were sieved to collect the smallest rubber particles. The GTR particles were subsequently sieved. As cryo-grinding usually results in quite small particles, it was possible to collect enough GTR_(d) particles with a mesh 120's (size <63 μm) to prepare the blends. Contrarily, the GTR_(h) crumbs obtained from HSM could have been collected in sufficient quantity only by using the sieving size <125 μm. To quantify their average size and their size distribution by μCT, the GTR particles were dispersed into an NR matrix at 5 wt%, a content sufficiently low to allow the analysis on isolated GTR particles (Figure 1a). The 2D representative tomography images of the resulting NR/GTR composites (Figures 1a and 1b) show different intensities of grey due to the density contrast of the phases. The whitest grey is ascribed to the waste particles, being denser owing to their high content in carbon black, and the continuous phase, namely the NR matrix, is represented by the darkest grey regions. White domains had been observed that represent some highly dense particles (talc from grinding, traces of zinc oxide originating from the sulphur vulcanization of the tire). A filter size has

been applied to remove their contribution. Quantitative observations reveal that the size distribution of the GTR_(g) is quite homogeneous compared to the size distribution of the GTR_(h). One may note that the largest sizes of GTR_(h) and GTR_(g) are found to be higher than the sieving size. This might be explained by the high aspect ratio of certain GTR particles that are sieved. The average size of the GTR_(g) and GTR_(h) are found to be equal to 34 and 83 μm, respectively. By making an analysis of isolated GTR particles, it has been found that the specific surface (object surface/volume ratio) was equal to 84 and 37 mm^{−1} for cryoground GTR and GTR obtained by HSM.

While the GTR_(h) particles show some limited size reduction as compared to the GTR_(d), the HSM process has been carried out with the aim of selectively breaking the covalent bonds (devulcanization), through the application of high shear forces. Such devulcanization is expected to occur in the whole volume of the GTR particles, as shown in Figure 1c. However, the GTR surface is more easily exposed to a further reaction with another phase (in our case, the NR matrix) during their blending and re-vulcanization in the presence of a new vulcanizing agent (in our case, the dicumyl peroxide). To investigate the reactivity of the GTR_(h) particles, we prepared three systems: a GTR powder without vulcanization agent, an NR, and an NR/GTR blend with a vulcanization agent (1.5 wt% of the NR phase). We cured all of them at 170 °C for 10 minutes by using a moving die rheometer (MDR) to track the evolution of the torque with time, indicative of the formation of crosslinks (Figure 2). Interestingly, from the naked eye's observation, the cured powder of GTR showed certain cohesion, suggesting the formation of possible interfacial bonds between the GTR particles.

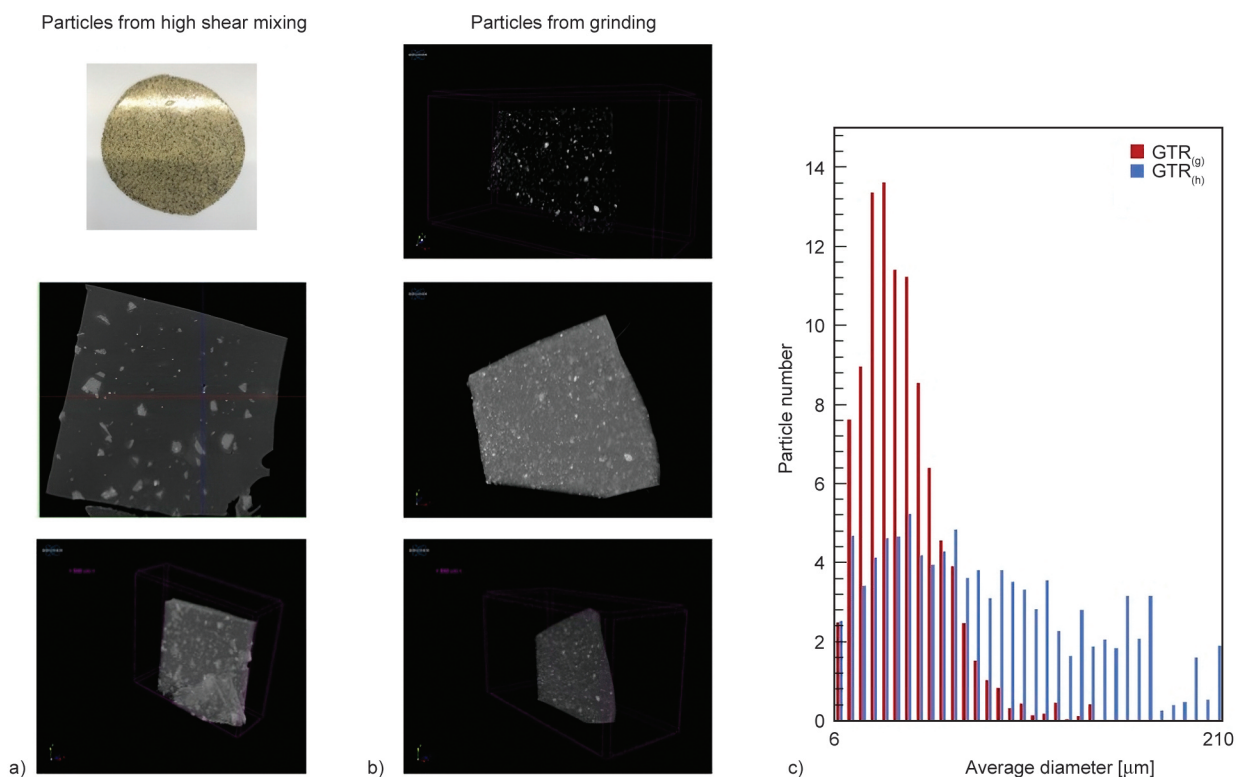


Figure 1. a) GTR_(h) and b) GTR_(g) particles obtained from the high shear mixing process and cryo-grinding process, respectively. μ CT was performed on NR/GTR blends containing 5 wt% of GTR to avoid possible aggregation for the GTR. c) GTR particle size distribution in number. The representative volumes of observations (represented in violet lines) correspond to approximate volumes of 7–13 mm³.

This statement is consistent with increased torque with time suggesting the formation of crosslinks of the resulting bulk powder (Figure 2a). This may originate from the vulcanization of the wastes by two possible concomitant mechanisms: (i) the activation of a residual sulphur vulcanization system persisting after the curing process of the pneumatic tyre and/or (ii) the re-activation of sulphur bonds broken after application of the high shear mixing process. Both the NR and NR/GTR blends show an increase of torque with curing time, confirming crosslinking reactions again. The minimum and maximum torque is logically found to increase with the addition of wastes, as they act, owing to their carbon black content, as reinforcing particles, in both unvulcanized and vulcanized states.

In filled rubber, the torque increase is larger, and the proportionality of the crosslink density to the torque increase is no longer true in the case of filled compounds since the contribution of fillers to the viscosity is higher in the vulcanized state [23, 24].

Nonetheless, the increment of the torque (Figure 2b) is found to be significantly higher in the NR/GTR blend (relative increment of 350%), compared to the NR (relative increment of 280%), and to the GTR

powder (relative increment of 26%). This suggests a higher reactivity in terms of crosslink creation. This may arise from the creation of supplementary bonds at the interface between the GTR particles and the NR matrix, resulting in the fixation of the GTR to the NR matrix, hence increasing the viscosity of the blend and hence the torque increment.

Given these previous rheological results, the effect of the GTR distribution, as well as their reactivity with the NR matrix, that results in both waste treatments and blends vulcanization, are also expected to have an impact on the small and large strain mechanical properties. This will be studied in the following.

Dynamic mechanical analysis (DMA) experiments were performed on the bulk powder GTR cured for 10 minutes at 170 °C and compared with the DMA response of the NR matrix cured in the same conditions (Figure 3) to further demonstrate the elastic response of the GTR bulk powder. Not only the aggregated GTR show cohesion, as previously observed, but they also show a small strain elastic response, with an elastic modulus increasing linearly from 7 to 11 MPa in the frequency range of 1–100 Hz. This result confirms the creation of interfacial bonds elastically active at the GTR surface, consistent with the

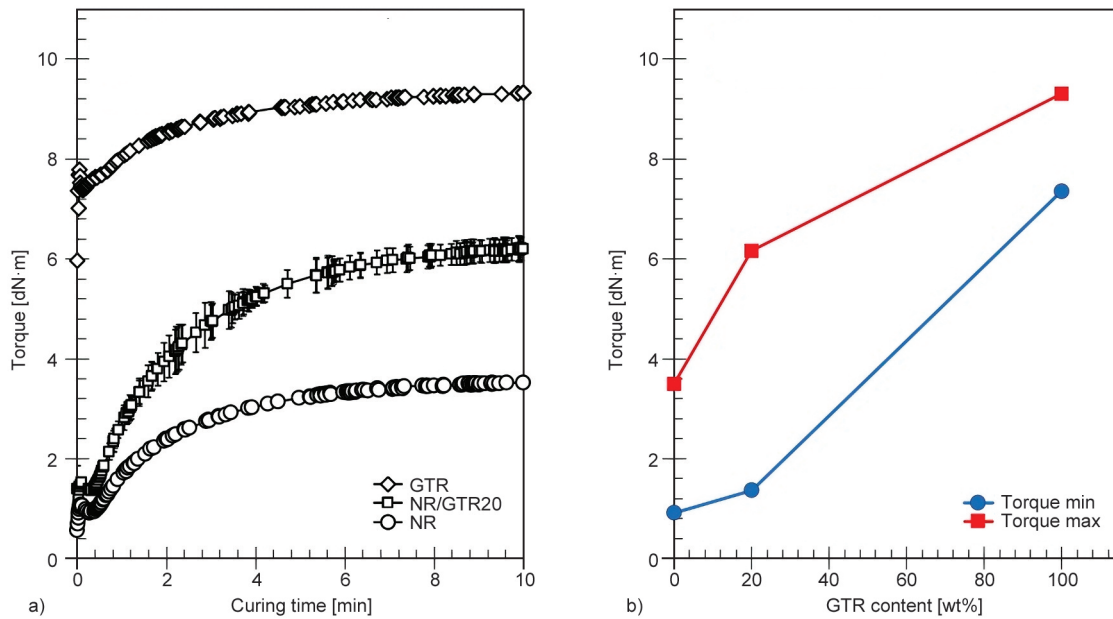


Figure 2. a) Torque *versus* curing time by using moving die rheometry (MDR) technique, performed on natural rubber matrix (NR), GTR_(h) powder obtained after the HSM process (see experimental section) and on NR/GTR_(h) material (see Table 1 for the materials nomenclature). b) Maximum and minimum torque during the MDR experiment.

torque increase in previously described rheology experiments.

Before further investigating the large strain response of the NR/GTR blends, as well as the reinforcing effect of the various phases (*e.g.*, rubber phase and carbon black (CB) present in the GTR), it is important to identify their fraction. Thermogravimetric Analysis (TGA) may be used to solve it. Most of the rubber is expected to decompose below 500 °C as shown

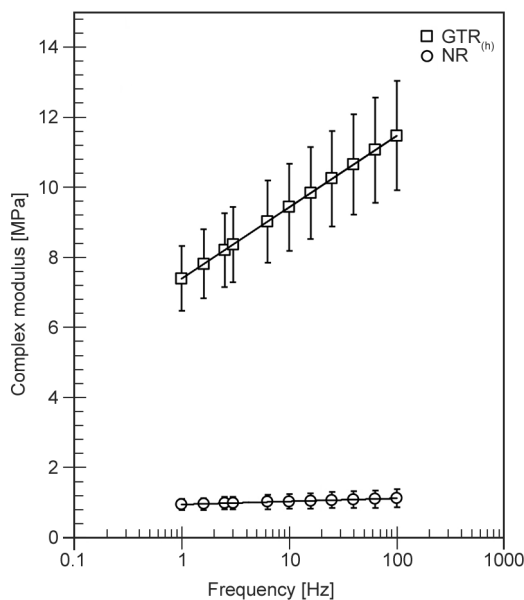


Figure 3. Complex modulus [MPa] *versus* frequency [Hz] (in log scale) for NR and GTR_(h) materials between 1 and 100 Hz at 0.5% of deformation.

on the TGA curves (Figure 4). It has been shown in the literature that the formation of short hydrocarbons attests to the thermal degradation of the rubber chains above 500 °C [25]. The remaining materials above 500 °C attest to the presence of non-rubber components, most likely CB aggregates and eventually, in a few proportions, some clay minerals that can arise from the application of the cryo-grinding process (see experimental section) for the series of materials based on HSM_(g). The mass loss of the NR matrix (Figure 4a) shows a single decomposition process with a maximum at around 350 °C, that corresponds to the degradation of the polyisoprene chains. The GTR particles show a distinct decomposition process: the degradation of the rubber phase is delayed as compared to the one of the NR, that is due to the presence of Styrene Butadiene Rubber (SBR) in the GTR with a higher decomposition temperature (around 430 °C). The material remaining at 500 °C corresponds to the non-rubber components. It mostly corresponds to the CB fraction, of similar quantity between GTR_(h) and GTR_(g), as both types of waste come from the same batch. Few amounts of talc used for the cryo-grinding process, which decomposes at temperatures close to 900 °C [26], may contribute to the total weight. This explains why the mass loss is slightly higher in GTR_(g) compared to GTR_(h) after rubber degradation. Figure 4b, 4c shows the thermal decomposition of NR/GTR blends as

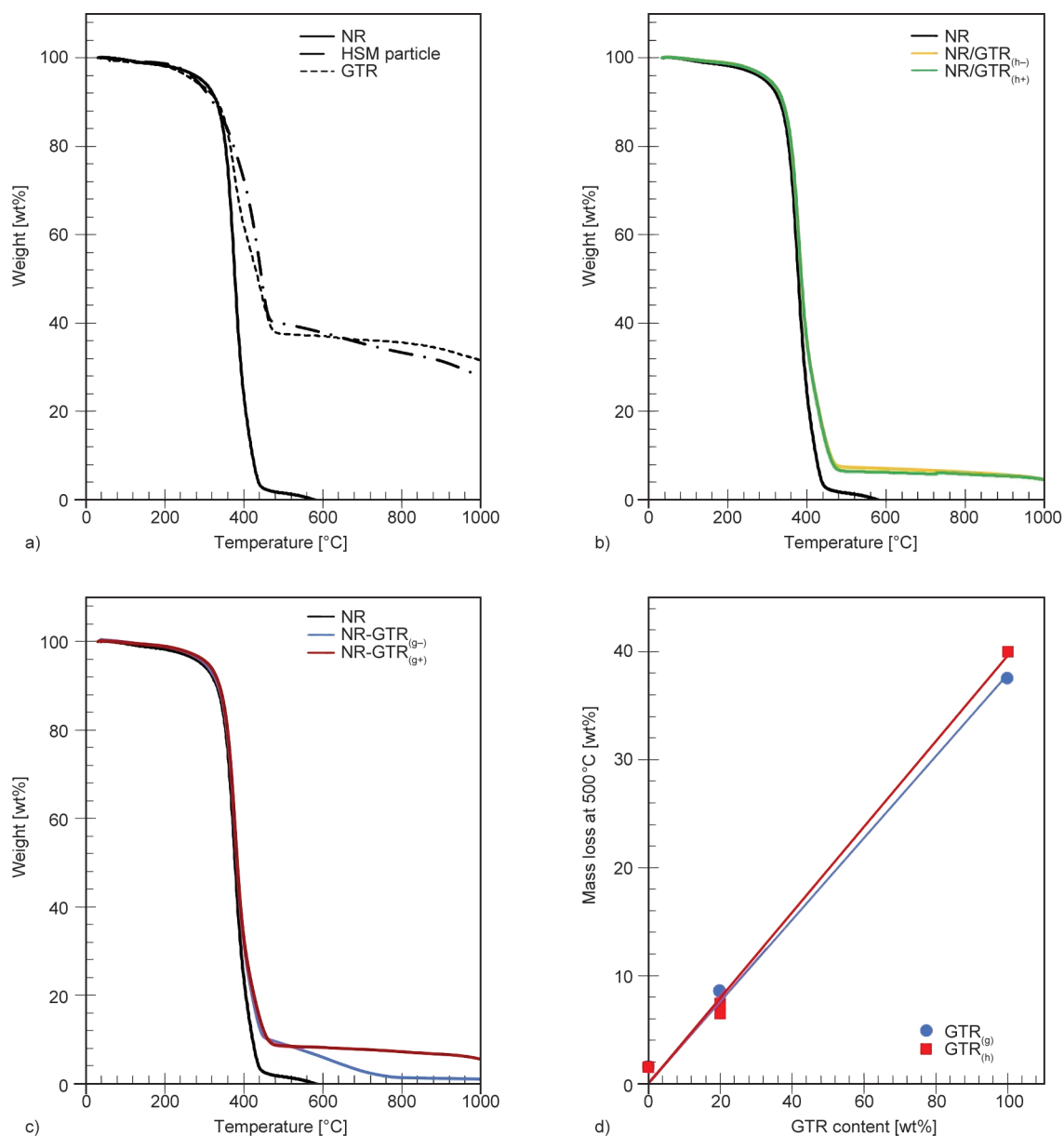


Figure 4. a), b), c) Thermogravimetric analysis curves of the various materials listed in Table 1. d) Mass loss at 500 °C versus the GTR content for the same series of materials.

compared to NR, highlighting the contribution of non-rubber components to be around 7–8 wt% at 500 °C. The remaining mass at 500 °C ascribed to non-rubber content expectedly follows a linear trend *versus* GTR content (Figure 4d). The GTR particles contain, on average, a total of 40 wt% of non-rubber elements. As the GTR represents the 20 wt% of the NR/GTR blends, this means that the non-rubber components occupy a total of 7–8 wt% in the NR/GTR blends.

An analysis of the chemical composition of the GTR and of the NR and NR/GTR blends, complementary to TGA, has been achieved by performing a Fourier transformed infrared spectroscopy (FTIR) (Figure 5).

The 1500–800 cm^{-1} region includes the absorbance bands of elastomeric components and non-elastomeric components (SiO_2 or carbon black). The peak at 698 cm^{-1} corresponds to the $(\text{C-H})_{\text{op}}$ bend of the mono-substituted benzene in the styrene butadiene rubber (SBR), present in the GTR^(g) but hardly visible in the GTR^(h). The peak at 830 cm^{-1} corresponds to the $=\text{C-H}$ out of plane bending in rubber molecules [29]. Natural rubber cis-isomer configurations can be observed at 870–780 cm^{-1} for all materials [30] and the peak at 1375 cm^{-1} corresponds to the (C-H) symmetric bend of the $-\text{CH}_3$ bond in NR [31]. The peak at 1450 cm^{-1} corresponds to the $-\text{CH}_2-$ stretching of the elastomeric phases:

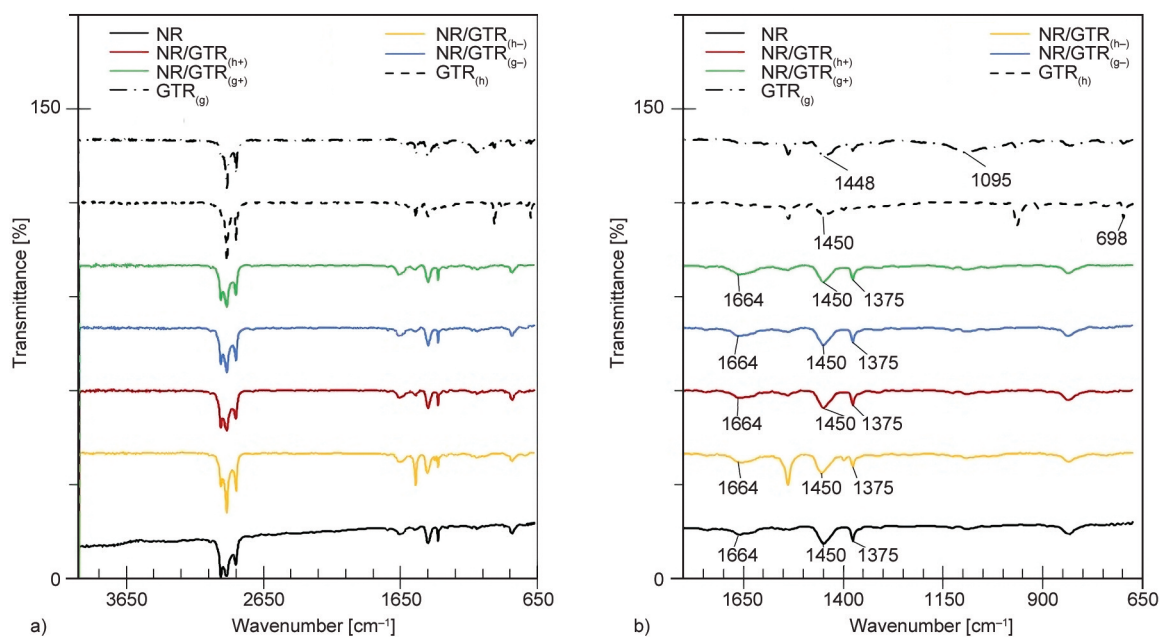


Figure 5. FTIR spectra from 650 to 4000 cm^{-1} of the $\text{GTR}_{(\text{h})}$, $\text{GTR}_{(\text{g})}$, and the different NR/GTR blends of the study. The curves had been shifted in the y-axis for the sake of clarity. a) full wavenumber range, b) selected wavenumber range between 650 and 1800 cm^{-1} .

NR molecules in the NR matrix and NR+SBR molecules in the GTR. The associated peak in the GTR is hence more intense as compared to the $-\text{CH}_3$ (C–H) symmetric bend. All the FTIR spectra show strong bands in the range of 3015–2744 cm^{-1} , indicative of the asymmetric and symmetric stretching frequency of the C–H groups (C– CH_3 and $-\text{CH}_2-$). The peak at 1095 cm^{-1} observed in the $\text{GTR}_{(\text{g})}$ may correspond to the Si–O stretching due to the presence of talc used for the grinding process, consistent with TGA results (Figure 5). When comparing the FTIR of the NR/GTR vulcanized with various amount of DCP, the C=C stretch (1664 cm^{-1}) was not significantly different in all cases. It has been suggested in the literature, in that case, a predominance of an abstraction route over a radical addition in the peroxide vulcanization of NR at 170 °C [29].

One may note here that the crosslinking agent, DCP, has been introduced at two distinct contents (+ or –) to account for the following assumption: all rubber phases, *i.e.*, NR matrix and rubber contained into the GTR particles, may react with the DCP. Within this assumption, the DCP content is chosen equal to 1.30 and 1.63 wt%, respectively. If, however, it is assumed that only the NR phase reacts (and the rubber phase in the GTR reacts only at the waste surface), the percentages of DCP are found equal to 1.5 and 1.88 wt% of the NR matrix (cf. Table 1).

The volume percent of CB was calculated using a density of 1.9 $\text{g}\cdot\text{mol}^{-1}$. The network chain density, ν , was calculated following a simple rule of the mixture and from the knowledge of the density and weight fraction of the rubber phase and CB particles (see Equations (1), (2) in the experimental section). One may note that, even if a non-extended study has been carried out about the devulcanization state of the wastes, in a previous publication [28], we showed that the cryoground GTR with size $<63 \mu\text{m}$ were found around 1.3 $\text{mol}\cdot\text{cm}^{-3}$.

The network chain density is found around $1.35\cdot 10^{-4} \text{mol}\cdot\text{cm}^{-3}$ in the case of the vulcanized NR (Figure 6), a network chain density close to the one of the cryoground GTR. Both the $\text{NR/GTR}_{(\text{g}-)}$ and $\text{NR/GTR}_{(\text{h}-)}$ have lower network chain density as compared to one of the NR. This may be explained by (i) the reaction of the rubber phase in the GTR particles with DCP that impedes efficient peroxide-vulcanization of the NR matrix and/or (ii) the concomitancy of both DCP degradation and sulphur reaction that may reduce the final crosslink density, as 1 mol of sulphur destroys 1 mol of DCP [27].

By increasing the quantity of DCP, the network chain density of the NR/GTR blend is found to increase from $1.1\cdot 10^{-4}$ to $2.15\cdot 10^{-4} \text{mol}\cdot\text{cm}^{-3}$. This drastic change in crosslink density may suggest a better reactivity of the GTR particles with DCP

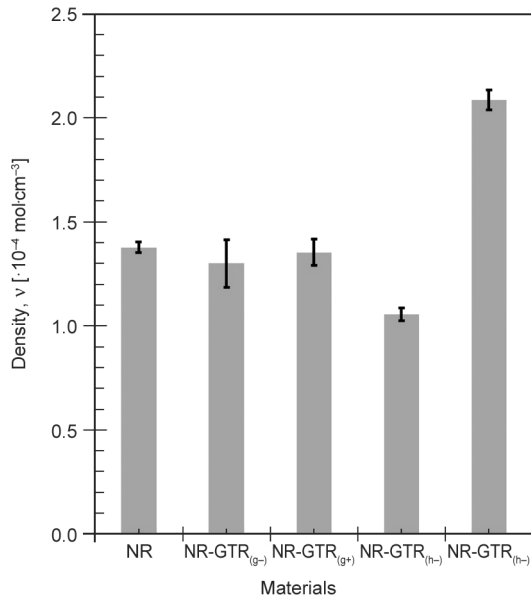


Figure 6. Network chain density of NR, NR/GTR_(g-), NR/GTR_(g+), NR/GTR_(h-) and NR/GTR_(h+). The symbols – and + indicate the quantity of crosslinking agent (DCP) introduced (see Table 1).

when compared with NR/GTR_(g). One explanation may be that migration of DCP from the NR matrix to wastes and/or migration from the remaining sulphur system from the GTR (from tire curing) to the NR matrix occurs. One may state indeed that large waste particles (obtained from HSM) limit the mutual migration of sulphur and DCP, owing to the lower surface area between the two phases (NR and GTR), hence promoting the formation of crosslinks. This apparent high reactivity of the NR/GTR_(h) blend with DCP is consistent with the large increase of torque seen during the MDR curing curve (Figure 1) as well as the elevated elastic modulus in DMA experiments (Figure 2). Such drastic changes in the

network chain density of the NR/GTR are expected to impact the large strain tensile properties, such as strain-induced crystallization abilities, as studied in the following section.

3.2. Tensile and strain-induced crystallization properties

Tensile properties of the NR/GTR blends using wastes obtained after grinding or after HSM processes were compared. Our vulcanized NR material shows hyperelastic behaviour with reinforcement at large strain, as seen in Figure 7a, which is usually ascribed to its ability to crystallize under strain. Even if the crystalline fraction in the NR remains minor (generally less than 20–25 vol.%), the high stiffness and orientation of the crystalline domains are known to reinforce the stress in the tensile direction, acting as temporary fillers.

One important usage of waste rubber for pneumatic tyre (GTR) in fresh rubber matrices relates to their mechanical reinforcement abilities. NR/GTR blends show similar tensile behaviour as compared to NR (Figures 7b, 7c). The tensile and strain-induced crystallization (SIC) properties of the NR and NR/GTR blends are shown in Figure 8. The elastic modulus – calculated by using the gaussian approximation [32] – has been found to slightly increase with the applied strain rate for all NR and NR/GTR blends (Figure 8a). Assuming a time-temperature equivalence in the elastic strain regime, an increase of the strain rate limits chains relaxation, and hence induces a higher chains stiffness. Possibly, more trapping of chains entanglements may occur with high strain rate, that also contributes to the increase of the elastic modulus (Figure 8a).

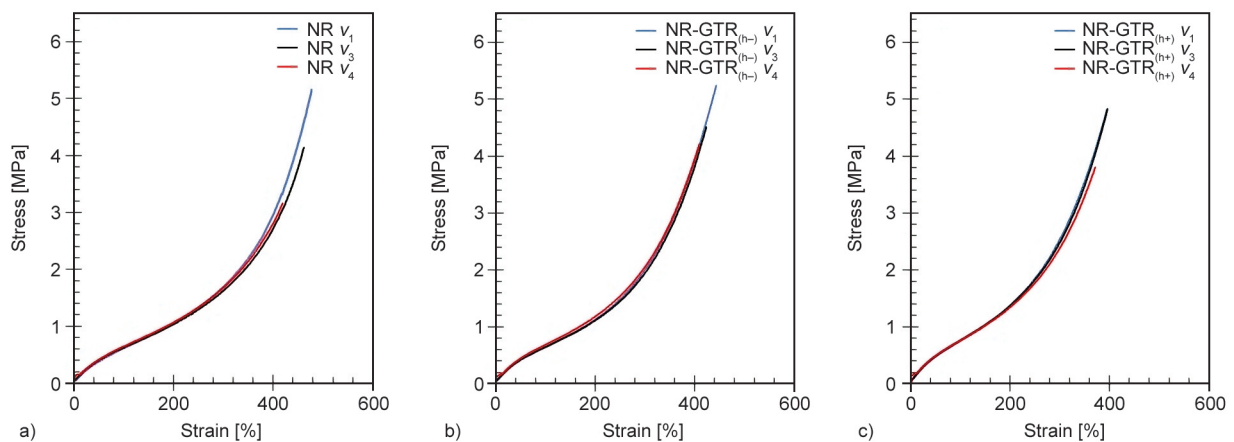


Figure 7. Room temperature tensile curves of NR (a), NR/GTR_(h-) (b) and NR/GTR_(h+) (c) blends for various strain rates of $v_1 = 1.1$ %/s, $v_3 = 11$ %/s and $v_4 = 222$ %/s.

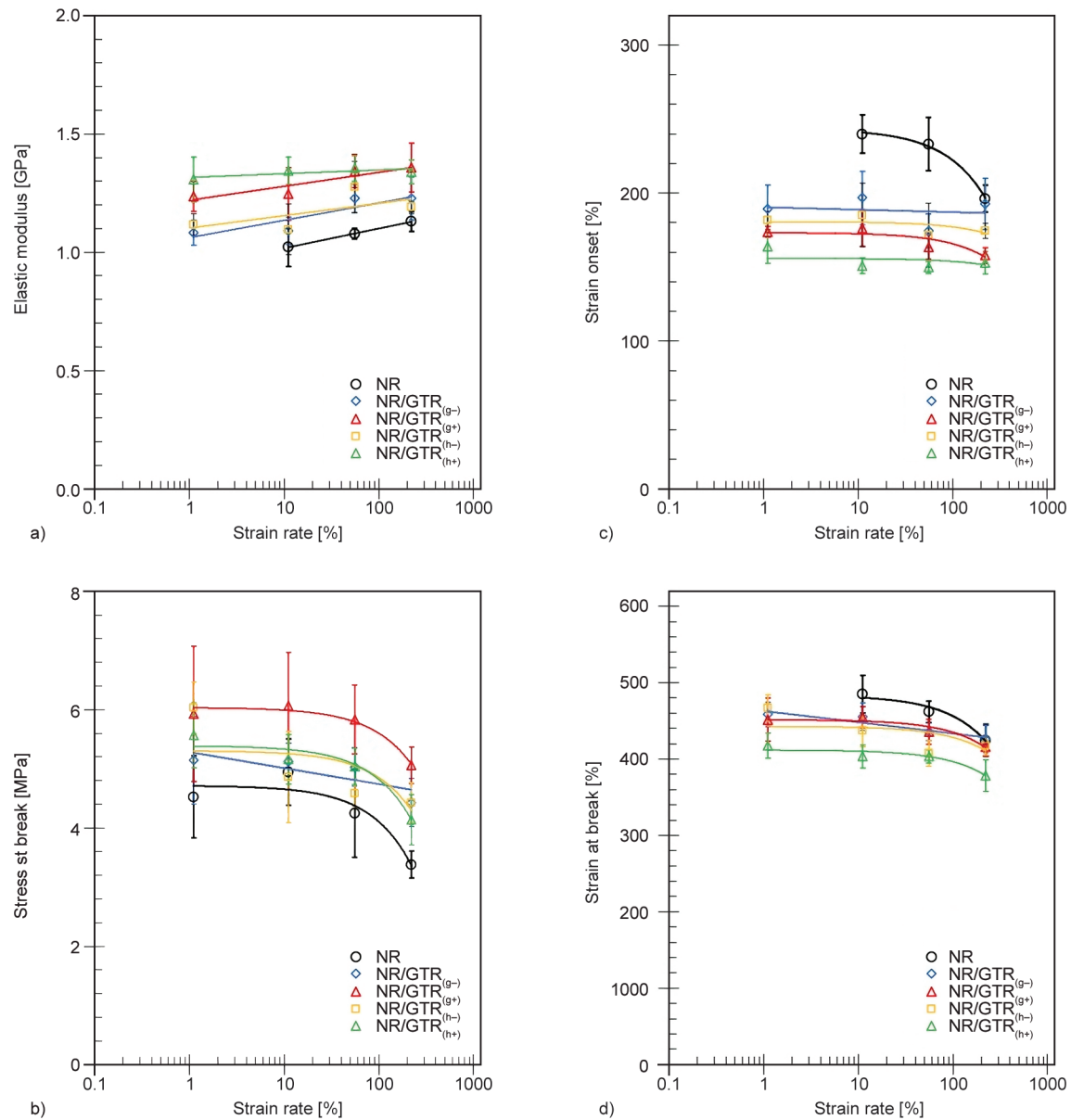


Figure 8. Room temperature tensile parameters of NR and NR/GTR blends as a function of the strain rate from 1.1, to 222 %/s: a) Elastic modulus, b) strain at crystallization onset, c) stress at break and d) strain at break.

The strain at crystallization onset estimates the appearance of the incipient strain induced crystals. It is used here to measure the possible effect of the waste particles on the improvement of SIC in the NR matrix. It has been suggested in previous works [18], that the deviation of the tensile behaviour from the gaussian approximation may be ascribed to the initiation of the strain induced crystalline phase that causes a large strain reinforcement. Such statement had been proven by direct characterization method of SIC such as the *in-situ* X-rays [17]. We applied the method used in that previous works to identify the strain at crystallization onset (Figure 8b). Only weak effect of the strain rate is observed, except for the pure vulcanized NR that tends to show a decrease

of the strain onset with strain rate. Stress at break (Figure 8c) is found to decrease for the highest strain rates studied (above 100 %/s), concomitantly with a decrease of the strain at break (Figure 8d). In such high strain rate conditions of sollicitation, the presence of highly oriented crystals in NR and NR/GTR, combined with the presence of waste rubber as reinforcing fillers, may contribute to the increased local strain in the amorphous part of the NR matrix, hence causing a premature failure. The tensile and strain-induced crystallization parameters were discussed for the highest strain rate studied (Figure 9), where possible applications can be found, such as the elastocaloric effect due to the generation of heating/cooling induced by crystallization/

melting processes near adiabatic conditions [18]. The effect of the presence of waste rubber on the tensile properties of rubber blends has been considered in the literature [33], where the presence of carbon black in the waste particles had been evoked to partly explain a mechanical reinforcement effect. The elastic modulus is found to decrease from NR to NR/GTR blends when lower DCP quantity is used but is found to increase from NR to NR/GTR blends when higher DCP quantity is used (Figure 9a), consistent with differences in the crosslink densities (Figure 5). Our results are consistent with the literature where the elastic modulus of rubber is increased in the presence of waste fillers [34]. In prior works, it has been shown that the property of the natural

rubber matrix to crystallize under strain could be improved by the presence of waste rubber [17]. The latter are playing the role of nucleating agents for SIC, by amplifying the local deformation in the NR matrix. In this study, this nucleating effect is shown for the two types of NR/GTR blends: in both cases, the higher the quantity of crosslinking agent, the lower the strain onset (Figure 9b). It has been shown in the literature that the strain at crystallization onset decreases while increasing the network chain density in a range between 0.76 and $1.93 \cdot 10^{-4} \text{ mol} \cdot \text{cm}^{-3}$ [35] for peroxide-cured NR. The higher the network chain density, the higher the chains alignment and the orientation along the stretching axis, favouring the occurrence of SIC. Our results do not show clear

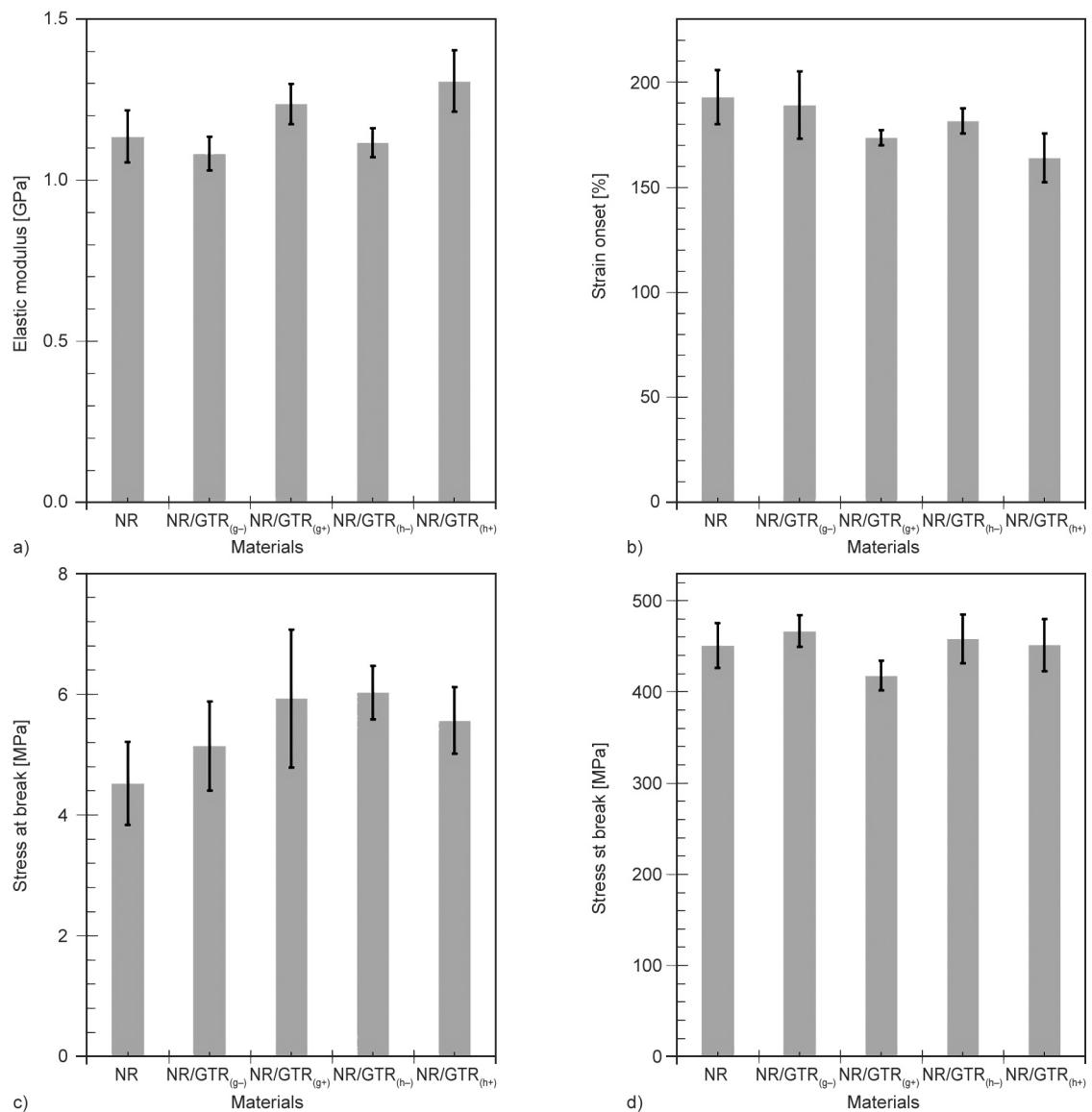


Figure 9. Mechanical parameters measured during tensile experiments performed at 21 °C and at the strain rate $v_4 = 222 \text{ \%}/\text{s}$: a) elastic modulus obtained from the Gaussian approximation, b) strain at crystallization onset estimated from the deviation of the tensile curve from the Gaussian approximation, c) stress at break and d) strain at break.

correlation between the network chain density and the strain at crystallization onset. Nonetheless, in our system, a better representation of the chains orientation is the elastic modulus (Figure 9a), as it considers both chemical crosslinks and entanglements trapped during the tensile test. The higher the elastic modulus, the lower is the strain at crystallization onset. The stress at break is found to increase in presence of GTR, likely due to both the reinforcement effect of the carbon black particles in the wastes but also owing the nucleation ability of these wastes to favour SIC (Figure 9c). One may note that in the case of NR/GTR_(h+) blends, tensile properties are decreased. This can be attributed to a higher quantity of cavitation originated at NR-GTR interface that may participate in materials softening, especially at such high strain rate conditions (222 %/s), favoured by the presence of larger waste particles obtained from HSM process (see Figure 1). Such correlation between stress softening and the occurrence of cavitation had been studied previously in filled EPDM in the same strain rate range [36]. The strain at break does not seem to be widely influenced by the presence of wastes, nor by the type of waste processing (Figure 9d).

The environment temperature is known to widely influence the strain-induced crystallization behaviour of NR materials and hence influence its associated mechanical reinforcement. Tensile tests carried out on NR and NR/GTR specimens at a given strain rate ($v_2 = 11$ %/s) and at various temperatures show hyperelastic behaviour with reinforcement at large strain (Figure 10). The latter is more pronounced when decreasing the temperature. This is likely ascribed to the promotion of SIC ability while decreasing

the temperature in the same temperature range, as shown in the literature [37, 38].

Elastic moduli are not found to be dependent on the temperature in the temperature range studied (Figure 11a). Nonetheless, the strain at crystallization onset is found to increase with the temperature (Figure 11b). It has been shown in the literature that -25 °C is the optimum temperature for thermal crystallization in both vulcanized NR and NR containing reinforcing fillers (carbon black or silica) [39] due to competition – at temperatures between the glass transition temperature and the melting temperature – between crystal nucleation (activated at low temperature) and molecular diffusion to make a crystal growing (activated at high temperature). It has also been shown that this optimum is between -25 and -10 °C when combined with thermal and strain-induced crystallization in the strain range of the present paper [40]. Our results obtained about the strain at crystallization onset reveal the same dependence on the temperature for both NR and NR/GTR. Interestingly, the addition of GTR into the NR matrix seems to slightly increase the optimum temperature of crystallization in comparison with pure NR. This shift is expected to occur when increasing the strain rate, as demonstrated by both experiments and physical modelling [40]. In the case of our blends, the presence of GTR fillers increases the local deformation in the crystallizing NR matrix, as well as its local strain rate, compared to the strain rate in the neat NR. As the strain rate is increased, the nucleation is forced to occur at higher strain, and the contribution of the nucleation term (driven by entropy force) is predominant and tends to shift the optimum temperature to higher values (see reference [40] for a detailed

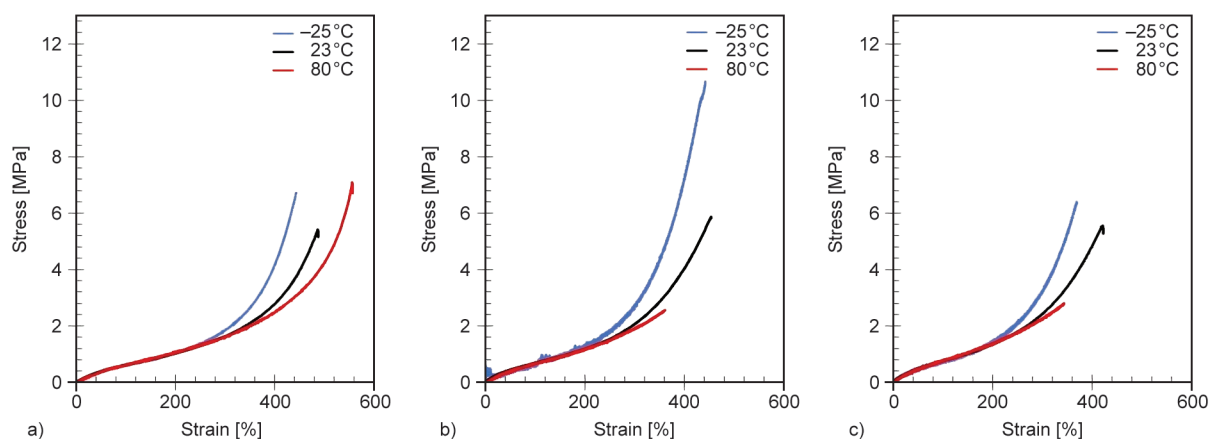


Figure 10. Tensile curves of NR (a), NR/GTR_(h-) (b) and NR/GTR_(h+) (c) at the strain rate of $v_2 = 11$ %/s and at various temperatures: -25 , 23 and 80 °C.

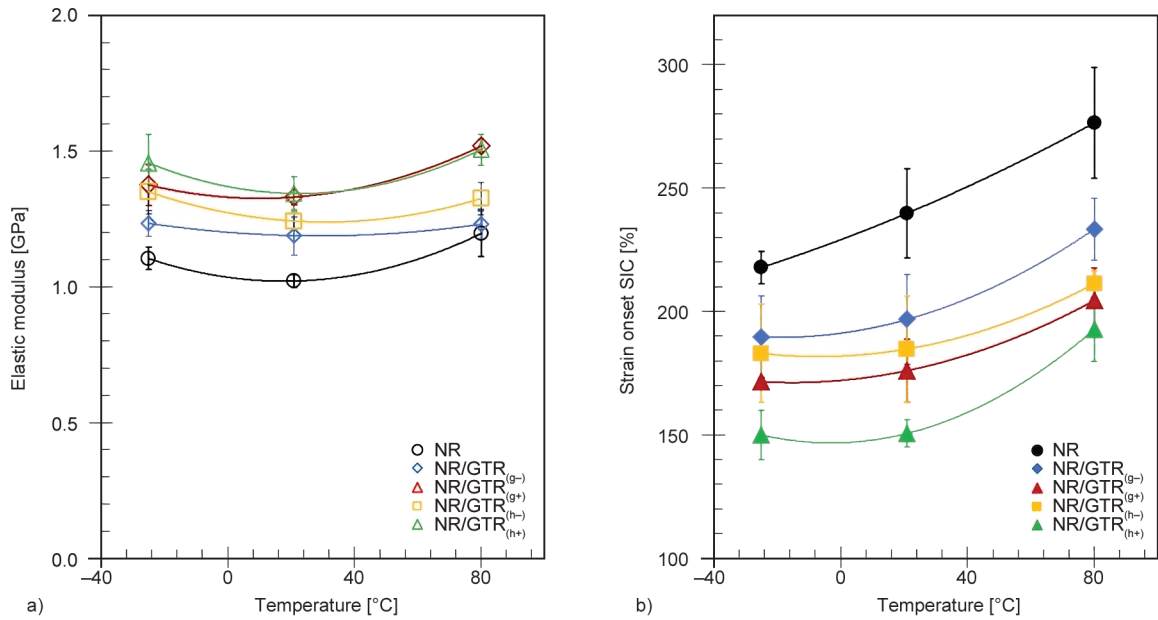


Figure 11. Elastic modulus (a) and strain at crystallization (b) onset of NR and NR/GTR blends at the strain rate of $v_2 = 11 \text{ \%}/\text{s}$ and at various temperatures: $-25, 21$ and $80 \text{ }^\circ\text{C}$.

demonstration). One interesting application is the possibility of these NR/GTR blends to operate in an optimum way (*i.e.*, when SIC occurs at the lowest strain) at a temperature close to room temperature. It may be useful for applications requiring SIC to occur at high strain rates, such as heating/cooling systems using the elastocaloric effect in NR, that may operate with usual temperatures close to $21 \text{ }^\circ\text{C}$ in countries with a temperate climate.

The effect of the GTR on elastic modulus and strain at crystallization onset are illustrated for the series of

tensile tests at $-25 \text{ }^\circ\text{C}$ (Figure 12). The presence of GTR is found to increase the blend's stiffness. One may note that the reinforcing effect of the GTR on the elastic modulus is more important at low temperatures (Figure 12a), in comparison with the results obtained at room temperature (Figure 9a). Similarly, the effect of the GTR on the strain at crystallization onset is more visible. The presence of GTR decreases the strain at crystallization onset, and the higher the crosslink density of the NR/GTR, the lower the strain at crystallization onset for the two types of

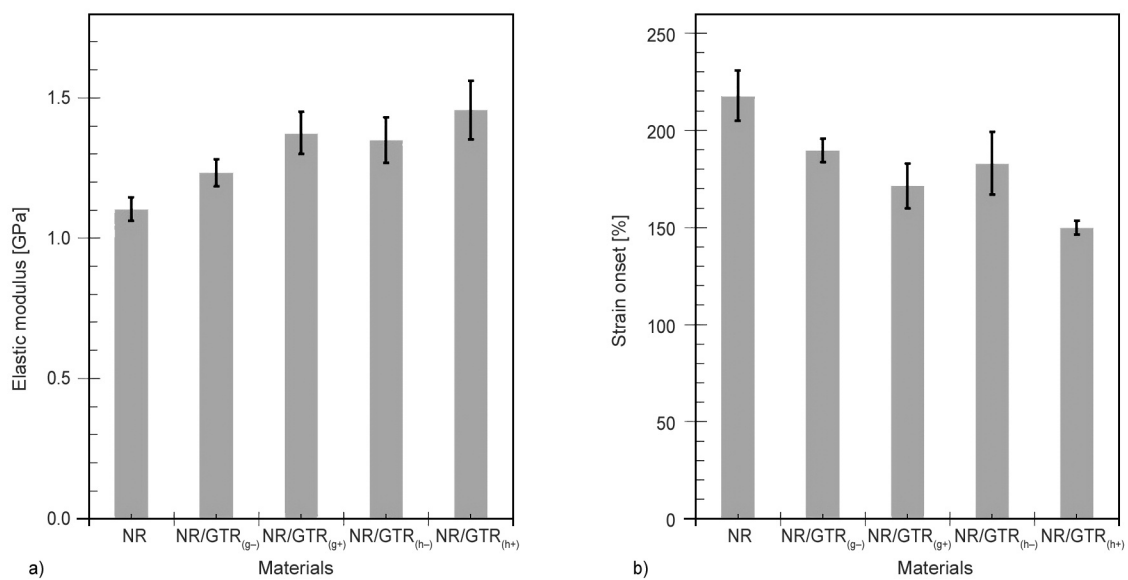


Figure 12. Mechanical parameters were measured during tensile experiments performed at $-25 \text{ }^\circ\text{C}$ and at the strain rate $v_2 = 11 \text{ \%}/\text{s}$: a) elastic modulus obtained from the Gaussian approximation, b) strain at crystallization onset estimated from the deviation of the tensile curve from the Gaussian approximation.

NR/GTR. Such conclusions are similar to previous results observed at 21 °C and at the strain rate $\nu_4 = 222$ %/s (Figure 9c, Figure 9d). Moreover, the NR/GTR blends containing GTR particles obtained with HSM (GTR_(h)) show the highest elastic modulus. This result is consistent with the literature that shows that the elastic modulus of rubber blends using waste latex is increased while increasing the waste diameter, while the finest diameters are closer to the theoretical expectations from the Einstein equation [41]. Consistent with such an increase of elastic modulus, SIC onset is found to appear at the lowest strain for NR/GTR_(h), confirming a trend seen from results at 21 °C and at the strain rate $\nu_4 = 222$ %/s (Figure 9a, Figure 9b).

Until now, single tensile loading had been applied on the NR and NR/GTR blends. To make the NR/GTR blends suitable for industrial applications, the cyclic behaviour must be investigated. High strain rate strain-induced crystallization may indeed generate an elastocaloric effect that can be used for heating/cooling devices working under cyclic loading to generate continuous heating and/or cooling with operating time. In the present paper, a series of incremental tests were performed (see Table 2 for the testing conditions). The loading conditions and the evolution of the stress-strain behaviour in such type of experiments is illustrated for the NR/GTR_(h+) in Figure 13. The first cycles show hyperelasticity and reversibility with the absence of mechanical hysteresis. However, from an applied deformation at and

above 300%, the cycles induce a dissipation of the mechanical energy that is most likely due to the occurrence of SIC.

Such energy dissipation is considered as a signature of SIC. It is calculated from the area of the mechanical cycle and express in MJ·m⁻³ (or equivalently in MPa). The detailed procedure for the estimate of such energy dissipation is given in reference [18]. When potted against the maximum applied strain, it results in a progressive increase that directly related to the progressive building of the crystalline domains upon deformation (Figure 14). In such cyclic conditions, once again, the presence of GTR is found to act as nucleating agent for SIC. The higher the crosslink density for the NR/GTR blends, the more pronounced is the nucleating effect for both types of NR/GTR using different varieties of waste rubber treatments.

In a last series of tests, the NR and NR/GTR blend are studied by applying continuous cycles of an amplitude of 200% after the application of a pre-deformation of 400%. Such conditions are expected to generate strain-induced crystallization during loading and full melting during unloading, hence associated with mechanical dissipation. In all samples, both maximum stress (Figure 15a) and dissipated energy (Figure 15b) are found to decrease with the number of cycles. The drastic decrease in the dissipated energy within the first cycles is likely due to the decrease in the crystallization/melting abilities. This is particularly true for the NR/GTR blends, especially

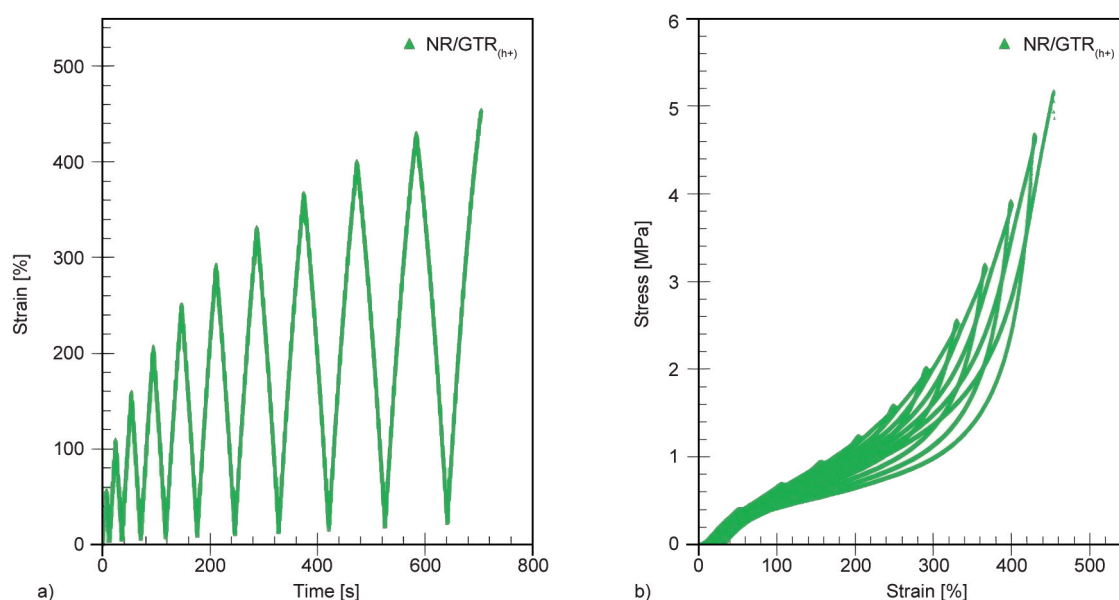


Figure 13. Cyclic loading of the NR/GTR_(h+) during incremental tests (a) and stress-strain behaviour during such type of test (b).

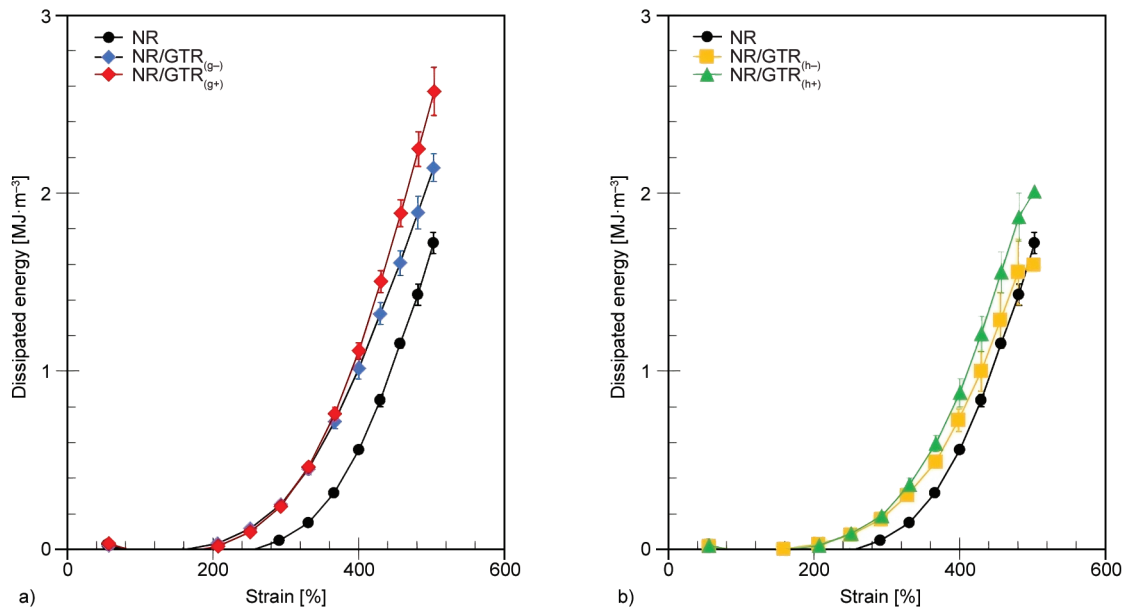


Figure 14. Evolution of the dissipated energy *versus* strain during incremental cycles for a) NR/GTR blends using cryoground GTR compared with neat NR and for b) NR/GTR blends using GTR passed through HSM process compared with neat NR.

those with higher network chain densities. In such types of experiments, a memory effect of the strain-induced crystals may cause the persistence of a fraction of the crystalline phase after unloading, as had been demonstrated in vulcanized NR [42]. This likely results in a decrease of the energy dissipation associated with its further crystallization/melting in subsequent cycles. After the application of hundreds of cycles, the NR/GTR blends with the highest network chain density show the best ability to dissipate

mechanical energy, with the highest value obtained for the blends using cryoground GTR (GTR_(g)). Such ability may be related to the fact that the blends containing the finest GTR particles, independently of the quality of the NR/GTR interface, possibly faceless cavitation, and better distribute the stress in the NR matrix. These results suggest these blends be interesting materials for potential elastocaloric properties while working into heating/cooling devices, owing to their possible ability to continuously

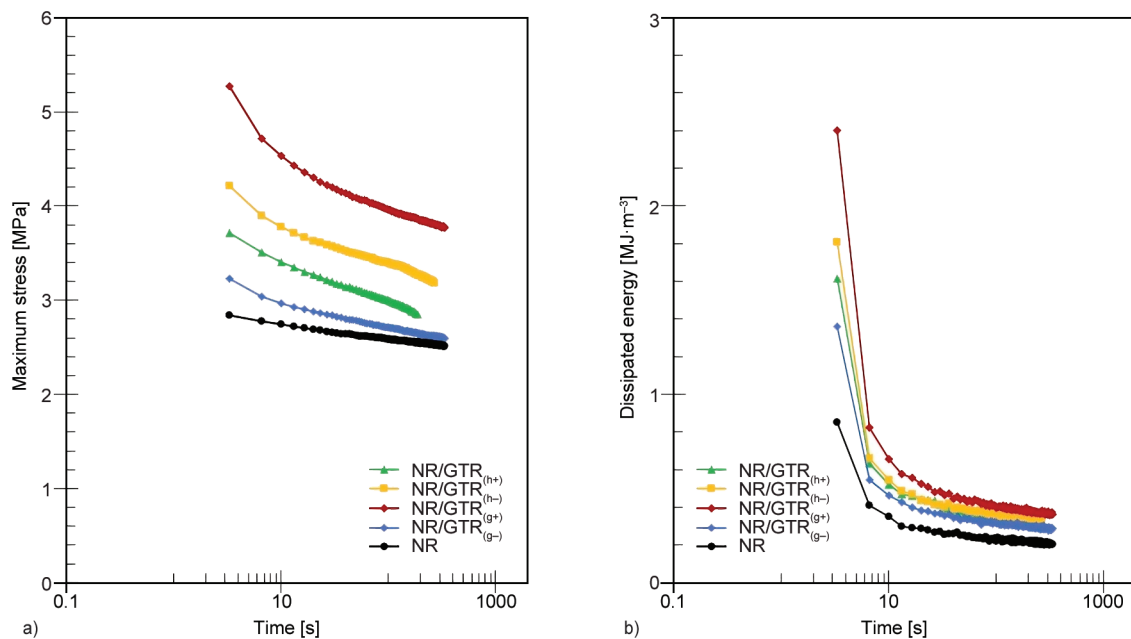


Figure 15. Maximum stress was measured during the cyclic tests at a strain rate of 120 %/s. A pre-deformation of 400% has been applied followed by a cyclic test with a strain amplitude of 200%: a) maximum stress, b) dissipated energy

generate heat and cool during repetitive mechanical cycles.

4. Conclusions

We have prepared peroxide-cured waste/natural rubber blends by internal mixer and by hot press. These blends contained a natural rubber matrix and waste rubber from the pneumatic industry (ground tyre rubber) that were obtained by two distinct mechanical recycling processes: GTR_(g) by cryo-grinding and GTR_(h) by high shear mixing process. On one side, it has been shown that the cryo-grinding process resulted in the obtention of the finest particles, as demonstrated by μ CT. On the other side, rheology and dynamic mechanical analysis performed on GTR powder obtained from HSM and on NR/GTR blend revealed an elastic response that suggests the formation of interfacial strength between the GTR particles and between the GTR particles and the NR matrix as compared to the blend using cryoground particles. The tensile properties of NR/GTR blends using both types of GTR treatment were investigated under several conditions by varying the tensile speed (from 1.1 to 222 %/s), the specimen temperature (from -25 to 80 °C) and the mechanical path (single cyclic loading or incremental cycles). It has been shown that owing to the highest degree of crosslinking in the NR/GTR using GTR obtained from HSM, the elastic modulus was the highest, and the strain at crystallization onset was the lowest during single tensile loading. Contrarily, in more drastic conditions of solicitation, such as cyclic loadings, the NR/GTR blends using cryoground GTR show the highest tensile properties as well as a higher capacity to generate strain-induced crystallization. This suggests a better accommodation of the strain in such types of blends (less molecular scale damage such as crosslinks breakage, chains scission, or less decohesion at NR/GTR interface). The results suggest that the HSM is a promising process for waste rubber recycling to enhance the tensile properties of NR but shows a limitation under cyclic conditions due to possible damage of the material due to (i) a high level of crosslinks and/or (ii) the loss of the interfacial strength after the application of a series of cycle due to too a strong localization of the stress because of the large size of the waste particles. A possible improvement would consist in combining cryo-grinding and HSM processes to use the advantage of both

techniques: size reduction from cryo-grinding and higher interfacial strength from the HSM. Finally, the measure of the devulcanization state of the GTR, especially from the HSM process, by using swelling and Soxhlet extraction, would be of great interest to optimize the re-vulcanization process.

Acknowledgements

N. Candau acknowledges the Spanish Ministry of Science and Innovation (Project TED2021-129952A-C33, and the group eb-POLICOM/Polimers i Compòsits Ecològics i Biodegradables, a research group of the Generalitat de Catalunya (Grant 2021 SGR 01042). We acknowledge Rodrigo Diaz-Vargas from the REP-International company, for performing the high shear mixing process as well as the curing experiments carried out on the waste rubber.

References

- [1] European Commission: European strategy for market development of innovative use of tyre recycled materials. (2023).
- [2] Mohajerani A., Burnett L., Smith J. V., Markovski S., Rodwell G., Rahman M. T., Kurmus H., Mirzababaei M., Arulrajah A., Horpibulsuk S., Maghool F.: Recycling waste rubber tyres in construction materials and associated environmental considerations: A review. *Resources, Conservation and Recycling*, **155**, 104679 (2020).
<https://doi.org/10.1016/j.resconrec.2020.104679>
- [3] European Commission: Recycling technology to introduce rubber from end-of-life tyres into production lines as virgin rubbers substitute. (2023).
- [4] Shu X., Huang B.: Recycling of waste tire rubber in asphalt and portland cement concrete: An overview. *Construction and Building Materials*, **67**, 217–224 (2014).
<https://doi.org/10.1016/j.conbuildmat.2013.11.027>
- [5] Goto M.: Chemical recycling of plastics using sub- and supercritical fluids. *Journal of Supercritical Fluids*, **47**, 500–507 (2009).
<https://doi.org/10.1016/j.supflu.2008.10.011>
- [6] de Sousa F. D. B., Scuracchio C. H., Hu G-H., Hoppe S.: Devulcanization of waste tire rubber by microwaves. *Polymer Degradation and Stability*, **138**, 169–181 (2017).
<https://doi.org/10.1016/j.polymdegradstab.2017.03.008>
- [7] Arabiourrutia M., Lopez G., Artetxe M., Alvarez J., Bilbao J., Olazar M.: Waste tyre valorization by catalytic pyrolysis – A review. *Renewable and Sustainable Energy Reviews*, **129** 109932 (2020).
<https://doi.org/10.1016/j.rser.2020.109932>
- [8] Junghare H., Hamjade M., Patil C., Girase S. B., Lele M. M.: A review on cryogenic grinding. *International Journal of Current Engineering and Technology*, **7**, 420–423 (2017).

- [9] Hrdlička Z., Hrdlička Z., Břejcha J., Šubrt J., Vrtiška D., Malinová L., Čadek D., Kadeřábková A.: Ground tyre rubber produced *via* ambient, cryogenic, and waterjet milling: The influence of milling method and particle size on the properties of SBR/NR/BR compounds for agricultural tyre treads. *Plastics, Rubber and Composites*, **51**, 497–506 (2022).
<https://doi.org/10.1080/14658011.2021.2008713>
- [10] Diaz R., Colomines G., Peuvrel-Disdier E., Deterre R.: Thermo-mechanical recycling of rubber: Relationship between material properties and specific mechanical energy. *Journal of Materials Processing Technology*, **252**, 454–468 (2018).
<https://doi.org/10.1016/j.jmatprotec.2017.10.014>
- [11] Zhang X-X., Lu C-H., Liang M.: Preparation of rubber composites from ground tire rubber reinforced with waste-tire fiber through mechanical milling. *Journal of Applied Polymer Science*, **103**, 4087–4094 (2007).
<https://doi.org/10.1002/app.25510>
- [12] Karger-Kocsis J., Mészáros L., Bárányi T.: Ground tyre rubber (GTR) in thermoplastics, thermosets, and rubbers. *Journal of Materials Science*, **48**, 1–38 (2013).
<https://doi.org/10.1007/s10853-012-6564-2>
- [13] Roychand R., Gravina R. J., Zhuge Y., Ma X., Youssf O., Mills J. E.: A comprehensive review on the mechanical properties of waste tire rubber concrete. *Construction and Building Materials*, **237**, 117651 (2020).
<https://doi.org/10.1016/j.conbuildmat.2019.117651>
- [14] De D., Panda P. K., Roy M., Bhunia S.: Reinforcing effect of reclaim rubber on natural rubber/polybutadiene rubber blends. *Materials and Design*, **46**, 142–150 (2013).
<https://doi.org/10.1016/j.matdes.2012.10.014>
- [15] Barrera C. S., Cornish K.: High performance waste-derived filler/carbon black reinforced guayule natural rubber composites. *Industrial Crops and Products*, **86**, 132–142 (2016).
<https://doi.org/10.1016/j.indcrop.2016.03.021>
- [16] Chandran V., Nagarajan L., Thomas M. R.: Evaluation of vibration damping behavior of different sizes of waste tyre rubber in natural rubber composites. *Journal of Composite Materials*, **52**, 2493–2501 (2018).
<https://doi.org/10.1177/0021998317748467>
- [17] Candau N., Oguz O., Federico C. E., Stoclet G., Tahon J-F., Maspoeh M. L.: Strain induced crystallization in vulcanized natural rubber containing ground tire rubber particles with reinforcement and nucleation abilities. *Polymer Testing*, **101**, 107313 (2021).
<https://doi.org/10.1016/j.polymertesting.2021.107313>
- [18] Candau N., Vives E., Fernández A. I., Maspoeh M. L.: Elastocaloric effect in vulcanized natural rubber and natural/wastes rubber blends. *Polymer*, **236**, 124309 (2021).
<https://doi.org/10.1016/j.polymer.2021.124309>
- [19] Candau N., Vives E., Fernández A. I., Oguz O., Corvec G., Federico C. E., Fernandes J. P. C., Stoclet G., Maspoeh M. L.: Observation of heterogeneities in elastocaloric natural/wastes rubber composites. *Express Polymer Letters*, **16**, 1331–1347 (2022).
<https://doi.org/10.3144/expresspolymlett.2022.96>
- [20] Flory P. J., Rehner J.: Statistical mechanics of cross-linked polymer networks II. Swelling. *Journal of Chemical Physics*, **11**, 521–526 (1943).
<https://doi.org/10.1063/1.1723792>
- [21] Sheehan C. J., Bisio A. L.: Polymer/solvent interaction parameters. *Rubber Chemistry and Technology*, **39**, 149–192 (1966).
<https://doi.org/10.5254/1.3544827>
- [22] Kraus G.: Swelling of filler-reinforced vulcanizates. *Journal of Applied Polymer Science*, **7**, 861–871 (1963).
<https://doi.org/10.1002/app.1963.070070306>
- [23] Vieyres A.: Influence of filler/polymer interface on reinforcement, strain-induced crystallization and tear resistance in reinforced natural rubber. PhD These, Ecole Doctorale Matériaux de Lyon (2013).
- [24] Robertson C. G., Hardman N. J.: Nature of carbon black reinforcement of rubber: Perspective on the original polymer nanocomposite. *Polymers*, **13**, 538 (2021).
<https://doi.org/10.3390/polym13040538>
- [25] Fernández-Berridi M. J., González N., Mugica A., Bernicot C.: Pyrolysis-FTIR and TGA techniques as tools in the characterization of blends of natural rubber and SBR. *Thermochimica Acta*, **444**, 65–70 (2006).
<https://doi.org/10.1016/j.tca.2006.02.027>
- [26] Liu X., Liu X., Hu Y.: Investigation of the thermal decomposition of talc. *Clays and Clay Minerals*, **62**, 137–144 (2014).
<https://doi.org/10.1346/ccmn.2014.0620206>
- [27] Thitithammawong A., Uthaipan N., Rungvichaniwat A.: The influence of mixed conventional sulfur/peroxide vulcanization systems on the mechanical and thermal properties of natural rubber/polypropylene blends. *Journal of Elastomers and Plastics*, **44**, 419–432 (2012).
<https://doi.org/10.1177/0095244311432781>
- [28] Candau N., Oguz O., Albiter N. L., Förster G., Maspoeh M. L.: Poly(lactic acid)/ground tire rubber blends using peroxide vulcanization. *Polymers*, **13**, 1496 (2021).
<https://doi.org/10.3390/polym13091496>
- [29] Rajan R., Varghese S., George K. E.: Role of coagents in peroxide vulcanization of natural rubber. *Rubber Chemistry and Technology*, **86**, 488–502 (2013).
<https://doi.org/10.5254/rct.13.87984>
- [30] Yahya Y. S. R., Azura A. R., Ahmad Z.: Effect of curing systems on thermal degradation behaviour of natural rubber (SMR CV 60). *Journal of Physical Science*, **22**, 1–14 (2011).
- [31] Litvinov V. M., De P. P.: Spectroscopy of rubbers and rubbery materials. iSmithers Rapra Publishing (2002).
- [32] Treloar L. R. G.: The physics of rubber elasticity. Oxford University Press, New York (1975).

- [33] Zedler L., Przybysz M., Klein M., Saeb M. R., Formela K.: Processing, physico-mechanical and thermal properties of reclaimed GTR and NBR/reclaimed GTR blends as function of various additives. *Polymer Degradation and Stability*, **143**, 186–195 (2017).
<https://doi.org/10.1016/j.Polymdegradstab.2017.07.004>
- [34] Zitzumbo R., Alonso S., Estrada-Monje A., Becerra M. B., Avalos F., Medina-Torres L.: Mechanical properties, dynamic mechanical analysis and molecular cross-linking of GTR/NR re-vulcanized blends. *Progress in Rubber, Plastics and Recycling Technology*, **38**, 280–294 (2022).
<https://doi.org/10.1177/14777606221127370>
- [35] Ikeda Y., Yasuda Y., Hijikata K., Tosaka M., Kohjiya S.: Comparative study on strain-induced crystallization behavior of peroxide cross-linked and sulfur cross-linked natural rubber. *Macromolecules*, **41**, 5876–5884 (2008).
<https://doi.org/10.1021/ma800144u>
- [36] Candau N., Oguz O., Peuvrel-Disdier E., Bouvard J-L., Maspoch M. L., Corvec G., Pradille C., Billon N.: Effect of the strain rate on damage in filled EPDM during single and cyclic loadings. *Polymers*, **12**, 3021 (2020).
<https://doi.org/10.3390/polym12123021>
- [37] Candau N.: Compréhension des mécanismes de cristallisation sous tension des élastomères en conditions quasi-statiques et dynamiques. PhD These, Lyon, INSA (2014).
- [38] Xie Z., Sebald G., Guyomar D.: Temperature dependence of the elastocaloric effect in natural rubber. *Physics Letters A*, **381**, 2112–2116 (2017).
<https://doi.org/10.1016/j.physleta.2017.02.014>
- [39] Chenal J. M., Chazeau L., Bomal Y., Gauthier C.: New insights into the cold crystallization of filled natural rubber. *Journal of Polymer Science Part B: Polymer Physics*, **45**, 955–962 (2007).
<https://doi.org/10.1002/polb.21105>
- [40] Candau N., Laghmach R., Chazeau L., Chenal J-M., Gauthier C., Biben T., Munch E.: Influence of strain rate and temperature on the onset of strain induced crystallization in natural rubber. *European Polymer Journal*, **64**, 244–252 (2015).
<https://doi.org/10.1016/j.eurpolymj.2015.01.008>
- [41] Mathew G., Singh R. P., Nair N. R., Thomas S.: Recycling of natural rubber latex waste and its interaction in epoxidised natural rubber. *Polymer*, **42**, 2137–2165 (2001).
[https://doi.org/10.1016/S0032-3861\(00\)00492-4](https://doi.org/10.1016/S0032-3861(00)00492-4)
- [42] Candau N., Laghmach R., Chazeau L., Chenal J-M., Gauthier C., Biben T., Munch E.: Strain-induced crystallization of natural rubber and cross-link densities heterogeneities. *Macromolecules*, **47**, 5815–5824 (2014).
<https://doi.org/10.1021/ma5006843>

Research article

In situ catalyzed poly(ϵ -caprolactone)/organic rectorite nanocomposites with excellent electrochemical performance

Limin You, Shifan Zhang, Zhuoxiong Huang, Wanle Pi, Jiaqi Liu, Rui Ma* 

Faculty of Materials Science and Chemistry, China University of Geosciences, 430074 Wuhan, China

Received 8 May 2023; accepted in revised form 4 August 2023

Abstract. In recent years, solid polymer electrolytes (SPE) has attracted much attention because of its good safety and environmental stability, among which poly(ϵ -caprolactone) (PCL) based solid electrolyte film is one of the most potential materials. We have adopted the method of synthesizing polymer nanocomposites with natural clay, which can effectively meet the needs of electrolytes. In this study, cetyl trimethyl ammonium bromide (CTAB) was used to modify rectorite (REC), and the ϵ -CL monomer is inserted between the rectorite silicate layers. PCL/organic rectorite (OREC) nanocomposites were synthesized by *in situ* intercalation polymerization. The yield of the polymer nanocomposite could reach 93.6% when the molecular weight of the polymer nanocomposite was 39 000. The effects of OREC addition on the morphology, thermal stability, and electrochemical properties of PCL/OREC nanocomposites were investigated by various characterization methods. The temperature can be increased by 50 °C when the thermal decomposition is 50 wt%, and the crystallinity decreases by 4.6%. Composite polymerelectrolytes (CPEs) (PCL/OREC) showed a good electrical conductivity of $1.13 \cdot 10^{-4} \text{ S} \cdot \text{cm}^{-1}$ at 60 °C and an excellent capacity retention rate of 96.7% after 100 cycles at 0.5 C current density. This study has important guiding significance for the development of polymer nanocomposites as solid electrolytes.

Keywords: biopolymer, ring-opening polymerization, electrical property, poly(caprolactone), clay

1. Introduction

Poly(ϵ -caprolactone) (PCL) is a synthetic biodegradable polyester that is compatible with a variety of polymers and is one of the most promising biodegradable polymers in the market at present [1]. Moreover, due to the unique lithium-ion complexation and transport mechanism, PCL-based solid polymer electrolyte (SPE) has a wide electrochemical stability window and high lithium ion migration number [2–5], so PCL can be applied to the preparation of SPE. However, the poor thermal stability and semi-crystallinity of PCL [6] limit the cell cycle performance and ionic conductivity of PCL-based solid electrolytes. The addition of organic layered silicates as nanoparticles to PCL can ameliorate these limitations. However, the compatibility and dispersion of natural mineral materials in polymers are poor. If the

traditional physical blending method is used to prepare polymer composite materials, uneven dispersion may occur in silicate mineral polymer materials, and poor compatibility leads to the reduction of mechanical and thermal properties of composite materials [7]. And the presence of larger mineral particles in the polymer matrix creates a lot of ‘Blocks’ which in part blocks the movement of ions, resulting in lower conductivity. In order to overcome these difficulties, the method of *in situ* intercalation polymerization is adopted. By *in situ* polymerization of monomers between layers, the silicate layer is stripped, and the large particle size is converted to a smaller size and distributed uniformly in the polymer matrix. As Ilsouk *et al.* [8] prepared poly(ϵ -caprolactone)/organomodified Moroccan beidellite clay through *in situ* polymerization, Moroccan beidellite

*Corresponding author, e-mail: ruima@cug.edu.cn
© BME-PT

clay was well stripped and dispersed in PCL, which is consistent with other relevant reports [9–11]. In addition to improving the thermal stability of polymer, the addition of nano-sized particles enhanced the activity of polymer molecular chains, thus improving the ionic conductivity of polymer electrolytes. Due to the nano-dispersion of the silicate layer, the properties of ordinary materials are completely different from those of composite materials with inorganic components dispersed at the micron level. Unexpected properties were observed, such as large increases in thermal stability, mechanical strength, and permeability to gases such as oxygen and water [12, 13].

Compared with silicate minerals such as montmorillonite and kaolin, there is relatively little research on rectorite nanocomposites, so there is potential for research and development. Natural rectorite is a special layered silicate mineral composed of octahedral mica and octahedral montmorillonite layers stacked in a 1:1 ratio, with good colloid properties and cation exchange capacity [14, 15]. Because of the special layered structure, it has the characteristics of both mica and montmorillonite [16]. Recently, rectorite (REC) has been widely used in polymer modification. It was found that the mechanical and thermal properties of the polymer were greatly enhanced with the introduction of REC [17]. In addition, rectorite is more resistant to heat and is a better barrier than montmorillonite because of its higher aspect ratio [18].

Considering the dual advantages of excellent cation exchange and the low cost of REC, cetyl trimethyl ammonium bromide (CTAB) was used to modify rectorite to obtain organic rectorite (OREC). PCL/OREC nanocomposites were synthesized by intercalating ϵ -CL monomer into OREC layers and *in situ* intercalation polymerization. The optimum synthesis conditions of PCL/OREC nanocomposites were studied by changing the ratio of initiator to OREC. The effects of OREC incorporation on the morphology, thermal stability, and electrochemical properties of PCL/OREC nanocomposites were investigated by various characterization methods.

2. Experimental

2.1. Materials

Ca-Rectorite (Ca-REC) (95% purity) was purchased from Lingshou Country Deheng Mineral Products Co., Ltd (Hebei, China). Hexadecyl trimethyl

ammonium bromide (CTAB, 99% purity) was purchased from Shanghai Aladdin Bio-Chem Technology Co., Ltd (Shanghai, China). Tin 2-ethylhexanoate ($\text{Sn}(\text{Oct})_2$, 98% purity) was purchased from Shanghai Macklin Biochemical Co., Ltd. (Shanghai, China). Methanol, dichloromethane, hydrochloric acid and Al_2O_3 (99.9% metals basis, α -phase, 30 nm, 99% purity) were purchased from Sinopharm Chemical Reagent Co., Ltd (Shanghai, China). ϵ -caprolactone (ϵ -CL, 99% purity) was purchased from Shanghai Aladdin Bio-Chem Technology Co., Ltd (Shanghai, China).

2.2. Purification of rectorite

10 g REC was added to 100 ml deionized water and stirred to a uniform liquid phase, then 3 g sodium hexametaphosphate was added as dispersant and stirred at room temperature for 5 h. The solution was poured into the centrifugal tube and the upper solid was collected after high-speed centrifugation; the lower black solid was removed as impurities, and then an appropriate amount of deionized water was added for washing. This process was repeated three times. After drying and grinding, purified REC is stored in a dry environment.

2.3. Organization of rectorite

REC was added to 1 mol/l hydrochloric acid solution with a solid-liquid ratio of 1:20. Disperse for 15 min with ultrasound and stir for 12 h. The solution was poured into a centrifuge tube and washed three times until the pH value approached 7. After drying for 12 h at 80 °C, the acid REC was obtained by grinding. 5 g acidified REC was added to 50 ml deionized water, stirred evenly, and 0.879 g CTAB was added. The reaction was performed at 60 °C for 5 h under a nitrogen atmosphere, followed by high-speed centrifugation and deionized water washing for three times. The supernatant was taken, and no bromine ions were detected with silver nitrate solution, dried at 80 °C for 12 h, and OREC was obtained by grinding.

2.4. Synthesis of PCL/OREC nanocomposites

PCL/OREC nanocomposites were prepared by monomer intercalation *in situ* polymerization. A certain amount of ϵ -CL and OREC was added to the branching flask, and the samples were dispersed by ultrasonic for 30 min in a nitrogen atmosphere and stirred at 66 °C for 12 h. A certain amount of $\text{Sn}(\text{Oct})_2$ was added to the system as a catalyst, and

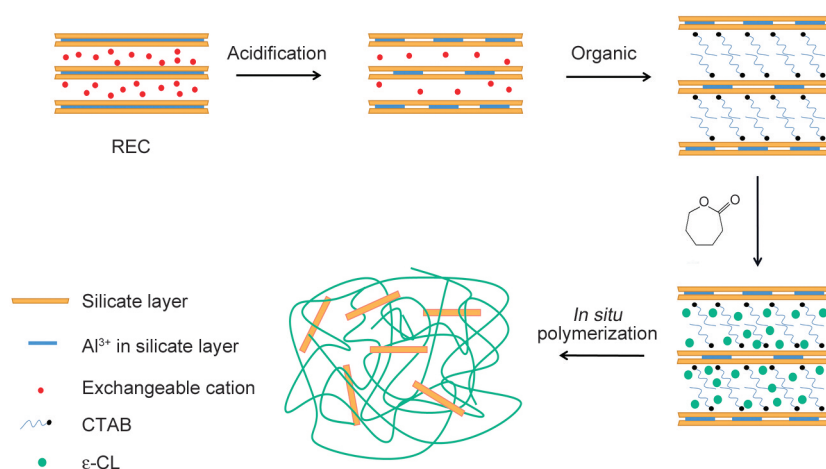


Figure 1. Mechanism of PCL/OREC synthesis.

the flask was stirred in an oil bath at 140 °C for 24 h after being purged with nitrogen three times. At the end of the reaction, an appropriate amount of methylene chloride was added to the system to dissolve the product. When the product was completely dissolved, excessive methanol was added and placed in the refrigerator overnight. After the product is precipitated from the solution, it is washed and filtered with methanol to remove unreacted monomers and catalysts. The product was dried at a vacuum of 40 °C for 48 h, then weighed and yield calculated. The general procedure is illustrated in Figure 1.

2.5. Synthesis of composite polymer electrolytes (CPEs)

In the glove box, an appropriate amount of pure PCL or PCL/OREC nanocomposites and LiTFSI were dissolved in an appropriate amount of dimethyl carbonate, in which LiTFSI accounted for 20% of the mass of the polymer and stirred at 60 °C for 1 h. Then 15 wt% Al₂O₃ powder was added and stirred for a certain time under continuous heating. When the system was completely evenly dispersed, the solution was poured onto a glass plate with a spatula to form a film and dried at room temperature for 24 h to remove residual solvents. The resulting CPE film was cut into 19 mm diameter disks and assembled into coin-shaped cells in a glove box.

2.6. Characterization

The phase and composition of the samples were characterized by X-ray powder diffraction (XRD, Bruker D8 Advance, Bruker AG, Saarbrücken, Germany) using Cu K_α radiation ($\lambda = 0.15406$ nm) and characterized by Fourier transform infrared

spectrometer (FTIR, ThermoFisher Nicolet iS50, Thermo Fisher Scientific, Massachusetts, USA). Thermal analysis was performed in nitrogen at a heating rate of 10 °C·min⁻¹ from 30 to 600 °C (TG, Netzsch STA 2500, Netzsch, Selbu, Germany). The morphology and structure were examined by scanning electron microscopy (SEM, Hitachi SU8010, Hitachi Corporation, Tokyo, Japan and GeminiSEM 300, Carl Zeiss AG, Oberkochen, Germany). The thermal behavior of the samples was performed by differential scanning calorimetry (DSC, Discovery DSC 25, TA Instruments, Newcastle, USA). Firstly, the samples were heated from ambient to 80 °C at a heating rate of 20 °C·min⁻¹ and held isothermally at 80 °C for 10 min; secondly, the samples were cooled from 80 to -80 °C at a cooling rate of 20 °C·min⁻¹ and held isothermally for 10 min; and finally, the samples were again heated from -80 to 80 °C at a heating rate of 20 °C·min⁻¹. The chemical structures of the samples were recorded by nuclear magnetic resonance (¹H-NMR, Bruker 400M, Bruker AG, Saarbrücken, Germany). The number-average molecular weight (M_n) of the samples was determined using gel permeation chromatography (GPC, Breeze 2 Hplc 1525, Waters Corporation, Massachusetts, USA). The dynamic thermomechanical analyzer (DMA) was used, and the test conditions were as follows: using a single cantilever fixture, the test temperature range was -120 to 30 °C, the test frequency was 1 Hz, and the heating rate was 2 °C·min⁻¹ (Discovery DMA850, TA Instruments, Newcastle, USA). The ionic conductivities of the membranes were determined by electrochemical impedance spectroscopy (EIS, Zennium X, Zana Electrochemistry, Kronach, Germany). The charge and discharge tests

were performed from the LAND system (LAND, CT2001A, Wuhan Shenglan Electronic Technology Co., Wuhan, China). For cycling performance, the cells were charged and discharged with a 0.5 C rate.

3. Results and discussion

3.1. Structural analysis of REC and OREC

FTIR spectra of REC and OREC are shown in Figure 2. In the FTIR spectra of REC, the peak at 3620 cm^{-1} was related to the tensile vibration of the hydroxyl group of the Al–OH unit in rectorite. The peak values of 3419 and 1637 cm^{-1} are correlated with H–O–H tensile vibration and bending vibration of H_2O [19]. The peak at 1050 cm^{-1} is attributed to Si–O–Si tensile vibration in the plane. A peak of 822 cm^{-1} was associated with the bending vibration of Si–O–Al, while the peak of 822 cm^{-1} disappeared in FTIR spectra of acid-treated OREC. These results showed that the strength of the Si–O–Al band was weakened after acid treatment, and part of Al^{3+} in the surface skeleton was dissolved. Meanwhile, it was further indicated that acid treatment could change the surface properties of rectorite without destroying the structure of the original rectorite [20, 21], which was consistent with other layered silicate minerals with similar structures, such as montmorillonite and talc [22, 23]. In the FTIR spectrum of OREC, the broad peak at 3590 cm^{-1} and the peak at 1637 cm^{-1} were attributed to the tensile vibration and bending vibration of adsorbed water molecules. Compared with the vibration peak at 1050 cm^{-1} in the REC spectrum, the OREC spectrum moves to a higher wave number of 1100 cm^{-1} , corresponding to the out-of-plane Si–O–Si tensile vibration after acid treatment [24, 25]. At peak

values of 2927 , 2852 , and 1454 cm^{-1} , they were correlated with characteristic peaks of alkyl chains of surfactants, indicating [26] CTAB molecules were successfully grafted onto the surface of REC.

Figure 3 shows the X-ray diffraction data for REC and OREC. The interlayer distance of rectorite was obtained from the peak position (d_{001} -reflection) of X-ray diffraction data. In the X-ray diffraction data of REC, the d_{001} -reflection of phyllosilicate at $2\theta = 7.20^\circ$ corresponds to the interlayer distance of 12.3 \AA . In the X-ray diffraction data of OREC, the d_{001} -reflection of phyllosilicate at $2\theta = 4.98^\circ$ corresponds to the interlayer distance of 17.7 \AA . These data show that the d_{001} crystal plane spacing of rectorite increases by 5.4 \AA interlayer distance after organic treatment. Cetyltrimethyl ammonium bromide (CTAB) has a long alkyl chain structure and enters the silicate layer through ion exchange with REC [27]. Cationic surfactants can effectively increase the interlayer spacing of clay, thereby effectively reducing the interaction force between clay sheets [28] and improving the compatibility between natural clay and polymer.

The surface morphologies of REC and OREC were characterized by SEM images. It can be observed from Figure 4a that there is uneven particle size in the original REC, and the particle surface is rough, presenting a jagged and irregular sheet structure. As the layers are closely superimposed on top of each other, the spacing between the layers is almost indistinguishable. However, in the SEM image of OREC (Figure 4b), the particle size becomes smaller, the size distribution becomes uniform, more pore structures appear, the layered structure becomes loose,

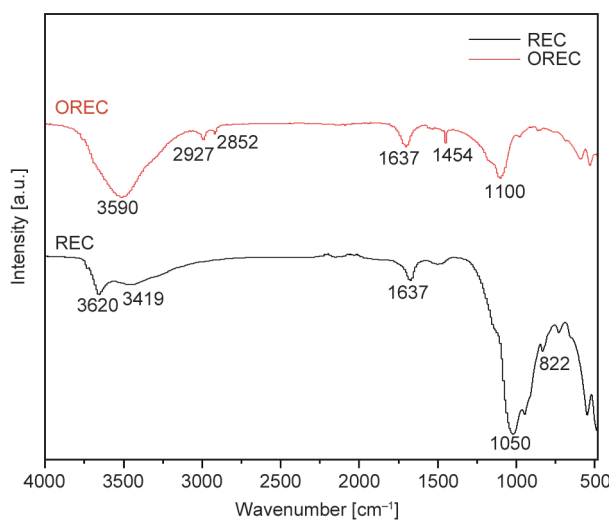


Figure 2. FTIR spectra of REC and OREC.

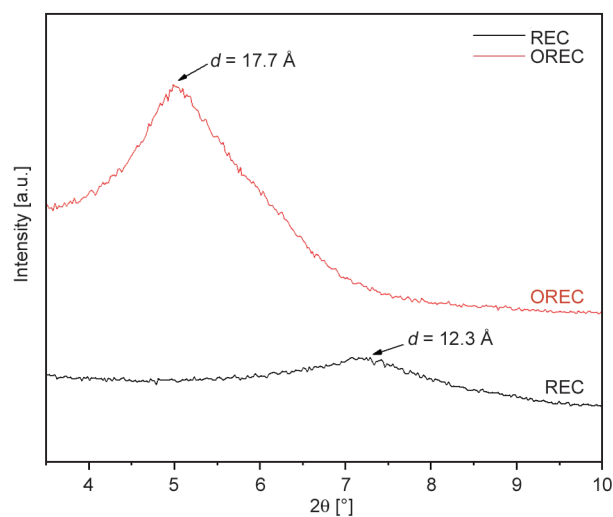


Figure 3. X-ray diffraction patterns of REC and OREC.

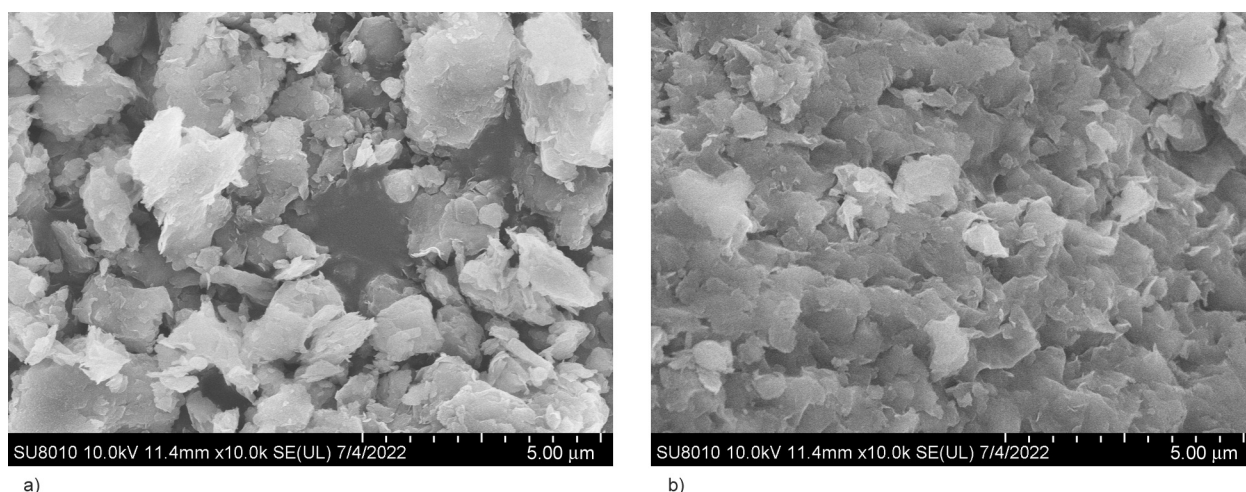


Figure 4. SEM images of a) REC and b) OREC.

and the layered stepped structure can be clearly seen. The results showed that after acid treatment and organic modification, the interlayer spacing increased and became more conducive to monomer entry. This result is consistent with the analysis of XRD.

3.2. Characterization of PCL/OREC nanocomposites

Figure 5 shows the NMR hydrogen spectrum, and the analysis reveals the chemical structure of the sample. $^1\text{H-NMR}$ (CDCl_3 , δ [ppm]): 2.2 (H_a , 2H), 1.7 (H_b , 4H), 1.4 (H_c , 2H), 4.1 (H_d , 2H). The results confirm the successful synthesis of PCL [29].

To study the optimum ratio of initiator $\text{Sn}(\text{Oct})_2$ and OREC in the polymerization of $\epsilon\text{-CL}$. Table 1 shows the effects of different initiator/monomer (I/M) mass ratios on the conversion rate and polymer dispersion index PDI (M_w/M_n) of nanocomposites when OREC addition amounts are 1, 2 and 4 wt%, respectively. As

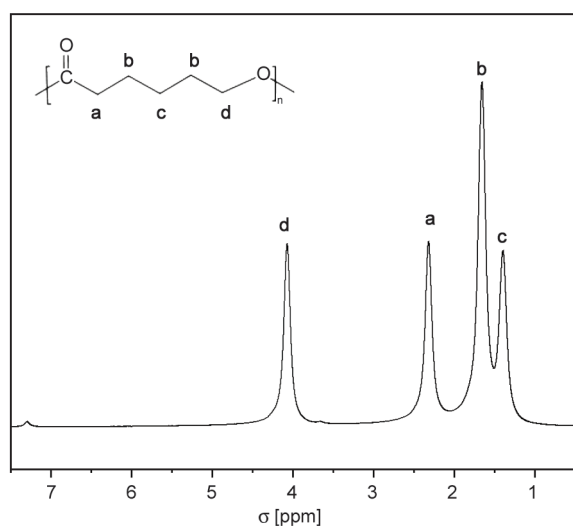


Figure 5. NMR hydrogen spectrum of PCL.

can be seen from the above table, the best conditions for composite synthesis are OREC with $I/M = 0.2$ and 2 wt%. Therefore, the subsequent tests were carried out with this sample.

When OREC content was increased to 2 wt%, a decrease in polymer dispersion index was observed. This is because the chain growth in the clay layer is limited at the beginning of polymerization, and these chains are not easy to participate in the transesterification reaction. When the chain grows long enough to achieve the effect of stripping, this protection will disappear [30]. The dispersion of rectorite in PCL was greatly improved after the stripping effect occurred, and the inorganic/organic interface effect was enhanced. After acid treatment, some Si–O–Al structures in rectorite are dissolved, resulting in the formation of more Si–OH. These surface hydroxyl groups can attack the C–O bond in the caprolactone monomer and achieve the purpose of ring-opening polymerization [31]. Therefore, a portion of the PCL molecular chain grows on the surface of the REC; we believe that rectorite and

Table 1. Effect of different ratios on conversion, molecular weight, and PDI of polymer nanocomposites.

Sample	OREC [%]	I/M [wt%]	CR [%]	M_n [$\text{g}\cdot\text{mol}^{-1}$]	PDI
1	1	0.1	89.60	32000	1.65
2	1	0.2	88.00	36000	1.61
3	1	0.4	86.50	35000	1.84
4	2	0.1	89.20	34000	1.39
5	2	0.2	93.60	39000	1.23
6	2	0.4	95.60	35000	1.50
7	4	0.1	89.40	19000	1.61
8	4	0.2	94.40	22000	1.58
9	4	0.4	92.00	20000	1.78

$\text{Sn}(\text{Oct})_2$ cooperate to catalyze ϵ -CL polymerization. When the clay concentration reached 4 wt%, clay stripping became difficult and resulted in shorter molecular chain growth lengths and lower molecular weight of polymers. At these concentrations, stripped and unstripped rectorite co-existed in the composite, leading to an increase in PDI.

Figure 6 shows the X-ray diffraction data of PCL with different amounts of rectorite. It can be observed that the diffraction peak of the d_{001} crystal plane of rectorite exists in PCL with a mass fraction of OREC of 4 wt%, which indicates that part of rectorite is not stripped when the amount of rectorite is too large. However, when a low amount of rectorite was added, no d_{001} crystal plane was observed, indicating that the interlayer distance became infinite and rectorite was completely stripped and dispersed in PCL. At the same time, the peak width of 1%OREC to 4%OREC is significantly different. With the increase of OREC addition, the peak width of PCL/OREC XRD curve is wider, and the peak height is lower, indicating that the presence of

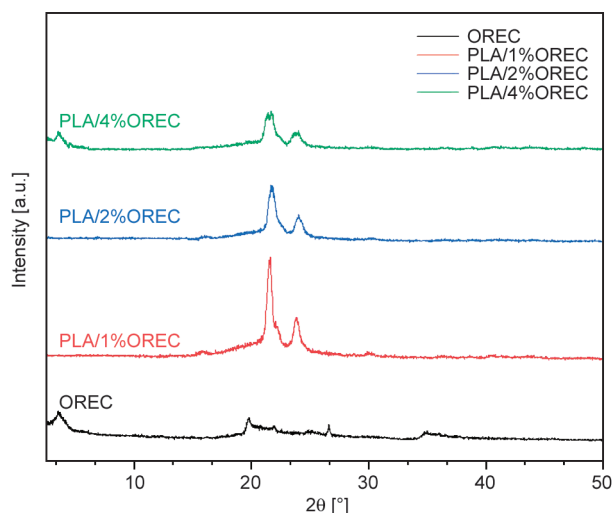


Figure 6. X-ray diffraction data of PCL with different amounts of rectorite.

OREC can reduce the crystallinity of PCL, and the crystallinity of PCL/OREC is lower with the increase of OREC addition.

Figure 7 shows SEM images of pure PCL and PCL/OREC with different OREC content, which are

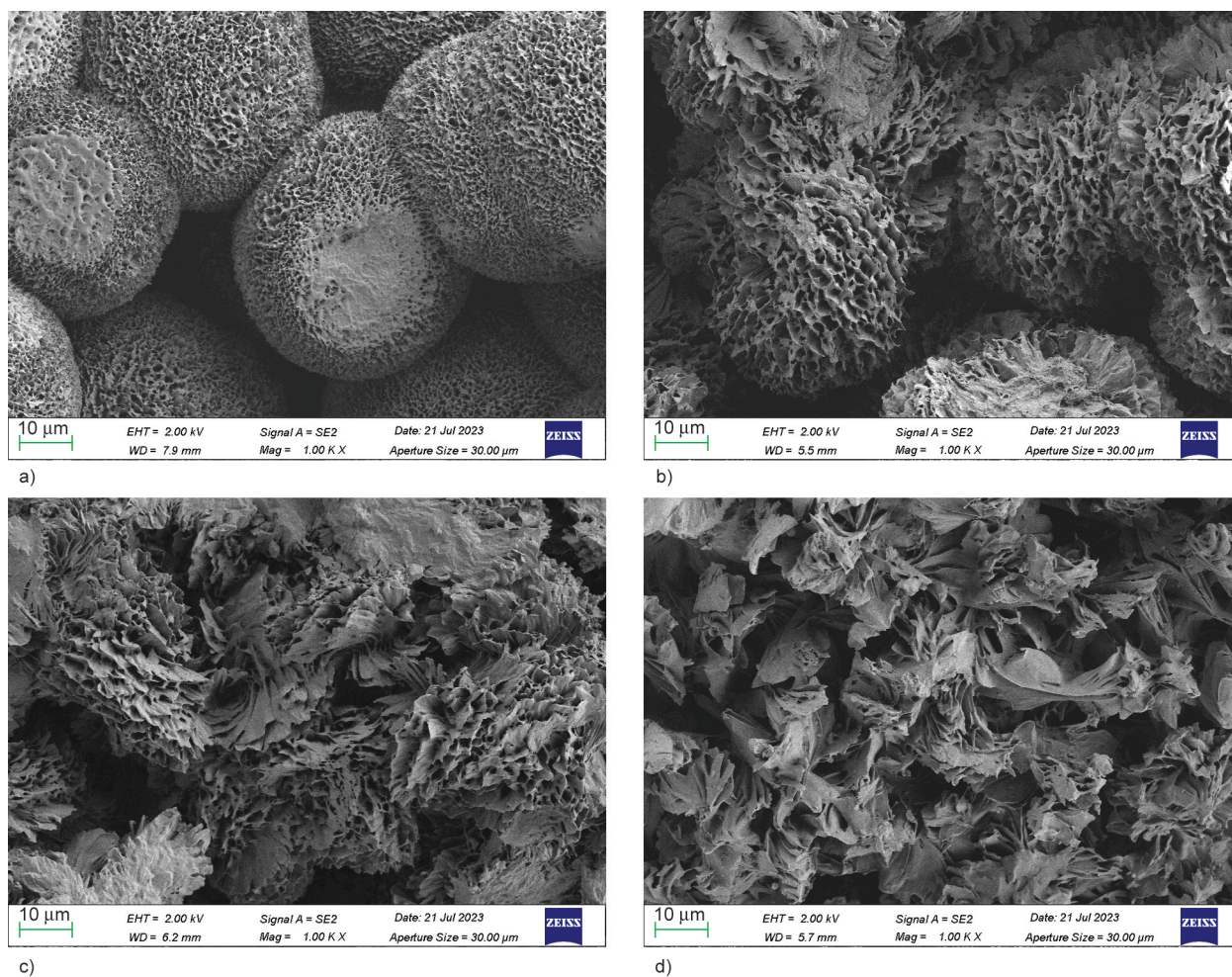


Figure 7. SEM images of a) pure PCL, b) PCL/1%OREC, c) PCL/2%OREC and d) PCL/4%OREC.

sectional images obtained by brittle fracture after liquid nitrogen cooling. As can be seen from Figure 7a, pure PCL shows a well-organized and well-grown spherulite structure, while dispersed rectorite exists in PCL/OREC, and the mobility of the chain is limited, leading to imperfect crystallization, which does not allow the growth of well-developed spherulite structure [32]. It can be seen from Figure 7b–7d that with the increase of OREC content, the spherulite structure in the crystallization process of PCL is gradually weakened, the amorphous region increases and the overall structure becomes loose. This shows that the addition of OREC can inhibit the crystallization of PCL and thus change the polymer structure. Moreover, no mineral was observed, indicating that rectorite completely dispersed in PCL. Thermogravimetric analysis (TGA) was used to study the thermal degradation behavior of nanocomposites at a heating rate of $10\text{ }^{\circ}\text{C}\cdot\text{min}^{-1}$. Figure 8 compares pure PCL with nanocomposites containing 1, 2, and 4 wt% OREC. Compared with pure PCL, the temperature at which the nanocomposite loses 50 wt% increases with the increase of rectorite content and reaches an increase of $50\text{ }^{\circ}\text{C}$ at 4 wt%. This shift to higher temperatures may be due to the barrier properties conferred by the highly anisotropic nanoparticles and the formation of carbon, resulting in reduced permeability/dispersion of oxygen and volatile degradation products through the sample. This indicates that the addition of rectorite can effectively improve the thermal stability of PCL.

Figure 9 shows the DSC curves of different samples. The melting temperature (T_m), melting enthalpy (ΔH_m), and crystallinity (χ_c) data obtained from

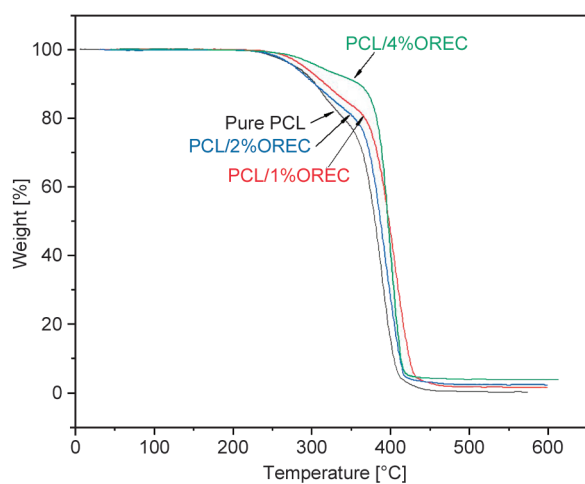


Figure 8. Thermogravimetric analysis of pure PCL and PCL with different content of OREC.

DSC curves are shown in Table 2. Crystallinity was calculated using the ratio of the heat of melting per gram of sample determined by DSC measurements to the heat of melting corresponding to 100% crystalline PCL ($156\text{ J}\cdot\text{g}^{-1}$) [33]. As shown in Table 2, compared with pure PCL, the melting temperature of PCL/OREC nanocomposite basically remains unchanged. However, the melting enthalpy of PCL/OREC decreased with the increase in OREC content, and the crystallinity decreased by 4.6% at 4% OREC. The crystallinity of the PCL/OREC nanocomposite is reduced because the stripped OREC nanoparticles in the nanocomposite limit the mobility of the PCL chain to a certain extent, thereby reducing the crystallinity of the matrix [34, 35]. This is consistent with the results of the previous XRD analysis. In polymers, ionic conduction predominantly occurs in amorphous regions through the local segmental motion [36]. The reduced crystallinity makes the polymer chain segments more flexible, which has a beneficial effect on electrical conductivity [37].

Dynamic mechanical analysis (DMA) is one of the most effective methods to investigate the molecular motion of polymers. It can describe the modulus of

Table 2. The melting temperature (T_m), melting enthalpy (ΔH_m), and crystallinity (χ_c) data of PCL and PCL with different content of OREC.

Sample	T_m [°C]	ΔH_m [J·g ⁻¹]	χ_c [%]
Pure PCL	57.6	69.8	44.7
PCL/1%OREC	57.5	67.5	43.3
PCL/2%OREC	57.7	64.6	41.4
PCL/4%OREC	57.3	62.6	40.1

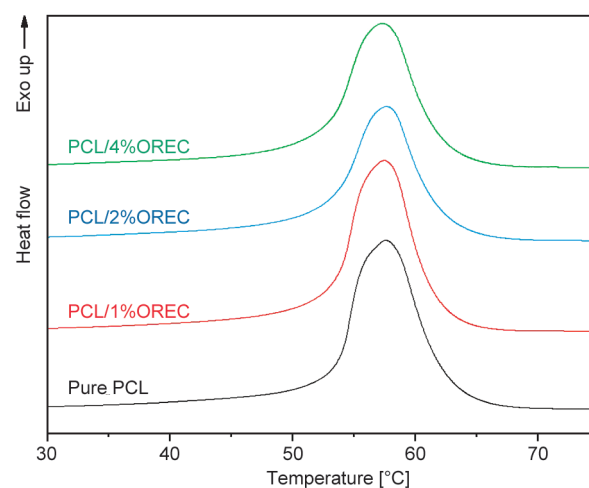


Figure 9. DSC curves of pure PCL and PCL with different content of OREC.

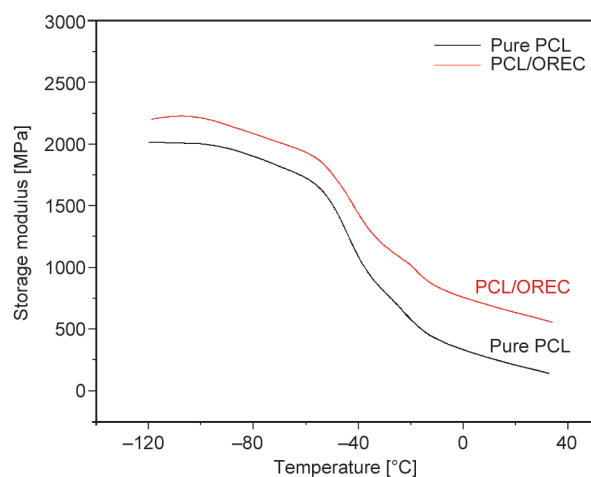


Figure 10. The curve of energy storage modulus of PCL and PCL/OREC.

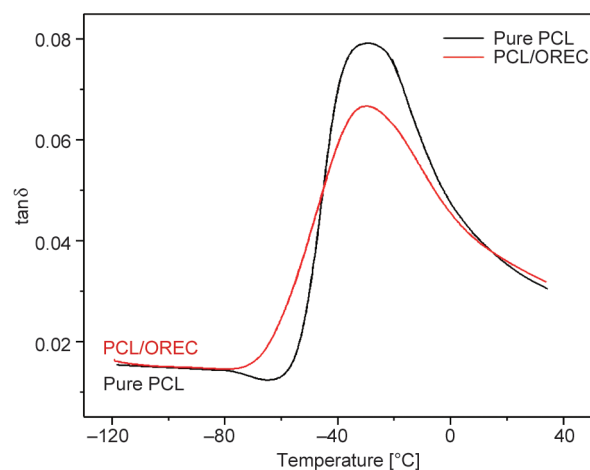


Figure 11. Relationship between temperature and $\tan \delta$ of PCL and PCL/OREC.

materials, investigate the mechanical internal friction of materials, and explore the molecular motion of various units. The relationship between material microstructure and material properties can be studied.

Figure 10 shows the variation curve of energy storage modulus of PCL and PCL/OREC with temperature. As can be seen from the figure, the energy storage modulus of PCL/OREC nanocomposite is higher than pure PCL at different temperatures. The increase in energy storage modulus is due to the uniform dispersion of nanoparticles in the matrix and the strong interaction between nanoparticles and the PCL matrix. The increase of energy storage modulus is beneficial to the practical application of PCL materials at higher temperatures.

As can be seen from Figure 11, the T_{α} value of PCL/OREC corresponds to -30.5°C , while that of pure PCL corresponds to -28.1°C . This phenomenon indicates that the addition of nanoparticles as internal plasticizers increases the distance between polymer molecular chains [38] and reduces the internal friction between polymer chains. Therefore, the degree of interaction between polymer chains decreases, and the T_{α} value decreases. In addition, compared with pure PCL materials, the maximum value of $\tan \delta$ of composites with nanoparticles is reduced, mainly because the volume effect caused by the dilution effect after filler is added has a certain effect on the reduction of loss factor. Moreover, there is a strong interaction between the nanoparticles modified by CTAB and the PCL matrix, which can reduce the peak internal friction of the composite [39]. Therefore, the addition of nanoparticles enhances the activity of molecular chains in the system,

thus improving the ionic conductivity of polymer electrolytes.

The ionic conductivity of solid electrolytes is a direct reflection of the ionic conductivity in the material. To obtain ionic conductivity, an AC impedance test is first performed to obtain electrochemical impedance spectroscopy (EIS). Solid electrolyte membrane CPEs (pure PCL and PCL/OREC) was made, and the AC impedance spectrum obtained by testing was shown in Figure 12. The results showed that PCL/OREC samples showed lower ionic resistance compared with pure PCL at temperatures greater than 30°C . The conductivity values of the samples can be calculated separately, and the results are shown in Table 3. Obviously, in the range of 40 to 60°C , the conductivity of CPEs (PCL/OREC) is improved compared with that of CPEs (pure PCL). The possible reason is that the addition of inorganic nanoparticles affects the growth pattern of PCL molecular chains, resulting in branched structures that can provide relatively short ion transport paths, reduce the crystallinity of the polymer, and improve the ionic conductivity of the electrolyte. At the same time, uniformly dispersed stripped OREC reduces the intermolecular hydrogen bond strength between the polymer network molecules and increases the proportion of amorphous domains associated with lithium-ion migration, which ultimately improves the ionic conductivity of the sample [40, 41].

The way polymer solid electrolytes transport ions is through the movement of chain segments [42, 43]. The ionic conductivity of pure PCL and PCL/OREC is not much different at room temperature because the chain structure of PCL is relatively static at low

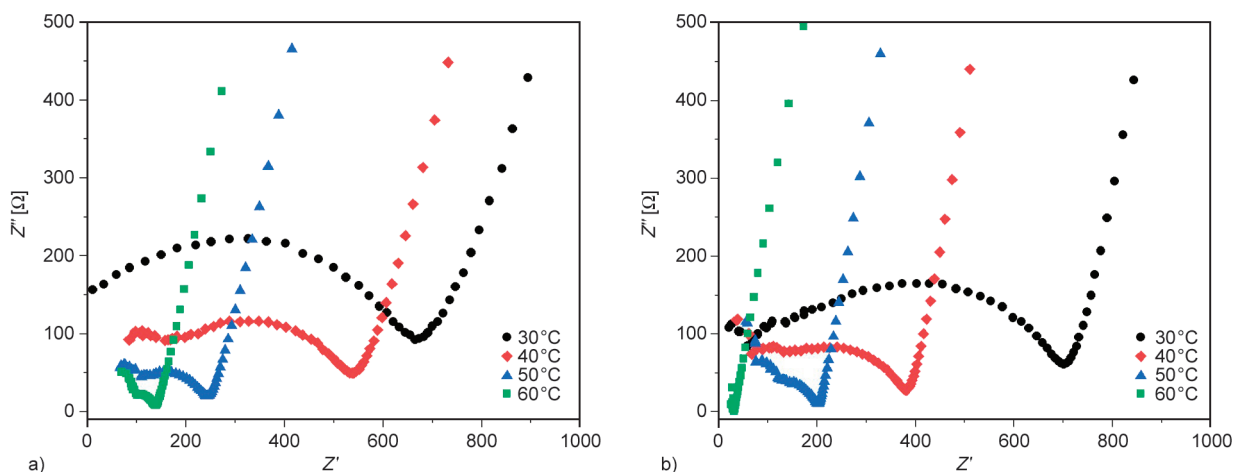


Figure 12. Nyquist plot of a) CPEs (pure PCL) and b) CPEs (PCL/OREC).

Table 3. Ionic conductivity of pure PCL and PCL/OREC at different temperatures.

Sample	Ionic conductivity [S·cm ⁻¹]			
	30°C	40°C	50°C	60°C
CPEs (pure PCL)	0.56·10 ⁻⁵	0.73·10 ⁻⁵	0.16·10 ⁻⁴	0.27·10 ⁻⁴
CPEs (PCL/OREC)	0.52·10 ⁻⁵	0.95·10 ⁻⁵	0.18·10 ⁻⁴	1.13·10 ⁻⁴

temperatures, and the activity capacity of PCL and PCL/OREC chains is similar. However, the activity of polymer nanocomposite chains is better at higher temperatures. At the same time, the operating temperature of the battery is generally higher than the normal temperature. At more than 30°C, the chain movement of PCL/OREC is better, lithium ions are easier to transmit, and the ionic conductivity is higher.

LFP//CPE//Li cells were assembled to evaluate the electrochemical performance of the prepared CPEs (PCL/OREC) in lithium solid-state batteries. The experimental temperature is 60°C, the theoretical specific capacity is set to 170 mAh·g⁻¹, and the test con-

dition of the rate charge and discharge experiment is the current density of 0.5 C. As shown in Figure 13, the discharge capacity shows an upward trend with the increase in the number of cycles, indicating that the activation process of the battery is slow. The reversible discharge capacity is maintained at 181.2 mAh·g⁻¹, and a specific discharge capacity of about 174.2 mAh·g⁻¹ was shown after 100 cycles, indicative of good capacity retention at 96.7%.

4. Conclusions

In this paper, the organic rectorite (OREC) was prepared by acid treatment and CTAB modification, and the structural changes of REC before and after modification were obtained by XRD, FTIR and SEM. The ε-CL monomer was intercalated and dispersed into the layered structure of OREC, and the PCL/OREC nanocomposites were successfully synthesized by *in situ* intercalation polymerization. The yield and molecular weight of PCL/OREC were investigated

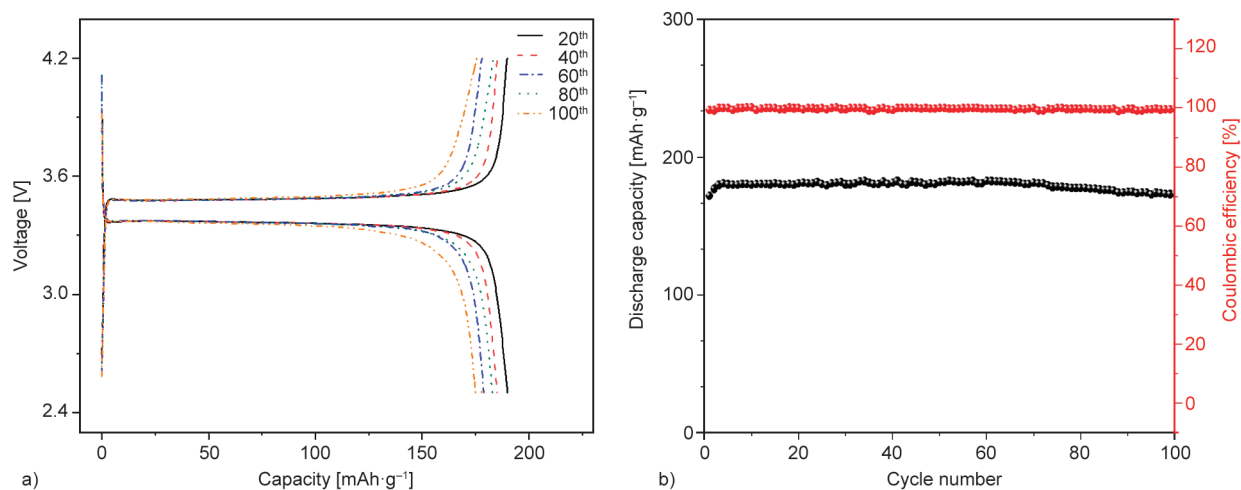


Figure 13. a) Charge and discharge profiles and b) cycle performance of CPEs (PCL/OREC) in LiFePO₄/CPEs/Li-battery.

by orthogonal experiment, and the best formula was obtained. The XRD and SEM micrographs show that OREC exists in a stripped state in PCL matrix with good dispersion. By TG and DSC tests, it was found that the addition of OREC made PCL have higher thermal stability and lower crystallinity. Moreover, through DMA analysis, PCL/OREC has higher energy storage modulus and stronger molecular chain motion ability compared with pure PCL. In addition, PCL/OREC has strong electrical conductivity at higher temperatures and exhibits enhanced cyclic stability. We expect that the synthesis of PCL/OREC nanocomposites by *in situ* intercalation polymerization not only provides a reliable method for PCL-based nanocomposites, but also provides a wider application prospect for PCL materials.

Acknowledgements

This work was financially supported by the Key Research and Development Program of Hubei (2021BAA175).

References

- [1] Vertuccio L., Gorrasi G., Sorrentino A., Vittoria V.: Nano clay reinforced PCL/starch blends obtained by high energy ball milling. *Carbohydrate Polymers*, **75**, 172–179 (2009).
<https://doi.org/10.1016/j.carbpol.2008.07.020>
- [2] Ye W., Zaheer M., Li L., Wang J., Xu H., Wang C., Deng Y.: Hyperbranched PCL/PS copolymer-based solid polymer electrolytes enable long cycle life of lithium metal batteries. *Journal of the Electrochemical Society*, **167**, 110532 (2020).
<https://doi.org/10.1149/1945-7111/aba3fd>
- [3] Woo H. J., Majid S. R., Arof A. K.: Transference number and structural analysis of proton conducting polymer electrolyte based on poly(ϵ -caprolactone). *Materials Research Innovations*, **15**, 49–54 (2013).
<https://doi.org/10.1179/143307511x13031890747697>
- [4] Fonseca C. P., Rosa D. S., Gaboardi F., Neves S.: Development of a biodegradable polymer electrolyte for rechargeable batteries. *Journal of Power Sources*, **155**, 381–384 (2006).
<https://doi.org/10.1016/j.jpowsour.2005.05.004>
- [5] Eriksson T., Mindemark J., Yue M., Brandell D.: Effects of nanoparticle addition to poly(ϵ -caprolactone) electrolytes: Crystallinity, conductivity and ambient temperature battery cycling. *Electrochimica Acta*, **300**, 489–496 (2019).
<https://doi.org/10.1016/j.electacta.2019.01.117>
- [6] Bhagabati P., Chaki T. K., Khastgir D.: Panoptically exfoliated morphology of chlorinated polyethylene (CPE)/ethylene methacrylate copolymer (EMA)/layered silicate nanocomposites by novel *in situ* covalent modification using poly(ϵ -caprolactone). *RSC Advances*, **5**, 38209–38222 (2015).
<https://doi.org/10.1039/c4ra15723k>
- [7] Wan C., Qiao X., Zhang Y., Zhang Y.: Effect of different clay treatment on morphology and mechanical properties of PVC-clay nanocomposites. *Polymer Testing*, **22**, 453–461 (2003).
[https://doi.org/10.1016/s0142-9418\(02\)00126-5](https://doi.org/10.1016/s0142-9418(02)00126-5)
- [8] Ilsouk M., Raihane M., Lahcini M., Meri R. M., Zicāns J., Cimdina L. B., Kharas G. B.: Bionanocomposites poly(ϵ -caprolactone)/organomodified Moroccan beidelite clay prepared by *in situ* ring opening polymerization: Characterizations and properties. *Journal of Macromolecular Science Part A: Pure and Applied Chemistry*, **54**, 201–210 (2017).
<https://doi.org/10.1080/10601325.2017.1282229>
- [9] Nabgui A., El Assimi T., El Meziane A., Luinstra G. A., Raihane M., Gouhier G., Thébault P., Draoui K., Lahcini M.: Synthesis and antibacterial behavior of bio-composite materials-based on poly(ϵ -caprolactone)/bentonite. *European Polymer Journal*, **156**, 110602 (2021).
<https://doi.org/10.1016/j.eurpolymj.2021.110602>
- [10] Wu T-M., Wu C-Y.: Biodegradable poly(lactic acid)/chitosan-modified montmorillonite nanocomposites: Preparation and characterization. *Polymer Degradation and Stability*, **91**, 2198–2204 (2006).
<https://doi.org/10.1016/j.polymdegradstab.2006.01.004>
- [11] Kotal M., Bhowmick A. K.: Polymer nanocomposites from modified clays: Recent advances and challenges. *Progress in Polymer Science*, **51**, 127–187 (2015).
<https://doi.org/10.1016/j.progpolymsci.2015.10.001>
- [12] Gain O., Espuche E., Pollet E., Alexandre M., Dubois P.: Gas barrier properties of poly(ϵ -caprolactone)/clay nanocomposites: Influence of the morphology and polymer/clay interactions. *Journal of Polymer Science Part B: Polymer Physics*, **43**, 205–214 (2005).
<https://doi.org/10.1002/polb.20316>
- [13] Shen Y., Yu X., Wang Y.: Facile synthesis of modified rectorite (M-REC) for effective removal of anionic dye from water. *Journal of Molecular Liquids*, **278**, 12–18 (2019).
<https://doi.org/10.1016/j.molliq.2019.01.045>
- [14] Yang H., Weijun L., Weiqing W., Qiming F., Jing L.: Synthesis of a carbon@rectorite nanocomposite adsorbent by a hydrothermal carbonization process and their application in the removal of methylene blue and neutral red from aqueous solutions. *Desalination and Water Treatment*, **57**, 13573–13585 (2015).
<https://doi.org/10.1080/19443994.2015.1074120>

- [15] Zhang H., Zhu C., Yan K., Yu J.: Effect of rectorite and its organic modification on properties of bitumen. *Journal of Materials in Civil Engineering*, **27**, C4014002 (2015).
[https://doi.org/10.1061/\(ASCE\)MT.1943-5533.0000972](https://doi.org/10.1061/(ASCE)MT.1943-5533.0000972)
- [16] Yuan L., Gu A., Liang G., Ma X., Lin C., Chen F.: Properties and structures of novel cyanate ester/organic rectorite nanocomposites. *Polymer Engineering and Science*, **52**, 2443–2453 (2012).
<https://doi.org/10.1002/pen.23198>
- [17] Wang L., Wang Y-Q., Zhang L-Q., Wu Y-P.: Rectorite powder modified by butadiene-styrene-vinyl pyridine rubber: Structure and its dispersion in styrene-butadiene rubber. *Journal of Applied Polymer Science*, **127**, 765–771 (2013).
<https://doi.org/10.1002/app.37781>
- [18] Szeluga U., Kumanek B., Trzebicka B.: Synergy in hybrid polymer/nanocarbon composites. A review. *Composites Part A: Applied Science and Manufacturing*, **73**, 204–231 (2015).
<https://doi.org/10.1016/j.compositesa.2015.02.021>
- [19] Chen H., Yang H., Xi Y.: Highly ordered and hexagonal mesoporous silica materials with large specific surface from natural rectorite mineral. *Microporous and Mesoporous Materials*, **279**, 53–60 (2019).
<https://doi.org/10.1016/j.micromeso.2018.12.014>
- [20] Du C., Yang H.: Investigation of the physicochemical aspects from natural kaolin to Al-MCM-41 mesoporous materials. *Journal of Colloid Interface Science*, **369**, 216–222 (2012).
<https://doi.org/10.1016/j.jcis.2011.12.041>
- [21] Wang W., Wang A.: Preparation, characterization and properties of superabsorbent nanocomposites based on natural guar gum and modified rectorite. *Carbohydrate Polymers*, **77**, 891–897 (2009).
<https://doi.org/10.1016/j.carbpol.2009.03.012>
- [22] Angaji M. T., Zinali A. Z., Qazvini N. T.: Study of physical, chemical and morphological alterations of smectite clay upon activation and functionalization *via* the acid treatment. *World Journal of Nano Science and Engineering*, **3**, 161–168 (2013).
<https://doi.org/10.4236/wjnse.2013.34019>
- [23] Du C., Yang H.: Simple synthesis and characterization of nanoporous materials from talc. *Clays and Clay Minerals*, **57**, 290–301 (2009).
<https://doi.org/10.1346/ccmn.2009.0570302>
- [24] Zhang R., Zheng P., Ma X.: Preparation and catalytic properties of magnetic rectorite-chitosan-Au composites. *Journal of Alloys and Compounds*, **690**, 381–389 (2017).
<https://doi.org/10.1016/j.jallcom.2016.08.131>
- [25] Huang M., Tu H., Chen J., Liu R., Liang Z., Jiang L., Shi X., Du Y., Deng H.: Chitosan-rectorite nanospheres embedded aminated polyacrylonitrile nanofibers *via* shoulder-to-shoulder electrospinning and electrospraying for enhanced heavy metal removal. *Applied Surface Science*, **437**, 294–303 (2018).
<https://doi.org/10.1016/j.apsusc.2017.12.150>
- [26] Yang H., Deng Y., Du C., Jin S.: Novel synthesis of ordered mesoporous materials Al-MCM-41 from bentonite. *Applied Clay Science*, **47**, 351–355 (2010).
<https://doi.org/10.1016/j.clay.2009.11.050>
- [27] Megherbi R., Mrah L., Marref M.: Maghnite: An innovative inorganic reinforcement used in the synthesis of polystyrene nanocomposites with optimized thermal and mechanical properties. *Iranian Polymer Journal*, **31**, 223–236 (2021).
<https://doi.org/10.1007/s13726-021-00995-w>
- [28] Sun Z., Park Y., Zheng S., Ayoko G. A., Frost R. L.: Thermal stability and hot-stage Raman spectroscopic study of Ca-montmorillonite modified with different surfactants: A comparative study. *Thermochimica Acta*, **569**, 151–160 (2013).
<https://doi.org/10.1016/j.tca.2013.07.022>
- [29] Liao L. Q., Liu L. J., Zhang C., He F., Zhuo R. X., Wan K.: Microwave-assisted ring-opening polymerization of ϵ -caprolactone. *Journal of Polymer Science Part A: Polymer Chemistry*, **40**, 1749–1755 (2002).
<https://doi.org/10.1002/pola.10256>
- [30] Lepoittevin B., Pantoustier N., Devalckenaere M., Alexandre M., Kubies D., Calberg C., Jérôme R., Dubois P.: Poly(ϵ -caprolactone)/clay nanocomposites by *in situ* intercalative polymerization catalyzed by dibutyltin dimethoxide. *Macromolecules*, **35**, 8385–8390 (2002).
<https://doi.org/10.1021/ma020300w>
- [31] Yang G., Ma R., Zhang S., Liu Z., Pei D., Jin H., Liu J., Du W.: Microwave-assisted *in situ* ring-opening polymerization of ϵ -caprolactone in the presence of modified halloysite nanotubes loaded with stannous chloride. *RSC Advances*, **12**, 1628–1637 (2022).
<https://doi.org/10.1039/d1ra07469e>
- [32] Di Maio E., Iannace S., Sorrentino L., Nicolais L.: Isothermal crystallization in PCL/clay nanocomposites investigated with thermal and rheometric methods. *Polymer*, **45**, 8893–8900 (2004).
<https://doi.org/10.1016/j.polymer.2004.10.037>
- [33] Yeh J-M., Yao C-T., Hsieh C-F., Lin L-H., Chen P-L., Wu J-C., Yang H-C., Wu C-P.: Preparation, characterization and electrochemical corrosion studies on environmentally friendly waterborne polyurethane/Na⁺-MMT clay nanocomposite coatings. *European Polymer Journal*, **44**, 3046–3056 (2008).
<https://doi.org/10.1016/j.eurpolymj.2008.05.037>
- [34] Omori S., Matsushita M., Kato F., Ohki Y.: Effect of crystallinity on electrical conduction characteristics of poly(l-lactic acid). *Japanese Journal of Applied Physics*, **46**, 3501–3503 (2007).
<https://doi.org/10.1143/jjap.46.3501>
- [35] Deng X., Liu F., Luo Y., Chen Y., Jia D.: Preparation, characterization and application of polymeric diols with comb-branched structure and their nanocomposites containing montmorillonites. *European Polymer Journal*, **43**, 704–714 (2007).
<https://doi.org/10.1016/j.eurpolymj.2006.12.003>

- [36] Li Z., Fu J., Zhou X., Gui S., Wei L., Yang H., Li H., Guo X.: Ionic conduction in polymer-based solid electrolytes. *Advanced Science*, **10**, 2201718 (2023).
<https://doi.org/10.1002/advs.202201718>
- [37] Zhou Y-K., He B-L., Zhou W-J., Huang J., Li X-H., Wu B., Li H-L.: Electrochemical capacitance of well-coated single-walled carbon nanotube with polyaniline composites. *Electrochimica Acta*, **49**, 257–262 (2004).
<https://doi.org/10.1016/j.electacta.2003.08.007>
- [38] Pagacz J., Pielichowski K.: PVC/MMT nanocomposites. *Journal of Thermal Analysis and Calorimetry*, **111**, 1571–1575 (2012).
<https://doi.org/10.1007/s10973-012-2484-2>
- [39] Zhang R., He X., Lai Z., Yang D.: Effect of some inorganic particles on the softening dispersion of the dynamics of butyl rubber. *Polymer Bulletin*, **74**, 1031–1043 (2016).
<https://doi.org/10.1007/s00289-016-1761-9>
- [40] Yeh J-M., Kuo T-H., Huang H-J., Chang K-C., Chang M-Y., Yang J-C.: Preparation and characterization of poly(o-methoxyaniline)/Na⁺-MMT clay nanocomposite via emulsion polymerization: Electrochemical studies of corrosion protection. *European Polymer Journal*, **43**, 1624–1634 (2007).
<https://doi.org/10.1016/j.eurpolymj.2007.01.040>
- [41] Wang J., Yu X., Wang C., Xiang K., Deng M., Yin H.: PAMPS/MMT composite hydrogel electrolyte for solid-state supercapacitors. *Journal of Alloys and Compounds*, **709**, 596–601 (2017).
<https://doi.org/10.1016/j.jallcom.2017.03.157>
- [42] Lu Y., Li L., Zhang Q., Niu Z., Chen J.: Electrolyte and interface engineering for solid-state sodium batteries. *Joule*, **2**, 1747–1770 (2018).
<https://doi.org/10.1016/j.joule.2018.07.028>
- [43] Chen R., Qu W., Guo X., Li L., Wu F.: The pursuit of solid-state electrolytes for lithium batteries: From comprehensive insight to emerging horizons. *Materials Horizons*, **3**, 487–516 (2016).
<https://doi.org/10.1039/c6mh00218h>

Research article

How introduction of deposit-refund system (DRS) changes recycling of non-drinking bottle PET wastes

Janka Bobek-Nagy¹, Róbert Kurdi¹, András Kovács², Lilla Simon-Stöger¹,
Márton Szigeti³, Csilla Varga^{1*}

¹Sustainability Solutions Research Lab, University of Pannonia, 10 Egyetem str., 8200 Veszprém, Hungary

²Department of Materials Engineering, University of Pannonia, 10 Egyetem str., 8200 Veszprém, Hungary

³Research Group of Corrosion, University of Pannonia, 10 Egyetem str., 8200 Veszprém, Hungary

Received 10 June 2023; accepted in revised form 15 August 2023

Abstract. Under the era of circular economy, the deposit-refund system (DRS) for *e.g.* polyethylene terephthalate (PET) is thought to be a good choice to achieve a more structured plastic recycling. The present research has the aim to make a comprehensive description and a practical guideline in order to evaluate how collection and separation system influence the quality and efficiency of mechanical recycling of PET. The DRS has been symbolized by manually collected bottles with (BCL) and without (B) caps and labels. Samples have been given from the selective income (SI) and the sorting residue (SR) of a manual selective waste sorting plant and PET fraction of refuse derived fuel (RDF). Based on preliminary qualification results such as melt flow indices (MFI), PET bottles are worth selecting into the main colours like water clear, blue, and all the others together, referred to as PET-A, PET-B, and PET-D fractions of the sorting plant. The SR seemed to be a beneficial raw material for PET recycling as both mechanical and rheological properties were proper enough. PET separated from the Mechanical Biological Treatment (MBT) plant as RDF showed the worst processing and mechanical properties, but both can be improved with deeper precleaning. X-ray tomography (CT) scans have shown a correlation between the source of waste and the gas void structure which influence the macroscopic mechanical properties.

Keywords: recycling, mechanical properties, rheology, computed tomography, deposit-refund system

1. Introduction

1.1. Regulation of waste management in Hungary

Among environmentally harmful wastes plastic is one of the most challenging ones on a world scale [1–7]. Packaging dominates the usage of plastics accounting for nearly 40% of plastic consumption [8–10]. The European Union (EU) continuously makes huge efforts both to reduce the amount of plastic packaging waste and to recycle post-consumer waste. One of the acts was the legislative framework to control plastic packaging waste. The latest big step of the European Commission toward a circular economy was acceptance of the Plastic Strategy in

2018 [11]. Along with the European Union Action Plan for the circular economy which allocates the entire action plan of increasing the quality of plastics recycling the ‘Plastics Waste’ EU strategy forces to make all plastic packaging recyclable by 2030 [11, 12]. For achieving goals of the European Union Action Plan for a circular economy appropriate institutions, systems, and incentives appear to be crucial in order to define and build a holistic approach to increase the quality of plastics recycling [11, 13, 14]. Additionally, secondary raw materials were stated by the European Green Deal to be mandatory for the market from 2019 [15]. According to the Single-Use Plastic (SUP) directive, polyethylene terephthalate

*Corresponding author, e-mail: varga.csilla@mk.uni-pannon.hu

© BME-PT

(PET) drinking bottles will be demanded 25% recycled plastic from 2025 and 30% from 2030 [16]. The European Union boosts all the countries to create and introduce innovative models for plastic production and consumption to achieve circularity in a shorter time frame. The deposit-refund system (DRS) for wastes such as plastics and glass is only one of the models. Furthermore, the European Parliament is encouraged to establish the national DRS schemes destined for the unionization of models under EU law for the EU single market [17]. Hungary as a member of the EU harmonized the waste regulation in the country. The Hungarian Parliament accepted the amendment of the Waste Law [18] which contributed to the domestic introduction of the DRS in the next years. In accordance with the aforementioned the National Waste Management System is currently under major reconstruction with respect to fit requirements for a more sustainable circular economy [19]. In Hungary, the DRS system is going to be extended for PET drinking bottles either besides aluminium beverage can and glass bottles. In the return system planned in Hungary, the disposed drinking water and beverage bottles are collected in commercial units as cleanly as possible. It is important to note, that the DRS is destined for the compilation of drinking bottles, meanwhile, other PET products than bottles such as detergent, soap, and rinsing flasks among others will remain in the selective waste or regrettably in the municipal solid waste [20].

1.2. Waste management in the North-Balaton region

Waste management in Hungary is under a huge transformation as MOL Plc. won the Hungarian state concession tender for municipal waste management services. The concession agreement is for 35 years with a commencement date of July 1, 2023. The North-Balaton Waste Management Nonprofit Ltd. (NBWN Ltd., in Hungarian: Észak-Balaton Hulladékgazdálkodási Nonprofit Kft.) is one of the 28 Hungarian regional waste management public service companies. NBWN Ltd. is responsible for waste management in more than 158 settlements in Veszprém country consisting of more than 126 000 households. NBWN Ltd. contributes to six other waste management public services accounting for local waste collection, separation, and temporary storage. Avar Ajka Nonprofit Ltd. is in charge of waste management in 48 towns and villages. The enterprise is

competent in collecting household waste from more than 20 000 sources and as a public service collects both the selectively disposed household wastes and the selective waste yards on the streets. Households are required to collect only the packaging wastes such as paper, cardboard, plastic, and metal in a ‘yellow or blue’ bin. The glass packaging wastes are compiled in containers for glasses on the streets. Avar Ajka Ltd. operates a manual sorting site in Ajka with a capacity of 7630 tonnes/year for packaging wastes such as plastic, paper, cardboard, glass, metal and also the mix of them. The incoming waste is weighed and then placed into the manual sorting conveyor and separated in the 12-position manual sorting line (Figure 1).

The recyclable fractions are paper and cardboard, aluminium, PET, high-density polyethylene (HDPE) and polypropylene (PP), foil furthermore magnetizable metals. PET wastes are separated into three fractions, namely coloured PET as PET-D, water clear PET as PET-A, and bluish PET as PET-B. The sorted PETs are only drinking bottles, other PET wastes are ended in sorting residue. The highest quantity in weight in the income household selective waste is paper, cardboard, newspaper fraction (34%), 20% is glass waste, 8% is PET (all types), 6% is foil and 26% is sorting residue. The other sorted fractions count at most 3%. Values were calculated for the 2021 base year, however, the last five years gave the same rates [21].

Sorting residues are grouped and transported to another resides of the NBWN Ltd. into Királyszentistván. In Királyszentistván a waste separation plant with 120 000 tonnes/year household solid waste capacity is working to enrich the wastes energetically utilizable, for instance, refuse derived fuel (RDF). Mechanical biological treatment (MBT) is carried out on the non-hazardous waste inside the plant. The first step of the mechanical processing is the weighing and shredding of the waste into 250–350 mm particle size. Afterwards, the magnetizable metals are separated. The next step is a rotary sieve wherein the biological waste under 80 mm particle size is removed for further treatment. Residue over 80 mm is usually divided into two parts by an air-separation unit. The heavy fraction containing mostly stones and bricks goes to the landfill directly. The light and middle fractions are driven into an eddy current sorter to recover the aluminium wastes. The next process polyvinyl chloride (PVC) removal from the light and medium PET

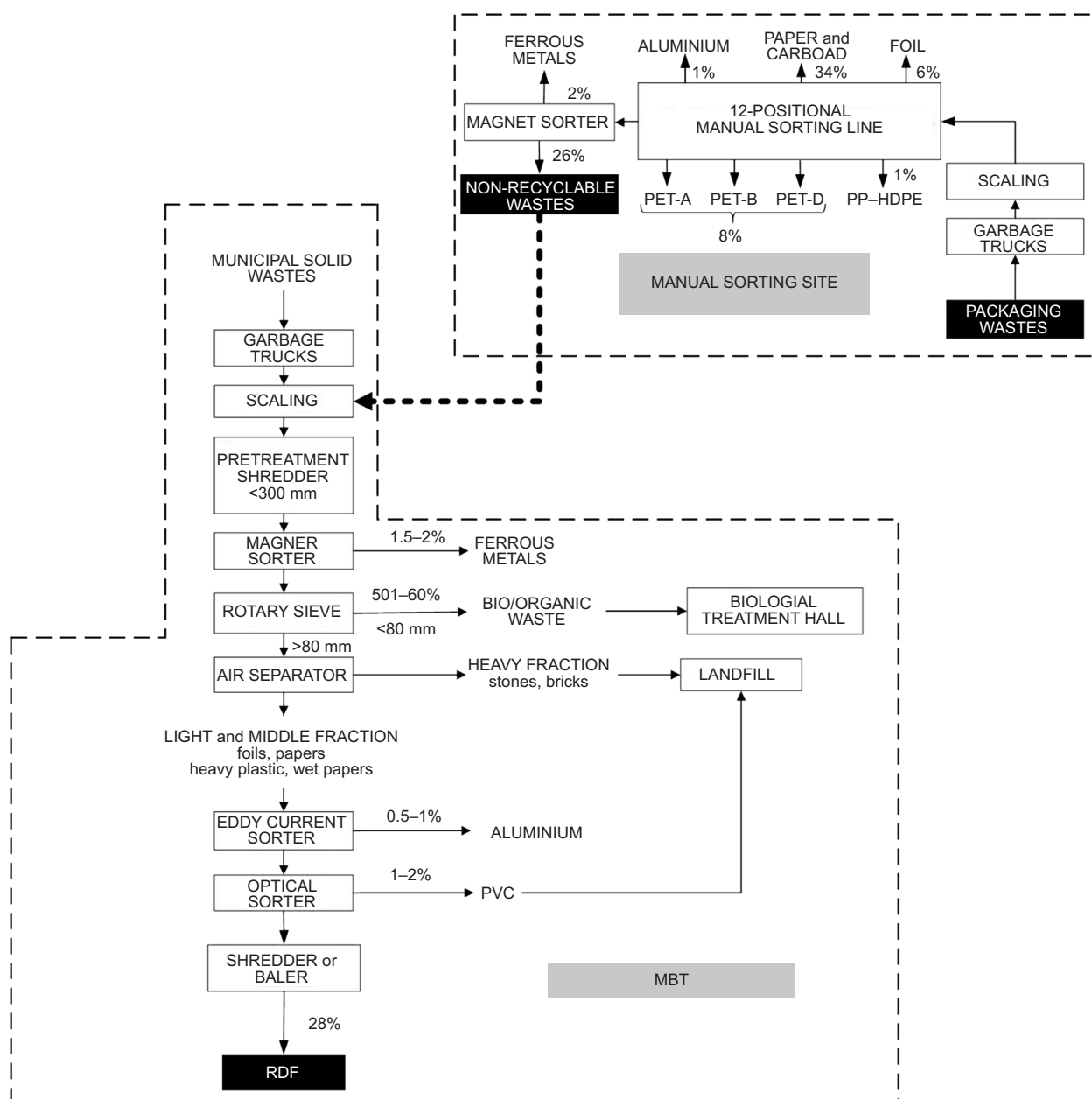


Figure 1. The waste streams through the manual sorting site (Ajka) and MBT plant (Királyszentistván), the source of PET samples for the research was highlighted in black.

fractions remained by an optical sorting machine. The sorted PVC is deposited into the landfill either. The halogen-free residue for RDF is balled or shredded and balled. 92% of the total plant income is directed to the MBT site whereby 77% of it is going through the separation line. In the end, 28% of RDF is generated from the separated household waste. Values were also calculated for the 2021 base year, however, the last five years gave the same rates either [21].

1.3. PET recycling from different waste sources

The composition of plastic mixtures originated from an open-loop recycling process as described

in Figure 1 could be rather complex; therefore, chemical incompatibility and inhomogeneity of various plastics had to be taken into account. The drawbacks of recycling of the plastic mixtures can be successfully managed by the proper separation as one of the crucial steps in plastic recycling. Moreover, secondary raw materials gain higher economic values when the concentration of contaminants, e.g. other types of plastics, are kept at lower levels [22]. However, contaminants are not the only cause for the reduction in the properties of the recycled plastic product resulting in lower economic values. The other crucial step is the reprocessing. It is well-known, that reprocessing of plastic waste with various types of

equipment of melt processing techniques such as extrusion and injection moulding can lead to the deterioration of product properties because of molecular weight reduction and degradation effects [23]. PET has become one of the most popular packaging materials and the main problem is the large volume of waste produced within an extremely short time. Huge efforts have already been made towards recycling PET, especially recycling into higher value-added products since landfilling is not an option for disposal anymore [24]. Melt extrusion is one of the general processes for the mechanical recycling of plastics resulting in PET pellets without significant changes in the chemical structure of the polymer chain. Within the EU, PET bottles are recycled by over 50%, becoming the most recyclable product up-to-date [7]. PET-based products other than bottles, such as films and fibres, do not achieve such high recycling rates as PET bottles. Most of them end in the RDF fraction of waste which is the most difficult to recycle into higher value-added products. Because important mechanical properties usually reduce due to degradation during reprocessing designation mechanical recycling of PET as down-cycling often occurs [25]. PET upcycling applications started with Coca-Cola to reuse beverage bottles [26]. The recycling industry started with mechanical PET transformation into value-added products such as clothes. Different end products such as containers, films, nonwoven fabrics, and other plastics can also be produced from waste PET [26]. Plenty of researchers applied PET waste as a replacement for aggregate in cement concrete as a reinforcement in the form of fibers or even as raw material for the production of activated carbon [24, 26]. Numerous publications describe opportunities for the synthesis of polyester resin on a PET waste basis either [24]. There is increased interest in the application of recycled plastic materials in pavement and PET was a widely used candidate in many studies as a partial replacement for the aggregate [27–33]. For example, the highest resistance to permanent deformation was obtained by using 20% of PET as a partial replacement moreover, PET as a modifier improved fatigue life either [30, 34]. Contaminants in PET waste cause serious problems, e.g. PVC decomposes and hydrochloric acid gas releases resulting in the colour-changing and degradation of molecules. Energy consumption and costs are saved through recycling if plastics are reprocessed without separation from other materials

or cleaning steps can be minimized [22, 24]. Alswaleem and Alrefaie [23] investigated only the influence of paper contaminants on the mechanical properties and processability of post-consumer PET. One of their most important results was that the toughness of reprocessed post-consumer PET bottles drastically decreased in the presence of paper. The other important result was that the presence of PE as caps or cap rings and labels did not seem to alter its moldability and mechanical properties. Researchers also paid attention to minimizing the number of melt processing steps of reprocessing post-consumer PET in order to avoid deterioration of its mechanical properties [23].

Since choices of consumers can either support or hinder the circularity of plastic reuse, our study basically aims to present the values of PET waste since its most important properties are good enough for higher value-added products, moreover, the research concentrates on wastes of PET products other than bottles either aimed to fill a research gap. Real PET is not a model PET raw material for demonstrating the waste origin, but such a PET waste stream, that comes from everyday life from humans as waste either selectively collected or not. The study focused on processing opportunities and mechanical properties of different real PET wastes containing polyolefins as contaminants. Experiments were carried out with waste PETs derived from the selective collection and different stages of the separation line of plastic sorting plants. Although the material structural analysis used to be applied to determine the properties of composites or structured materials [35], in the case of waste materials the effects of contamination (e.g. organic residues), as well as the preparation processes (e.g. melt currents, viscosity, pressure condition, temperature), can be followed exactly by X-ray tomography which is a novel and untraditional analysis technique in the field of polymer recycling researches.

2. Experiments

2.1. Raw materials

The ‘selective income’ sample (SI) was a typical ‘yellow/blue bin’ waste which is originated from the input of the Avar Ajka Ltd. plant (Ajka, Hungary). The second sample was the ‘sorting residue’ of the manual sorting plant of Avar Ajka Ltd. signed as SR (Ajka, Hungary). That kind of residue is transported to the waste plant of Királyszentistván. The third

sample was derived from the RDF waste supplied by the sorting plant of Királyszentistván (Hungary). The waste samples were sorted for PET by an optical sorting machine (Black UNISORT P1000 R, Steinert GmbH, Cologne, Germany). The optical sorting machine is working in the near-infrared wavenumber range ($1000\text{--}1700\text{ cm}^{-1}$). The machine is unique because its spectrum library is editable with spectra of new or unknown materials of the software either. The equipment is also able to separate the black materials because the separation of the matters is achieved beyond the conveyor. The sensor unit is arranged above the conveyor and the beam source that lights the conveying material stream is also built into that module. The emitted beam is infrared light and the reflected light by the materials is absorbed and measured by the camera system. The PC processes and evaluates the measured spectra and the results are directed to the controller unit. At the end of the belt, 80 pieces of pneumatic nozzles are positioned responsible for the separation of the detected objects. The composition of real waste samples for the experiments was identified by the near infrared (NIR) apparatus first. The investigated input sample (SI) of the manual sorting plant consisted of paper and

cardboard (22%), glass (11%), and other plastics mainly PP, low-density polyethylene (LDPE), HDPE, polystyrene (PS) (44%), and PET waste (23%). In that sample, the PET wastes were typically drinking bottles. In the sorting residue sample (SR) the initial content was 10% metal, 69% other plastic waste and the PET was 21% wherein the bottles of washing and shower gels were significant. In the RDF fraction 20% was waste glass, 21% resulted in PET and 59% was other plastics. After optical sorting, the SI and SR samples contained 10% impurity which is mostly HDPE as bottle cap and PP label of the bottle.

In the RDF sample, the label appears as contamination nearby the HDPE bottle cap and PP bottle label (Figure 2). As a raw material for experiments two other waste PET samples were sorted by hand from the selective collection of only PET drinking bottles symbolizing the bottles from DRS to be introduced. One sample 'B' (Veszprém, Hungary) was just the PET bottle without any cap or label. The second one 'BCL' (Veszprém, Hungary) was the whole PET bottle with label and cap.

After separation, PET samples were shredded in a shredder (GRS 183A9, DIPRE, San Giorgio delle Pertiche, Italy) and classified by a sieve with a



Figure 2. NIR separated and shredded PET samples from real waste a) SI, b) shredded SI, c) SR, d) shredded SR, e) RDF, f) shredded RDF (SI – selective income; SR – sorting residue; RDF – refuse derived fuel).

diameter of 5 mm (Figure 2). The shredded samples were soaked for a day in tap water. The process was carried out two times. The shredded samples were dried at 60 °C for 16 hours before filament extrusion, the moisture content was below 0.02 wt% for all samples after the procedure.

2.2. Methods

PET samples were prepared in a twin screw laboratory extruder (LabTech LTE 20-44, LabTech Engineering Ltd., Samutprakarn, Thailand). The screw speed was 100 rpm for each sample, and the temperature profile varied between 245 and 265 °C depending on the origin of the waste. Tensile properties were measured under laboratory conditions at room temperature and at 48% of relative humidity with an universal tensile testing machine (INSTRON 5967, Instron, Norwood, Massachusetts, USA) with a cross-head speed of 90 mm/min. The extruded filament samples were conditioned at 60 and at 105 °C for 4 hours before measurements. Filaments with dimensions of 2 mm averaged diameter and 150 mm averaged length were prepared for mechanical tests. Tensile strength and elongation at break results were taken from the average of a minimum of 11 parallel measurements. Rheological properties of the pre-conditioned granulated filaments were measured with a capillary rheometer (CEAST Smart Rheo 2000, CCSi, Inc., Akron, Ohio, USA) at 255 °C after three minutes of preheating time and shear rate below 10 000 1/s. Five PET waste-based extruded samples were scanned at a resolution of approximately 6 µm using CT scanner (Nikon XT H 225 ST, Nikon Metrology, Leuven, Belgium). The average time per scan was 21 min and 1250 projections images were captured in two frames per projection mode. The samples were scanned a voltage of 165 kV and a current of 65 µA. For the analysis and visualization, the VG Studio Max 2022/2 software pack was applied. These measurement settings were able to show the microporosity as well as the inclusion content of the extruded rods, which gives useful information about the inner structure of the scanned bodies.

All DSC measurements were done on a reaction calorimeter (C80 D, Setaram, Mougins, France). The PET waste samples were weighted on a Mettler Toledo analytical scale (ML204 NewClassic, Columbus, Ohio, USA) and was put into an aluminium foil sample holder (weight differences between the sample and reference holders were

±5.0 mg). A standard stainless-steel cell was used for the measurements without PTFE joints. The sample was first pre-heated to 30 °C using 0.1 °C/min heating rate and was held at that temperature for 2.0 hours. The analysis was done using 0.8 °C/min heating rate from 30 to 300 °C. The observed reproducibility was within 0.5 °C of the specified parameters throughout the measurements. DSC results were taken from the average of three parallel measurements. The results were analysed using the Calisto software (version 1.076).

3. Results and discussion

3.1. Raw material characterization

All the colours of PET bottles from the selective collection at the Department were separately collected for at least a two-year period then ground and different batches were identified with melt flow index (MFI) (Figure 3) values. An MFI tester (CEAST 7024000, CCSi, Inc., Akron, Ohio, USA) was used to determine melt flow indices of the PET samples at 255 °C under a load of 2.16 kg. Waste PET bottles had MFI values between 12 g/10 min and 20 g/10 min dependent on the colour of the bottle (Figure 3e). MFI of batches of water clear (Figure 3a) and green colours (Figure 3b) were close to the average values but occasionally with high standard deviation (SD). MFI of the blue PET bottles was the most unbalanced (Figure 3c). Collecting waste PET bottles in mixed form without any separation based on colours resulted in MFI within a wide range of average values and extremely high standard deviations (Figure 3d).

In accordance with the confidence of MFI values and the colour of PET, the separation of drinking bottles by colour is beneficial from the aspect of recycling. In further experiments, DRS was symbolized by blue colour bottles based on the MFI values that were all the same as of mixed colour bottles.

Shredded samples originated from hand selection and collection systems showed similar behaviour toward parameter change with the purity. Furthermore, because of the corresponding signals became less intensive certain thermal properties could not be identified to an exact point by differential scanning calorimetry (DSC) (Figure 4, Table 1). Glass transition temperature (T_g) of the RDF sample elevated by 12.5 °C compared to the SI. Similarly, for the hand selected samples the T_g increased by 5.4 °C for the BCL sample compared to the B sample. Based on

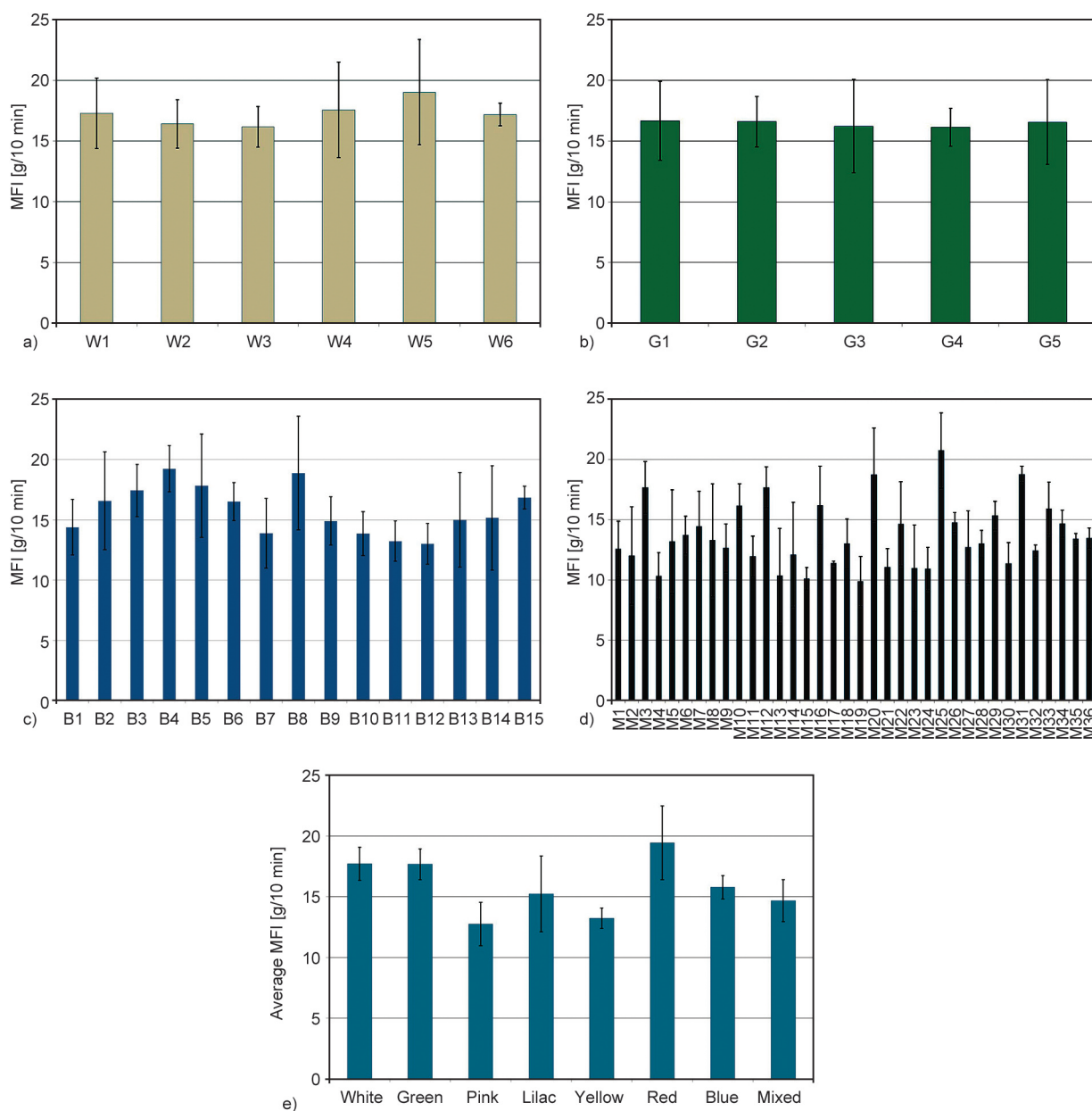


Figure 3. MFI values of waste PETs selected by the colour of the bottles a) water clear (W), b) green (G), c) blue (B), d) mixed (M), e) averaged.

the level of impurities, minor endothermic peaks and an elongated exothermic baseline shifts were observed between 134.9 to 239.6 °C indicating the melting and different phase transitions of the polyolefin content. Both the cold crystallization (T_{cc}) and

the melting temperature (T_m) decreased by a small extent within 3.0 °C overall depending on the level of impurity. However, no T_{cc} value appeared in the RDF sample indicating that the impurities mask the phase transition.

Table 1. Main data from the DSC analysis.

Sample	(1) – T_g [°C]	(2) – T_{cc} [°C]	(5) – T_t [°C]
SI	74.9	115.5	256.9
SR	85.5	113.9	256.0
RDF	87.4	N/A*	253.8
B	70.9	117.1	260.3
BCL	76.3	116.3	258.1

*Phase transition masked by impurities

3.2. Melt flow index of the waste PETs

MFI values of waste PET from the different origins at 255 °C and under the load of 2.16 kg were represented in Figure 5. Wastes were identified as ground material. Waste PET from the selective collection of mixed bottles had the lowest MFI (15 g/10 min), indicating the highest molecular weight among the waste PETs. Both selective income (SI) and sorting

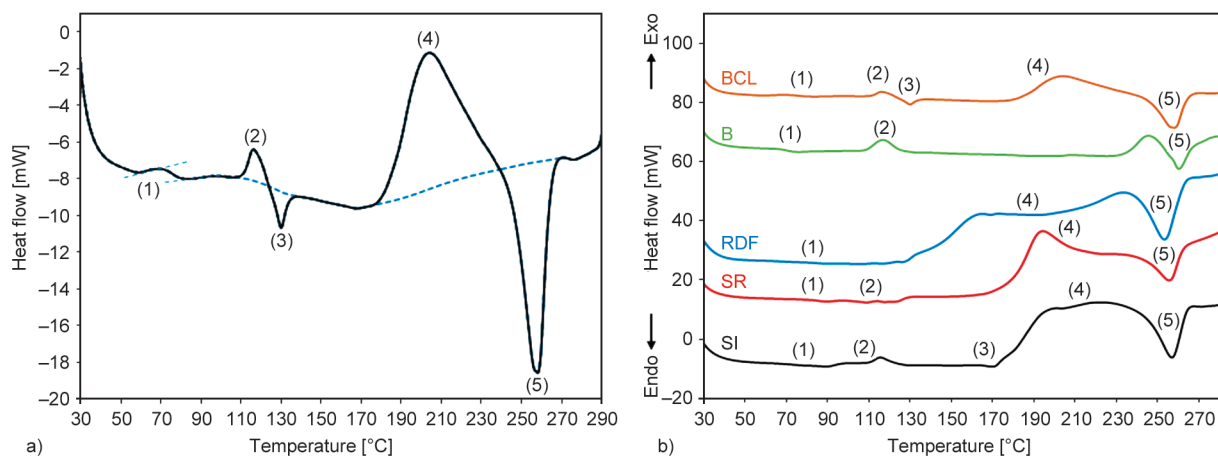


Figure 4. The DSC analysis and evaluation (BCL (a)) of the shredded PET waste samples (b). (1): T_g – glass transition; (2): T_{cc} – cold crystallization; (3): T_{endo} – endotherm peak, polyolefin component melting; (4) T_{exo} – exothermic peak, polyolefin component phase transition and (5): T_m – melting. (SI – selective income; SR – sorting residue; RDF – refuse derived fuel; B – bottle; BCL – bottle with cap and label).

residue (SR) were the same and had higher (~30 g/10 min) MFI than that of only PET bottles. MFI of SI and SR were 50% higher than waste PET bottles ground with the caps and labels (~20 g/10 min) together, demonstrating that the polyolefin content of those real waste PETs shifted the MFI advantageously to the same direction and extent. Waste PET sorted from the RDF had outstandingly high MFI (~50 g/10 min) also with extremely high standard deviation (~10 g/10 min), as expected. A wide quality range of waste PET was supposed to be the consequences of degradation effects during the lifetime via the lower molecular weight of the molecules.

All kinds of waste PET were reprocessed by extrusion moulding and qualified first with MFI. Results were summarized in Figure 5. No significant differences (2–5 g/10 min) between MFIs of the ground and regranulated materials appeared, providing that extrusion parameters were set advantageously. Reprocessing made sense, at least in a narrower range of SD for the MFI. Therefore, regranulated wastes generally were more homogeneous than the only ground materials. Furthermore, SD was at least the same (~2 g/10 min) for regranulates from the SI and SR as for BCL. The average MFI (~30 g/10 min) of regranulated PET from SI and SR were the same, but 60% higher than the only PET sorted from bottles without cap and label. Therefore, the molecular weight of the PET materials from the selective collection containing not only drinking bottles (SI) was thought to be lower than that of only PET drinking

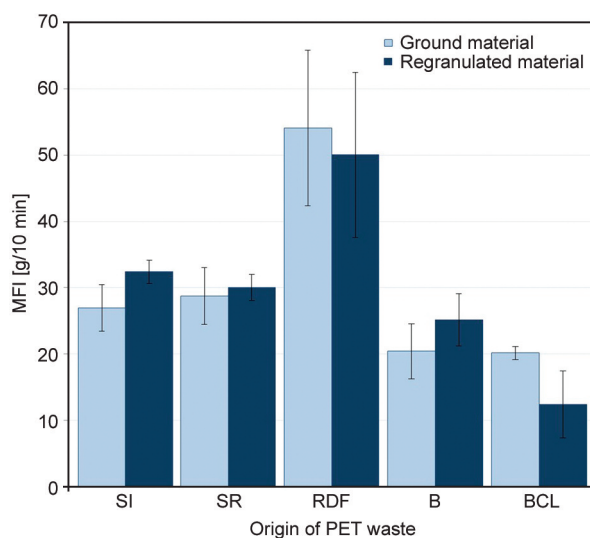


Figure 5. MFI values of PET wastes from different sources and with different pretreatment. (SI – selective income; SR – sorting residue; RDF – refuse derived fuel; B – bottle; BCL – bottle with cap and label).

bottles. MFI of PET sorted from RDF was doubled probably because of the drastic deterioration of molecular weight as PET in RDF was degraded to a much higher extent and its quality changed in a wide range.

MFIs of regranulated SI and SR are not the same as regranulated waste PET bottles ground with the caps and labels together indicating that the polyolefin content of those real waste PETs shifted the MFI in the opposite direction. The reason behind the phenomenon was that the polyolefin content of SI and SR came not only from the caps and labels of drinking

bottles, but PET residues were also other than only bottles. Just as a short conclusion of MFI results, it was stated that PET A/B/D fractions are worth selecting because of their higher values as secondary raw materials since PET wastes (SI and SR) had much higher MFI, therefore lower molecular weight values. The wide range of MFI of real PET waste makes both the reprocessing and the quality control more difficult. Caps and labels beside the PET did not cause such significant deterioration that might be difficult to manage during reprocessing. Alsewilem and Alrefaie arrived at the same statements [23].

3.3. Results of capillary rheological measurements of the waste PETs

During the investigation of reprocessing conditions of waste PETs from different origins, capillary rheological measurements were carried out at the same temperature and in the same shear rate range in order to make a correct comparison of the results. Viscosity curves (Figure 6) were identified in the typical shear rate range not only for extrusion moulding but also for injection moulding. Viscosity curves of waste PETs showed the same trends in the whole shear rate range investigated. SI and SR samples had not only the same trend of viscosity but also the same values. The lowest viscosities were given by the waste PET derived from RDF in sync with the high MFI values aforementioned. Differences in the viscosities among the waste PETs disappeared in the shear rate range of injection moulding; therefore, processing parameters during injection moulding could be rather independent of the origin of waste PET.

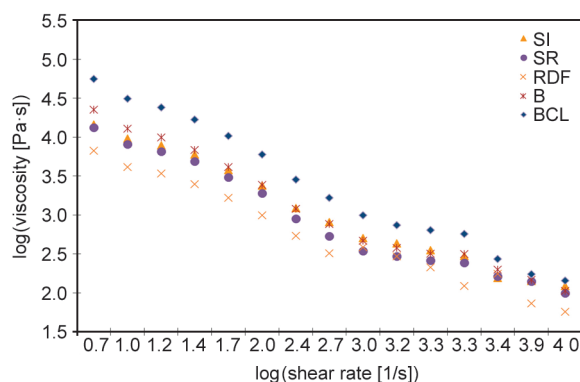


Figure 6. Viscosity of extruded PET wastes from different sources.

(SI – selective income; SR – sorting residue; RDF – refuse derived fuel; B – bottle; BCL – bottle with cap and label).

Viscosities of waste PETs (Figure 6) were the same in the region for injection moulding except the one sorted from RDF. The former phenomenon was believed to be a sign of the same processing parameters for waste PET regranulates (SI, SR and B) by injection moulding. Regranulate of PET bottles represented exactly the same viscosity curve as the SI and SR regranulates. PET bottles are worth sorting as selectively collected PET bottles with cap and label (BCL) had higher viscosities than the other PET waste streams in the shear rate region of extrusion moulding, forecasting also better mechanical properties of the extruded filaments. Reprocessing of waste PET materials caused an average viscosity increase of 5–7%, which can be partially drawn back to the measurement standard deviation.

3.4. Assessment of mechanical properties of the recycled PETs

Not only determination of the advantageous processing parameters is essential in plastic recycling for achieving a seemingly homogeneous sample, but also the level of mechanical properties. The tensile test is one of the most informative and fast measurements to identify the possible application fields. In our research, pellets originated from different qualities of PET waste were extrusion moulded, and tensile test of the extruded filaments was carried out. Since tensile properties of filaments conditioned at both 60 and 105 °C were measured, information was collected about samples conditioned at both below and above temperature of glass transition of the PET. Samples conditioned at 105 °C were expected to be brittle [36]. Specimens were broken almost promptly after tensile stress, reflected by only a few percent but no more than 7% for the elongation at break (Figure 7a). The highest value of elongation at break (EB) was measured for the sample from selectively collected PET waste and it was stated that the more contaminated the PET waste was the lower the elongation at break became regardless of the pre-conditioning parameters. No relevant difference was found between SI and SR, but an outstandingly brittle sample was obtained by processing PET originated from RDF. The latter is revealed by elongation at break being only 1–2%. Even the EB of the same sample conditioned at 60 °C was only 2%. Elongation at break of the samples conditioned at 60 °C was higher compared to the samples conditioned at 105 °C

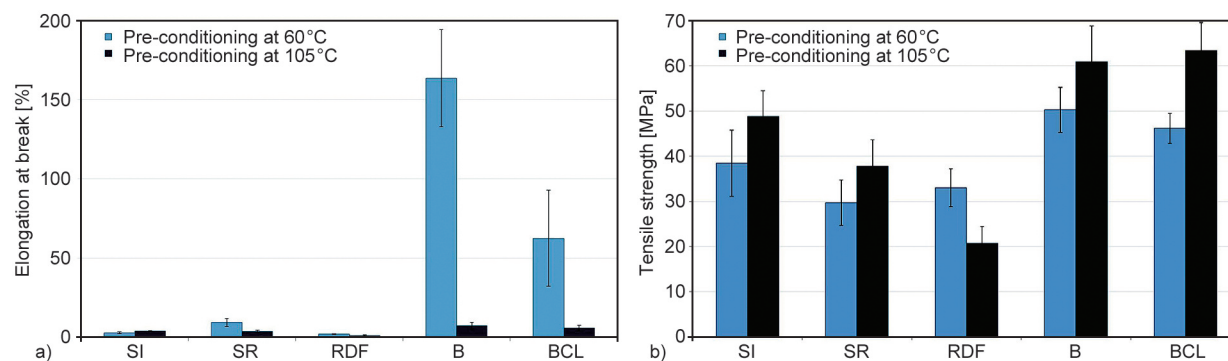


Figure 7. Elongation at break (a) and tensile strength (b) of extruded PET wastes from different sources. (SI – selective income; SR – sorting residue; RDF – refuse derived fuel; B – bottle; BCL – bottle with cap and label).

considering all of the waste PET grades, but the degree of the difference was dependent on the origin of the waste. High EB (approx. 150%) was only observed for the sample of selectively collected just PET material when pre-conditioning was carried out at 60 °C. Favourable EB (62%) was achieved in waste PET containing both cap and label meanwhile the degree of SD indicated inhomogeneity of the samples either. Close cold crystallization temperature was first thought to be responsible for the significant difference in EB of the samples with the same composition because a stiffer material with higher strength was produced, when pre-conditioning had been carried out at 105 °C (Figure 7b).

PET collected selectively (sample B) possessed the highest tensile strength (approx. 60 MPa), which was the less dependent on the pre-conditioning temperature (Figure 7b). The tensile strength of the sample from the PET bottle processed with cap and label together (BCL) decreased by only 10% compared to the one from just PET bottles collected selectively. Standard deviation also reduced, which was presumably caused by processing polyolefins accompanied to the PET [23]. The tensile strength of PET samples derived from the waste sorting plant reached only a maximum 40 MPa if pre-conditioning was at 60 °C before measurements. No significant difference at the same pre-conditioning was observed in the tensile strengths of the recycled PET samples originated from the fractions of SR and RDF. Approx. 30 MPa of tensile strength was achieved for both of the latter, which refers to the tensile strength level of general original polyolefins. Increasing pre-conditioning temperature up to 105 °C resulted in the improvement of tensile strength by an average of 20% increase, which could be basically accounted for

thermal treatment closer to the cold crystallization processes mentioned before except for the RDF. A general conclusion about the homogeneity of a sample can be drawn from the level of the SD for tensile properties. Lower standard deviation referred, on the one hand, to better homogeneity of a sample produced from a waste resource, and on the other hand, to the similar extent of degradation processes within the sample caused by extrusion moulding. Inhomogeneity of a sample, *i.e.* higher standard deviations, may be caused by both quality of the waste material and the degradation reactions occurring during the processing.

Overall, it can be stated that in the later step in the sorting process, the waste PET came from less the pre-conditioning temperature affected EB. Therefore, inhomogeneity and a wide quality range of waste PET were suggested to be the crucial factors and not the cold crystallization.

3.5. Results of computed tomography investigation of the extruded waste PETs

Results shown in Figure 8 demonstrated the potential of X-ray tomography (CT) techniques to investigate the correlation between the source and properties of the wastes as well as the emerging inner structure of the samples. It can be clearly established that the uncontaminated B and BCL samples contain no gaseous inner porosity and inclusions of higher X-ray absorption coefficient (*e.g.* metal contamination) in the detectable size range (above 6 μm). These results highlight that the tensile tests show the real bulk properties of that samples without any influence of inner geometrical inhomogeneities. In the case of real waste, characterized by SI, SR, and RDF extruded rods, the structure is much more complex.

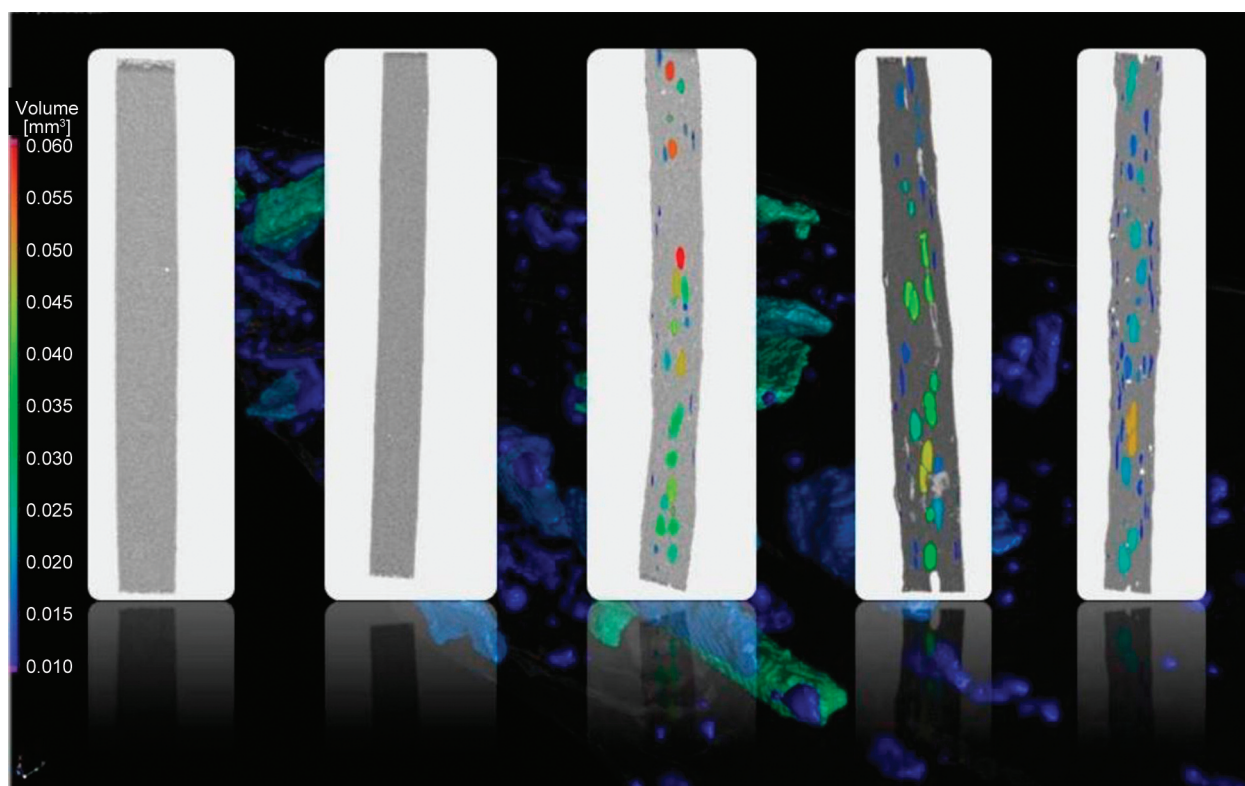


Figure 8. 2D slices produced from the 3D CT measurement of extruded samples. Coloured surfaces characterize the micro-voids of the samples, while bright surfaces (white colour areas) belong to the inclusions. The image used as background is the 3D visualisation example of inclusions in the SR sample. (2D images characterize the results of B, BCL, SI, SR and RDF samples from left to right). (SI – selective income; SR – sorting residue; RDF – refuse derived fuel; B – bottle; BCL – bottle with cap and label).

They contain simultaneously gaseous pores and inclusions of higher atomic numbers (*e.g.* metal particles). Therefore, it is proven that these material systems have to be treated as composite materials during the generally performed material testing techniques. While the material inhomogeneities can enhance the mechanical properties as a particle, a fibre, or plate reinforcement because of the appropriate adhesive forces due to its original task (the background image of [Figure 8](#)), the material vacancies can decrease the material cross-section making weak points in the structure. The voids have a certain degree of crack-stopping role, but investigating elastic material systems does not have a significantly positive influence on the mechanical properties. Summarized, it was proven and supported by the structural analysis, that the organic contamination content of the real plastic wastes produces gaseous voids in the structure because of the heat treatment during the recycling. Furthermore, the inhomogeneities of higher atomic numbers (metals) can be detected with various morphologies depending on the origin of waste.

These parts significantly influence the properties of the produced recycled materials.

4. Conclusions

Due to the effort of the European Union to reduce the amount of single-use plastics and increase the rate of recycled plastic products, especially PET bottles, introduction of a deposit-refund system for PET drinking bottles has been urged. The aim of that study was to investigate recycling of PET wastes, particularly of non-drinking bottle types. The PET wastes were sampled from different real waste streams such as from a selective waste sorting plant, namely its selective income (SI) and its sorting residue (SR). PET waste was also separated from RDF from the MBT plant. The deposit-refund system (DRS) was symbolized by collected in-home bottles with (BCL) and without (B) caps and labels.

Since PET drinking bottles possess higher mechanical strength and elongation than the secondary raw material consisting of all kinds of PET wastes (SI),

in consequence, the introduction of a deposit-refund system on PET drinking bottles is highly recommended. PET bottles are worth selecting into PET-A, PET-B and PET-D fractions. The selective income (SI) containing all kinds of PET wastes and the sorting residue (SR) containing PET wastes except drinking bottles can be extruded at the same temperature profile and extrusion speed. Samples from both aforementioned waste PETs (SI, SR) had the same rheological and mechanical properties indicating on the first hand, that the absence of the PET drinking bottle waste did not cause significant property change and on the second hand, that PET selected from SR can be at least as advantageous secondary raw material as the SI. PET wastes derived from RDF showed the worst processing and mechanical properties. That behaviour was dedicated to the foreign organic compounds bonded to the PET waste unless it was carefully washed and conditioned before extrusion moulding. Based on the results, more serious washing pretreatment was suggested for achieving better performance of PET waste derived from the RDF fraction. X-ray tomography measurements showed a correlation between the source of waste plastic (purity) and the gas void structure (quantity and morphology) which influence essentially the obtained macroscopic mechanical properties.

In conclusion, based on our experimental results, it can be determined that valuable PET waste suitable for recycling is available beyond the drinking-bottles. However, this raises several other questions that need to be studied in the future, such as those summarized in the followings. The willingness of the citizens to engage in selective waste collection, the development of programs related to incentivizing selective waste collection, which can involve both educational activities and financial incentives (e.g. PAYT (pay-as-you-throw), DRS etc.), and the situation of the vulnerable segment of the population involved in collecting recyclable materials to earn some income are all points that need to be examined. These aforementioned aspects are planned to be studied within the framework of a comprehensive study in the future.

Acknowledgements

Supported by the ÚNKP-22-5 New National Excellence Program of the Ministry for Culture and Innovation from the source of the National Research, Development and Innovation Fund. This publication/research has been supported by the National Research, Development and Innovation Office through the project nr. 2022-1.1.1-KK-2022-00002, titled ‘Establishment of a waste management competence center at the University of Pannonia’.

References

- [1] An J., Wu F., Wang D., You J.: Estimated material metabolism and life cycle greenhouse gas emission of major plastics in China: A commercial sector-scale perspective. *Resources, Conservation and Recycling*, **180**, 106161 (2022).
<https://doi.org/10.1016/j.resconrec.2022.106161>
- [2] Grogan A. E., Mallin M. A., Cahoon L. B.: Investigation of polyethylene terephthalate (PET) drinking bottles as marine reservoirs for fecal bacteria and phytoplankton. *Marine Pollution Bulletin*, **173**, 113052 (2021).
<https://doi.org/10.1016/j.marpolbul.2021.113052>
- [3] Kautish P., Sharma R., Mangla S. K., Jabeen F., Awan U.: Understanding choice behavior towards plastic consumption: An emerging market investigation. *Resources, Conservation and Recycling*, **174**, 105828 (2021).
<https://doi.org/10.1016/j.resconrec.2021.105828>
- [4] Kunthawatwong R., Sylisomchanh L., Pangdaeng S., Wongs A., Sata V., Sukontasukkul P., Chindaprasirt P.: Recycled non-biodegradable polyethylene terephthalate waste as fine aggregate in fly ash geopolymer and cement mortars. *Construction and Building Materials*, **328**, 127084 (2022).
<https://doi.org/10.1016/j.conbuildmat.2022.127084>
- [5] Nasir N. H. M., Usman F., Saggaf A., Saloma: Development of composite material from recycled polyethylene terephthalate and fly ash: Four decades progress review. *Current Research in Green and Sustainable Chemistry*, **5**, 100280 (2022).
<https://doi.org/10.1016/j.crgsc.2022.100280>
- [6] Sasao T.: Why is plastic recycling expensive? Hybrid panel data analysis of recyclable plastic containers and packaging in Japan. *Resources, Conservation and Recycling*, **185**, 106505 (2022).
<https://doi.org/10.1016/j.resconrec.2022.106505>
- [7] Singh A. K., Bedi R., Kaith B. S.: Composite materials based on recycled polyethylene terephthalate and their properties – A comprehensive review. *Composites Part B: Engineering*, **219**, 108928 (2021).
<https://doi.org/10.1016/j.compositesb.2021.108928>
- [8] Geyer R., Jambeck J. R., Law K. L.: Production, use, and fate of all plastics ever made. *Science Advances*, **3**, e1700782 (2017).
<https://doi.org/10.1126/sciadv.1700782>

- [9] Kan M., Miller S. A.: Environmental impacts of plastic packaging of food products. *Resources, Conservation and Recycling*, **180**, 106156 (2022).
<https://doi.org/10.1016/j.resconrec.2022.106156>
- [10] Ronkay F., Molnar B., Gere D., Czigany T.: Plastic waste from marine environment: Demonstration of possible routes for recycling by different manufacturing technologies. *Waste Management*, **119**, 101–110 (2021).
<https://doi.org/10.1016/j.wasman.2020.09.029>
- [11] Galati A., Alaimo L. S., Ciaccio T., Vrontis D., Fiore M.: Plastic or not plastic? That's the problem: Analysing the Italian students purchasing behavior of mineral water bottles made with eco-friendly packaging. *Resources, Conservation and Recycling*, **179**, 106060 (2022).
<https://doi.org/10.1016/j.resconrec.2021.106060>
- [12] Penca J.: European plastics strategy: What promise for global marine litter? *Marine Policy*, **97**, 197–201 (2018).
<https://doi.org/10.1016/j.marpol.2018.06.004>
- [13] European Commission: Report from the commission to the European Parliament, the Council, the European Economic and Social Committee and the Committee of the Regions on the implementation of the Circular Economy Action Plan (2019).
- [14] Polyportis A., Mugge R., Magnier L.: Consumer acceptance of products made from recycled materials: A scoping review. *Resources, Conservation and Recycling*, **186**, 106533 (2022).
<https://doi.org/10.1016/j.resconrec.2022.106533>
- [15] Matthews C., Moran F., Jaiswal A. K.: A review on European Union's strategy for plastics in a circular economy and its impact on food safety. *Journal of Cleaner Production*, **283**, 125263 (2021).
<https://doi.org/10.1016/j.jclepro.2020.125263>
- [16] European Parliament: Directive (EU) 2019/904 of the European Parliament and of the Council of 5 June 2019 on the reduction of the impact of certain plastic products on the environment (2019).
- [17] European Commission: Commission implementing decision (EU) 2021/1384 of 13 August 2021 on the request for registration of the European Citizens' Initiative entitled 'ReturnthePlastics: A citizen's initiative to implement an EU-wide deposit-system to recycle plastic bottles' pursuant to regulation (EU) 2019/788 of the European Parliament and of the Council (2021).
- [18] Hungarian Parliament: Act CLXXXV of 2012 on waste (in Hungarian) (2023).
- [19] Hungarian Parliament: Act II of 2021 amending certain laws on energy and waste management (in Hungarian) (2021).
- [20] Boros A., Kurdi R., Lukács Z. P., Sarkady A., Banász Zs.: Opinion of the Hungarian population on the reform of beverage packaging deposit-refund system. *Sustainability*, **13**, 6373 (2021).
<https://doi.org/10.3390/su13116373>
- [21] North-Balaton Waste Management Nonprofit Ltd.: General data request for the last five closed year (in Hungarian) (2022).
- [22] Dorigato A.: Recycling of polymer blends. *Advanced Industrial and Engineering Polymer Research*, **4**, 53–69 (2021).
<https://doi.org/10.1016/j.aiepr.2021.02.005>
- [23] Alsewailam F. D., Alrefaie J. K.: Effect of contaminants and processing regime on the mechanical properties and moldability of postconsumer polyethylene terephthalate bottles. *Waste Management*, **81**, 88–93 (2018).
<https://doi.org/10.1016/j.wasman.2018.09.052>
- [24] Utracki L. A., Wilkie C. A.: *Polymer blends handbook*. Kluwer, Dordrecht (2002).
- [25] Sang T., Wallis C. J., Hill G., Britovsek G. J.: Polyethylene terephthalate degradation under natural and accelerated weathering conditions. *European Polymer Journal*, **136**, 109873 (2020).
<https://doi.org/10.1016/j.eurpolymj.2020.109873>
- [26] Sharifian S., Asasian-Kolur N.: Polyethylene terephthalate (PET) waste to carbon materials: Theory, methods and applications. *Journal of Analytical and Applied Pyrolysis*, **163**, 105496 (2022).
<https://doi.org/10.1016/j.jaap.2022.105496>
- [27] Abuaddous M., Taamneh M. M., Rabab'ah S. R.: The potential use of recycled polyethylene terephthalate (RPET) plastic waste in asphalt binder. *International Journal of Pavement Research and Technology*, **14**, 579–587 (2021).
<https://doi.org/10.1007/s42947-020-0120-2>
- [28] Ameri M., Nasr D.: Performance properties of devulcanized waste PET modified asphalt mixtures. *Petroleum Science and Technology*, **35**, 99–104 (2017).
<https://doi.org/10.1080/10916466.2016.1251457>
- [29] Esfandabad A. S., Motevalizadeh S. M., Sedghi R., Ayar P., Asgharzadeh S. M.: Fracture and mechanical properties of asphalt mixtures containing granular polyethylene terephthalate (PET). *Construction and Building Materials*, **259**, 120410 (2020).
<https://doi.org/10.1016/j.conbuildmat.2020.120410>
- [30] Kabir S. F., Sukumaran S., Moghtadernejad S., Barjasteh E., Fini E. H.: End of life plastics to enhance sustainability of pavement construction utilizing a hybrid treatment of bio-oil and carbon coating. *Construction and Building Materials*, **278**, 122444 (2021).
<https://doi.org/10.1016/j.conbuildmat.2021.122444>
- [31] Xu X., Chen G., Wu Q., Leng Z., Chen X., Zhai Y., Tu Y., Peng C.: Chemical upcycling of waste PET into sustainable asphalt pavement containing recycled concrete aggregates: Insight into moisture-induced damage. *Construction and Building Materials*, **360**, 129632 (2022).
<https://doi.org/10.1016/j.conbuildmat.2022.129632>
- [32] Merkel D. R., Kuang W., Malhotra D., Petrossian G., Zhong L., Simmons K. L., Zhang J., Cosimbescu L.: Waste PET chemical processing to terephthalic amides and their effect on asphalt performance. *ACS Sustainable Chemistry and Engineering*, **8**, 5615–5625 (2020).
<https://doi.org/10.1021/acsschemeng.0c00036>

- [33] Rahman W. M. N. W. A., Wahab A. F. A.: Green pavement using recycled polyethylene terephthalate (PET) as partial fine aggregate replacement in modified asphalt. *Procedia Engineering*, **53**, 124–128 (2013).
<https://doi.org/10.1016/j.proeng.2013.02.018>
- [34] Moghaddam T. B., Karim M. R., Syammaun T.: Dynamic properties of stone mastic asphalt mixtures containing waste plastic bottles. *Construction and Building Materials*, **34**, 236–242 (2012).
<https://doi.org/10.1016/j.conbuildmat.2012.02.054>
- [35] Garcea S. C., Wang Y., Withers P. J.: X-ray computed tomography of polymer composites. *Composites Science and Technology*, **156**, 305–319 (2018).
<https://doi.org/10.1016/j.compscitech.2017.10.023>
- [36] Nagy B., Varga Cs., Kontos K., Simon-Stöger L.: Remarkable role of experimental olefin-maleic-anhydride copolymer based compatibilizing additives in blends of waste PET bottles and polyamide. *Waste and Biomass Valorization*, **12**, 3035–3047 (2021).
<https://doi.org/10.1007/s12649-020-01253-5>